POLITECNICO DI MILANO

Facoltà di Ingegneria dei Processi Industriali
Dipartimento di Energia

Experimental and Modeling Analysis of the Catalytic Partial Oxidation of Light Hydrocarbons at 1-4 bar

Supervisors: **Prof. Alessandra BERETTA**

Prof. Gianpiero GROPPI

Co-examiners: **Prof. Pio FORZATTI**

Ing. Alessandro DONAZZI

Ing. Dario LIVIO

Master Thesis of:
Mattia BOGOTTO 765704
Marco Ferruccio DELLAVEDOVA 770482

Anno accademico 2011-2012

LIST OF CONTENTS

LIST OF FIGURES

LIST OF TABLES

ABSTRACT

In the last two decades the catalytic partial oxidation (CPO) of methane has been extensively studied both experimentally and theoretically. A significant amount of data is available in the literature concerning the catalytic materials, the catalyst stability, the reaction mechanism, the impact of diffusive limitations and the reactor design. Recently, the focus of research shifted toward the study of the CPO of heavier fuels, such as LPG or logistic fuels (gasoline, kerosene, diesel) with interest in potential commercial applications such as the on-board and distributed production of H_2 and syngas. For these fuels, it is generally understood that complete conversion of reactants and high syngas selectivity can be obtained by using Rh-based catalysts supported on honeycomb or foam monoliths and those major challenges concern the catalyst deactivation, in terms of coke production, and the thermal behavior of the reactor, in terms of temperature of the surface hot spot. Thanks to its wide availability and possibility of being stored as a liquid, propane can be regarded as a case molecule for studying CPO of light hydrocarbons.

CPO can be carried out at millisecond contact times, under autothermal conditions to yield high selectivity to syngas. These features allow for the design of simple and compact reactors, with fast dynamic response and low heat capacity, which are ideal for mobile and stationary production of synthesis gas. Despite of these advantages, CPO reactors operate under extremely high gradients of temperature and of composition and with complex fluid and kinetic patterns, where mass and heat transfer are coupled with the surface process. In fact the CPO process mainly occurs as a sequence of exothermic and endothermic steps, wherein the hydrocarbon is partially oxidized and later converted to synthesis gas by endothermic steam reforming. These high surface temperatures can cause a local loss of activity of the catalyst, which produced a dangerous autocatalytic increase of the temperature, ultimately leading to the instable performance of the whole reactor. Because of the presence of these gradients, concentrated at the inlet of the reactor, the behavior of the system could not be fully described by the unique analysis of gas composition at the exit of the reactor. So the spatially resolved sampling technique was herein applied to investigate the process. In literature, there are many references about the evolution of these profiles under conditions of atmospheric pressure; while appears to be little explored, due to experimental difficulties, the evolution under pressurized condition. In particular, data of C_3H_8-CPO tests relating to temperature behavior and concentration profiles are not present. The purpose of this thesis work is the development

of a technique which allows an analysis of the temperature behaviors and concentration profiles in CPO system under pressurized conditions. The spatial resolution technique, based on the introduction of a mobile probe in the reaction environment, is particularly critical in systems operated under pressurized conditions. In fact, the presence of an orifice in which is put the moving capillary, necessary to measure the concentration profiles or temperature behaviors, does not allow the performance of tests under pressurized conditions. In this work, in order to measure the thermal and composition profiles, a new sealing system was developed. It allowed to carry out CPO-tests in a pressure range between 1-4 bar. After the development and the verification of the experimental technique of data collection, the performances of a CPO pilot scale reformer were studied at different pressures. The experimental data obtained with the spatially resolved sampling technique were compared with the simulations obtained by using a monodimensional, dynamic, adiabatic, single channel and heterogeneous model.

The experiments were performed over a 2% wt/wt $Rh/\alpha\text{-}Al_2O_3$ catalysts coated over 400 CPSI cordierite honeycomb monoliths. This geometric configuration was chosen because the honeycomb monoliths offer several advantages: availability in the open literature of methodologies for catalytic deposition in uniform, compact and thin layers, reliability of correlations of heat and mass transfer coefficient even at very low Reynolds numbers, low pressure drops, good heat transfer properties and low heat capacity. The experiments were conducted with a flow rate equal to 10 Nl min^{-1}. The C/O ratio during the CH_4-CPO tests was equal to 0.9, while during the C_3H_8-CPO tests the C/O ratio is equal to 0.85. The behavior of the system was investigated at progressively increasing pressure from 1 to 4 bar. The temperature behaviors, both CH_4-CPO tests and C_3H_8-CPO tests, showed that a variation of pressure, did not change significantly the value of the hot-spot temperature, while the change of temperature appeared to be evident in the last part of the catalyst (downstream the hot-spot), where they reached their respective values of thermodynamic equilibrium. Also the concentration profiles showed a trend in the final section of the catalyst, where the thermodynamic equilibrium was reached: the selectivity to syngas decreases when the pressure increases. However, the concentration profiles of the reactants and products did not show significant changes in the first section of the catalyst (kinetic zone). A detailed modeling analysis was then used as a further investigation tool to understand the chemical-physical mechanisms, at different pressure values, occurring in the first 5 mm of the catalyst.

During the C_3H_8-CPO test, an increase of the concentration values of intermediate species (C_2H_4,C_2H_6,C_3H_6) is showed when the pressure increased. These species showed a peak (in

section between 0,5-0,7 cm of the catalyst) due to an initial production by cracking reaction in gas-phase followed by a consumption of these species.

We verified the consumption of hydrocarbons species, which was due to the steam reforming reactions promoted by the catalyst surface, confirming, with an experimental test, the hypothesis developed in previous work by modeling analysis.

Since, in C_3H_8-CPO tests under pressurized conditions, an increase of carbon deposits was also observed downstream the catalyst.

Some tests were carried out to collect and analyze the carbon deposits, in order to better understand the mechanism of formation. These analysis showed that the CO disproportionation reaction, which is promoted by a catalytic metal surface, is probably the principal way of carbon formation.

ESTRATTO IN LINGUA ITALIANA

Negli ultimi anni l'ossidazione parziale catalitica (CPO) di metano è stata ampiamente studiata sia dal punto di vista sperimentale che teorico. In letteratura vi è una significativa quantità di dati riguardo al catalizzatore utilizzato, al meccanismo di reazione, all'impatto delle resistenze diffusive sul processo e al design del reattore. Recentemente, molti studi sono stati effettuati riguardo la CPO di combustibili più pesanti del metano come il GPL, benzina o diesel per la produzione di syngas (una miscela di CO e H_2) per applicazioni di piccola e media scala. Per questi combustibili, è possibile assicurare una conversione completa dei reagenti ed elevate selettività a CO e H_2 utilizzando catalizzatori a base di rodio supportati su monoliti a nido d'ape (honeycomb) o su schiume.
Uno dei principali problemi è la disattivazione del catalizzatore sottoposto ad elevati stress termici (sintering), e formazione di importanti quantità di coke che possono alterare il comportamento del catalizzatore per fouling. Il propano, grazie alla sua ampia disponibilità e alla possibilità di essere immagazzinato come combustibile liquido, può essere considerato una molecola di riferimento per lo studio della CPO di idrocarburi leggeri.

La reazione di CPO può essere condotta con tempi di contatto dell'ordine dei millisecondi e in condizioni autotermiche, ottenendo elevate selettività a syngas. Queste caratteristiche consentono un design del reattore semplice e compatto con rapide risposte dinamiche e bassa capacità termica. Queste condizioni sono ideali per la produzione di syngas in applicazioni mobili e stazionarie. Nonostante questi vantaggi, i reattori di CPO operano con forti gradienti di temperatura e composizione e con una complessa interazione fra fluidodinamica, processi chimici e processi di trasferimento di calore e materia. Il processo di CPO avviene principalmente con una sequenza di step esotermici ed endotermici, in cui il combustibile è prima di tutto parzialmente ossidato e successivamente convertito a syngas dalle reazioni endotermiche di steam reforming. Come conseguenza, all'interno del volume catalitico si stabiliscono notevoli gradienti di temperatura e composizione. Le elevate temperature della superficie causano perdite di attività del catalizzatore dando luogo ad un pericoloso incremento autocatalitico della temperatura e rendendo instabile il comportamento termico dell'intero reattore. A causa della presenza di questi gradienti il comportamento del sistema non può essere descritto solamente mediante l'analisi della composizione dei gas in uscita dal

reattore. Per questa ragione, nel presente lavoro di tesi è stata applicata la tecnica di risoluzione spaziale.

Questa tecnica consente di seguire direttamente all'interno del reattore l'evoluzione dei profili assiali di temperatura e di composizione, mantenendo il reattore adiabatico.

In letteratura scientifica, sono presenti molti riferimenti riguardo l'evoluzione di questi profili in condizioni di pressione atmosferica, mentre risulta essere poco studiata, a causa di difficoltà sperimentali, l'evoluzione in condizioni di pressioni più elevate. In particolare, non sono presenti dati relativi all'evoluzione dei profili di temperatura e di concentrazione di prove condotte C_3H_8-CPO in pressione. Questo lavoro di tesi ha avuto come obbiettivo principale lo sviluppo di una tecnica che permetta un'analisi degli andamenti dei profili di temperatura e di concentrazione sistemi CPO in pressione.

La tecnica della risoluzione spaziale, poiché prevede l'introduzione di una sonda mobile nell'ambiente di reazione, risulta essere critica in sistemi operanti in pressione. Infatti la presenza di un orifizio in cui viene alloggiato il capillare mobile, necessario alla misura dei profili di concentrazione o che ospita gli strumenti adibiti alla misura dei profili di temperatura, non permette lo svolgimento di test in pressione.

In questo lavoro, per poter misurare i profili termici e di composizione in un reattore che opera in pressione, si è dapprima sviluppato un nuovo sistema di tenuta, che ha permesso lo svolgimento di CPO-test in un campo di pressione compreso tra 1-4 bar.

Dopo lo sviluppo e la verifica della tecnica sperimentale di raccoglimento dei dati, si è studiato il comportamento del sistema CPO in condizioni di diverse pressioni di esercizio. I risultati ottenuti nei test eseguiti con alimentazione di metano e di propano sono stati successivamente confrontati con le simulazioni ottenute dal modello monodimensionale, dinamico ed eterogeneo, adiabatico, a singolo canale sviluppato in precedenti lavori.

Tutti gli esperimenti di CPO sono stati condotti con catalizzatori 2%wt/wt Rh/α-Al_2O_3 depositati su monoliti a nido d'ape di cordierite (400 CPSI). Questa configurazione geometrica è stata scelta poiché offre molti vantaggi: disponibilità di ampia letteratura riguardante le metodologie per la deposizione del catalizzatore, attendibilità delle correlazioni per il trasferimento di materia e calore anche a bassi numeri di Reynolds, basse perdite di carico, buone proprietà di trasferimento di calore e bassi calori specifici.

Gli esperimenti sono stati condotti a 10 Nl min^{-1} mantenendo un rapporto costante C/O di 0.9 nelle prove con alimentazione di metano e un rapporto C/O di 0.85 nel caso di test condotti con alimentazione di propano. Durante queste prove la pressione è stata progressivamente incrementata da 1 a 4 bar. I profili termici, sia nel caso di test alimentati a CH_4 sia nei test

alimentati a C_3H_8, mostrano che una variazione di pressione non comporta variazioni di temperatura significative nella prima sezione del catalizzatore in cui è presente l'hot-spot termico, mentre la variazione di temperatura risulta essere evidente nella zona a valle dell'hot-spot termico dove i profili di temperatura raggiungono i rispettivi valori di equilibrio termodinamico.

Anche i profili di concentrazione mostrano un trend nella zona finale del catalizzatore dove, a seguito del raggiungimento dell'equilibrio termodinamico: si raggiungono selettività minori a syngas con l'incrementare della pressione di esercizio.

Un'analisi modellistica dettagliata è stata quindi utilizzata come un'ulteriore strumento di indagine per comprendere i meccanismi chimico-fisici, al variare della pressione operativa, che avvengono nei primi 5 mm del catalizzatore.

Durante i test CPO condotti con alimentazione di propano, si è evidenziato che l'aumento della pressione comportava anche un aumento di concentrazione nella sezione del catalizzatore compresa tra 5-7 mm di "intermedi idrocarburici": etano, etilene e propilene. Questi mostrano un andamento a massimo dovuto ad una formazione iniziale per reazione di cracking in fase omogenea seguito da un consumo di tali specie.

Tramite prove sperimentali, è stato verificato che il consumo di queste specie (etano, etilene e propilene) è dovuto prevalentemente da reazioni eterogenee di steam reforming promosse dal catalizzatore, che funge da quench chimico pulendo il flusso gassoso da potenziali precursori di soot.

Le prove condotte sulla CPO di propano in pressione, hanno evidenziato aumento di depositi carboniosi a valle del catalizzatore. Per questo motivo, sono state effettuate prove che hanno avuto come obbiettivo la raccolta di questi depositi per effettuare delle analisi morfologiche utili all'individuazione del meccanismo di formazione. Queste analisi, assieme a delle altre analisi di carattere termodinamico, hanno mostrato che il meccanismo di disproporzione del CO, accelerato da una catalisi di tipo metallico, è probabilmente il responsabile di tale formazione.

INTRODUCTION

The production of synthesis gas is of great importance in the chemical industry, because synthesis gas is the feedstock for methanol and Fischer-Tropsch synthesis. An important resource for synthesis gas production is natural gas, which consists mainly of methane. Unfortunately, natural gas occurs often in remote locations, and costly transportation motivates the research to transform it to synthesis gas and finally to transportable liquids. Conventional steam-reforming technology is not suited for decentralized synthesis gas production, because steam reformers are large, expensive plants that cannot be scaled down for small-scale operations in remote gas fields. An alternative to steam reforming is the catalytic partial oxidation, which has received a considerable attention during the last 15 years. In fact, it provides close to 100% methane conversion and syngas yields >90% in millisecond contact times by operating at high reaction temperatures, which in turn can be accomplished by running the process adiabatically. Since the catalytic partial oxidation is fast and exothermic, it is suitable to realize compact reformers, which have a rapid response to transient load demands. These aspects make this process suitable for remote gas field applications, and also for all stationary and mobile applications related to the recent development of a small-to medium scale technology for the production of syngas and H_2. The stationary applications include the production of H_2-rich steams for the fuelling of hydrogen-driven vehicles or residential cogeneration systems, but also for the enhancement of gas turbines performances through the development of H_2 stabilized combustors. On board applications deal with the used of solid fuels cells (SOFTs) for auxiliary power units (APUs) on heavy duty to supply power to auxiliary cab devices (condition systems, GPS) and trailers (cryogenic circuits). On-board generation of syngas may also be applied on conventional ICE vehicles to speed up the cold-start phase of catalytic converters and to serve as reducing gas for NOx trap regeneration and for the SCR of NOx.

The large-industries often works under pressurized conditions, for this reason is important a detailed study of the thermal behavior along the axis of the catalyst. In fact, the pressure can modify the response of heat transfer, mass transfer and surface chemistry, which are typical of the CPO process. Also the gas-phase chemistry is directly proportional to the pressure, which involves a probable carbon formation for condensation of the olefins products. The carbon

deposition can deactivate the catalytic process through the fouling, for this reason is essential a study of these phenomena to guarantee a reliable and durable catalytic process.

In Chapter 1 a review of the state of art of the CPO of light hydrocarbons and its commercial applications are realized.

Chapter 2 describes the pilot-scale reformer, the instruments for data acquisitions, the startup and shut-down procedures and the operating conditions. This chapter also presents the temperature and species probe in the spatial sampling technique, which allow to measure the axial temperature and composition profiles and the preparation and the characterization of Rh-coated monoliths.

Chapter 3 reports the development of the new systems necessary to carry out a CPO-test under pressurized conditions.

Chapter 4 shows the monodimensional, dynamic heterogeneous model of the reactor and the kinetic scheme adopted both for CH_4 and for C_3H_8-CPO.

Chapter 5 describes the CH_4-CPO tests at 1-4 bar, and the comparison between the experimental data with the model prediction.

Chapter 6 describes the C_3H_8-CPO tests at 1-4 bar, and the comparison between the experimental data with the model prediction. Afterwards, an experimental test demonstrates that the C_{2+} species are consumed by steam reforming reaction promoted by the surface of the catalyst.

Chapter 7 displays the thermodynamic analysis about the possible ways of carbon formation and a set of tests carried out to collect the deposits. Afterwards the analysis (TPO, XRD, Raman) on the carbon collected during the C3H8-CPO test are showed.

CHAPTER 1

STATE OF THE ART

1.1 INTRODUCTION

Beginning from the sixties of last century the technologies for the production of energy from fossil fuels had a transition to a new era where the reduction of pollutants was important. In fact the combustion of fossil fuels produces great quantities of carbon dioxide, but also many chemical species some of which are toxic for many living organisms. In this scenario natural gas has gained a position of great importance because of its abundance [1]. In fact according to the International Energy Agency (IEA) the world's energy demand from natural gas, which consists mainly of methane, is expected to increase by 30-40% in a 25 years perspective [2]. Even though the world has large deposits of natural gas, most are located in remote areas and consequently it must be transported across large distances to reach its market with high cost of storage and transportation. Therefore the conversion of methane to more useful and easily transportable chemicals (as liquid) has been given high priority by scientists. But the selective attack of the molecule to break one C-H bond and to substitute a hydrogen with another functional group (for example the group –OH) is difficult because of high CH_3-H(g) bond dissociation energy (439.3 kJ/mol). Different methods of methane activation have been investigated, but yields tend to be low to compete with oil because the products are more reactive than methane. For example in the direct oxidation of methane to methanol, or formaldehyde the maximum yields so far obtained were around 8% and 4% respectively [3]. At this time, the only economically available route for the conversion of methane into more valuable chemicals is via synthesis gas. Synthesis gas can then be converted to paraffin liquid fuels through Fischer-Tropsch reaction on Fe, Co, Ru and similar metals:

$$n\,CO + 2n\,H_2 \rightarrow \left(-CH_2-\right)_n + n\,H_2O \qquad (1.1)$$

or to methanol over Cu/ZnO and then to gasoline by MTG process over zeolite catalyst [4]. Synthesis gas is also used for the production of methanol, dimethyl ether, acetic acid and ox alcohols. Moreover the synthesis gas is a energy carrier from which hydrogen is often produced. In the last years, hydrogen has been the centre of attention of public opinion as a possible 'pole star' of a new energy future because it is a clean vector (if burnt, produces only water)[4].

1.2 SYNTHESIS GAS PRODUCTION

Synthesis gas can be produced from various fossil sources, such as natural gas, naphtha, residual oils, coke from petroleum and coal. Natural gas, however is the raw material of greatest interest. Several commercial processes for production of synthesis gas are available, depending on the purpose of industrial application: steam reforming, partial oxidation, autothermal reforming.

Steam reforming:

$$CH_4 + H_2O \leftrightarrow CO + 3\,H_2 \tag{1.2}$$

The first description of a process for the conversion of hydrocarbons with steam was published in 1868 using CaO as a medium, resulting in the formation of $CaCO_3$ and hydrogen. In 1890 Mond and Langer improved the process by using a nickel catalyst, and it was subsequently used, in combination with Fisher-Tropsch technology, by Germany in World II and South Africa during the Apartheid era for the synthesis of chemical such as fuels and alcohols [2]. The reaction is strongly endothermic (ΔH^0_{298}= 206 kJ mol^{-1}) and leads to gas expansion. This means that it is favored at low pressure and at high temperature. The steam reforming, in industrial practice, is carried out at 900°C at the pressure of 15-30 atm in a fired tube reformers (Figure 1.1), which are fired heater with catalyst (nickel supported on oxide carrier, typically Al_2O_3 or ZrO_2) filled tubes placed inthe radiant part of the heater [6]. The superficial contact time is 0.5-1.5 s, which corresponds to residence times of several seconds. The methane conversion, in steam reactions, is typically in the order of 90-92%, with a synthesis gas composition similar to that determined by thermodynamic equilibrium [4]. The principal disadvantages of the steam reforming is that only the 35-50% of the total energy

input, given by external combustion of the fuel gas, is absorbed by the reforming process. Therefore the heat of fuel gas is usually used in the convective part of the reformer by preheating the feedstock and generating steam, thus bringing the overall thermal efficiency over 85%. Another critical aspect of steam reforming is the formation of carbonaceous residues which can occur according to these reactions:

$$2CO \rightarrow C + CO_2 \tag{1.3}$$

$$CH_4 \rightarrow C + 2\,H_2 \tag{1.4}$$

$$CO + H_2 \rightarrow C + H_2O \tag{1.5}$$

The carbon formation must be prevented for two reasons. Firstly, coke deposition on the active sites of the catalyst leads to deactivation. Secondly, carbon deposits can cause total blockage of the reformer tubes, resulting in the development of 'hot spots' [7]. One of the methods for limiting the formation of carbonaceous species is the use of a high steam/methane ratio in the feed mixture. As an increase in this ratio also involves a cost increase, it is preferable to use the lowest steam/methane ratio compatible with the necessity of controlling the formation of carbonaceous residue. Typical values of this ratio range from 2 to 5, depending on the synthesis gas and use.

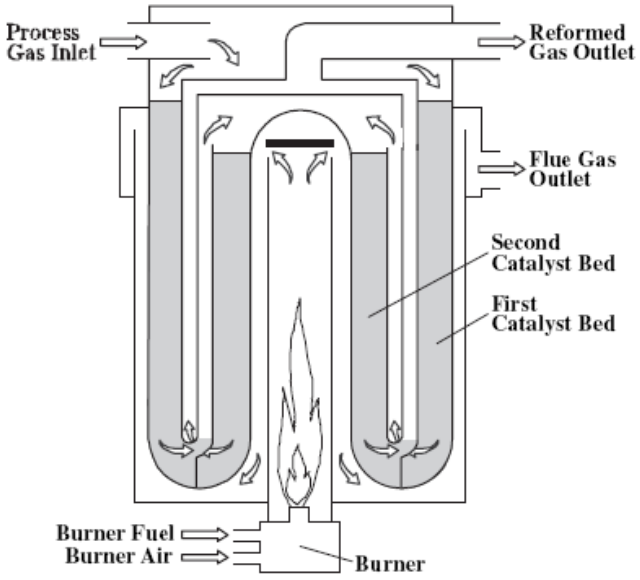

Figure 1.1: Heat exchange reformer.

Non-catalytic partial oxidation

$$CH_4 + \frac{1}{2}O_2 \rightarrow CO + 2\,H_2 \tag{1.6}$$

The reaction is slightly exothermic (ΔH^0_{298} = -37 kJ mol^{-1}), therefore can be performed in burner without the catalyst. In the absence of the catalyst the temperature must be sufficiently high to reach the total conversion of methane, in fact the temperature of the gas at the outlet is about 1000-1100 °C. This process is not suited for small-scale production because it operates at 30-100 atm and with pure O_2 to prevent NOx formation and the high temperature [4].

Autothermal reforming (ATR)

$$CH_4 + \frac{3}{2}O_2 \rightarrow CO + 2\,H_2O \tag{1.7}$$

$$CH_4 + H_2O \rightarrow CO + 3H_2 \tag{1.8}$$

$$CO + H_2O \rightarrow CO_2 + 2\,H_2 \tag{1.9}$$

This process was developed by the Danish company Haldor Topsoe at the end of 1950s. The process combines partial oxidation and steam reaction in a single reactor and in this case the heat for the reforming reaction is supplied by combustion of part of the reactants. The overall reaction is adiabatic, meaning that there is no exchange of heat with the surroundings (except a very limited heat loss). The ATR reactor (Figure 1.2) consists of a burner, a combustion chamber and a catalyst bed, all of which are contained in a refractory lined pressure shell. A mixture of natural gas and steam is partially converted by pressurized combustion under fuel-rich conditions in the combustion chamber. The temperature in the combustion chamber is in the range of about 1100-1300°C near the catalytic bed and up to more 2500°C in the flame core depending upon the process conditions. In the combustion chamber also the steam reforming and the water gas shift take place in homogeneous phase due to the high temperatures. In reality a very large number of chemical reactions take place in the combustion chamber involving radicals. The oxygen is quantitatively consumed by the combustion reactions. However, the methane conversion is not complete in the combustion chamber. In fact the final conversion of methane takes place in the catalytic bed. The synthesis gas leaving the ATR reactor at chemical equilibrium typically between 850 and 1100°C. ATR reactor is soot-free under normal circumstances. The fuel rich combustion takes

place in a turbulent diffusion flame and intensive mixing is required to prevent soot formation. Soot formation is unwanted and would reduce the carbon efficiency of the process, besides soot particles should be removed from the synthesis gas [7].

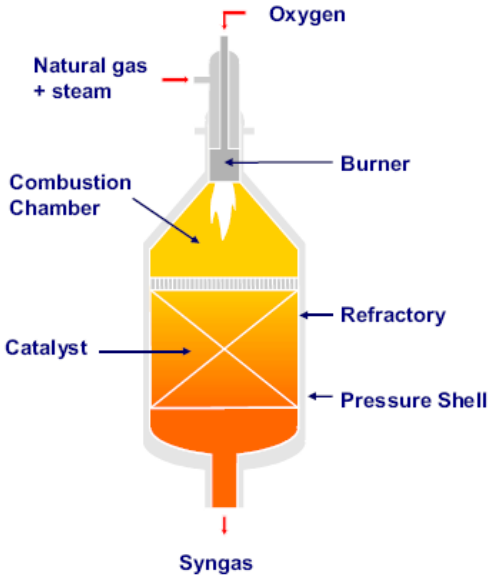

Figure 1.2: ATR reactor.

1.3 CATALYTIC PARTIAL OXIDATION

The technologies described in the previous section are in commercial use today for the production of synthesis gas. However, substantial efforts to develop new technologies are undertaken due to the fact that the most intensive part of large-scale plat is the synthesis gas generation (SGU). The focus is to reduce or to eliminated the used of oxygen and/or to reduce the size of the reactor in SGU [5]. In this respect catalytic partial oxidation (Figure 1.3) has received particular attention because it is one of the most attractive technologies for the production of syngas and hydrogen in small and medium scale [8]. In fact, CPO can be carried out in compact reactors with rapid dynamic response and with low heat capacity, which is ideal for mobile and stationary small scale production of syngas. Besides, the catalytic partial oxidation has thermodynamic advantages with respect to a reforming process [3].

1. The reaction is mildly exothermic (ΔH^{0}_{298}= -37 kJ mol^{-1}), while steam reforming is highly endothermic (ΔH^{0}_{298}= 206 kJ mol^{-1}). Thus, a partial oxidation reactor would be more economical to heat. In addition it can be combined with endothermic reactions, such as steam reforming or dry reforming with carbon dioxide to make this processes more energy efficient.
2. The stoichiometric H2/CO ratio is around 2 and this ratio is ideal for the downstream process avoiding the need to remove valuable hydrogen, which is produced in excess in steam reforming.
3. The gas product has a low content of carbon dioxide, which must often be removed before using synthesis gas downstream.
4. This technology avoids the need for large amounts of expensive superheated steam. However, an oxygen separation plant, which is also expensive, may be required in the cases where nitrogen is undesirable in high-pressure downstream processes. Air can however guarantee the autothermal operation and is desirable in small scale applications.

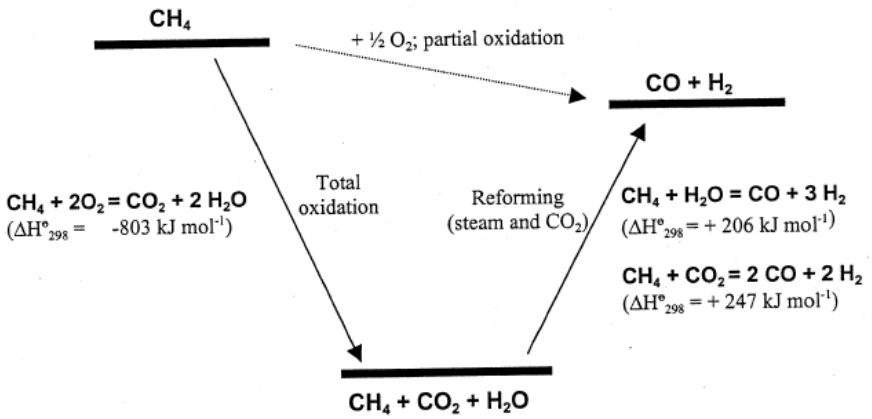

Figure 1.3: Thermodynamic representation of the partial oxidation of methane.

Even though the advantages, previously described, the catalytic partial oxidation has hot spot in the inlet section, which can deactivate the catalyst [9].

1.3.1 CATALYST DEVELOPMENT

The first papers detailing with the catalytic partial oxidation of methane to synthesis gas were published in 1929 by Liander [10], in 1933 by Padovani and Franchetti [11] and by Prettre [12]. However, high yields of synthesis gas were only obtained at temperatures in excess of 850°C. The latter studies showed that below this temperature non-equilibrium products distributions were observed. In addition, carbon formation over the supported nickel catalysts used was not studied in any detail. Because of these factors, as well as the success of the steam reforming process, partial oxidation was left aside for decades. In 1970 Huszar et al [13] examined the importance of diffusion effects during methane partial oxidation by studying the reaction of 25% CH4/air mixture over a single grain of Ni/mullite catalyst in the temperature range 760-900°C. They saw ignition and extinction characteristic of the catalytic system. They observed also that Ni catalyst would deactivate in an oxidizing environment because of $NiAl_2O_4$ formation, but the activity could be partially recovered by hydrogen treatment. They concluded that the formation of H_2/CO required the presence of reduced metallic Ni, achieved by using O_2 deficient condition, and that the kinetics of the overall process were limited by the rate of diffusion of O_2, which at the catalytic surface was essentially zero, allowing the Ni to be maintained in the zero valence state. In the late 1980s Green and co-workers [3] began a renaissance in the study of methane partial oxidation. While investigating trends in the behavior of the lanthanides for oxidative coupling using pyrochlores containing noble metals and rare earth metals, they observed high yields of synthesis gas. This time no carbon could be seen on the post reaction samples, and confirmation of this was obtained by high resolution electron microscopy. This observation prompted a detailed investigation of stoichiometric methane partial oxidation over noble metals, and other catalysts, by a very substantial number of research group. Compared to the early success of methane steam reforming, catalytic partial oxidation remained almost unexplored until 1990. As a consequence, the publications appearing in the 1990s were for the most part concerned with catalyst screening, although the effect of the principal system proprieties such as operating temperature and pressure were also studied. By the ends of 1993-1994the focus began to shift towards improving the catalyst stability and performance. A more important results was reported by Hickmann and Schmidt [14,15] who studied the reaction using an adiabatic short-contact time reformer at atmospheric pressure with catalyst based on noble metals and they obtained conversions near to the thermodynamic equilibrium.

In conclusion, the experimental studies up 1993-1994 revealed several important aspects in catalytic partial oxidation of methane as the effect of nitrogen dilution and total pressure, an apparent thermodynamic limitation, mass transfer limitations and the importance of accurate temperature measurement [16]. The first simulation of methane partial oxidation over Pt and Rh surfaces were given by Hickmann et al. [17]. The model consisted of elementary steps including adsorption, desorption and surface reactions. Presently, the research for the process of catalytic partial oxidation regards:

- the optimization of the catalyst and the support;
- the reaction mechanism;
- the optimal reactor design.

Recently, the catalytic partial oxidation of logistic fuel such as gasoline and diesel has gained particular attention due to its potential to provide the fuel for on-board and on-site fuel cells. Reliable long-term applicability of CPO of logistic fuels called for a better understanding of the complex interaction between gas phase and surface precursor reactions, homogeneous gas-phase reactions as well as mass and heat transfer. The major experimental challenge is the complexity and variability of the fuel composition, which demands for rapid screening of CPO of many fuel components and mixture, that means a rapid analysis of the product composition is needed to study many components and mixtures at varying parameters. Besides, although physical proprieties of logistic fuels are regulated by several specifications, the chemical composition is varying within broad ranges, affected by the feedstock of the refinery or geographic/seasonal customization of the fuel. Consequently, the studies of the catalytic partial oxidation of logistic fuels are commonly restricted either on the detailed investigation of simple reference fuels, which can be a single-component, such as i-octane or on the parameterization of empirical models to describe reactor performance [18]. Also the propane is drawing attention in hydrogen production studies because it is a constituent of LPG.

Moreover, due to its composition (short aliphatic C3-C4 chains and absence of sulphur or other electronegative atoms), LPG is reported to present some significant advantages compared to heavier feedstock, especially in terms of catalytic resistance to deactivation led by limited carbon deposition. The catalytic partial oxidation of propane is more exothermic than that of methane and autothermal applications can be realized easily, but it is necessary to identify the operating conditions. In fact modeling studies, as reported by Tavazzi et al. [19]

showed that concentrated propane/air mixtures caused temperature peaks of the surface near 1000°C, which are expect to irreversibly deactivate the catalyst. Independent of the downstream process, the reactor should be operated at pressure of up to 40 bar where the ideal pressure depends on the specific downstream technology. in recent years L.D Schmidt and co-workers published a study of the CH_4-CPO under pressurized conditions [71]. they investigated the effect up to 55 bar over Rh coated foam monolith at a carbon to oxygen ratio of 1 and found that the selectivity to syngas and conversion were no affected significantly over this pressure range. They had shown that on Rh catalyst the effect of pressure is negligible up to at least 1.1 MPa at constant mass flow rate. This is due to mass transfer limitations, which are not affected at constant mass flow rate by pressure (Figure 1.4).

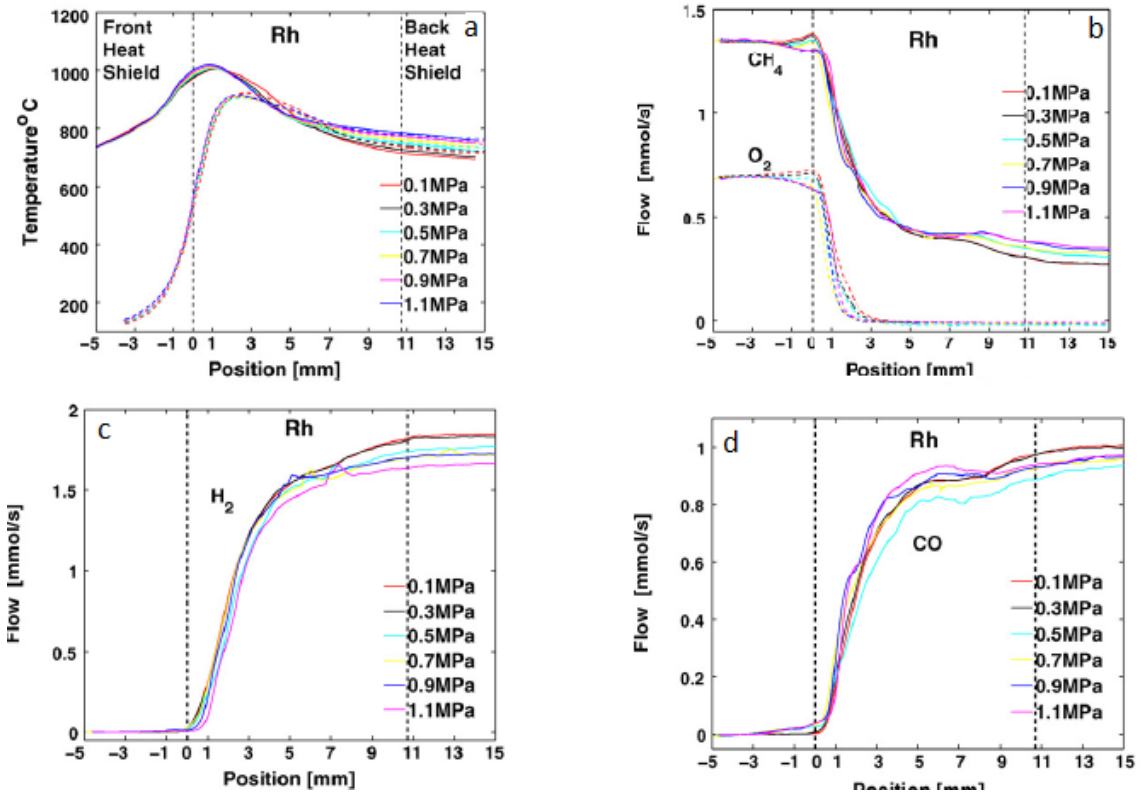

Figure 1.4: Temperature and composition profiles through the catalyst as measured by the pyrometer (surface, T_{pyro}) and thermocouple (gas, T_{TC}) [panel a]; CH_4 and O_2 [panel b]; H_2 [panel c], and CO [panel d] at pressure from 0.1 to 1.1 MPa at constant mass flow rate.

The implementation of the technology CPO with heavier hydrocarbons has revealed the formation of soot, this topic is relevant for CPO under pressurized condition because the pressure can increase the rate of reaction of carbon formation. C.T. Goralsky and L.D. Schmidt [72] said that at higher operating pressure homogeneous chemistry should play a larger role because gas phase chemistry scales with P^2 . Deutchman and co-workers [73] also

studied gas-phase reaction on catalytic reforming with higher hydrocarbons and they demonstrated the importance of the study of the gas-phase chemistry to better understand the carbon formation and the deactivation of the catalyst by fouling phenomena.

1.3.2 REACTION MECHANISM

The mechanism for the catalytic partial oxidation of methane to synthesis gas has been the subject of a debate which to date is still not completely settled. Two distinct mechanisms have been proposed for explaining the formation of syngas [3].

- *Direct oxidation mechanism*

This mechanism, also called pyrolisis-oxidation, assumes that H_2 and CO are primary reaction products formed in the oxidation zone at the catalyst entrance. This mechanism assumes that a dissociative adsorption of CH_4 with the formation of carbon species and H adatoms occurs at the entrance. Then surface carbon reacts with surface oxygen to CO and hydrogen atoms combine to H_2. So the basic reactions are:

$$CH_4 \rightarrow C_S + 4H_S \tag{1.10}$$

$$C_S + O_S \rightarrow CO \tag{1.11}$$

$$H_S + H_S \rightarrow H_2 \tag{1.12}$$

The by-products CO_2 and H_2O are formed by their combustion between oxygen and H_2 and CO, but also for the reaction of methanation:

$$H_2 + \frac{1}{2}O_2 \rightarrow H_2O \tag{1.13}$$

$$CO + \frac{1}{2}O_2 \rightarrow CO_2 \tag{1.14}$$

The main evidence in favour of the direct path is the observation of syngas at extremely short time, in presence of unreacted O_2 [20]. H_2O and CO are in this case interpreted as non-selective oxidation products.

- *Indirect oxidation mechanism*

This mechanism, also called combustion-reforming, postulates two-zone model with strongly exothermic CH_4 combustion at the catalyst entrance, followed by strongly endothermic steam and CO_2 reforming downstream. In this reaction mechanism the synthesis gas is the secondary product. Therefore the reactions are:

$$CH_4 + 2O_2 \rightarrow CO_2 + 2H_2O \quad (1.15)$$

$$CH_4 + H_2O \rightarrow CO + 3H_2 \quad (1.16)$$

$$CH_4 + CO_2 \rightarrow 2CO + 2H_2 \quad (1.17)$$

One major proof of the existence of such an exothermic-endothermic sequence has been the observation of sharp hot-spot temperature at the entrance or on reduced syngas yields and increasing total oxidation products with decreasing time contact time [21].

Published mechanism studies follow essentially two approaches. One approach is due to the study methane CPO under realistic conditions (high catalyst temperatures and atmospheric or elevated temperature). Typically, in this studies the reaction mechanism is inferred from the outlet concentration. Such an approach is claimed to be not rigorous for the kinetics analysis, since frequently both direct and indirect scheme can equally justify the data. Another approach uses well-defined isothermal lower-pressure or diluted conditions different from the technical application. An example is the TAP experiment with isothermal conditions, either under vacuum or diluted atmosphere. Depending on the experimental conditions, different product development is inferred and different mechanistic conclusions are drawn. Recently, a new capillary sampling technique combined with a quadrupole mass spectrometry has been developed and applied in autothermal reactors over Rh and Pt foams [22-25]. Spatial and temporal resolved data have been collected inside the catalyst bed under both transient and steady-state conditions. The results have shown that the reactor can be divided into a short, initial oxidation zone, where H_2 and CO are produced by direct oxidation in the presence of gas phase O_2, followed by a reforming zone where the syngas are formed by steam reforming.

Tavazzi and at. [26] had carried out a kinetic study of CH_4-CPO over Rh catalyst at low Rh load using an isothermal annular reactor, wherein heat and mass transfer artifacts are

minimized and high space velocities allow to skip the thermodynamic control. Strong pieces of evidence were obtained in favour of an indirect kinetic scheme because of:

- shape of the temperature profiles where a maximum was always present at the beginning of the catalyst, followed by a progressive decrease of the temperature along the layer, consistent with the occurrence of an exothermic-endothermic reaction sequence;
- the selectivity to H_2 decreased markedly at increasing GHSV (gas hourly space velocity).

The data could be described by a scheme consisting of methane oxidation, reforming reactions, the reversible WGS reaction, and the consecutive oxidations of H_2 and CO.

1.3.3 CATALYSTS

The production of synthesis gas by oxidation reactions can be performed in the short contact time regime. Short contact times reactors hold the promise of greatly reducing the reactor volume. Short contact times can be reached by using structured catalytic system where the catalytically active materials are deposited on the structured ceramic or metallic substrates. This group of structured catalyst includes monolithic catalysts with honeycomb structure, ceramic foams, corrugates-plate catalyst with cross-flow or parallel channels as well as metallic gauzes. The honeycomb monoliths result in much shorter start up because of their better heat transfer proprieties and lower heat capacity. Also, at flow rates of practical interest, honeycombs performer better than packed beds in terms of conversion, selectivity and pressure drops. The effort to minimize the pressure drop over the catalytic system led to the development of corrugates monolithic reactor based on FecrAlloy (Figure 1.4), an alloy containing aluminium (0.5-12%), chromium (20%), yttrium (1-3%), iron and kanthal (an alloy containing aluminium, chromium, cobalt and iron). Additionally, honeycomb monoliths offer several advantages for experimental investigations and its quantitative analysis; among them representativeness of the laboratory-scala data; avaibility in the open literature of well-established methodologies for catalytic deposition in uniform compact and thin layer and the ability to monitor the axial temperature profiles along the channel by means of multiple thermocouple and the reliability of correlation for heat and mass transfer coefficient even at very low Reynolds number. Most of these aspects make honeycombs preferable to foams for the kinetic investigation.

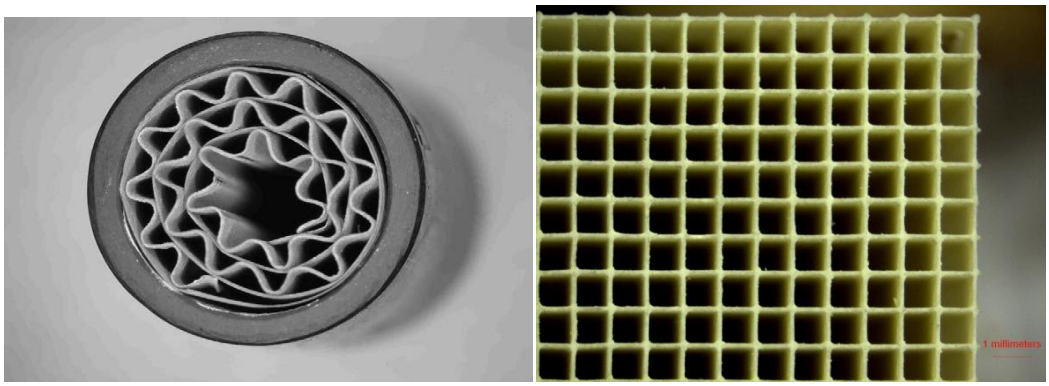

Figure 1.5: Corrugate monolith (left) and cordierite honeycomb monolith 600 CPSI (right).

A large number of different catalyst have been suggested for the catalytic partial oxidation of methane. Noble metals, nickel, and to a lesser extended cobalt are active in the CPO process. However, not all these catalyst are stable on a long term basis and the choice of a particular metal is often a balance between several critical parameters. These parameters comprise the catalytic activity and the long-term stability, the selectivity towards synthesis gas production, a lower propension towards unwanted side-reactions (especially carbon formation), the sensitivity towards sulphur poisoning and the price of the active element. Nickel catalysts show the highest activity, and they are attractive due to their low price. However, nickel catalyst are particularly sensitive to sulphur poisoning and to thermal sintering. Noble metal are generally recognized as superior in terms of activity and stability in CPO of methane as compared to metal based transition catalyst, but there are marked difference between the individual noble metals. Palladium is prone to rapid carbon formation at low O_2/HC stoichiometries leading to a build-up of pressure drop over the catalyst, but also catalyst based on platinum has revealed a propensity toward carbon formation [27]. A stable catalytic performance with low (<400°C) light-off temperatures in the CPO process can be obtained using rhodium, but often the rhodium price is prohibitive for large-scale facilities. Palladium, ruthenium and iridium catalyst are considerably less active than rhodium catalyst, but exhibit sufficient activity for many practical applications [28]. It was proved that the best noble metal is rhodium because of the high selectivity to H_2, the low volatility and the resistance to coke formation [15].

Many of the critical parameters for the choice of the active phase metal also depend on the choice of the support as specific metal-support interactions can influence the reducibility of a metal oxide or stabilise the particle dispersion of the metal. Widely investigation support phase are ZrO_2, TiO_2, CeO_2 and Al_2O_3. The optimal support would maintain the dispersion of

the active phase and would ensure thermal stability also in severe operating condition. It was proved that Rh/α-Al_2O_3 is a catalytic system adapted for the partial oxidation of methane to synthesis gas [29].

Other aspect of catalyst proprieties such as selectivity may also come into play when choosing a catalyst for industrial applications. The selectivity to higher hydrocarbons is important as they are prone to polymerize and form carbon in downstream equipment. The phenomenon is most pronounced when pure oxygen is applied as oxidiser, while negligible amounts are formed with air as the oxidant and using platinum or rhodium [28]. Besides, the effect of temperature on the homogeneous reactions is important.

In Table 1.1 are reported the principal geometry and catalyst proposed in literature.

Catalyst	**contact time**	**reference**
Sponge		
Rh	100	[30]
Pt	100	[30]
Sinlge gauze		
Pt	0.21	[31]
Pt/10% Rh	0.21	[14]
Foam		
11.6% wt% Pt	0.5	[15]
4 wt% Pt	1	[33]
4 wt% Rh	1	[33]
9.8 wt% Rh	<10	[15]
0.56 wt% Rh	<10	[15]
9.9/9.9 wt% Rh/Pt	<10	[15]
0.1 wt% Pt	40	[32]
0.1 wt% Rh	40	[32]
0.1 wt% Rh	75	[34]

Honeycomb monoliths		
1.5 wt% Pt	10	[15]
1.5 wt% Rh	140	[15]
5 wt% Ni	70	[35]
5 wt% Pd	70	[36]

Table 1.1: Catalyst and geometry used in the experimental studies of CPO of methane.

The hydrogen production from catalytic partial oxidation of propane was studied by Venvik and at [36] in alumina foams and microchannel metallic monolith (Frecralloy). The temperature profiles obtained along the catalyst/reactor axis under comparable condition show that the gradient are smaller in the Rh/Al_2O_3/Fecroalloy microchannel reactor than in the Rh/Al_2O_3 foams. Besides, the Rh/Al_2O_3 foams show significant deactivation upon a few temperature cycles under reactant exposure, while no deactivation is observed for the Rh/Al_2O_3/Fecroalloy microchannel reactor.

1.4 CPO TECNOLOGICAL APPLICATIONS

The catalytic partial oxidation, as previously mentioned, is suitable for stationary and mobile application related to the development of a medium to small scale technology for the production of syngas and H_2.

1.4.1 FUEL CELLS

The CPO can be used in fuel cell, in particular in molten carbonate fuel cells (MCFC) and in solid oxide fuel cell (SOFC) because these types run on a mixture of hydrogen and carbon monoxide and they have resistance to poisoning by impurities in the fuel. Therefore it is possible to operate the cell directly on hydrocarbon fuel without the need of a system to remove all the trace of CO. The SOFCs are more used because of the freedom in the carrying out forms and volumes.

The solid oxide fuel cell is characterized by having a solid ceramic electrolyte, which is a metal oxide. The basic component of the SOFT are the cathode, at which oxygen is reduced to

oxide ions, which then pass through the solid electrolyte under electrical load, to anode, where they react with the fuel, hydrogen and carbon monoxide, producing water and CO_2, as well as electricity and heat (Figure 1.6). The theoretical maximum efficiency is very high, in excess of 80%. The SOFC operates at elevated temperature, conventionally between 800-1000°C. In small-scale devices being developed for stand-alone or remote applications, oxygen or air is used as oxidant rather than steam to convert the fuel in syngas. In fact the cost and the complexity associated with using large quantities of stem, which makes its use less favourable in small-scale applications. In fact, the use of the oxygen, or air, is much simple and cheaper in terms of configuration and manufacture. However, it leads to an inherent efficiency due to the large energy loss in oxidising the hydrocarbon. Besides, if an excess of oxygen is used then will be the a tendency for full oxidation to CO_2 and H_2O, which cannot be electrochemically oxidised and so there is a further loss of efficiency compared to the using steam as oxidant. Although for most SOFCs under normal operation steam will be used to internally reformer the natural gas, self-sustained internal reforming is precluded during the start-up from cold and the operation at low power levels because of the strongly endothermic nature of steam reforming. While the partial oxidation of hydrocarbons, being exothermic, offers the potential for the start-up and self-sustaining operation of internally reforming SOFTs running on natural gas or other hydrocarbons at lower power [37].

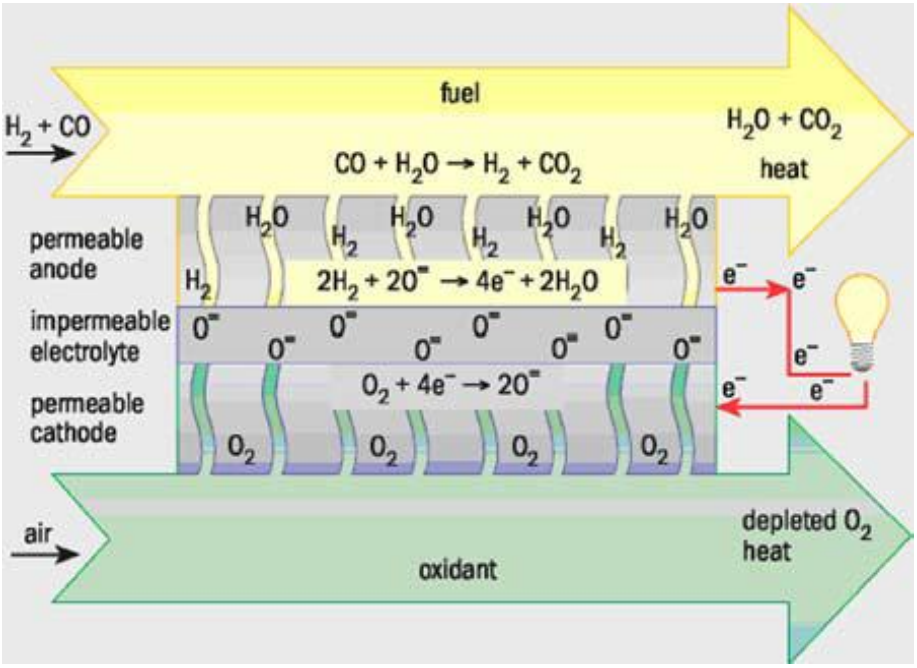

Figure 1.6: Operating principle of a solid oxide fuel cell.

Delphi automotive system has developed a gasoline fuelled APU (auxiliary power unit) on base of a solid oxide fuel cell stack (SOFC) [38]. In passenger vehicles, it is intended to supply energy to the vehicle electrical system and to power an air conditioning unit. At the current stage of the development the system has an output of around 2kW. The overall system is comparably compact, featuring a power density upper 33 Wl^{-1}. Also APU concepts have been presented, that combine a PEM fuel cell (polymer electrolyte membrane) with a fuel processor, enabling the use of a variety of hydrocarbons instead hydrogen. Contrary to the SOFC the PEM requires a carbon monoxide free anode gas supply. Hence, the fuel processor are rather complex, because aside from the reformer a carbon monoxide cleaning unit has to be integrated. In comparison to APU applications these system have a much higher power output ranging above 50 kW and reach much higher power density. The fuel cell-based auxiliary power unity (APU) can be designed for much higher power outputs with a much efficiency compared to the conventional electrical power generation in today's internal combustion engines via engine and generator. APU allows to be independent from engine operation and electrical energy is available any time, even when engine is turn of.

1.4.2 CATALYTIC COMBUSTION

The CPO is also studied for power application. In fact it can be used within gas turbine combustor. This system is composed by a compressor, a combustion chamber and a turbine (Figure 1.7).

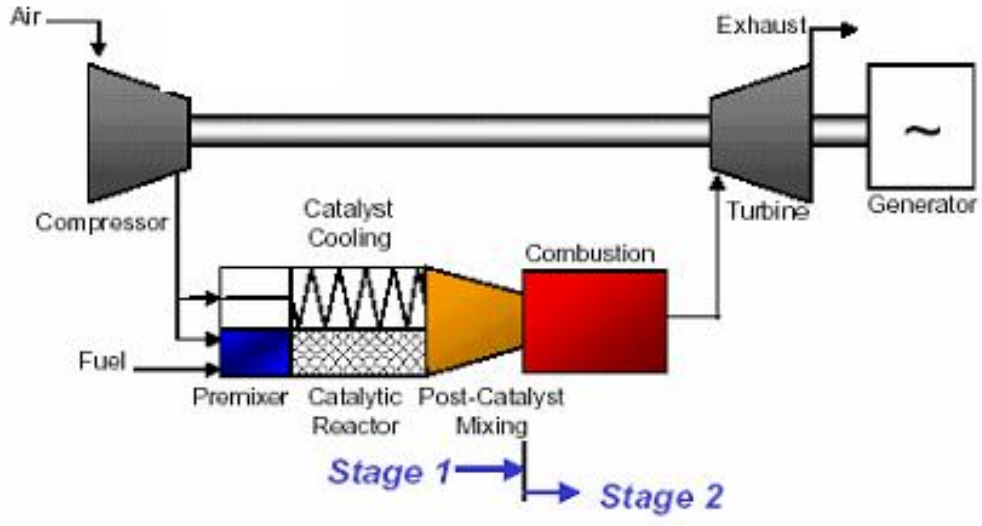

Figure 1.7: Flow diagram of gas turbine combustor.

The combustion chamber with rich catalytic learn burn (RCL) is based on two step (Figure 1.8) [39]:

- Catalytic partial oxidation in rich condition, where only a portion of the inlet air (15%) is mixed with the fuels. While the remaining air is mixed with the stream coming from the catalyst exit cooling the catalyst. During this phase there is not NO_x emission.
- Homogeneous combustion operating in very weak conditions. Due to high dilution combustion, with H_2 high percentage, is done at low temperature, thus reducing NO_x emission.

The RCL process allows to work outside the inflammability limit, to prevent the pre-light off or flame flashback, to reduce the deactivation of the catalyst because the excess of fuel reduces the area surface oxidation and the metal volatility. Finally the operations in rich region are more tolerant of variations in both air and fuel flow.

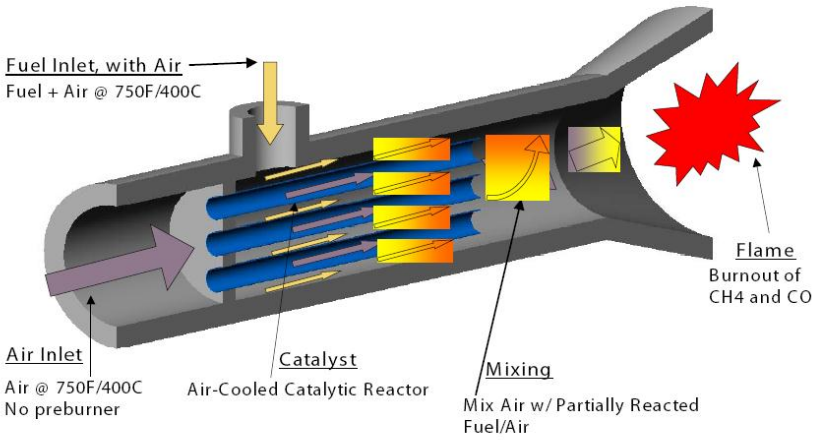

Figure 1.8: RCL combustion system.

CHAPTER 2

LAB-SCALE REFORMER AND EXPERIMENTAL PROCEDURES

2.1 INTRODUCTION

In this work the CPO experiments are performed in a pilot-scale reformer, placed under fume hood: the rig is capable of feeding mixtures of methane (or propane)/air up to 45 Nl min^{-1}. In the first part of the chapter, the pilot-scale reformer (Figure 2.1) and the instruments for the data acquisition will be described. Afterwards, the start-up and shut-down procedures and the operating conditions will be explained. Finally, the last two paragraphs will present the preparation and the characterization of Rh-based catalysts.

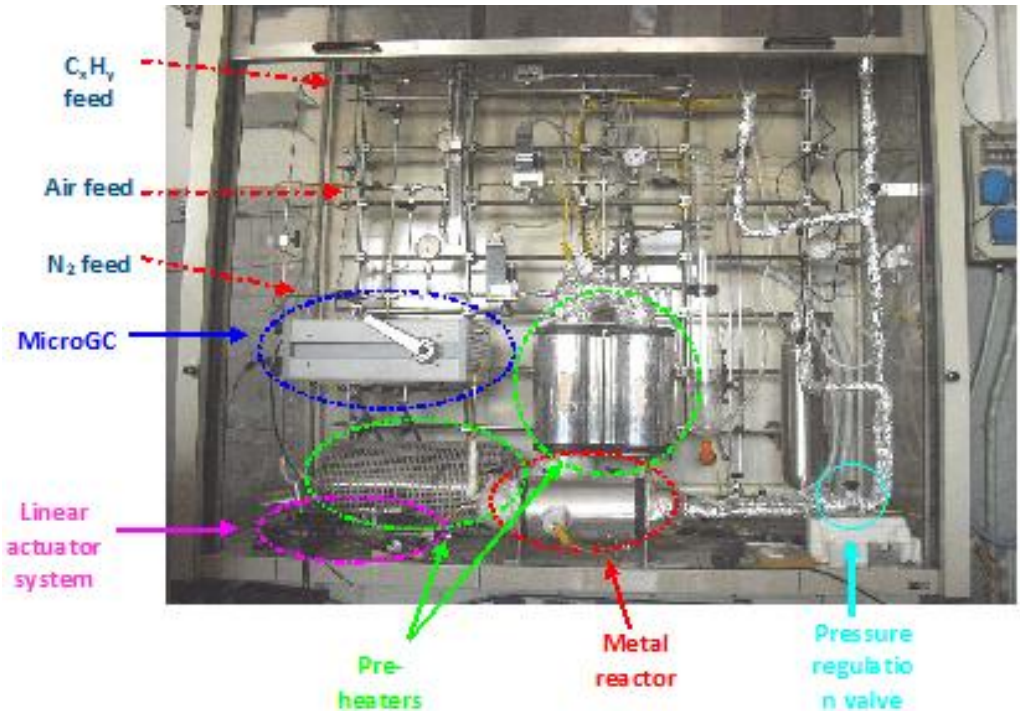

Figure 2.1: Pilot-scale reformer.

The experimental rig, reported in Figure 2.2, can be divided in three different sections: feed, reaction and gas analysis. These sections are connected through stainless steel lines of ¼ inch nominal diameter.

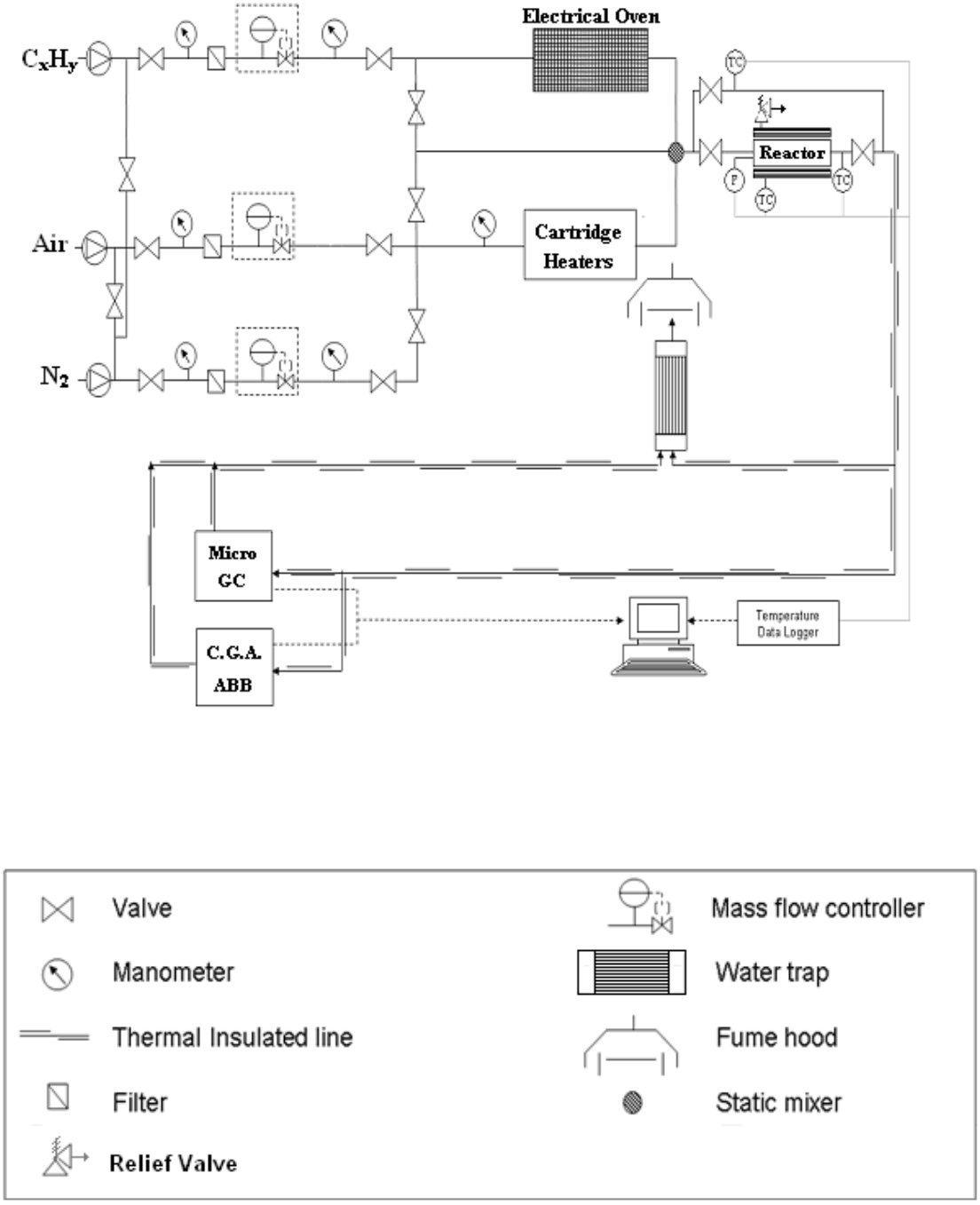

Figure 2.2: Experimental rig.

2.2 FEED SECTION

In the feed section three different lines are present, which feed the gas flow to the reactor:

- the first line is used to feed methane or propane, stored in gas tanks outside the laboratory;
- the second line is used to feed air, stored in gas tanks outside the laboratory, connected in parallel to ensure a continuous flow ;
- the third line is used to feed nitrogen coming from a liquid nitrogen tank outside the building.

The nitrogen line is connected with lines of the reactants in order to feed high flow of nitrogen during the preheating and the shut-down procedures.

The gas tanks are equipped with pressure reducers, which allow to decompress the gas from the storage pressure (200 bar) to the operating pressure (5.5 bar). Each feed line consists of:

- Intercept valve (placed at the beginning of the feed line) on the low pressure line coming from the gas tank;
- Bourdon pressure gauge (with a full scale of 7 bar);
- Rotameter (only for CH_4/C_3H_8 and air lines) which allows to have an immediate evaluation of the flow in the line;
- Metallic mesh filter to protect the equipment from gas impurities;
- Digital mass flow controller (DMFC);
- Bourdon pressure gauge;
- Intercept valve.

The digital mass flow controllers are of 5850S by Brooks Instruments with maximum flow equal to:

- 15 $Nlmin^{-1}$ calibrated on methane;
- 30 $Nlmin^{-1}$ calibrated on air;
- 15 $Nlmin^{-1}$ calibrated on carbon dioxide.

The mass flow controllers of fuel and air are connected to PC and controlled via Brook Smart Control software. Only the mass flow controller on the nitrogen line is controlled with a manual knob. For every mass flow control a calibration line is obtained measuring the volumetric flow of the gas, through bubble flowmeter, at increasing the set point of DMFC opening. The slope and the intercept of the calibrated line are obtained by linear regression of the experimental data. We calibrate every instruments at different pressure.

An example of calibrated line is reported in Figure 2.3.a and in the Figure 2.3.b for propane:

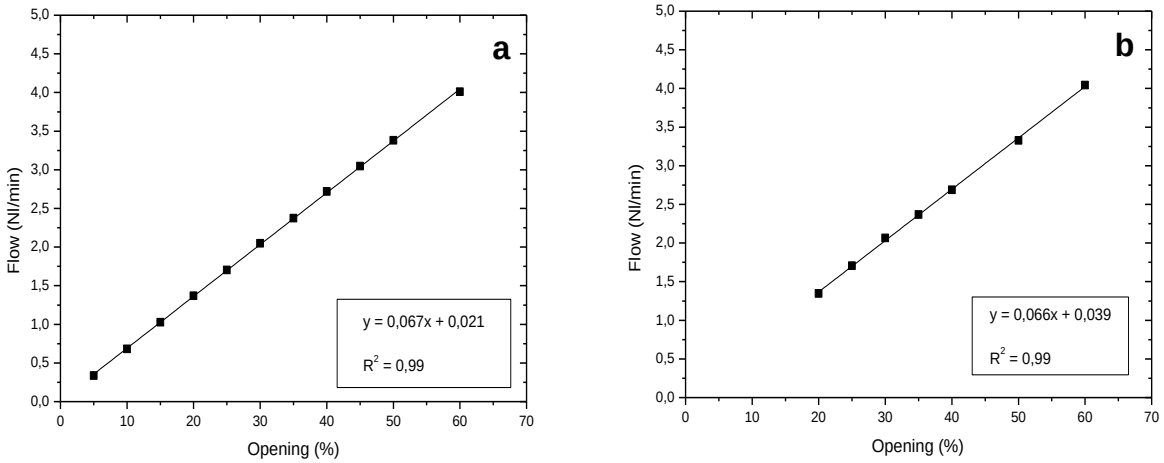

Figure 2.3: Calibrated line for DMFC of Propane @ 1 bar (panel a), @ 3 bar(panel b).

The feed section is also equipped with a separated preheating system of the reactants flows:

- On the air feed two Watlow® Starflow cartridge heaters are present, whose electrical resistance allows a maximum temperature of 650°C and 800°C respectively;
- On the fuel feed an electrical oven is installed, which is divided in three zones, with three independent temperature controllers connected to thermocouples.

For safety reason we feed nitrogen to both the pre-heater systems and we run experiments in autothermal condition (describes in paragraph 2.5.1): in order to avoid to enter into the flame limits.

In order to limit the heat dissipation, every line is thermally insulated with a thick layer of quartz wool and then with a tape made of glass wool. Right before the reactor, the reactants are mixed in a Sulzer® static mixer.

2.3 REACTOR

The reaction section is composed of the lab-scale adiabatic reformer which can process higher flows than those feed in a normal lab-scale rig. The reactor is a quartz tube in order to prevent coke formation and it can be isolated through a by-pass line and two intercept valves. The quartz tube has a length of 11.7 cm, an inner diameter of 2.5 cm and an outer diameter of 2.8 cm. It is inserted in a stainless steel cylinder which allows the connection with the feed lines. The thermal insulation is obtained by wrapping the reactor with a very thick layer of quartz wool taping.

Inside the quartz tube, there is the catalytic bed which is Rh/α-Al_2O_3 supported on 400 CPSI cordierite honeycomb monolith. Cordierite is a ceramic material ($2MgO{\cdot}2Al_2O_3{\cdot}5SiO_2$), which is considered a good support because it does not interact with the washcoat layer, it has low coefficient of thermal expansion and high thermal stability due to high melting point (1450 °C).

The typical internal layout adopted in the CPO tests (Figure 2.4) is obtained by a previous optimization study [40] and consists of:

- FeCrAlloy® foam (total length of about 2.2 cm), acting as flow mixer and front heat shield, minimizing axial heat dispersions;
- void space (about 1.0 cm long), it allows to achieve a good mixing of the gas;
- catalytic monolith (about 2.6 cm long);
- void space (about 1.8 cm long) with the same function of the void space before of catalytic bed;
- inert cordierite monolith (about 1.8 cm long), which has the function of back heat shield.

The quartz tube and all the part inside are wrapt in a Dalfratex® tape to prevent by-pass. This material is composed of quartz filaments and it combines the flexibility of the fibrous structure with the refractory propriety of quartz. This tape can resist up to 1000°C continuously and up to 1600°C for limited time periods.

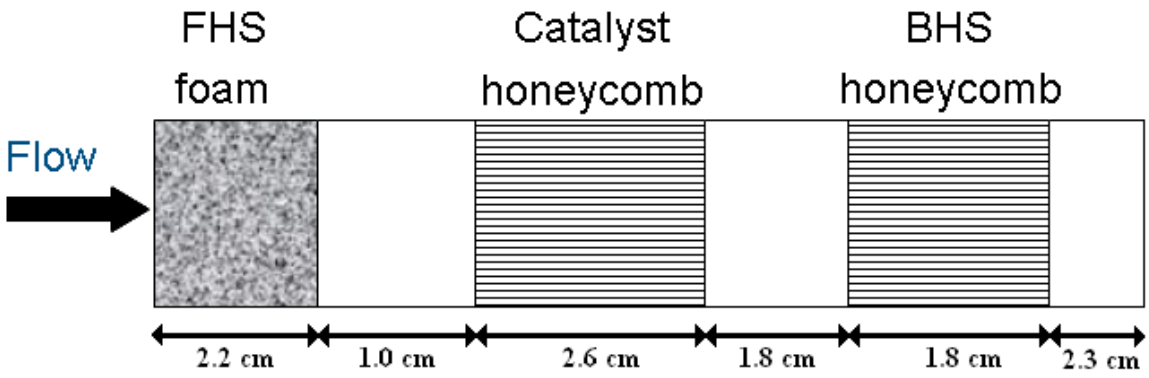

Figure 2.4: Standard configuration.

In this work, other configurations are also studied in order to analyze the carbon deposition. These configurations differ from the standard one for the length of the empty space and for the insertion of filters behind the BHS (Figure 2.5):

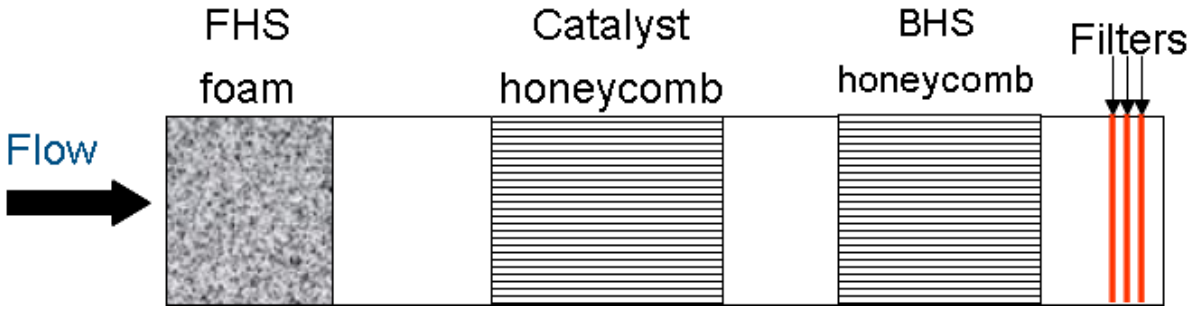

Figure 2.5: Coke analysis configuration.

Temperature measurements are acquired by telescopic or capillary thermocouple, whose values are automatically recorded by a temperature data recorder of Pico® technology. Furthermore, for the acquisition of the temperature of the surface of the catalyst a pyrometer with optical fiber is used. The pyrometer is an IGA5-LO model of Impact Mikron Infrared.

The reactor is equipped with two K – type thermocouples as shown in Figure 2.6. The thermocouples are sheathed in Inconel®. Even if Inconel® is composed of about 70% nickel (a very good steam reforming catalyst. One of these thermocouples is placed in a steel sheath and measures the radial inlet gas temperature at about 7 cm from the inlet section of reactor. The telescopic thermocouple is placed downstream of the reactor (back TC) and can slide in a central channel of the monolith, measuring the axial temperature profile.

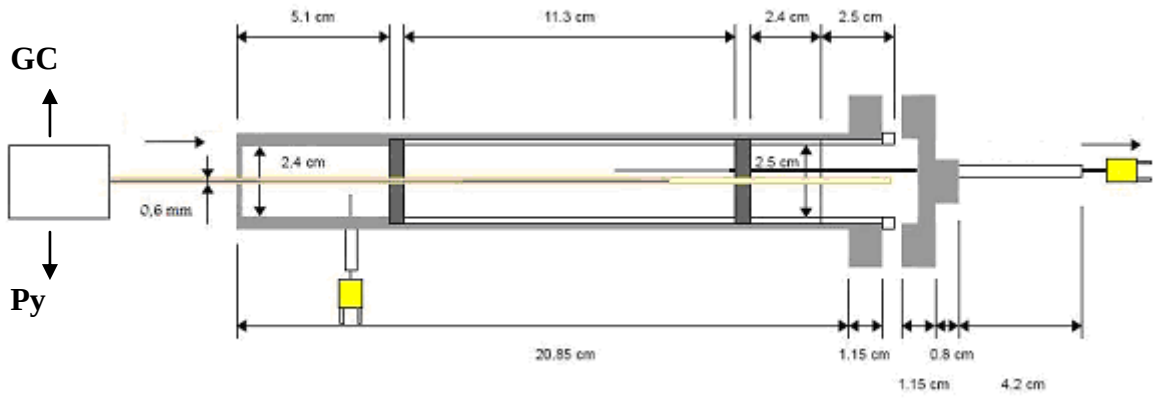

Figure 2.6: Reactor diagram.

At the inlet, the reactor has a spatial sampling device for the species and temperature measurements. This spatial sampling device consists of fused silica capillary having a polyimide coating on the outside that makes the capillary flexible for handling but burns off quickly during the first use. The fused silica capillary serves as duct to sample species into gas chromatograph or as an access point for thermocouple or optical fiber to measure the temperature. The capillary can also withstand temperatures in excess of 1200 making it a robust probe in this high temperature reactor. Furthermore fused silica is essentially transparent to radiation and its low surface area and poor catalytic proprieties minimize the capillary's impact in the reactor system. The fused silica capillary is inserted in the central channel of the catalytic monolith.

The sampling capillary exits the reactor by passing through a sealing system (chapter 3). The lower end of the capillary is connected to a ported micro-volume tee (1/16, 75 mm bore, ss). The opposite port can be used to insert the thermocouple or the fiber optic into the capillary if the temperature profiles are measured. Otherwise, in the tests of measurement of the composition profiles, the opposite port is connected to a stainless steel capillary (with 1/16 nominal diameter) that is in turn connected to the micro-gas chromatogram. The tee is mounted on a liner actuator Zaber TLA-16, controlled from PC. In this way the capillary can be moved up and down with a sub-mm resolution. The capillary is used as an inert sleeve thin capillary thermocouple or the optical fiber connected with the pyrometer. Otherwise the same capillary is connected to the micro-gas chromatograph in order to measure the concentration of reactants and products. This system is used to collect spatially resolved temperature and concentration profiles along the axis of the reactor. The temperature probe and composition will be described in details in chapter 3.

2.4 GAS ANALYSIS SECTION

The analysis of the composition of reactants and products mixture can be performed in two different devices depending on the type of analysis. The ABB® AO2000 series instrument is used for continuous analysis and it allows to quantify CH_4, CO, CO_2, O_2 and H_2. A micro-gas chromatograph Agilent 3000 of Agilent Technologies is used for steady-state analysis. In the next paragraphs the micro-gas chromatograph and the continuous gas analyzer will be described in detail.

2.4.1 MICRO-GAS CHROMATHOGRAPH

A micro-gas chromatograph is characterized by lower volume and time of analysis than those of a traditional gas chromatograph. The instrument used in this work has two columns both using argon as carrier gas:

- molecular sieves (5Å) to separate H_2, O_2, N_2, CH_4, CO;
- Plot Q to separate CH_4, CO_2, C_2H_4, C_2H_6, H_2O, C_3H_6, C_3H_8.

The carrier gas, stored in gas cylinders outside laboratory, are used at 5.5 bar as imposed by constructor to ensure the correct working of pneumatic parts, which used carrier gas as instrumental gas. Besides, the carrier gas must not have impurities so that the analysis is not influenced; at the same time, high purity gases results in better sensitivity and longer column life. For these reasons, the line of carrier gas has set up a filter (2μm) to absorb dust and an O_2 trap because concentration of oxygen should be below 1-2 ppm.

The characteristics and operating conditions of the two columns are reported in Table 2.1

	Molecular sieves (5Å)	Plot Q
Type of column	capillary	capillary
Length [m]	10	8
Diameter [mm]	0.32	0.32
Temperature [°C]	90	70
Injector temperature [°C]	100	100
Pressure [psi]	30	22
Injection time [ms]	400	40
Analysis time [s]	180/360	180/360

Table 2.1: Characteristic and operating conditions of Micro-GC column.

The analysis time is 180 s in methane/air experiments, while 360 s for propane/air tests. This difference is due to the different retention times of the gas species.

The components of the mixture are separated by the columns of the micro-gas chromatograph and analyzed with a thermal conductivity detector (TCD). The TCD is used to measure the thermal conductivity, which depends on the composition of the gas mixture. The TCD consists of four tungsten-rhenium filaments in a Wheatstone bridge as shown in Figure 2.7.

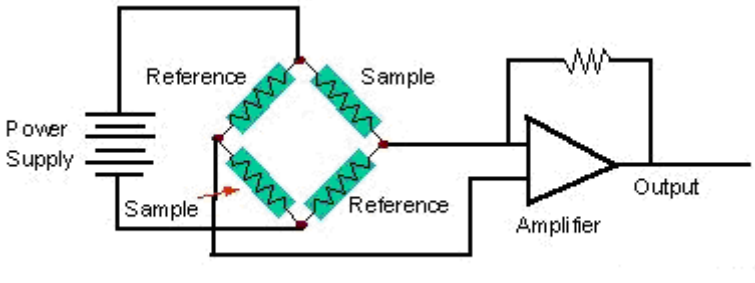

Figure 2.7: Wheatstone bridge for TCD detection.

Electric current flows through the four filaments causing them to heat up. The carrier gas flows across the filament, removing the heat at a constant rate. When a sample molecule (with different thermal conductivity) exits from the column and flows across the two sample filaments, the temperature of the filaments changes, unbalancing the Wheatstone bridge and generating a peak as the sample molecules transits through the detector. The voltage signal produced is proportional to the difference in the thermal conductivity between the column effluent flow (sample components in carrier gas) and the reference flow of the carrier gas alone. The voltage signal produced is proportional to the number of molecules passing through the detector at any given time. If the voltage signal (μV) produced by the detector TCD is plotted as function of the time, a chromatogram will be obtained. In the chromatogram, each peak corresponds to a separate component which is characterized by a retention time. So for well-separated peaks, the total number of molecules of each component is proportional to the area under the peak. To convert the peak area to the concentration of the species, the peaks must be calibrated. Only in this way, it is possible to quantify the chromatographic data. There are different types of quantification methods. In this work the internal standard method is used by introduction of the response factor of the reference species. According to this method, the inlet and outlet flow rate of the reference species must be known, so in this case nitrogen is chosen because it is an inert.

The response factor of a generic species is defined as:

$$\alpha_i = \frac{Q_i / Q_{N_2}}{A_i / A_{N_2}} \tag{2.2}$$

where:

- Q_i, Q_{N2} are the volumetric flow rate of i-species and N_2;
- A_i, A_{N2} are the peak area of i- species and N_2.

From Eq. 2.2 it results that the response factor of nitrogen is equal to the unity.

The Plot Q column does not separate N_2, in fact in the chromatogram there is a unique peak for N_2, O_2, CO and H_2. On the opposite, the molecular sieves column can separate these four

species and so it is possible to calculate the relative ratio between the four species and to identify the fraction of the peak area corresponding to nitrogen in Plot Q column. The response factors of the species separated by Plot Q column are related to this pseudo N_2 peak.

The response factors of each species are experimentally obtained through analysis of a calibrated mixture. Table 2.2 reports retention time and response factor of each species.

Species	Column	Retention time [min]	α_i
H_2	molecular sieves	0.500	0.087
O_2	molecular sieves	0.618	0.830
N_2	molecular sieves	0.754	1.000
CH_4	molecular sieves	1.048	0.413
CO	molecular sieves	1.387	1.063
Air+CO+H_2	Plot Q	0.885	-
CH_4	Plot Q	0.950	0.413
CO_2	Plot Q	1.101	2.144
C_2H_4	Plot Q	1.250	0.926
C_2H_6	Plot Q	1.321	0.873
H_2O	Plot Q	2.253	0.358
C_3H_6	Plot Q	4.157	0.792
C_3H_8	Plot Q	4.851	0.929

Table 2.2: Micro-GC calibration with retention time and response factor of the different species.

2.4.1.1 DATA ELEBORATION

The results of gas chromatograph analysis are two chromatograms obtained by molecular sieves and Plot Q column respectively. An example of chromatograms is shown in Figure 2.8.

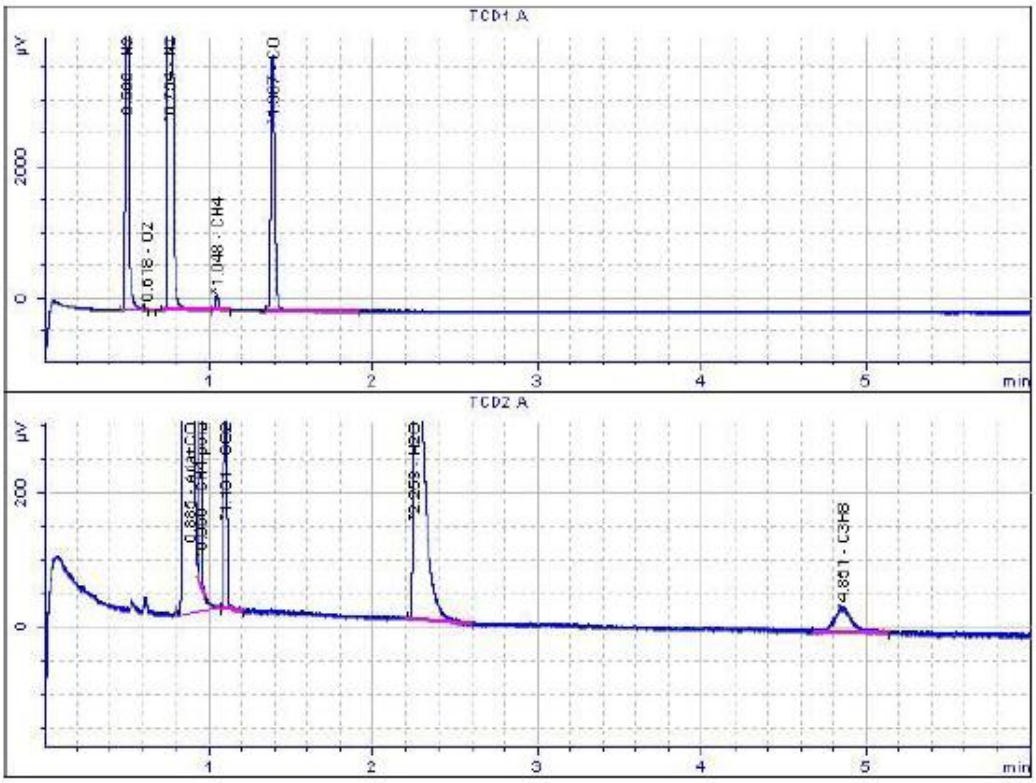

Figure 2.8: Example of gas chromatogram.

Thanks to the micro-GC software it is possible to integrate the area of each peak. Once the area of each peak is calculated, it is possible to obtain the volumetric flow of each component through the response factors and the volumetric flow of nitrogen, as follows (2.3):

$$Q_i = \alpha_i \cdot Q_{N_2} \cdot \frac{A_i}{A_{N_2}} \tag{2.3}$$

The molar flows for every species are calculated according to the following correlation (2.4):

$$F_i = \frac{Q_i}{0.022414} \tag{2.4}$$

Then, the molar fractions of every species are calculated (2.5):

$$y_i = \frac{F_i}{\sum_i F_i} \tag{2.5}$$

Once the molar fraction of each species is determined, it is possible to calculate the reactants conversions and the selectivity to hydrogen and carbon:

$$\chi = 1 - \frac{F_{C_3H_8}^{OUT}}{F_{C_3H_8}^{IN}} \tag{2.6}$$

$$\chi = 1 - \frac{F_{O_2}^{OUT}}{F_{O_2}^{OUT}} \tag{2.7}$$

$$Sel_C = \frac{F_i^{OUT} \cdot nC_i \cdot 100}{FC_{converted}} \tag{2.8}$$

$$Sel_H = \frac{F_i^{OUT} \cdot nH_i \cdot 100}{FH_{converted}} \tag{2.9}$$

In order to check the accuracy of the analyses the atomic balance of carbon, hydrogen and oxygen are defined as follows:

$$BC = \frac{\sum_i F_i \cdot nC_i}{FC_{converted}} \tag{2.10}$$

$$BH = \frac{\sum_i F_i \cdot nH_i}{FH_{converted}} \tag{2.11}$$

$$BO = \frac{\sum_i F_i \cdot nO_i}{FO_{converted}} \tag{2.12}$$

Where:

- nC_i is the number of carbon atoms of the i-species;
- nH_i is the number of hydrogen atoms of the i-species;
- nO_i is the number of oxygen atoms of the i-species;
- $FC_{converted}$ is the molar flow of converted carbon atoms;
- $FH_{converted}$ is the molar flow of converted hydrogen atoms;
- $FC_{converted}$ is the molar flow of converted oxygen atoms.

Every balance is defined as ratio between the carbon, hydrogen, oxygen atoms present in the outlet mixture and the converted carbon, hydrogen, oxygen atoms. The balance must be equal to 1 because a balance over the unity indicates an overestimation of the products, on the other hand a balance under the unity indicates an overestimation of the conversion.

In the experiments the error is less than 5%, except in the tests of sampling of the axial composition profile where the hydrogen balance closes to < 8%. In same tests water is calculated by closing the oxygen mass balance to 1.4.

2.4.2 CONTINUOUS GAS ANALYZER ABB

The mixture is sucked by a membrane pump with a flow rate of about 60 l $h^{-1}$and an overpressure of 0.05 bar, which are necessary conditions for the optimal working of the analysis modules. Upstream the analyzer, the mixture is dehumidified by a condenser and dried through specific filter because water damages the instrument. Then the mixture is sent to the gas analyzer (Figure 2.9). The output signal is the volumetric concentration of the anhydrous mixture.

At the beginning of every week the instrument is manually calibrated using three different span gases coming from high pressure cylinder:

Figure 2.9: Continuous gas analyzer.

- Span 1: mixture of H_2 in N_2 at 20.34%;
- Span 2: mixture of CO_2, CO, CH_4 in N_2 respectively at 16.09%, 23.97% and 24.01%;
- Span 3: mixture of O_2 in N_2 at 20.96%;
- Zero gas: nitrogen of line.

The continuous gas analyzer is composed by three different modules connected in series:

- *Uras 14* (Infrared Photometer) for the analysis of CH_4, CO and CO_2 ;
- *Magnos 106* (Magneto-mechanical) for the analysis of O_2;
- *Caldos 17* (Thermal conductivity-Silicon sensor) for the analysis of H_2.

- **Module Uras 14**

Uras 14 is a NDIR (non-dispersive infrared) process photometer that measures up to four components simultaneously and continuously. The measurement principle is based on the capacity of the molecules to absorb specifically the radiation in the medium infrared between 2 μm and 12 μm. In fact, each molecule absorbs infrared light at wavelengths representative of the types of present bonds. The amount of absorbed IR light is proportional to concentration of the molecules, in accordance with the Lambert-Beer law:

$$A = \varepsilon \cdot \ell \cdot c \tag{2.13}$$

$$I = I_o \cdot 10^{A} \tag{2.14}$$

where I_o is the initial light intensity emitted from the infrared lamp (measured in pure air), I is the intensity of light reaching the end the detector (with sample gas present), A is the absorbance in units of length^{-1}, l is the path length, ε is the molar extinction coefficient in concentration $^{-1}$and length^{-1} and c is the concentration.

The energy absorbed by molecules is converted in kinetic energy, causing the molecules to speed up and thus heat the gas.

The Uras 14 module is composed by (Figure 2.10):

- infrared lamp;
- chopper wheel;
- sample cell;
- calibration cell;
- opto-pneumatic detector.

During the measurement the heating coil generates an infrared radiation which passes through a chopper wheel, so that background signal can be off set from the desired signal, and then in a filter. Then the infrared beam is directed alternately through the two parallel optical cells, sample cell and calibration cell. The calibration cell continuously contains a reference gas, in this case nitrogen, so that a reference signal is supplied. Before the detector there is another

filter to eliminate all light except the wavelength that the selected gas molecules can absorb. In this way the other gas molecules do not adsorb light at this wavelength, do not affect the amount of light reaching the detector. In the opto-pneumatic detector, containing the sample gas, the radiant energy absorbed by the fill gas causes a change in temperature and thereby a change in the pressure in the detector. This change in pressure evokes an electrical signal via membrane capacitor.

In this work the module Uras 14 is used for measuring of CO, CH_4 and CO_2 and their concentration is determined connecting the detectors in series.

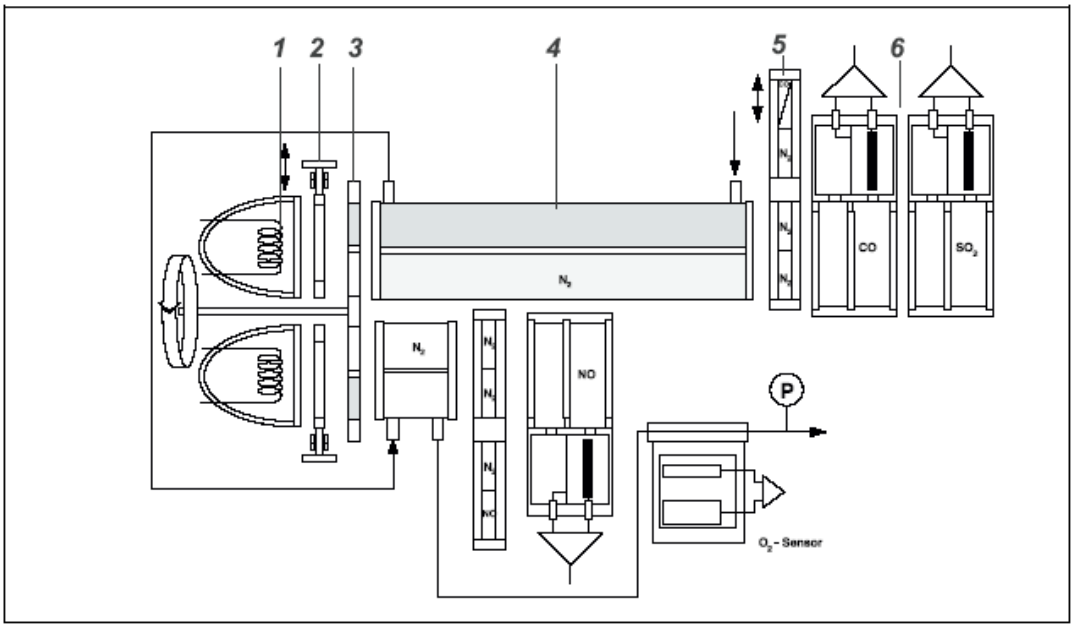

1 Emitter
2 Aperture
3 Chopper wheel
4 Sample cell
5 Adjusting unit / Calibration cell
6 Receiver

Figure 2.10: Schematic representation of module Uras 14.

- **Module Caldos 17**

In the Caldos 17 module the principle of measurement is based on the different thermal conductivity between gases. The module is composed by (Figure 2.11):

- thermostatic chamber;
- support with flange and sample chamber with electronic sensor to measure the temperature;
- thermal conductivity sensor;
- heater;
- thermal connections;
- plug connections.

The thermal conductivity sensor is a micromechanical-made silicon chip with thin-film resistors and a membrane which separated hydrogen from the analyzer flow. In this way the flow does not influence the measurement. The sensor is located in a thermostatically-controlled stainless steel enclosure with a temperature of 60°C in order to prevent any influence of ambient temperature alterations. Besides, the sensor is not place in the main flow to prevent the influences by sample gas changes.

Silicon based sensor are used because this material allows a rapid measurement and extremely small measuring ranges.

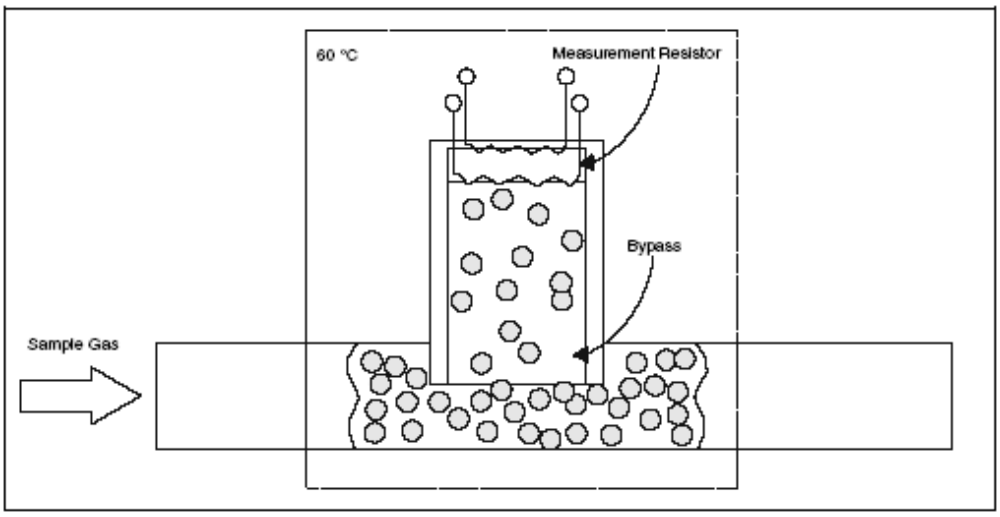

Figure 2.11: Schematic representation of module Caldos 17.

- **Module Magnos 106**

The measuring principle of the Magnos 106 is based on the paramagnetic propriety of oxygen. In fact oxygen has a relatively high magnetic susceptibility as compared to other gases such as nitrogen, helium, argon, etc. and exhibits a paramagnetic behaviour.

The Magnos 106 module (Figure 2.12) is composed by:

- thermostatic chamber;
- thermal connections;
- permanent magnet;
- flow control;
- temperature indicator and control;
- plug connection.

The paramagnetic sensor consists of a cylindrical shaped container inside of which is placed a small glass dumbbell. The dumbbell is filled with inert nitrogen and suspended on a taut platinum wire within a non-uniform magnetic field generated by a strong permanent magnet mounted outside the camber. The dumbbell is design to move freely as it is suspended from the wire. When a sample gas containing oxygen is processed through the sensor, the oxygen molecules are attracted to the stronger of the two magnetic fields. This causes a displacement of the dumbbell which results in the dumbbell rotating. Then a precision optical system measures the degree of rotation of the dumbbell. In this system a light source photodiode generates a beam which a mirror, placed on the dumbbell, deflects onto the photodector, resulting in the generation of an electronic signal. The signal current is amplified and fed back to a conducting coil at the dumbbell. In this way an opposite current is applied to restore the dumbbell to its normal position. The current required to maintain the dumbbell in its normal state is directly proportional to the partial pressure of oxygen. The measurement module is placed in a thermostatic chamber in order to prevent the influences of ambient temperature changes. This paramagnetic sensor offers excellent accuracy over a range of 1% to 100% oxygen.

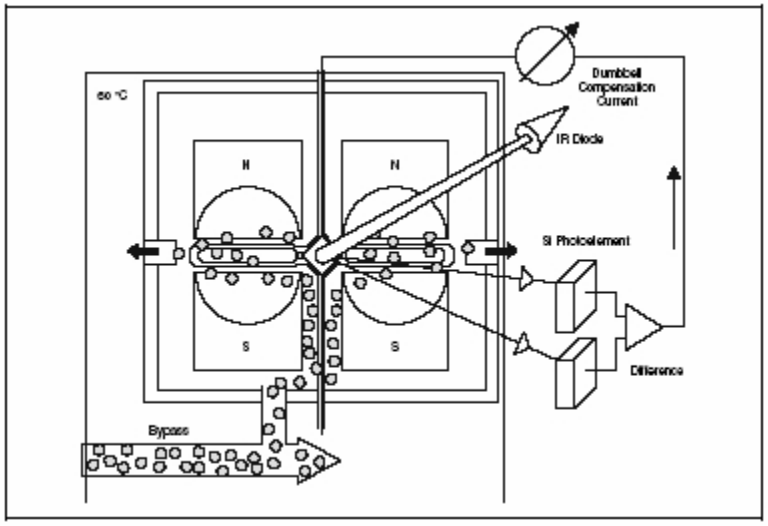

Figure 2.12: Schematic representation of module Magnos 106.

2.5 EXPERIMENTAL PROCEDURES

2.5.1 START-UP PROCEDURE AND CPO TESTS

The first operation is the switching on of the fume hood to remove the exhaust gases. Then the gas cylinders of carrier and reactants are opened. The pressure of the reactants and of the carrier gases is adjusted to 5.5 bar.

Subsequently, the mass flow controllers are activated via PC and the percentage opening is adjusted to the desired set-point. Then the micro-gas chromatograph is turned on and set to analysis method conditions (the analysis method condition will be described in the chapter 3).

At this point, the preheating procedure starts. The three zones of the electrical oven are set to 400°C, the two cartridge heaters, whose maximum working temperatures are 650 °C and 800 °C, are set to 440°C and 560 °C, respectively. Such set points are able to reach a sufficiently high inlet gas temperature for the light-off at standard flow rate. Moreover, to prevent the water condensation, through heating socks, the lines downstream of the reactor are heated at 120°C.

The start-up is done with preheated catalytic bed. In this method the valves are arranged so that a high flow of nitrogen (usually 21 Nl min^{-1}) can be fed to the reactor which is preheated. When the temperature of the catalytic bed reaches about 350°C, the valves are arranged to by-

pass the electrical oven and the two cartridge heaters and the reactants are fed to the reactor at room temperature. Afterwards the pressure is calibrated at the right pressure working on the Pressure regulation valve, Figure 2.1.

After steady state conditions are reached, temperature or composition axial profiles are sampled.

2.5.2 SHUT-DOWN PROCEDURE

At the end of each experiments, the system is depressurized and the reaction is turn off with a cold flow of nitrogen, then it is continuously fed to the reactor to cool it down.

At the end of every day the lines and the cells of the continuous gas analyzer are purged with a nitrogen flow and the shut-down method for the micro-GC is activated from the PC. Once the columns temperature is below 50°C, the micro-GC can be turned-off. Finally, the intercept valves and gas cylinder are closed.

2.5.3 STANDARD OPERATING CONDITIONS

In this work CH_4 CPO tests are first performed in the following operating conditions

- total flow rate from 10 $Nlmin^{-1}$;
- CH_4/Air feeding mixture corresponding to 27.3 % CH_4, 15.3 % O_2, 57.4% N_2;
- pressure from 1 to 4 bar.

Subsequently propane/air mixtures are investigated in this operating conditions:

- total flow rate of 10 $Nlmin^{-1}$;
- C_3H_8 concentration 9 %;
- pressure from 1 to 4 bar.

Both CH_4 and C_3H_8 experiments are carried out under autothermal conditions, at a slightly over stoichiometric O_2/C ratio, equal to 0.56 to prevent carbon formation.

2.6 SPATIAL SAMPLING TECHNIQUE

The catalytic partial oxidation operates under extremely sharp gradients of temperature and of composition, where mass and heat transfer are coupled with the surface process.

Therefore, the behavior of the system could not be fully described by analyzing exclusively the gas composition at the exit of the reactor. The spatially resolved sampling technique is herein applied to investigate the behavior of the system. In fact, this technique allows to "look" directly inside the reactor through the measurement of axial temperature and composition profiles, while the reactor is maintained under adiabatic conditions. This technique was presented for the first time by Horn et al. [22] in order to measure the species and temperature profiles for the catalytic partial oxidation of methane on Rh-coated α-Al_2O_3 foams in steady-state.

2.7 SET UP OF TEMPERATURE PROBES

The correct measurement of the temperature for the gas phase and for the catalytic surface is crucial to interpret correctly the overall behavior of the reactor. In fact surface temperatures are obviously very important for the heterogeneous chemistry, which takes place on the supported metal catalyst, while the gas temperature are equally important for the homogeneous chemistry taking place in the empty volumes of the catalyst. A thermocouple or a optical fiber are the detectors which have been employed to measure the temperature profiles inside CPO catalysts. Temperature probe consists of a empty fused silica capillary (670 μm outer diameter and 530 μm inner diameter). The capillary contains a K-type thermocouple (inner diameter of 500 μm) or a optical fiber (Figure 2.13). In the case of the optical fiber, transparency of the capillary is required to gather all the radiation emitted by the surface.

Figure 2.13: Fused silica capillary with the thermocouple (left) and with the optical fiber (right).

Either in the case of thermocouple and optical fiber, the empty fused silica capillary is sealed at one end (Figure 2.14) to avoid any gas leakage. The sealing is obtained by heating with oxyacetylene torch until the capillary collapses on itself. The oxyacetylene torch is a type 55H200 of Kemper because it could achieve high temperatures needed for softening fused silica.

Figure 2.14: Sealed capillary.

2.8 OPTICAL FIBER PYROMETRY

The application of the optical fiber pyrometer in honeycomb monoliths for heterogeneous catalysis has been previously explored in the literature [57]. However, the technique is exclusively applied to NOx abatement experiments, wherein the conditions are almost isothermal. In recent works, optical fibers have also been applied to CPO due to the strong temperature gradients [58].

2.8.1 THEORICAL BASIS FOR THE RADIATION MEASURAMENT

All bodies radiate energy to their surroundings. The power radiated per unit area is called emittance, which for a blackbody (a body which absorbs all the radiation it receives and radiates in all wavelength interval) depends only on the temperature, according with the Stefan-Boltzmann law:

$$Q_b(T) = \sigma \cdot T^4 \qquad (2.15)$$

where σ is Boltzmann constant, which values 5.67 10^{-8} W/($m^2 \cdot K^4$).

Since the emittance is distributed over the entire spectrum, the monochrome emittance ($I_{\lambda,b}$) is introduced. The monochromatic emittance is the power emitted at a given wavelength so that:

$$Q_b(T) = \int_{\lambda_1}^{\lambda_2} I_{\lambda,b}(\lambda, T) \cdot d\lambda \tag{2.16}$$

The monochromatic emittance is defined by Planck law:

$$I_{\lambda,b}(T, \lambda) = \frac{C_1}{\lambda^5 \cdot \left(e^{C_2/(T \cdot \lambda)} - 1 \right)} \tag{2.17}$$

In the equation:

- C_1 is the first radiation constant = 3.7415 x 10^{16} watts/m^2

- C_2 is the second radiation constant = 1.43879 x 10^{-2} m.

This function is plotted for several temperature in Figure 2.15.

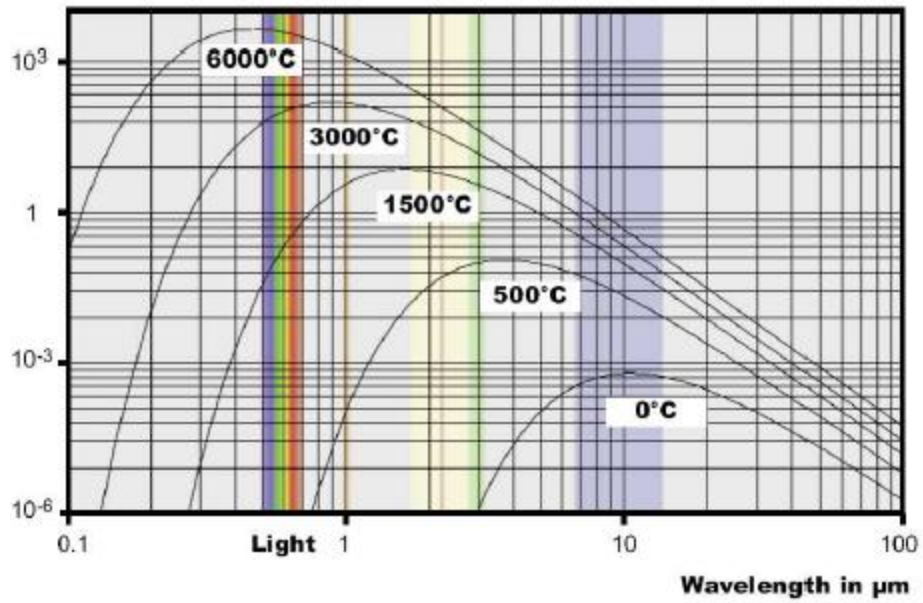

Figure 2.15:Radiation intensity as function of wavelength and temperature according to the Plank law.

The emission coefficient or emissivity ε is the ratio of the thermal radiation emitted by any object to the thermal radiation emitted by a black body radiation source at the same temperature.

$$\varepsilon(\lambda,T)=\frac{I_{\lambda}(\lambda,T)}{I_{\lambda,b}(\lambda,T)} \tag{2.18}$$

The emissivity depends on the material of the object and changes with wavelength, temperature or other physical proprieties [59].

2.8.2 PYROMETER

A narrow-band infrared pyrometer (Impac Infrared, IGA 5-LO) is used for the measurement of temperatures of the solid phase. The pyrometer consists of a measuring transducer connected to an optical fiber. The measuring transducer includes the lens system, the IR detector and the signal process. The infrared radiation emitted by the object of the measurement is collected by the lens. The aperture blocks unwanted peripheral rays.

The filter lets through only the selected spectral range. The portion passing the filter falls on the detector which transforms the infrared radiation into an electrical signal (Figure2.16) [60].

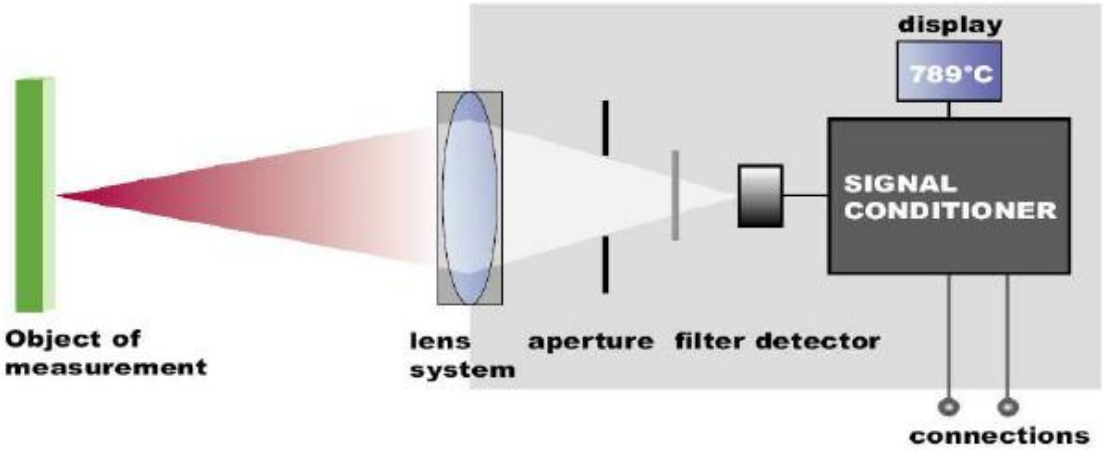

Figure 2.16:Components of the pyrometer.

The photon detector converts the UV-IR radiation in potential difference. The detector acts as an electron counter where the potential difference is proportional to the number of photons which fall on the surface.

2.8.3 OPTICAL FIBER

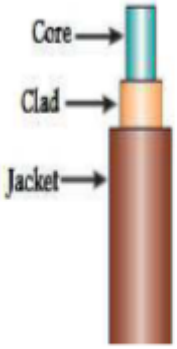

Figure 2.17 section of an optical fiber

The optical fiber is used as a probe for transmitting the radiation from the inlet part of the reactor to the measuring transducer. The structure of an optical fiber (Figure 2.17) consists of a central part called core, of refractive index nF, surrounded by a material called cladding of lower refractive index nC. In order to provide the guideline of the light, the core of the fiber is doped with a small percentage of a substance that increases the refractive index. In this way the electromagnetic waves can be confined in the core region and then transmitted by total internal reflection at the core/cladding boundary. In the present work, the core diameter of the optical fiber is 300 μm, while the diameter of the clad is about 330 μm. The fiber is coated with a polymeric jacket whose outer diameter is 370 μm. As the refraction index nF in the core, which is uniform, is higher than that nC of the cladding, a step-index waveguide is formed.

Therefore the principle of total reflection of a light ray can be applied. Considering a ray in air, which strikes the core of the fiber at an angle θl to the fiber axis, due to the refraction at the air/glass surface, the angle of the ray to the axis changes to θ as it enters the core in according with this formula (2.19):

$$\frac{sin\theta_l}{sin\theta} = n_F \tag{2.19}$$

If the ray strikes the core with an angle less or equal to the critical angle of acceptance, the ray propagates along the core because there are multiple reflections at the interface between the central core and the external cladding without loss of energy. Instead, if the ray strikes the core with a angle greater than the critical angle, partial reflections take place and some energy is lost by refraction into the cladding. After several successive reflections, very little energy is left in the core (Figure 2.18) [59].

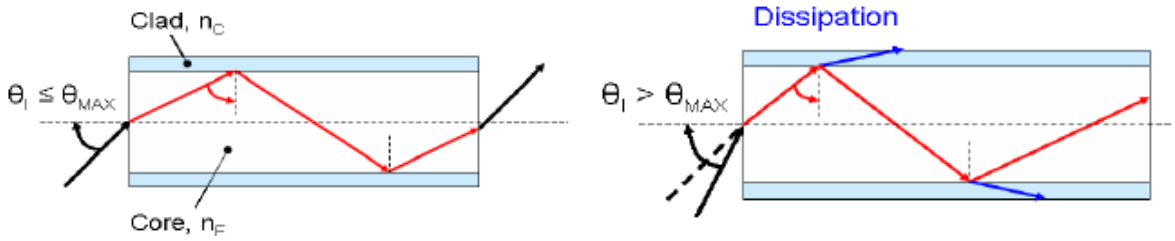

Figure 2.18: Reflection of ray in an optical fiber.

The critical angle of acceptance can be calculated knowing the refraction index of core, clad and the media, where the fiber is inserted, through this formula (2.20):

$$sin\theta_{MAX} = \frac{1}{n_{MEDIA}} \cdot \sqrt{\left(n_F^2 - n_C^2\right)} \tag{2.20}$$

The numerical aperture (N.A.) is an intrinsic characteristic of the fiber, which depends on the refractive indices of the core and the cladding material and it is defined as (2.21):

$$N.A. = sin\theta_{MAX} \cdot n_{MEDIA} = \sqrt{\left(n_F^2 - n_C^2\right)} \tag{2.21}$$

Considering that the core and the cladding is basically bulk fused silica, a weak influence can be expected in relative variation of the refraction indices with the temperature. The numerical aperture for the optical fiber adopted in the present work is 0.22 and it can be reasonably defined as a constant. The n_{MEDIA} also depends on the temperature and composition of the transmitting media: however, for the gas mixture considered in the present work deviation

from unity are negligible. As a consequence, it can be reasonably assumed that the angle is 12.7° under all the investigated conditions.

The cone of light rays, that a fiber collects and transmits, is termed acceptance cone and it depends on the tip of the fiber. A flat and a 45° tip have been considered (Figure 2.19).

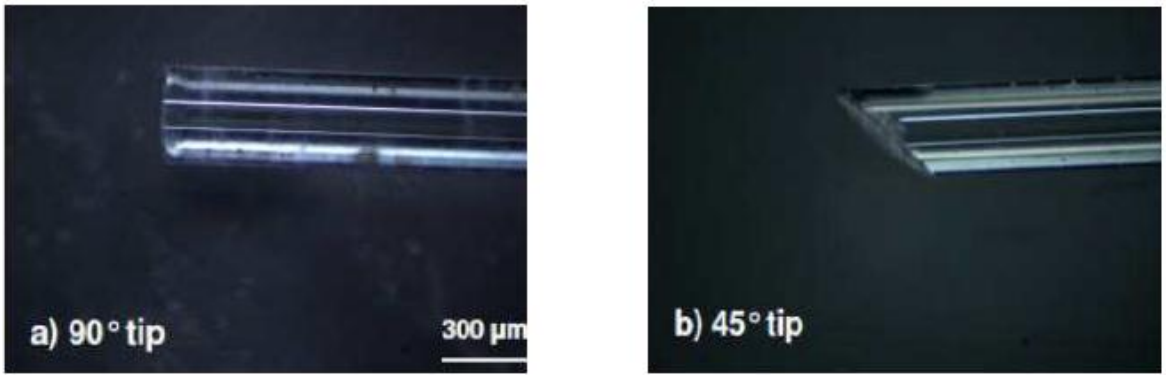

2.19: Optical fiber with a flat tip (a) and with 45° tip (b).

Experimentally, the acceptance cone can be visualized by directing a red laser beam inside the fiber, in the opposite way the incoming thermal radiation travels during the measurements. The laser beam crosses the tip, tracing the acceptance cones. The angle of the tip governs the orientation of the acceptance cone of the optical fiber. Flat tips exclusively transmit the radiation coming from the front of the fiber; in fact flat tips are front-looking probes (Figure 2.20). A no null gap is present between the actual position of the tip and the beginning of the radiating surface (segment AB in Figure 2.20). 45°polished tips predominantly accept radiation from the lateral direction, perpendicular to the fiber axis and opposite to the beveled surface. Due to total internal reflection, the beveled surface behaves like a turning prism, which directs the lateral radiation inside the fiber.

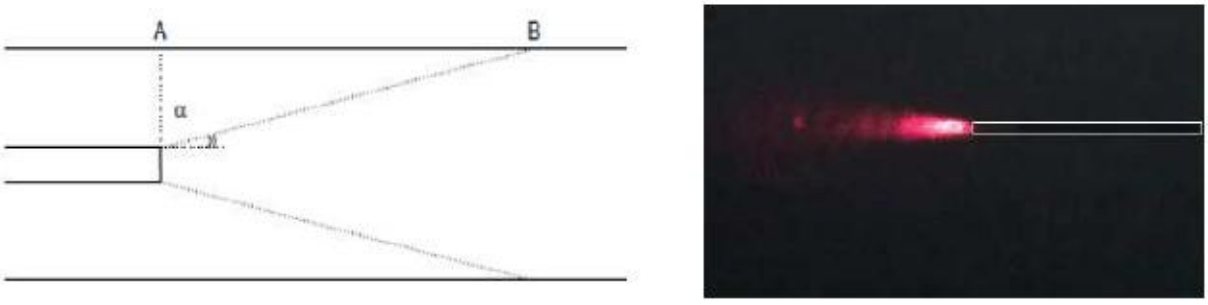

Figure 2.20:Acceptance cone of an optical fiber with a flat tip.

In the case of 45° cut fibers, a fraction of the incoming radiation is also collected from another direction, which was experimentally found at an angle of about 20° off the axis (Figure 2.21). The secondary acceptance cone is due to the radiation that enters the fiber by refraction through the beveled surface. The importance of the secondary contribution depends on the fiber materials, but in generally minor, less 10% of the relative intensity of the primary acceptance cone. Because of the secondary acceptance cones, when sliding in the channel, the 45° tip collects the radiation coming from the walls (segments AB and CD in Figure 2.21).

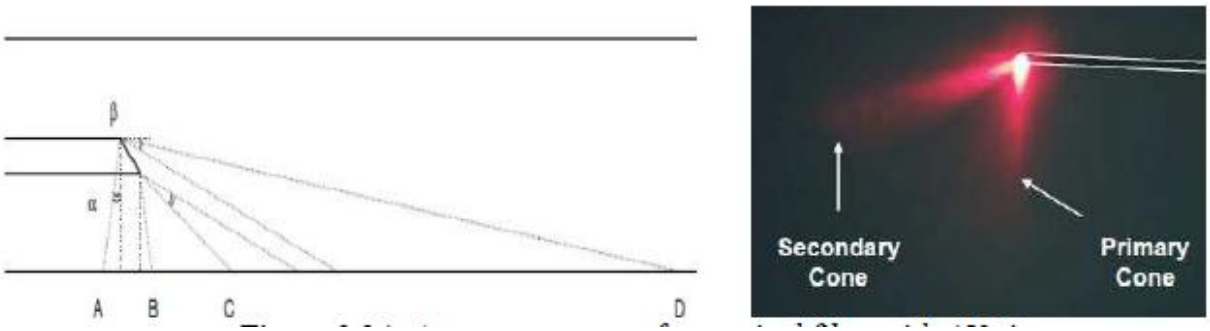

Figure 2.21: Acceptance cone of an optical fiber with 45° tip.

As reported in Donazzi et al. [58] the analysis of temperature profiles and of the goniometric characteristics of the optical fiber clearly indicates that 45° angled fibers are preferred for spatially resolved measurements, owing to the capability of looking at a precise spot on the surface of the catalyst support. In contrast, the use of 90° angled fibers leads to an average measurement, which underestimated the hot spot. For these reasons in this work optical fibers with 45° tip are used to sampled the axial temperature profiles.

2.8.4 CALIBRATION

The voltage output from a narrow band optical measuring in the wavelength range λmax-λmin is a function of the emissivity of the target surface ε_S, of the transmissivity of optical fiber and of the intervening media τ, of the gain of the detector R and of the radiance L.

$$V(T) = \int_{\lambda\,\min}^{\lambda\,\max} \varepsilon_S(\lambda) \cdot \tau(\lambda) \cdot R(\lambda) \cdot L(\lambda, T) \cdot d\lambda \qquad (2.22)$$

In general, the surface emissivity and the transmissivity of the optical fiber are not known and a calibration is required wherever a new material or a new fiber is tested. The surface emissivity ε_S is an intrinsic characteristic of the target material (in this case the catalyst) which depends on his roughness. As well, also the geometry of the catalyst support can lead to local variations of the surface emissivity. Different from the trasmissivity, which is fixed and calibrated by the manufacturer, the emissivity is an input parameter that has to be set before taking the measurement with the pyrometer. As received, the pyrometer was already calibrated against an artificial blackbody source ($\varepsilon_S = 1$) by using a 45° angled fiber. The standard procedure suggests to measure the temperature of the target surface and compare it with that of a reference blackbody source maintained at the same temperature.

If a lower temperature than that of the reference is found, the emissivity of the target surface is less than 1 and the emissivity parameter of the pyrometer is adjusted so that the two measurement match. The pyrometer output is calibrated by comparison with thermocouple measurements. The measurements are performed between 400 and 900°C, in stagnant air. A blank 400 CPSI cordierite honeycomb and two heat shields are placed in a quartz reactor, externally heated by a tubular furnace. The same standard internal layout adopted in the adiabatic reactor (in terms of relative distance between the honeycomb and the heat shield) is maintained. First, in order to obtain a surface emissivity close to the unity, the honeycomb is coated with a dull black-paint (Aremco High Emissivity Coating 840°C). The temperature profiles are collected both with the optical pyrometer than with the thermocouple, by sliding the quartz capillary in a central channel of the honeycomb. The capillary is moved exclusively within the channel and strictly isothermal temperature profiles are obtained. The profiles measured by the thermocouple matches the set point of the oven. The calibration reveals that the pyrometer measurements always overestimate the thermocouple measurements. Indeed, when setting the input emissivity parameter of the pyrometer at 1, the following linear correlation is derived through a linear regression of the experimental data (Figure 2.22):

$$T_{calibrated} = 0.936 \cdot T_{measured} + 22.9 \qquad (2.23)$$

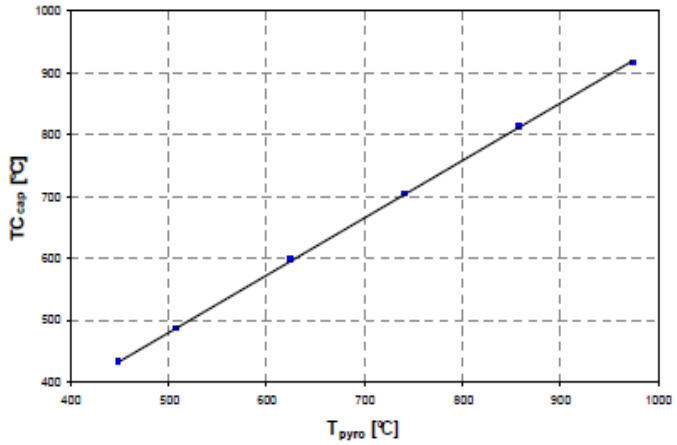

Figure 2.22: Calibrated line for the pyrometer.

Identical results are obtained also when a 90 ° angled fiber is used. The calibration is repeated with a catalytic sample: no difference is observed by comparison with black painted sample. This results allows to estimate a blackbody emissivity for the catalytic layer. The calibration is repeated with uncoated cordierite honeycomb (ε_S = 0.6 for cordierite) to understand if the blackbody emissivity is due to the roughness of the layer or to the geometry of the channel. Also in this case no difference is observed compared with the previous results. This indicates that the geometry of the catalyst support plays a dominant role in the pyrometer measurement. These results are in line with the emissivity enhancement effect that is present in cavities as a consequence of multi-reflection. A blackbody radiation can be achieved within an isothermal enclosure also in the case of a non blackbody emitter ($\varepsilon_S < 1$) if proper geometrical conditions are realized: a local apparent surface emissivity εA, which is a function of ε_S, of the diameter D of the enclosure and of the distance x of a target from the end section. For cylindrical holes with a surface emissivity larger than 0.6, the apparent emissivity approaches 1 when the ratio between x and D is larger than 6. In practice, unless ε_S is very small, a cavity more than only a few diameter deep emits the same amount of radiation of a infinitely deep cavity and can be approximated as a blackbody.

The channels of the honeycomb (30 mm long and 1.2 mm size) guarantees that a blackbody emissivity could be obtained sufficiently far off the exit section.

2.9 SPECIES PROBE

The species probe consists of an empty fused silica capillary through which the gases, from any axial position along the reactor, can be sampled and analyzed in micro-gas chromatograph. The design of the species probe is important to ensure that the suction of the species has a minimal impact on the overall system with respect to how much volume is sampled and how the species are removed. For further details we strongly suggest reference [67].

2.10 CATALYST PREPARATION

The preparation of catalytic honeycomb monoliths (Figure 2.23) is characterized by different subsequent steps: preparation of α-Al_2O_3 and of the catalytic powder, preparation of the catalytic slurry and finally the coating onto the primary support (cordierite).

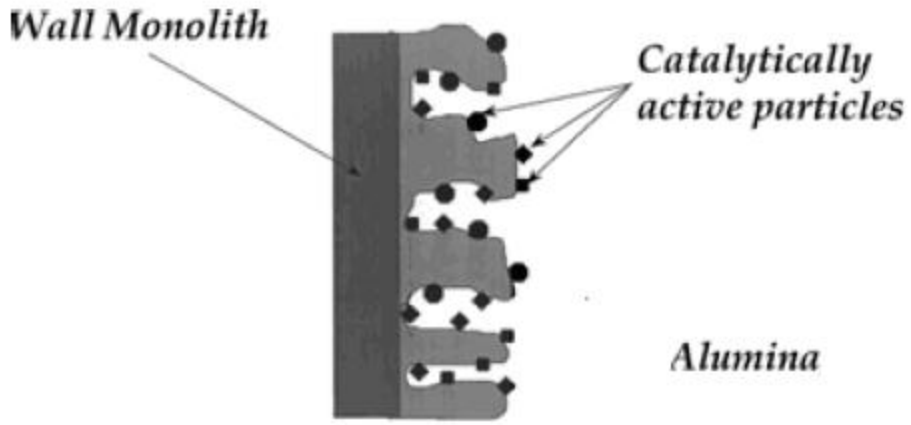

Figure 2.23: Catalytic monolith.

2.10.1 CATALYTIC POWDERS

α-Al_2O_3 (10 m^2/g) is used as thermally stable support. It is obtained by calcination in stagnant air at 1100 °C for 10 hours of commercial alumina (Sasol®, PURALOX Sba-200) which is mainly composed by γ-Al_2O_3 (96.9%). The calcination temperature is reached through a

temperature ramp with a rate of 1°C/min. At the end of the hold time the sample is cooled down to room temperature with a rate of 2 °C/min. In fact at 1100°C the transition of the alumina phase from γ to θ and then to α is complete.

The catalytic powders are prepared by incipient wetness impregnation of the α-Al_2O_3 support with a precursor of the active phase. This precursor is $Rh(NO_3)_3$ in aqueous solution at 14.68% w/w (Chempur®) and with a density of 1.62 g/ml. The technique consists of impregnating the α-Al_2O_3 powder with a solution (stock solution) of a thermo labile precursor of rhodium ($Rh(NO_3)_3$) and a sufficiently volatile solvent (water). According to this technique, the impregnating volume (Vt) must be equal to the total volume of the pores of the support (Vp) so that the porous volume is completely filled. The volume of the stock solution required to fill the volume of pores is calculated from the mass of catalytic powders:

$$V_t = V_p \cdot g_{dust} \tag{2.24}$$

To prepare a solution containing the required load of rhodium, it is necessary to calculate

the ml of precursor solution:

$$grammes_{Rh} = \frac{load_{Rh} \cdot g_{dust}}{1 - load_{Rh}} \tag{2.25}$$

$$ml_{solution Rh(NO_3)_3} = \frac{grammes_{Rh}}{density_{solution Rh(NO_3)_3} \cdot \omega_{Rh}} \tag{2.26}$$

where ωRh is the massive fraction of $Rh(NO_3)_3$.

The quantity of precursor has to be diluted up to the volume of solution needed to fill the pores completely (Vt). Since volumetric flask are available in fixed sizes, the solution is diluted in a volumetric flask of 5 ml. The dilution ratio is defined as the ratio between the volume of solution necessary to fill completely the pores and the volume of precursor containing the required mass of rhodium:

$$R = \frac{V_t}{ml_{solution Rh(NO_3)_3}} \tag{2.27}$$

In order to prepare 5 ml of solution containing the correct mass of rhodium it is necessary to take a quantity of precursor given by the ratio between 5 ml of solution and the value of R. In this way 5 ml of stock solution are obtained. From the stock solution, the volume required to fill the pores of support is sampled and this quantity is dripped onto the alumina powder through a burette until incipient impregnation. The small Rh quantity to deposit allows to impregnate just once. The catalytic powders are then dried at 110°C for 3 hours. During this phase the precursor is deposited inside the pores because of evaporation of the solvent.

2.10.2 SLURRY PREPARATION

The catalytic powder is mixed with water and nitric acid on the basis of a standard recipe studied in a previous work [41]. The recipe is defined as follows:

- 1.4 moles of HNO_3 per g of catalytic powder

- 1.7 ml of water per g of catalytic powder

- a number of ZrO_2 spheres so that their total weight is eight time the weight of

catalytic powder.

The suspension of catalytic powder, water and nitric acid is ball milled at 51 RPM for 24 hours.

The ball milling equipment (Figure 2.24) consists of a PET container (containing the slurry and ZrO_2 spheres) placed inside a ceramic jar at an inclination between 30° and 45° as compared to the horizontal axis. This position is obtained by filling the void space of ceramic jar with voluminous material. Then the jar is positioned on rotary rollers for 24 hours. During this treatment the catalytic powders are reduced in smaller particle through the chemical action of the acid. In this way the formation of agglomerates, which can precipitate, is prevented. Besides, there is also a mechanical action of the spheres of ZrO_2, which mill the catalytic particles.

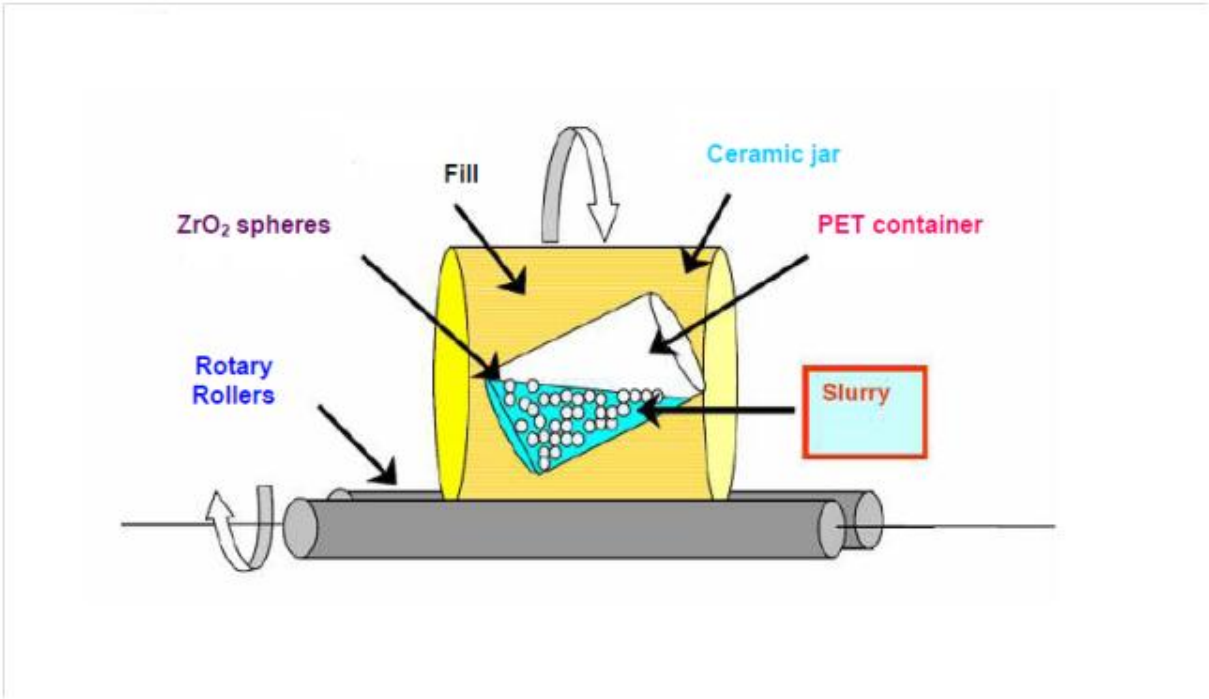

Figure 2.24: Ball milling technique.

2.10.3 MONOLITH COATING

Once the slurry is obtained, it must be deposited on honeycomb monoliths, which are shaped as cylinders (Table 2.2). Before starting the coating procedure the monoliths are washed with acetone to remove the superficial impurities due to handling. Then the lateral surface of the monoliths is covered by Teflon. Then a bohemite primer is deposited. The bohemite primer is prepared by dispersing 10% (w/w) of a commercial aluminum hydroxide powder (Disperal®, Condea Chemie) in a 0.4%(w/w) HNO_3 aqueous solution. After mixing for 10 min, a stable dispersion of bohemite is obtained. For the primer deposition, the supports are dipped in the bohemite dispersion and are dried at room temperature for 30 min. This results in the formation of a well adherent layer on the surface of the supports, which improves the adherence of the washcoat layer [42]. The weight of the primer is obtained by difference between the weight of the monolith before and after pre-coating with the primer. After pre-coating with the bohemite primer, the supports are dipped in the catalytic slurry. During this phase the channels of the monolith are filled with the slurry because of capillarity. As indicated in Figure 2.25, the excess of the slurry is blown out of the monolith channels with air flow at 8 bar resulting in a homogeneous catalytic layer.

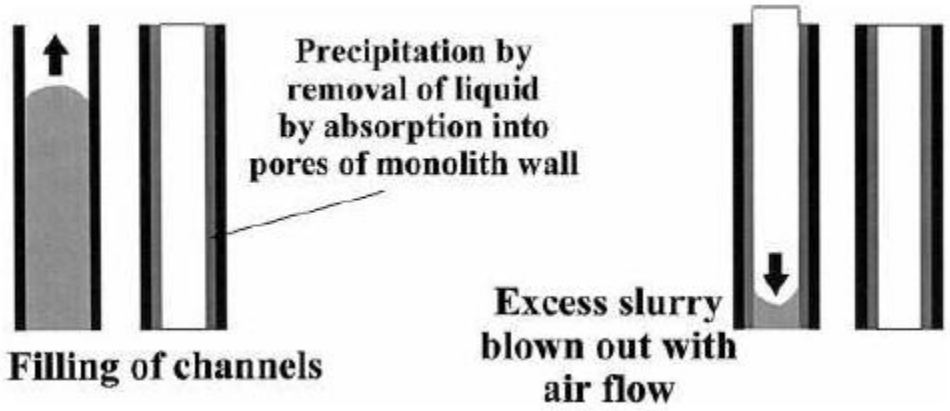

Figure 2.25: Application of slurry onto walls on monolith channels.

The coated samples are "flash" dried at 280°C for 5-10 minutes in a ventilated oven, so that the catalytic layer is fixed to the support. After the flash drying, the weight of the catalytic layer is evaluated by the difference with weight of the monolith with the primer. In Table 2.3 there are the properties of the monoliths used in the tests.

	Sample FHS6	**Sample FHS2**	**Sample FHS 5**
Primary Support	Cordierite	Cordierite	Cordierite
CPSI	400	400	400
Length [cm]	2,6	0,5	3,2
Diameter [cm]	2,4	2,4	2,4
Catalyst Density [g cm^{-3}]	1,38	1,38	1,38
Load [mg]	620	61	444
Thickness [µm]	14	7	8
Void grade	0,7	0,7	0,7

Table 2.3: Physical properties of the catalysts.

2.11 CATALYST CHARACTERIZATION

The catalytic samples are characterized with different techniques:

- X-ray diffraction (XRD);

- measurement of specific area (BET analysis);

- measurement of porous volume with mercury porosimetry.

2.11.1 X-RAY DIFFRACTION

The composition of the phase of the Al_2O_3 support is determined by a diffractometer for powder samples with vertical goniometer (Philips PW1710). The measurements are performed in these operating conditions:

- radiation: CuKα (λ=1.5Å) filtrated with a Ni filter;

- scanning interval: 2θ = 10-90°;

- scanning rate: 0.05° 2θ/s;

- count time: 12.5s.

The identification of the phase is made comparing the spectrum with the spectrum library (JCPDS) with an automatic research. The middle dimensions of the crystal are calculated with Scherrer equation (2.28):

$$\tau = \frac{(0.9 \cdot \lambda)}{(\pi / 180 \cdot \cos\theta \cdot \Delta 2\theta)} \qquad (2.28)$$

where τ is the middle dimension of the crystal, $\Delta 2\theta$ is the middle high and the breadth of the peak (evaluated through the Rietveld analysis of spectrum), λ is the wavelength of incident radiation and θ is the angle corresponding to the maximum peak of diffraction. In this work the X-ray diffraction is used to verify the composition of Al_2O_3. A X-Ray diaffractogram is reported in Figure 2.26 and it is possible to note that all the peaks are associated to α-Al_2O_3 underlining the finishing of the phase transition to α -phase.

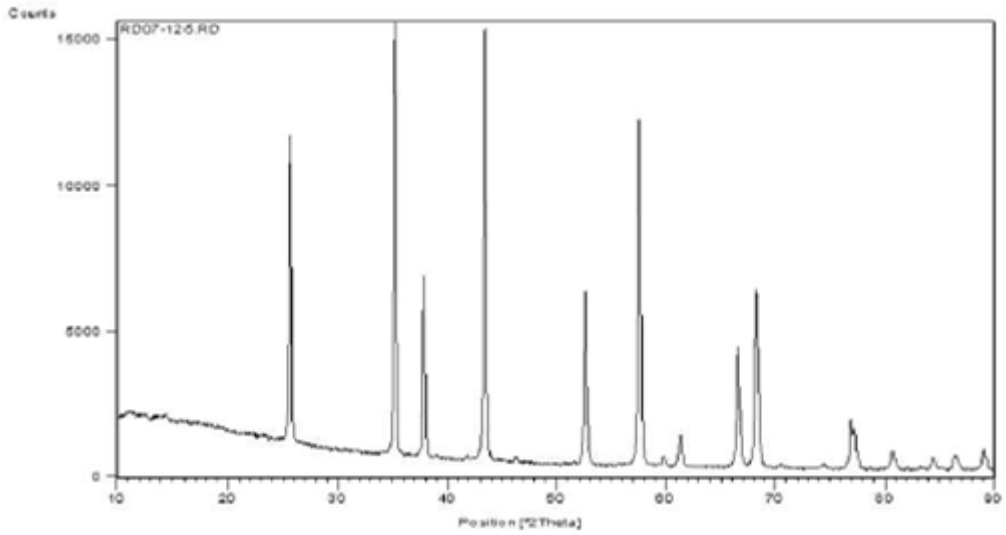

Figure 2.26: X-Ray diaffratogram.

2.11.2 BET ANALYSIS

The measurement of the specific surface area is performed with the Tristan instrument of Micromeritics, using the BET method (Brunauer, Emmett and Teller, 1938). This technique uses liquid N_2 at temperature of 77 K. The number of absorbed nitrogen moles increases with the pressure and the bond between these two quantities is given by the absorption isotherm. BET isotherm considers a multilayer absorption and it is based on these assumptions: the molecules absorb on a flat uniform surface of the solid with a uniform heat of absorption due to Van Der Waals forces;

- there is no lateral interaction between the gas and the solid;

- after the surface has become partially covered by absorbed molecules, other molecules can absorb either on the remaining surface or on top of adsorbed layer, and the heat of absorption of the subsequent layer is equal to the heat of liquefaction of the gas.

At low pressure ($P<0.35\ P°$) the experimental data (pressure-absorbed quantity) are described by BET isotherm:

$$\frac{n}{n_m} = \frac{C \cdot \frac{P}{P^\circ}}{\left(1 - \frac{P}{P^\circ}\right) \cdot \left[1 + (C-1) \cdot \frac{P}{P^\circ}\right]} \qquad (2.29)$$

where:

- P° is the vapor pressure of N_2 at saturation;

- *n* is the number of absorbed gas moles per gram of catalyst at the pressure P;

- *nm* is the number of absorbed gas moles per gram of catalyst corresponding to the fraction of the monolayer;

- *C* is the difference between the released heat for the absorption of one molecule on the surface and the released heat for the absorption of one molecule on subsequent layers of molecules already absorbed.

For the calculation of the specific surface area it is necessary to know the number of moles of nitrogen absorbed on the monolayer per gram of catalyst, calculated by Equation 2.29, and the area occupied by a nitrogen molecule:

$$Area = n_m \cdot Area_{N2} \cdot N_{av} \qquad (2.30)$$

where *Area* is the specific surface area expressed in [m2gcat -1], *AreaN2* is the area occupied by one molecule of N2 and Nav is the Avogadro number.

The specific surface area calculated through BET method is 7 m^2g^{-1}. This measurement is in according with the results of the X-ray diffraction, which shows that there is only the α phase.

2.11.3 MEASURAMENT OF THE POROUS VOLUME (MERCURY INTRUSION)

For the dry impregnation it is necessary to know with precision the porous volume of the support powder. So, in this work, the porous volume of α-Al_2O_3 is determined through mercury porosimetry. The measurement is performed with the AutoPore IV 9500 VI.05 porosimeter of Micromeritics. Since mercury does not spontaneously penetrate pores by capillary force because of its non-wetting property, it must be forced to go into the pores by

applying an external pressure (Figure 2.27). So after a pre-treatment at void grade up to 5 psi and a hold of 5 minutes, there are two different pressurizations:

- low pressure analysis (50-900 μmHg): during this phase mercury penetrates intraparticle spaces and breaks the aggregates;

- high pressure analysis (2-3300 μmHg): during this phase mercury penetrates the pores.

The required pressure to penetrate pores is inversely proportional to the size of the pores:

$$r_P = \frac{6300}{P} \tag{2.31}$$

where r_P is the radius of the pore expressed in [Å] and P is the pressure expressed in [atm].

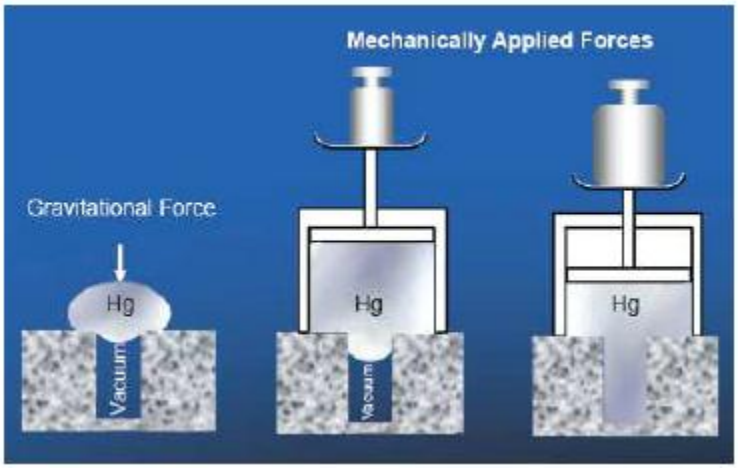

Figure 2.27: Mercury intrusion in the pore.

The porous volume of the Al_2O_3 sample is 0.2-0.3 cm^3g^{-1} with a mean diameter of the pores equal to 678 Å. The latter value is in line with the value of the specific surface area obtained by BET analysis.

CHAPTER 3

DEVELOPMENT OF THE EXPERIMENTAL SET UP FOR CPO TESTS UNDER PRESSURIZED CONDITIONS

This chapter initially reports the development of new components necessary to conduct a CPO test under pressurized conditions.
Two systems have been developed: the Sealing System and the Discontinuous Sampling System. In the following paragraphs these two systems will be illustrate, the tests which confirmed their behavior are going to be explain too.

3.1 SEALING SYSTEM

3.1.1 DESCRIPTION

The old sealing system is inappropriate to conduct a test under pressurized conditions because it does not guarantee a perfect sealing with a significant gas leaks and possible safety problems. The new Sealing System is shown in the Figure 3.1.

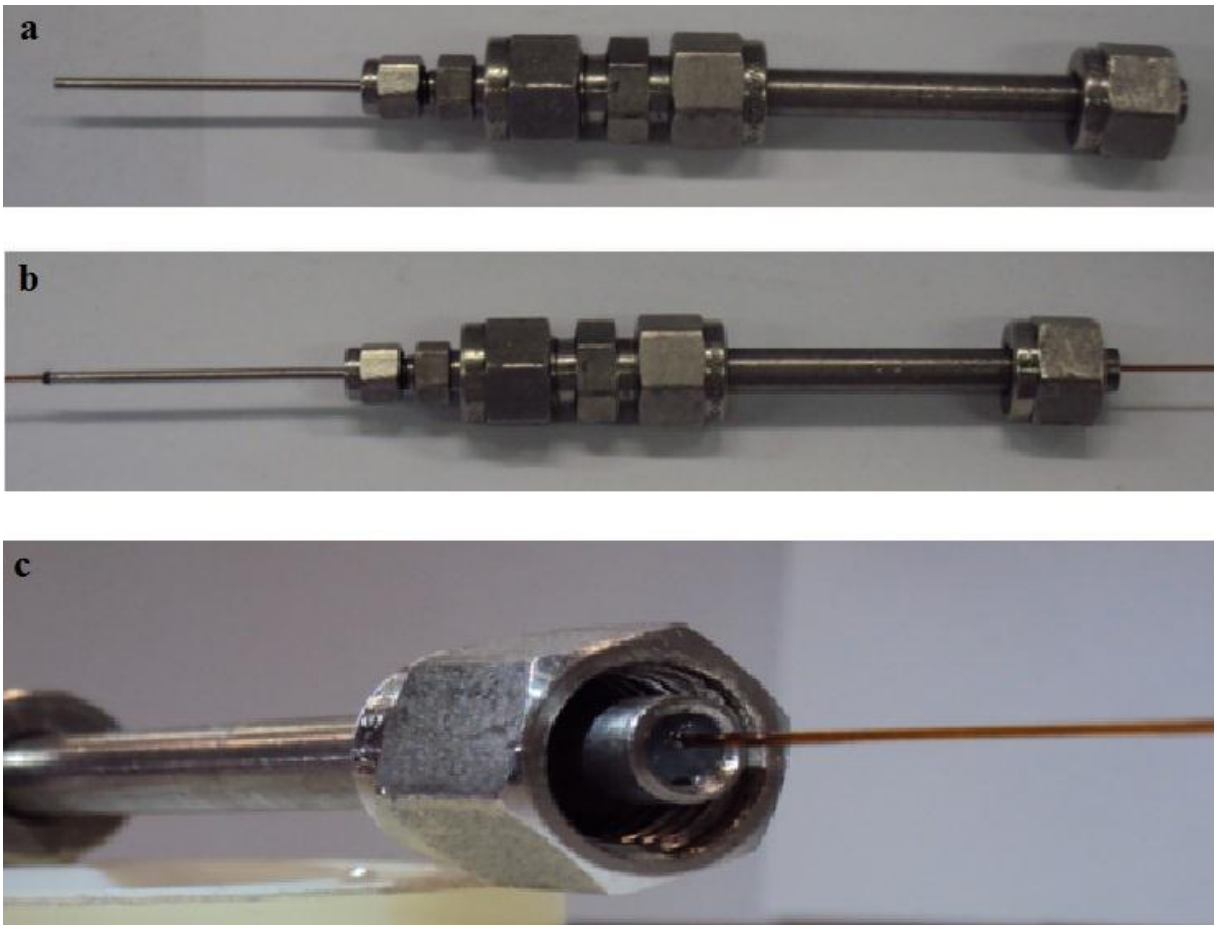

Figure 3.1: Sealing System (a), with an inner capillary (b), detail of reactor side filled by Silicone Gel(c).

The Sealing System is composed by two parts: the first one (connected with the reactor) is composed by a tube of 316 stainless steel of ¼ inch nominal diameter, 83mm in length. The second one is composed by a tube of 316 stainless steel of $^{1}/_{16}$ inch, 50 mm in length, Figure 3.1(a).

In the 1/4 inch nominal diameter tube, the seal of the gas is ensured by the large contact surface that stands between the capillary and the silicone gel. The tube with smaller inner diameter gives directionality during the movement of the capillary and it increases the sealing action by Dow Corning® silicone gel. Two tubes of $^{1}/_{16}$ inch with a different internal diameter had been used in this system: one of them has an internal diameter of 0,04 inch and it is used for gathering data from the temperature tests in which the capillary has an external diameter of 670 μm. In the composition test the capillary is smaller (340 μm) compared to the one used in the temperature analysis, for this reason a tube with a smaller internal diameter is used during the test (0,03 inch, 0,75 mm).

The cross section is shown in the Figure 3.2.

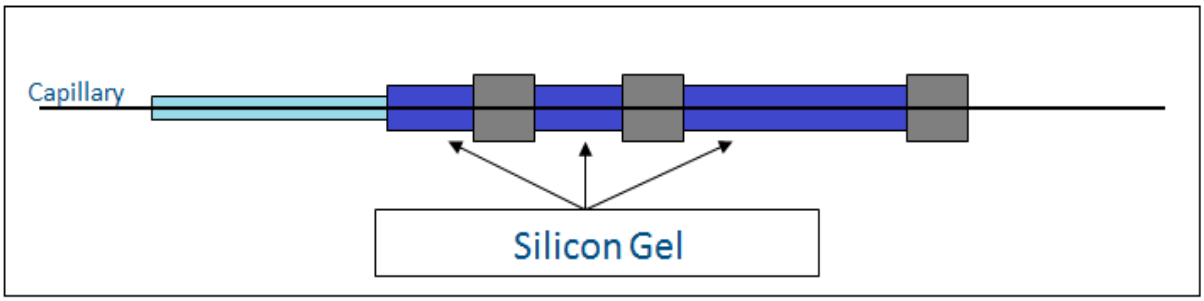

Figure 3.2: Sealing System: Cross-section.

The silicone gel allows the movement of the capillary, but thanks to its high viscosity it does not allow the gas to leak out. During the set-up of the reactor the silicone gel is put inside just in the blue section, meanwhile during the test, the gel is pushed inside the light blue section by pressure, this phenomenon increases the seal of the system, Figure 3.2. The physical properties of the gel are very important to have a satisfactory seal during the test. From the analysis of the physical properties the gel appears to be stable under the operating conditions. In fact ,the temperature that is measured in the zone in which is introduced the sealing system is lower than 200 °C because it is the maximum temperature that the gel can reach.

The most important physical properties of the silicone gel are described in table 3.1.

Method	**Test**	**Unit**	**Results**
	Service Temperature Range	°C	-40 ÷ +204
Fed Std 791	Bleed, after 24h at 200°C, max	percent	0.05
Fed Std 791	Evaporation, after 24h at 199°C, max	percent	1.1
ASTM D 2265	Drop point	°C	>300

Table 3.1: Physical properties of Dow Corning® High-Vacuum Grease silicone gel.

3.1.2 EXPERIMENTAL VALIDATION

The system has been tested with three different control experiments:

1. Leakage test at 4 bar: no gas flow, fixed capillary;
2. Leakage test at 4 bar: 10 Nl min^{-1} N_2 flow, fixed capillary;
3. Leakage test at 4 bar 10 Nl min^{-1} N_2 flow, moving capillary ;

All test are conducted at room temperature and with the following set-up procedure:

1) The gel is added to the Sealing system;
2) The capillary (670 μm outer diameter) closed in both sides is inserted into the Sealing System, Figure 3.1.b;
3) The Sealing System is connected to the metal case.
4) The output side of the capillary is cut to insert the thermocouple or to sample the gas.

The insertion of the capillary into the sealing system must be performed with caution to avoid the formation of bubbles inside the gel which could compromise the seal.

Leakage test at 4 bar: no gas flow, fixed capillary:

The first test consists of researching the presence of leaks in a completely fixed system. The Pressure Regulation Valve is completely closed and the Digital Mass Flow Controller (DMFC) of the nitrogen flow is switched-on. When the pressure inside the metal reactor reaches 4 bar the DMFC is switched-off, the capillary is not moved from its position during the test. In the following 10 minutes the presence of leaks and pressure losses is verified. No pressure loss and leakage of gas have been found. The test confirms the good performance of the system under these conditions. However, the system must guarantee a perfect seal even under dynamic conditions, in particular with moving capillary and in the presence of flow inside the reactor. For this reason other two kind of tests are performed.

Leakage test at 4 bar: 10 Nl min^{-1} N_2 flow and fixed capillary:

After the first test the Sealing System has been tested in presence of a nitrogen flow; the capillary is not moved from its position during this test. Initially the Pressure Regulation Valve is opened, afterwards the DMFC is set (10 Nl min^{-1}). Subsequently, the pressure is set to 4 bar through the Pressure Regulation Valve.

In the following 10 minutes the presence of leaks and pressure losses is verified. During the test gas leaks are not detected. After this experiment is possible to establish that the flow inside the metal case does not change the behavior of the sealing system.

Leakage test at 4 bar 10 Nl min^{-1} N_2 flow and moving capillary:

The last test consists of searching the presence of leaks in presence of a nitrogen flow (10 Nl min^{-1}) with the capillary in movement in order to simulate a real temperature test, which is the most critical for the sealing of the system because the displacement of the capillary appears to be three to five centimeters different to the original position. Initially the Pressure Regulation Valve is opened, afterwards the DMFC is set (10 Nl min^{-1}). Finally, the pressure is set to 4 bar. When the pressure is at steady state the capillary is moved by the linear actuator T-LA60A by Zaber® with a speed of about 1 cm min^{-1}. The test is done several times, and gas leaks and pressure losses are not detected.
The last test demonstrates the reliability of this system also with the moving capillary.

3.2 DISCONITNUOUS SAMPLING SYSTEM

3.2.1 DESCRIPTION

After the development and verification of the Sealing System, a Discontinuous Sampling System has been developed to permit the analysis of the gases under pressurized conditions so it is possible to study the effect of pressure on the species profiles.

The Discontinuous Sampling System (DSS) is composed by:

- 5 tubes of stainless steel of 1/16 inch nominal diameter 30 mm in length;
- 1 tube of stainless steel of 1/16 inch nominal diameter 80 mm in length;
- 2 Ball Valves (n° 1-3) by Swagelok®;
- 2 Low-Flow Metering Valves by Swagelok® (n° 4);
- 1 Regulation Valve by Swagelok® (n°2);
- 1 Bourdon pressure gauge;

The system is reported in the Figure 3.3.

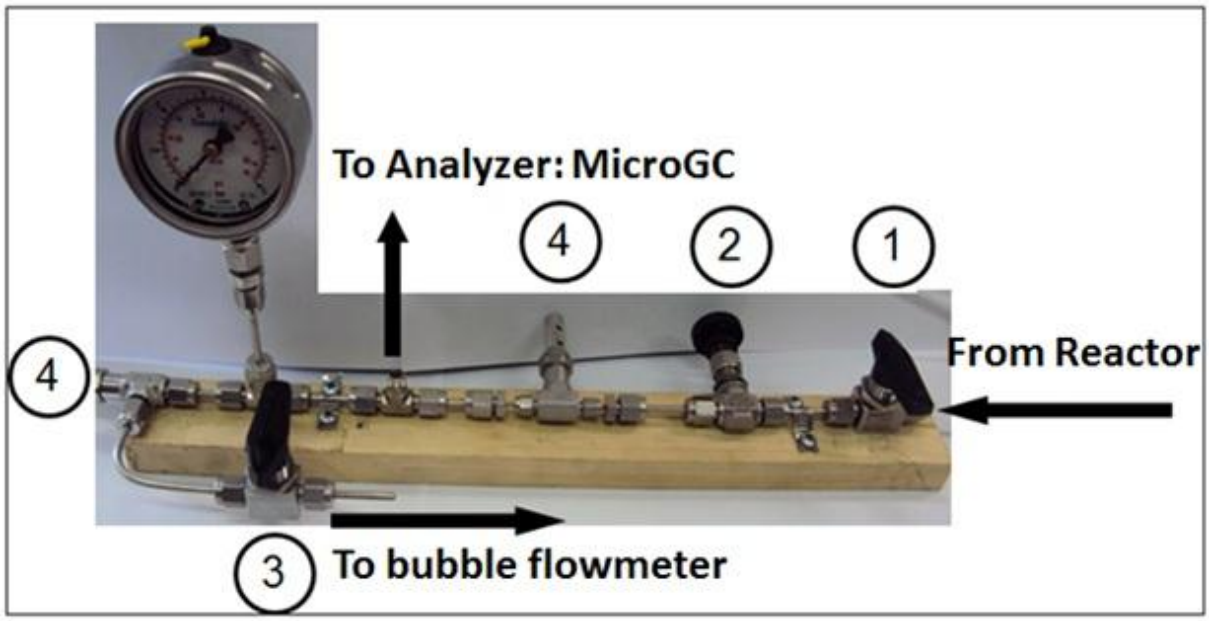

Figure 3.3:Discontinuos Sampling System.

Through the development of the sampling system two purposes have been satisfied: the possibility to analyze a gas at atmospheric pressure, and the possibility to regulate the flow inside the capillary.

The former is important because the MicroGC, described in chapter 2, used for the analysis of species in the gas phase, cannot work under pressurized conditions; the latter is fundamental to avoid to perturb the fluid dynamic inside the catalyst channel due to high flows sucked-in

by the capillary. In the previous works, the gas sampling was performed using a pump connected to the analyzer. The flow rate was about 5.5 Nl min^{-1}.

Under pressurized conditions the differential pressure between the reaction section and the sampling system causes high flows in the capillary with high errors of resolution. To have a small flow three valves are introduced: two Low-Flow Metering Valves n°4 and a Regulation Valve n°3, Figure 3.3. The high pressure drops of the Low Flow Metering Valves guarantee a small flow inside the capillary. The flow can be regulated by the Regulation Valve n°2 Figure 3.3 between a range of 2÷7 cc min^{-1}. The flow is verified in every test with a bubble flow-meter connected at the output side of the DSS as shown in Figure 3.3.

3.2.2 EXPERIMENTAL VALIDATION

After the development of the DSS, some tests are done to optimize the operating procedure. The purposes of the tests are: the development of an operating procedure aimed to guarantee an efficient cleaning inside the lines of the DSS and a correct pressure of the gas inside the DSS.

During the tests, the Discontinuous Sampling System is connected through a fused silica capillary (outer diameter of 340 μm and inner diameter of 200 μm). The capillary is opened in both sides. The metal case is equipped with the Sealing system shown previously in this chapter. Moreover the system is connected at the MicroGC and the output side is connected with a bubble flow-meter, as shown in Figure 3.3. Three different settings have been developed :

1) Setting for 1 bar test;
2) Setting for 2 bar test;
3) Setting for test at higher pressure (3 and 4 bar).

Setting for 1 bar test

For the tests at 1 bar, since there is not a pressure driving force necessary to fill-in the volume of DSS, it is not possible to sampling in a discontinuous mode. For this reason the configuration used is the following:

The DSS works in continuous flow: keep closed the valve n° 3 and keep opened the valve n° 1 (Figure 3.3) for all the time during the tests. The gas is sampling through the MicroGC pump, the sampling time is set to 30 seconds.

Setting for 2 bar test

For the 2 bar tests, since the pressure driving force between the metal case and the DSS (1 bar) is small, it is not possible to use the same method used in the tests at 3 and 4 bar (it will be described successively). The pressure inside the DSS is calibrated at 1.8 bar, therefore the sampling time of MicroGC is set to 8 seconds. The time of sampling is calculated to ensure a feed of gas to the analyzer at a pressure of 1.1 bar: in this way the pressure of the gas feeds at the analyzer is about at atmospheric pressure and the positive pressure prevents the ingress of atmospheric gas from the vent. However, because of the remaining gas in the system, there must be a wash before each analysis to avoid errors due to the residual gas.

Setting for 3 and 4 bar tests

Now it will be described in detail the tests which helped to establish the standard operating procedure of DSS. For these tests the pressure inside the DSS is calibrated at 2.2 bar, therefore the sampling time of MicroGC is set to 10 seconds.

Initially, the valves n° 1-3 are being closed, afterwards the DMFC of Nitrogen flow is set to 45.7% and the inner pressure is set to 4 bar. Before the test, the reactor is cleaned by N_2 flow (10 Nl min^{-1}) for 15 minutes. This operation is done to prevent the presence of atmospheric oxygen residue inside the reactor. Initially, the wash of the DSS is performed for 5 minutes: the valves n° 1 and n° 3 are being opened, then valve n°3 is closed. When the pressure inside the DSS reaches the right value the valve n°1 is closed too. After the sampling, both valves are opened again to clean the lines of the DSS. The results are reported in the Table 3.2.

n° sampling	A1/A2	yO_2 [%]	Washing time [min]
			5
1	0.00253	0.209	5
2	0.00196	0.162	3
3	0.00093	0.077	3
4	0.00079	0.066	3
5	0.00043	0.036	

Table 3.2:Sampling test: O_2=0%, N_2=100%, flow rate = 10 Nl min^{-1} , capillary flow= 5 cc min^{-1}

The y_{O2} represents the oxygen molar fraction in percentage. In the chapter 2, an example of a chromatograph analysis data elaboration is shown.

After the first analysis there is 0.209% of atmospheric oxygen due to incomplete cleaning of lines. After 5 minutes of cleaning in nitrogen Flow (valves n°1-3 open) the analysis procedure previously described is repeated. The second analysis shows a decrease of oxygen value (0.162%). The test is repeated three more times, with a washing time of 3 minutes, a decreasing trend is reported. These tests show a reliability of the DSS to analyze a gas stream of constant composition.

The next test is to evaluate the washing time following a variation of composition in the flow. This test is done to simulate a change of composition, following a displacement of the capillary during the test of composition: first of all the flow is set to 100% v/v of N_2 after the DSS is cleaned (as described previously). After checking the absence of oxygen in the DSS , the composition of the flow has been changed at 15% v/v of O_2 85% v/v of N_2. The results are reported in the Table 3.3.

n° sampling	A1/A2	yO_2 [%]	Washing time [min]
			5
1	0.21146	14.926	5
2	0.21272	15.002	3
3	0.21281	15.007	3
4	0.21295	15.016	

Table 3.3:Sampling test: O_2=15%, N_2=85%, flow rate = 10 Nl min^{-1}, capillary flow=5 cc min^{-1}

As the previous tests, after three analysis the sampling composition corresponds to the composition fixed with DMFC. These tests demonstrate that the Discontinuous Sampling System is adequate to do the test under pressurized conditions. In fact, this System gives a resolution reliable and stationary in a short time.

3.3 OPERANTING PROCEDURE

After these validation tests the operating procedure for the spatial sampling experiments are developed:

1. Start-up of the experiment for the spatial sampling test under pressurized conditions;
2. Waiting the steady state conditions;
3. Open the valves n° 1-3(Figure 3.3) to clean the lines of DSS (10 minutes);
4. Close the valve n° 3;
5. When the pressure inside the DSS is at the right pressure (1.8 bar for experiments at 2 bar, 2.2 bar for experiments at 3÷4 bar) close the valve n°1 (Figure 4.3);
6. Start the gas sampling;
7. Open the valves n°1-3 (Figure 3.3) to clean the lines of DSS (3 minutes).

CHAPTER 4

MONODIMENSIONAL MATHEMATICAL MODEL OF THE LAB-SCALE REACTOR

4.1 ASSUMPTIONS AND GOVERNING EQUATIONS

The experimental data are compared with the simulations of a mathematical model of the lab-scale reactor, developed in previous works [43]. The model is adiabatic, fixed bed, dynamic, heterogeneous and monodimensional. It can simulate the behavior of the reactor either with molecular, pseudo-steady-state kinetics, or with a single site C_1 microkinetic scheme. The model includes:

- the mass balances of the species for the gas phase and solid phase;
- the energy balances for the gas and solid phase;
- the momentum balance.

Accumulation terms are considered in all equations, except in the mass balance for the solid phase because of the smaller volume of fluid in catalyst pores compared to fluid volume in the bulk. Hence, steady-state conditions are considered for all the species of the solid phase. Besides, preliminary simulations showed that the relevance of the dynamics of the gas phase was negligible; nevertheless, the inclusion of the accumulation term in the equations improves the stability of the numerical solution. The equations of the model are listed in Table 4.1. In case the model incorporates the molecular scheme, the effective reaction rates are considered in the solid-phase mass balance equations. The a-priori solution of the diffusion and reaction

problems at a fixed reactor axial position (z) within the catalytic washcoat point out that the intraporous diffusional resistances for oxygen are greater by several orders of magnitude than for other species. Thus, intraporous diffusional resistances are accounted for by isothermal effectiveness factor only for combustion reactions, using the generalized Thiele modus method [44].

The effectiveness factor, considered exclusively in the case of O_2, is defined as:

$$\eta = \frac{tanh\,(\Phi)}{\Phi} \tag{4.1}$$

where Φ is the generalized Thiele modus, which is defined as:

$$\Phi = \frac{1}{\eta^{\infty}} \tag{4.2}$$

The value of η^{∞} for a generic kinetic is calculated with this formula:

$$\eta^{\infty} = \frac{\sqrt{2}}{\rho_l \cdot r_v \cdot C_{O_2}^w} \cdot \left(\int_{C_X^w}^{C_{O_2}^w} D_{eff,\ O_2} \cdot r_v(c) \cdot dc \right)^{1/2} \tag{4.3}$$

where:

- ρ_l is the thickness of the catalytic layer;
- $C_{O_2}^w$ is the superficial concentration of oxygen;
- $D_{eff,\ O_2}$ is the effective molecular diffusion of oxygen;
- C_X^w is the asymptotic concentration of O2 inside the catalyst, it is the limit of integration and it is zero, due to the fact that oxygen is the limiting reactant and is characterized by extremely fast rate of consumption;
- $r_v(C_{O_2}^w)$is the rate of consumption for oxygen.

In case the model incorporates the microkinetic scheme, the effectiveness factor is neglected. The deviation of the experimental system from the ideal adiabatic conditions is accounted for by introducing in the energetic balance of gas phase a global heat transfer coefficient between the reactor and the external environment. In fact, through the global heat transfer coefficient

(h_{ext}) it is possible to consider the radial dispersion of heat along the reactor: in this way, the behavior of the reactor can be simulated even if the value of the thermal efficiency α (par. 5.1) is less than the unity. The heat losses are defined by the integral:

$$\dot{Q}_{lost} = \int_{Zin}^{Zout} h_{ext} \cdot \left(T_{gas}(x) - T_{\infty}\right) \cdot \pi \cdot D \cdot dx \qquad (4.4)$$

Due to the high Peclet number, axial diffusion is neglected in the gas phase [45]. Gas-phase reactions are accounted for by using the detailed scheme of Ranzi et al.[70]. In line with the reference [47], in CH_4-CPO no contribution from homogeneous chemistry was found under our operating conditions. Instead, in C_3H_8-CPO the reactions in homogeneous phases become important.

Gas phase

Species mass balance equations:

$$\frac{\partial \omega}{\partial t} = -\frac{G}{\rho_g \cdot \varepsilon} \cdot \frac{\partial \omega_i}{\partial z} - \frac{a_v}{\varepsilon} \cdot K_{mat,i} \cdot \left(\omega_i - \omega_{i,wall}\right) + \left(\sum_{j=1}^{NR\hom} \nu_{i,j} \cdot r_j^{\hom} \right) \cdot \frac{MW_i}{\rho_{gas}}$$

Energy balance equation:

$$\frac{\partial T_g}{\partial t} = -\frac{G}{\rho_g \cdot \varepsilon} \cdot \frac{\partial T_g}{\partial z} - \frac{a_v}{\rho_g \cdot \varepsilon \cdot \hat{c}_{p,g}} h \cdot \left(T_g - T_s\right) - \frac{4}{d_{ret} \cdot \rho_g \cdot \varepsilon \cdot \hat{c}_{p,g}} \cdot h_{ext} \cdot \left(T_g - T_{amb}\right) + \left(\sum_{j=1}^{NR\hom} \nu_{i,j} \cdot r_j^{\hom} \cdot \left(-\Delta H_{R,j}\right) \right) \cdot \frac{MW_i}{\rho_{gas}}$$

Momentum balance equation:

$$\left(-\frac{1}{\rho_g} + \frac{G}{\rho_g^2 \cdot p} \right) \frac{dp}{dz} - \frac{G^2}{\rho_g^2 \cdot T_g} \cdot \frac{dT_g}{dz} = \frac{1}{2} \cdot \frac{G^2}{\rho_g^2} \cdot a_v \cdot f$$

Solid phase

Species mass balance equations:

$$0 = a_v \cdot \rho_s \cdot K_{mat,i} \cdot \left(\omega_i - \omega_{i,wall}\right) + \left(\sum_{j=1}^{NR} \nu_{i,j} \cdot r_j^{eff}\right) \cdot MW_i \cdot \rho_s \cdot \xi$$

Energy balance equation:

$$\frac{\partial T_s}{\partial t} = -\frac{a_v}{\rho_s \cdot (1-\varepsilon) \cdot \hat{c}_{p,s}} \cdot h \cdot \left(T_g - T_s\right) - \frac{k_{ax}^{eff}}{\rho_s \cdot \hat{c}_{p,s}} \cdot \frac{\partial^2 T_s}{\partial z^2} + \left(\sum_{j=1}^{NR} \nu_{i,j} \cdot r_j^{eff} \cdot \left(-\Delta H_{R,j}\right)\right) \cdot \frac{\xi}{\hat{c}_{p,s} \cdot (1-\varepsilon)}$$

Site balance:

$$\frac{\partial \theta_i}{\partial t} = \frac{s_i}{\Gamma_{Rh}}$$

Table 4.1: Model equations.

The boundary conditions and the initial conditions are listed in Table 4.2. The pressure and the temperature for the gas phase are fixed data. The radiative axial dispersion at the reactor boundaries is considered for the solid phase. Besides, the simulations account for the presence of an inert portion of support prior to the catalytic bed.

Boundary conditions

Reactor inlet:

$$\omega_{i,z=z_1} = \omega_{i,\,feed} \qquad T_{g,z=z_1} = T_{feed} \qquad P_{z=z_1} = P_{feed}$$

$$-k_{ax}^{eff} \cdot \left.\frac{\partial T_s}{\partial z}\right|_{z_1} = -\sigma \cdot \varepsilon_s \cdot \left(T_g^4 - T_s^4\Big|_{z_1}\right)$$

Reactor outlet:

$$-k_{ax}^{eff} \cdot \left.\frac{\partial T_s}{\partial z}\right|_{z_2} = -\sigma \cdot \varepsilon_s \cdot \left(T_g^4 - T_s^4\Big|_{z_2}\right)$$

Initial condition

$$\omega_i(z,0) = 0 \qquad T_g(z,0) = T_{g,\,feed} \qquad T_s(z,0) = T_{room}$$

Table 4.2: Boundary conditions and initial conditions.

The nomenclature of the previous equations is:

a_v specific area per unit volume [m^{-1}]

A reactor cross sections [m^2]

$\hat{c}_p$ specific heat [J/kg/K]

d_{cell} pore dimension [m]

f friction factor

G superficial mass flow rate [kg/m2/s]

h heat transfer coefficient [$W/m^2/K$]

h_{ext} heat transfer coefficient with the external environment [W/m^2/K]

$\Delta H_{R,j}$ heat of reaction [J/mol]

$K_{max,i}$ mass transfer coefficient [m/s]

L_{rct} reactor length [m]

k_{eff}^{ax} effective solid thermal conductivity [W/m/K]

P pressure [Pa]

r_j j-reaction rate [mol/kg$_{cat}$/s]

s_i production rate for i specie [mol/cm^2/s]

θ_i coverage site fraction [mol/cm^2]

Γ_{rh} site density [mol/cm^2]

T temperature [K]

z reactor axial coordinate [m]

ε bed void fraction

ε emissivity

ξ volumetric catalytic fraction

ρ density [kg/m^3]

σ Stefan-Boltzmann constant

ω weight fraction

Subscripts and superscripts

g gas phase

s solid phase

eff effective

Physico-chemical and transport proprieties are estimated according to the CHEMKIN correlations [48]. In particular, for the evaluation of the transport proprieties, the multi-average model of CHEMKIN package has been used.

4.2 NUMERICAL METHOD

The model consists of N partial differential equations (PDEs) and was solved numerically by the method of lines. The axial reactor length was split into a suitable number of grid points in each point the spatial derivates was approximated by the Euler Backward differential method. Thus, from a N PDEs problem, a N x $n_{grid\ points}$ DAE system was obtained. The DAE system was solved by the initial value C_{++} Class BzzDae for stiff problems [49] of the BzzMath 5.0 library [50]. This integrator can exploit the tridiagonal block structure of the Jacobian and resulted very efficient and robust. The convergence of the solution in time was checked by using the internal criteria of the integrator. A adaptive mesh refinement scheme was employed in the axial coordinate, by reducing the local error below a threshold, as follows: the initial steady state solution was obtained on a coarse equi-spaced grid. During an iteration, if the local error ε_i at the ith point is greater than $\varepsilon_{max,I,}$ a point is added between the ith and i+1th points. The procedure ended when at each axial point $\varepsilon_i < \varepsilon_{max,I}$. In the adaptive mesh refinement approach, the problem dimension increased progressively and the points were segregated where they were really needed.

4.3 KINETIC SCHEME

A steady-state molecular indirect-consecutive kinetic scheme of CH_4 partial oxidation over Rh catalyst can be incorporated in the reactor model. The kinetic scheme was developed on the basis of a wide experimental campaign in annular reactor at high space velocity [51]. Herein, CH_4 partial oxidation tests, as well as CH_4 steam reforming and CO and H_2 rich combustion tests were performed at varying the temperature, flow rate, and feed composition far from the thermodynamic equilibrium, under quasi-isothermal conditions and reduced impact of mass transfer limitations. All kinetic tests were run under diluted conditions.

The heterogeneous reactions and the corresponding kinetics expressions are listed in Table 4.3 where:

- η is the ratio of experimental reaction quotient and the thermodynamic equilibrium constant

$$\eta_{SR} = \frac{K_{P,SR}}{K_{eq,SR}} \quad with \quad K_{P,SR} = \frac{P_{CO} \cdot P_{H_2}^3}{\left(P_{CH_4} \cdot P_{H_2O}\right)} \tag{4.5}$$

$$\eta_{WGS} = \frac{K_{P,WGS}}{K_{eq,WGS}} \quad with \quad K_{P,WGS} = \frac{P_{CO_2} \cdot P_{H_2}}{\left(P_{CO} \cdot P_{H_2O}\right)} \tag{4.6}$$

$$\eta_{RWGS} = \frac{1}{\eta_{WGS}} \tag{4.7}$$

- σ is a "limiting" factor which multiplies the reaction rate incorporated within the mass balance in order to account for the limiting concentration of O_2, H_2O and CO_2 and it is defined as

$$\sigma = \frac{P_i}{10^{-5} + P_i} \tag{4.8}$$

where P_i is the partial pressure of O_2 for combustion reaction and CO_2 and H_2O for reforming reactions.

- $k_j(T)$ is kinetic rate constant calculated according to the Arrhenius form:

$$k_j(T) = k(T_{rif}) \cdot e^{\left[-\frac{Eatt}{R}\cdot\left(\frac{1}{T}-\frac{1}{Trif}\right)\right]} \tag{4.9}$$

Rate equation (mol $g_{cat}^{-1}s^{-1}$)	k_i^{873K} (mol/(atm g_{cat} s)$^{-1}$)	E_{act} (kJ/mol)
CH_4 total oxidation: $CH_4 + 2O_2 \rightarrow CO_2 + H_2O$		
$r_{tot_{ox}} = \frac{k_{tot_{ox}} \cdot P_{CH_4}}{1 + k_{ads_{H_2O}} \cdot P_{H_2O}} \cdot \sigma_{O_2}$	1.030×10^{-1}	92

CH_4 steam reforming: $CH_4 + H_2O \leftrightarrow 3H_2 + CO$

$$r_{SR} = \frac{k_{SR} \cdot P_{CH_4}\left(1-\eta_{SR}\right)}{1+k_{ads_{CO}} \cdot P_{CO} + k_{ads_{O_2}} \cdot P_{O_2}} \cdot \sigma_{H_2O}$$

1.027×10^{-1} 92

Direct water gas shift: $CO + H_2O \rightarrow CO_2 + H_2$

$$r_{WGS} = \frac{k_{WGS} \cdot P_{H_2O}\left(1-\eta_{WGS}\right)}{1+k_{ads_{H_2O}} \cdot P_{H_2O}} \cdot \sigma_{CO}$$

$$\eta_{WGS} < 1$$

6.831×10^{-2} 75

Reverse water gas shift: $H_2O + CO \rightarrow CO_2 + H_2$

$$r_{RWGS} = k_{RWGS} \cdot P_{CO_2}\left(1-\eta_{RWGS}\right) \cdot \sigma_{H_2}$$

$$\eta_{RWGS} < 1$$

1.276×10^{-2} 62

H_2 oxidation: $H_2 + 0.5O_2 \rightarrow H_2O$

$$r_{H_2ox} = k_{H_2ox} \cdot P_{H_2} \cdot \sigma_{O_2}$$

2.666×10^{3} 62

CO oxidation: $CO + 0.5O_2 \rightarrow CO_2$

$$r_{COox} = k_{COox} \cdot P_{CO} \cdot \sigma_{O_2}$$

1.937×10^{1} 76

Surface adsorption	$k_{ads,i}^{873K}$ (atm^{-1})	ΔH_{ads} (kJ/mol)
O_2	5.461	-73
H_2O	3.901×10^{2}	-37
CO	2.114×10^{2}	-57

Table 4.3: Kinetic scheme and parameter estimated.

Herein the reactions involved in the kinetic scheme will be described in detail:

- *CH_4 total oxidation*

$$r_{tot_{ox}} = \frac{k_{tot_{ox}} \cdot P_{CH_4}}{1 + k_{ads_{H_2O}} \cdot P_{H_2O}} \cdot \sigma_{O_2} \tag{4.10}$$

The expression shows that the total oxidation has a first-order dependence on CH_4 concentration and a zero-order dependence on the co-reactant concentration. The absence of any independence on the O_2 content in the reaction rate is coherent with the picture of a catalyst surface almost completely covered by O* adatoms, with a few sites for CH_4 adsorption, as pointed out in literature by experimental results over Rh and by numerical simulations with detailed kinetic models. Besides, the CH_4 combustion is moderately inhibited by water absorption, but this effect is little influenced by varying amount of water and this suggests that the available sites for H_2O adsorption are closed to the saturation.

- *CH_4 steam reforming*

$$r_{SR} = \frac{k_{SR} \cdot P_{CH_4}\left(1 - \eta_{SR}\right)}{1 + k_{ads_{CO}} \cdot P_{CO} + k_{ads_{O_2}} \cdot P_{O_2}} \cdot \sigma_{H_2O} \tag{4.11}$$

The expression adopted for steam reforming has a first order dependence on CH_4 and it is independent from water. The steam reforming is delayed in the presence of O_2 and is influenced by the competitive absorption of the reacting species. The nature of inhibition is uncertain and is presently under investigation though the means of theoretical analysis; besides there is an inhibition of CO (or syngas) because the experimental data can be well described by assuming that the surface is saturated by the absorption of CO.

- *Water gas shift*

$$r_{WGS} = \frac{k_{WGS} \cdot P_{H_2O}\left(1-\eta_{WGS}\right)}{1+k_{ads_{H_2O}} \cdot P_{H_2O}} \cdot \sigma_{CO} \qquad (4.12)$$
$$\eta_{WGS} < 1$$

The equation has a zero-dependence on CO and first-order dependence on H_2O and is valid only when the term η_{WGS} is lower than the unity. Besides, it contains an inhibition term due to H_2O adsorption. This term was introduced on the basis of CPO tests under concentrated conditions. In fact, while in highly diluted experiments (with CH_4 concentration lower than 4%) WGS was equilibrated, at increasing concentration of reactants, the reaction progressively deviated from the equilibrium and became kinetically controlled. So, the inhibition term due to water was explicitly added in order to describe the progressive divergence of WGS from the equilibrium.

- *Reverse water gas shift*

$$r_{RWGS} = k_{RWGS} \cdot P_{CO_2}\left(1-\eta_{RWGS}\right) \cdot \sigma_{H_2} \qquad (4.13)$$
$$\eta_{RWGS} < 1$$

Equation reports that RWGS is first order dependent on CO_2 and independent of H_2. The contribution of reverse water gas shift is negligible in the CPO runs, but numerical and experimental CPO and steam reforming data point out that it is not possible to use one equation comprising both the direct and reverse WGS steps. The direct and the reverse step must be treated as two distinct reactions with different kinetic dependences and a coherent approach to equilibrium. For this reason when RWGS is active (when η_{RWGS} is lower than the unity), the WGS is forced to be nil and vice versa, when WGS is active the RWGS rate is set equal to zero.

- *H_2 and CO oxidation*

$$r_{H_2ox} = k_{H_2ox} \cdot P_{H_2} \cdot \sigma_{O_2} \tag{4.14}$$

$$r_{COox} = k_{COox} \cdot P_{CO} \cdot \sigma_{O_2} \tag{4.15}$$

First-order rate is adopted in line with the kinetics of CH_4 combustion. The kinetic role of post-combustion reactions is negligible with diluted feed streams, while, in the case of concentrate mixtures, the consecutive oxidations contrast the equilibration of the WGS reaction and exert a control on H_2/CO ratio.

Besides, Donazzi at al. [52] had specifically addressed the kinetic role of CO_2 reforming, which was found to be negligible within the kinetic scheme of CH_4 catalytic partial oxidation over rhodium.

The kinetic constants obtained were referred to load and dispersion of rhodium in the 4% Rh/α-Al_2O_3 catalysts and then they were rescaled to the load and dispersion for the catalyst performed in the adiabatic reactor.

The model can also incorporate a single site C_1 microkinetic scheme, consisting of 82 surface reactions and 13 adspecies. It was derived according to a hierarchical multiscale methodology involving both semi-empirical methods (UBI-QEP) and first principle techniques [53,54]. The scheme was validated over a wide set of CH_4-CPO experimental data within an annular microreactor under quasi-isothermal conditions [51]. The resulting scheme was able to describe several reacting system, namely CH_4 pyrolysis and oxidation, steam reforming, H_2- and CO-rich oxidations, WGS and reverse WGS.

4.3.1 KINETIC EXPRESSION FOR PROPANE CPO

The reaction mechanism for the catalytic partial oxidation of propane was developed in strict analogy with the methane scheme. The model accounts for the formation of syngas through a consecutive scheme, consisting of deep oxidation and steam reforming of propane and methane, water gas shift, H_2 and CO post-combustion, and methanation. The kinetic expressions for the heterogeneous reactions were developed on the basis of a wide

experimental campaign in annular reactor [51,55] and are listed in Table 4.4 (in addition to the reactions show in Table 4.3).

Rate equation (mol $g_{cat}^{-1}s^{-1}$)	k_i^{873K} (mol/(atm g_{cat} s)$^{-1}$	E_{act} (kJ/mol)
C_3H_8 total oxidation: $C_3H_8 + 5O_2 \rightarrow 3CO + 7\ H_2$		
$r_{C_3H_{8ox}} = \frac{k_{C_3H_{8ox}} \cdot P_{C_3H_8}}{1 + k_{ads_{H_2O}} \cdot P_{H_2O}} \cdot \sigma_{O_2}$	3.036 x 10^{-1}	87
C_3H_8 steam reforming: $C_3H_8 + 3H_2O \leftrightarrow 3CO + 7H_2$		
$r_{SR\_C_3H_8} = \frac{k_{SR\_C_3H_8} \cdot P_{C_3H_8}\left(1-\eta_{SR\_C_3H_8}\right)}{1 + k_{ads_{CO}} \cdot P_{CO} + k_{ads_{O_2}} \cdot P_{O_2}} \cdot \sigma_{H_2O}$	2.486 x 10^{-1}	85
CO methanation: $CO + 3H_2 \rightarrow CH_4 + H_2O$		
$r_{Met} = k_{Met} \cdot P_{H_2} \cdot \left(1-\eta_{Met}\right) \cdot \sigma_{CO}$	1.2 x 10^{-3}	88

Table 4.4: Kinetic scheme and parameter estimated for propane CPO.

Subsequently the expression kinetic for propane-CPO will be described in detail.

- *C_3H_8 total oxidation*

$$r_{C_3H_{8ox}} = \frac{k_{C_3H_{8ox}} \cdot P_{C_3H_8}}{1 + k_{ads_{H_2O}} \cdot P_{H_2O}} \cdot \sigma_{O_2} \qquad (4.16)$$

The expression shows that the total oxidation has a first-order dependence on C_3H_8 concentration and a zero-order dependence on the co-reactant concentration, as in the case of

CH_4 total oxidation. The activity of the propane is higher than that of the methane because the propane has lower activation energy and the value of the pre-exponential coefficient is three times that of the methane. In a recent work [55] it was verified that the propane total combustion is inhibited by water, as in the case of methane.

- *C_3H_8 steam reforming*

$$r_{SR\_C_3H_8} = \frac{k_{SR\_C_3H_8} \cdot P_{C_3H_8}\left(1-\eta_{SR\_C_3H_8}\right)}{1+k_{ads_{CO}} \cdot P_{CO} + k_{ads_{O_2}} \cdot P_{O_2}} \cdot \sigma_{H_2O} \tag{4.17}$$

The expression adopted has a first order dependence on C_3H_8. The steam reforming is delayed in the presence of O_2 and for this reason a terms of inhibition of O_2 is considered. Furthermore there is another term of inhibition due to the CO absorption. In the formulation of this expression, an independence of water is assumed, coherently with the kinetic of methane steam reforming.

- *CO methanation*

$$r_{Met} = k_{Met} \cdot P_{H_2} \cdot \left(1-\eta_{Met}\right) \cdot \sigma_{CO} \tag{4.18}$$

The expression adopted has a first-order dependence on H_2. The reaction of methanation becomes important after syngas formation, therefore after 400°C and it influences the reaction of WGS and so the CO_2 production.

The other kinetic expressions are identical to that for the kinetic scheme of methane, previously described.

4.4 CATALYTIC BED PROPRIETIES

In this work the tests of CPO are performed on 400 CPSI cordierite monoliths (Table 2.3, chapter 2). A detailed list of the relevant input parameters of the simulations is reported in Table 4.5.

Honeycomb	
Diameter (mm)	24
Length (mm)	26
Channel opening (mm)	1.092
Void fraction (-)	0.75
Cordierite Density (g cm^{-3})	2.3
Cordierite Thermal Conductivity (W m^{-1} K^{-1})	2.5

Catalyst	
Density (g cm^{-3})	1.38
Rh load (% w/w)	2
Rh dispersion (%)	20
Catalyst dimensions	
Length (mm)	26
Weight (mg)	620
Thickness (μm)	14.88

Table 4.5: Relevant geometrical and physical properties of the honeycomb monolith.

The bed transport proprieties were accounted for by specific heat and mass transfer correlations. In the case of laminar flow in channel with square section the correlations of Shah and London were used:

$$Nu = 2.977 + \left(8.827 \cdot \left(10^3 \cdot Z^*\right)^{0.545}\right) \cdot exp\left(-48.2 \cdot Z^*\right) \qquad (4.19)$$

$$Sh = 2.977 + \left(8.827 \cdot \left(10^3 \cdot Z^*\right)^{0.545}\right) \cdot exp\left(-48.2 \cdot Z^*\right) \qquad (4.20)$$

where :

- $Z^* = \dfrac{z \cdot L_{ert}}{d_{cell} \cdot Re \cdot Sc}$ *for Sh*
- $Z^* = \dfrac{z \cdot L_{ert}}{d_{cell} \cdot Re \cdot Pr}$ *for Nu*
- $f = \dfrac{14}{Re}$
- $Re = \dfrac{d_{cell} \cdot G}{\mu \cdot \varepsilon}$

The effective thermal conduction of the solid is accounted for the correlation proposed by Lee and Aris [56] (4.21):

$$k_{ax}^{eff} = (1-\varepsilon) \cdot k_s + \frac{16}{3} \cdot \sigma \cdot 1.12 \cdot \frac{d_{cell}}{2} \cdot T_s^3 \qquad (4.21)$$

CHAPTER 5

ANALYSIS OF THE EFFECTS OF THE PRESSURE IN CH_4-CPO

5.1 INTRODUCTION

This chapter reports the results of a set of tests that is carried out to verify the influence of the pressure and to validate the experimental setup on CH_4-CPO reformer operating with Rh-coated honeycomb monoliths. The use of methane is due to a relative good knowledge of the effect of pressure in CH_4-CPO reformer.

The effect of pressure on CH_4-CPO, investigated by Schmidt and co-workers [71], has been herein studied through the application of a spatially resolved sampling technique and of a modeling analysis. The experiments are carried out in the lab-scale adiabatic reactor, described in chapter 2, with the improvements described in chapter 3 (Sealing System, Discontinuous Sampling System). All the experiments are performed in auto-thermal conditions, with Sample FHS 6 (its preparation and characteristics are detailed in 2.10 Table 2.3) in 'Standard Configuration', with 10 NL min^{-1} total flow rate and C/O ratio of 0.9 and progressively increasing of the pressure from 1 to 4 bar. The composition of synthesis gas and temperature of the gas phase have been compared with the values obtained by the adiabatic equilibrium. The algorithm uses to calculate the equilibrium is based on STANJAN® [62] bank data and it minimizes the free Gibbs energy at constant pressure and enthalpy. Besides, in each experiment the thermal efficiency is calculated to verify that the adiabatic condition is effectively realized. The thermal efficiency is the ratio between the experimental temperature rise and the theoretical adiabatic temperature rise of the gas phase:

$$\alpha = \frac{T_{EXP}^{OUT} - T_{EXP}^{IN}}{T_{ADIABATIC}^{OUT} - T_{EXP}^{IN}}$$

where T_{EXP}^{IN} is the inlet gas temperature, in auto-thermal conditions it corresponds to 25°C, T_{EXP}^{OUT} is the outlet gas temperature and it has been measured through a sliding thermocouple at the end of the channel, $T_{ADIABATIC}^{OUT}$ is the adiabatic temperature, calculates at the composition of the outlet gas mixture.

In all tests, we use the start-up procedures, described in chapter 2. The 'Pressure Regulation Valve' (Figure 2.1) is progressively closed to regulate the pressure inside the reactor. During this procedure, the temperature has been monitored to avoid the thermal run-away of the system. To check the temperature, we use a thermocouple inside the catalyst and we monitor the trend on PICOLOG® graph, an example is reported in Figure 5.1.

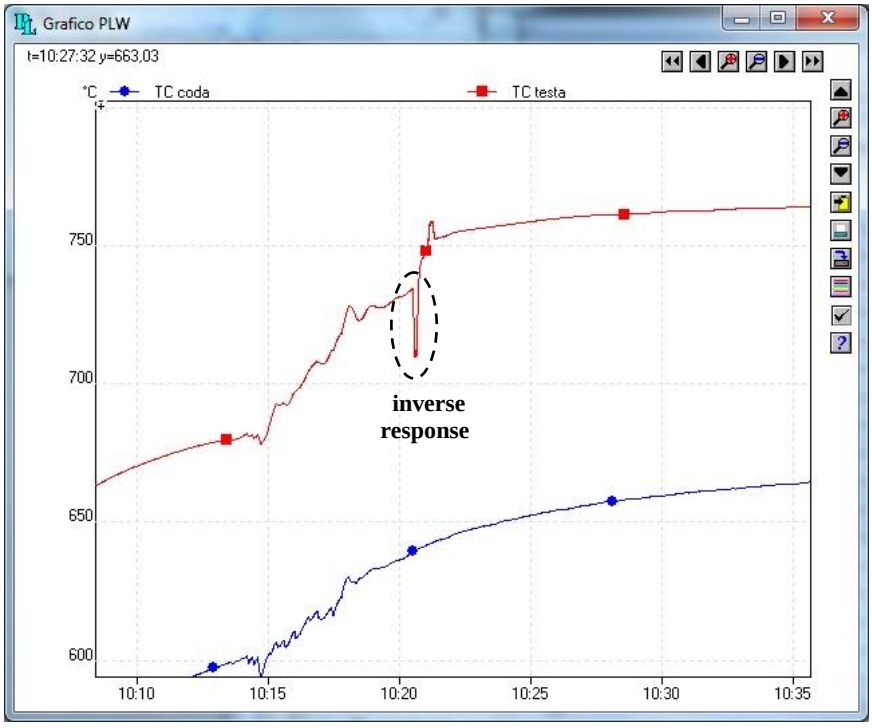

Figure 5.1: Typical temperature trend during the pressurization of the system

As shown in Figure 5.1, when we close the 'Pressure Regulation Valve', there is an inverse response of the temperature value because initially there is more cold reactants on the catalyst: when the pressure inside the reactor increases also the density of the gas phase increases and the temperature decreases for the bigger concentrations of cold reactants. Afterwards the exothermically reactions start and the temperature increases.

5.2 EFFECT OF PRESSURE ON THE THERMAL BEHAVIOR

The honeycomb monolith FHS 6 is tested by increasing progressively the pressure of the system from 1 to 4 bar. As underlined before, the spatial sampling technique is a highly informative tool that allowed to characterize the behavior of the system not only through the outlet temperature and composition (integral measurements), but especially through the reconstruction of the axial profiles (local measurements). The measured axial temperature profiles are reported in Figure 5.2.

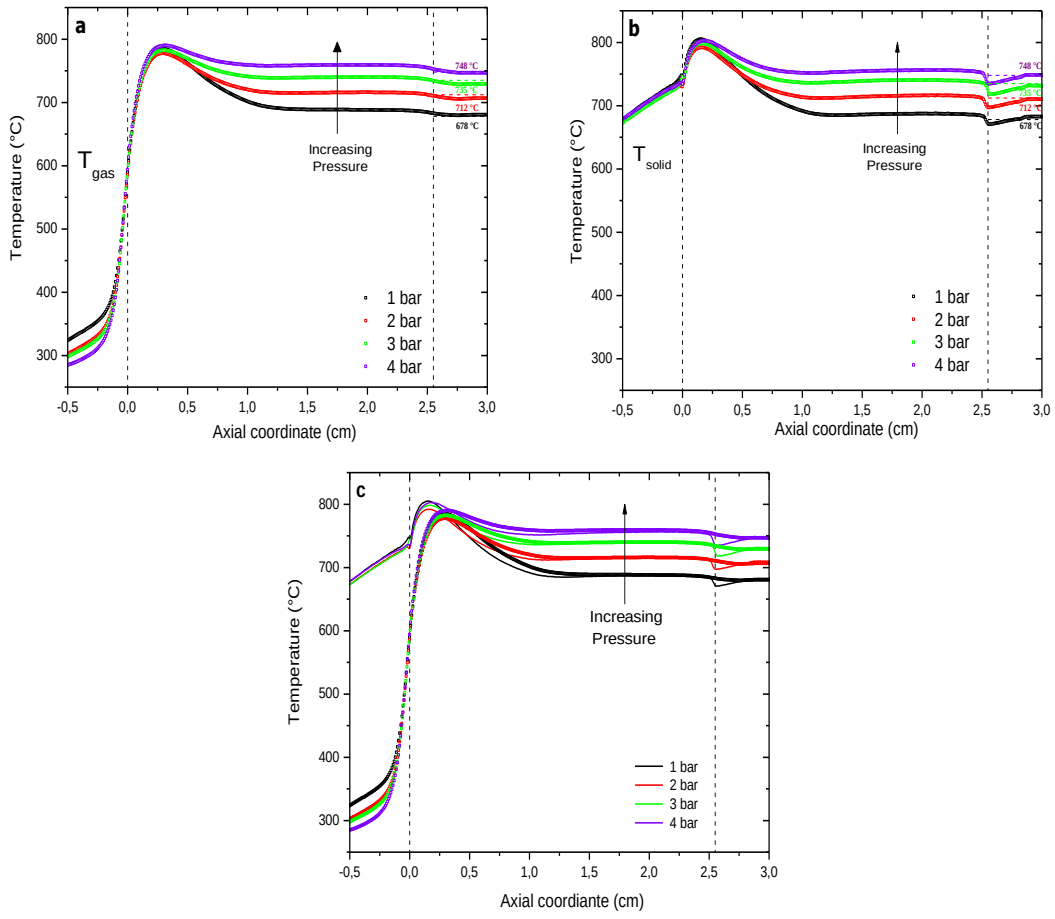

Figure 5.2: Temperature profiles for gas phase (panel a); solid phase (panel b); solid (solid lines) and gas(dot lines) phases (panel c) at different pressure. Honeycomb monolith, Sample FHS 6. Operating conditions: autothermal, C/O=0.9, 10 Nlmin^{-1} flow rate; P=1÷4 bar.

The measured profiles of temperature has the typical features of a CPO experiment: the temperature profiles shows that in the inlet section a hot spot for both phase is observed, the temperature surface also is much higher than the gas temperature as the heat generation at the catalyst surface is much faster than the heat transport to the incoming gas. Then, both the temperature profiles became relatively flat downstream of the hot-spot, thus suggesting that the thermodynamic equilibrium is reached.

The temperature profiles (Figure 5.2.a-b), of the gas and the solid phases, show that the hot spot, in the inlet section of the channel, is little influenced by pressure: a little decrease is observed passing from 1 to 2 bar, from 2 to 4 bar the temperature rise up with pressure increase (Table 5.1). Downstream of the hot spot, where the profile flattens, a positive effect of the pressure is measured, which is due to the prevailing control of thermodynamic equilibrium (Figure 5.1.c). The values of the maximum temperature measured by thermocouple and pyrometer, at different pressure, are reported in the Table 5.1.

Pressure [bar]	**T_{gas} [°C]**	**T_{solid} [°C]**	**C/O**	**y_{O_2}**
1	786	805	0.89	15.27
2	778	792	0.88	15.20
3	782	799	0.87	15.20
4	789	802	0.87	15.34

Table 5.1: Values of maximum temperature values measured by the thermocouple and by the pyrometer for the gas and the solid phase, respectively, at different pressure for the CH_4-CPO tests.

Table 5.1 shows that there is not apparently a link between the pressure and the temperature of the hot spot. The C/O ratio shows that the hot spot temperature is not even linked with the inlet composition, however the maximum value of temperature appears to link with the inlet oxygen molar fraction: a probable explanation is that the oxygen promoted the exothermic reaction, which lightly influences the balance between the exothermic and endothermic reactions.

Pressure [bar]		χ_{CH_4}	σ_{H_2}	σ_{CO}	T_{gas} [°C]	T_{solid} [°C]	α
1	exp	90%	89%	87%	684	671	1.01
	eq.	87%	91%	85%	679	-	
2	exp	86%	95%	90%	712	697	1.00
	eq.	85%	90%	86%	711	-	
3	exp	85%	93%	90%	736	723	1.01
	eq.	84%	90%	86%	732	-	
4	exp	84%	92%	87%	755	736	1.02
	eq.	83%	90%	86%	748	-	

Table 5.2: Comparison between the experimental data and the values of thermodynamic equilibrium about conversion of CH_4 and selectivity to Syngas.

Table 5.2 shows that, the thermodynamic equilibrium is effectively reached in fact, the temperature of the gas phase is in agreement with the adiabatic temperature calculates by STANJAN®; further proof is the unit value of the thermal efficiency.

5.3 EFFECT OF PRESSURE ON THE SPECIES PROFILE

The honeycomb monolith FHS 6 is tested by increasing progressively the pressure of the system from 1 to 4 bar to evaluate the effect of pressure on the species profile. The concentration profiles of the reactants, CH_4 and O_2, are reported in Figure 5.3

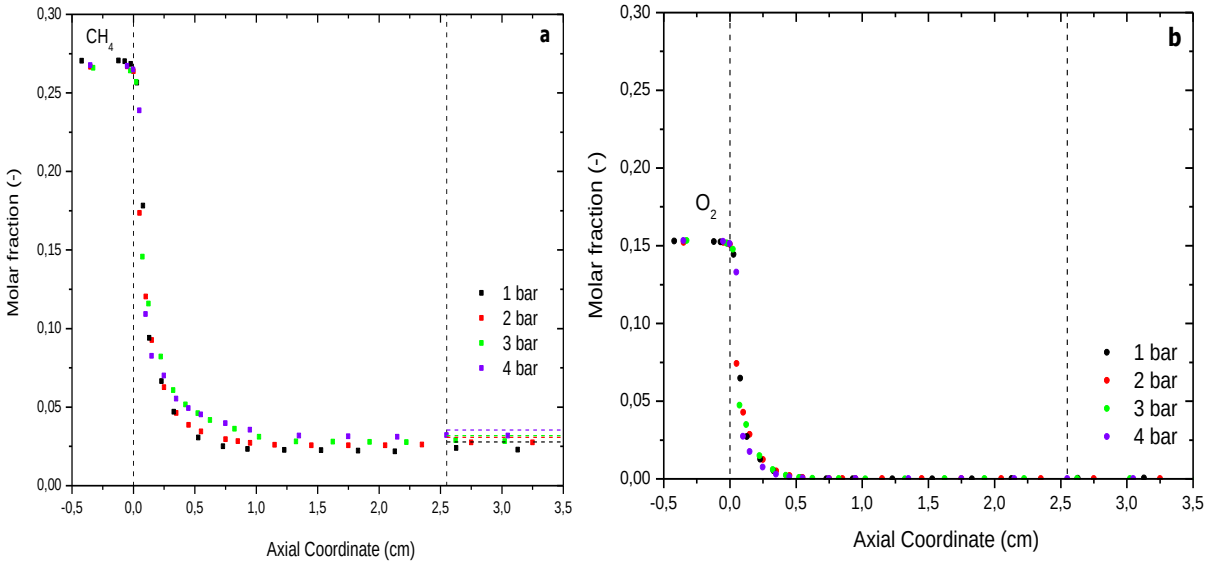

Figure 5.3: Axial concentration profiles of the reactants measured (a-b) at different pressure 1÷4 bar. Honeycomb monolith, Sample FHS 6. Operating conditions: autothermal, C/O=0.9, 10 Nlmin^{-1} flow rate.

As the Figure 5.3 shows, the increase of the pressure has a limited influence on the species. Like observed with the thermal behavior, the pressure influences only the thermodynamic equilibrium (the last part of the profile). To better appreciate such a limited influence on the first part of catalyst, ruled by kinetic, the Figure 5.4 is a zoom of the inlet part of the catalyst, which better shows the zone where the reactants are consumed.

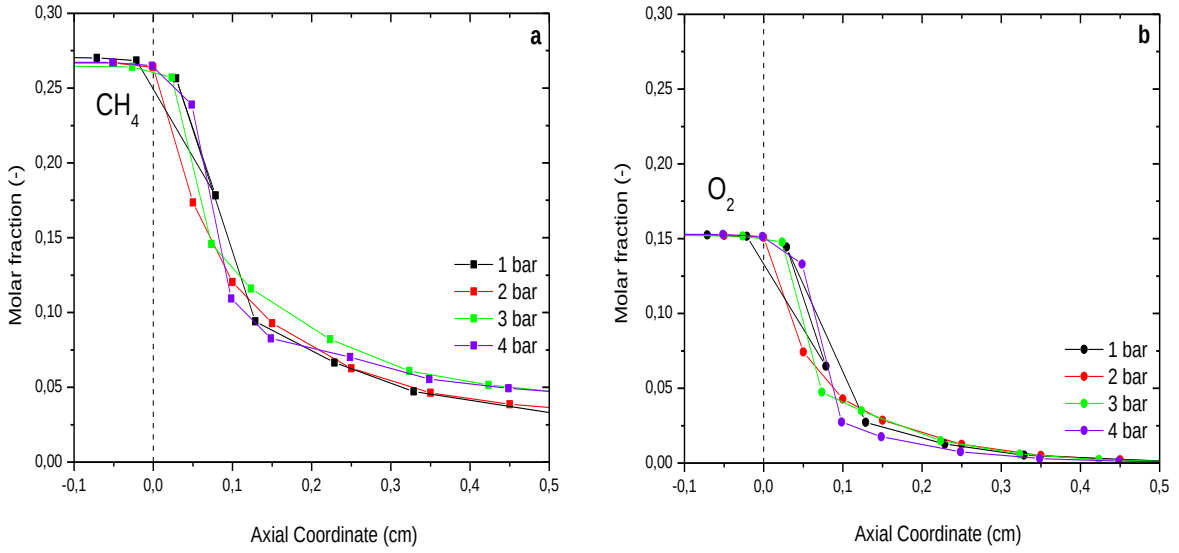

Figure 5.4: Magnification of the first 5mm of the catalyst: axial concentration profiles of the reactants measured (a-b) at different pressure 1÷4 bar. Honeycomb monolith, Sample FHS 6. Operating conditions: autothermal, C/O=0.9, 10 Nlmin^{-1} flow rate.

The magnification of the inlet part of the catalyst shows that the profiles are note overlapping, however a systematic trend is not displayed. This is probably due to the experimental error or to the intrinsic variability of the measurement.

The products profile reflects the reactants profile: in fact the pressure influences only the thermodynamic equilibrium, Figure 5.5. Furthermore the H_2 and H_2O concentration profiles display a double trend. After the comparison between the experimental data with the model predictions (paragraph 5.4.), we suppose that it is probably due to the experimental error.

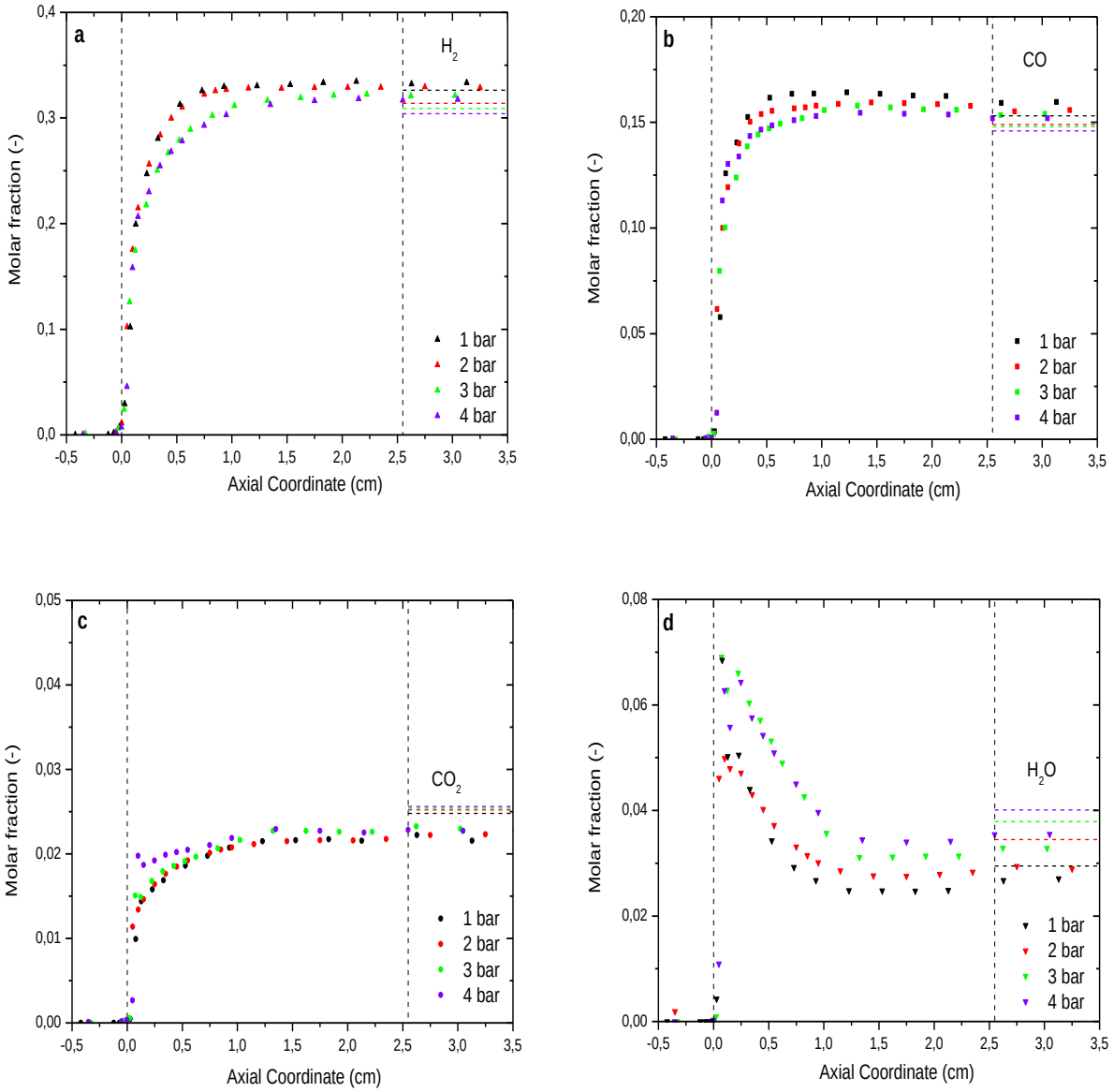

Figure 5.5: Axial concentration profiles of the products measured (a-b) at different pressure 1÷4 bar. Honeycomb monolith, Sample FHS 6. Operating conditions: autothermal, C/O=0.9, 10 Nlmin^{-1} flow rate.

Finally a comparison test at 1 bar is performed in order to verify the catalyst deactivation.

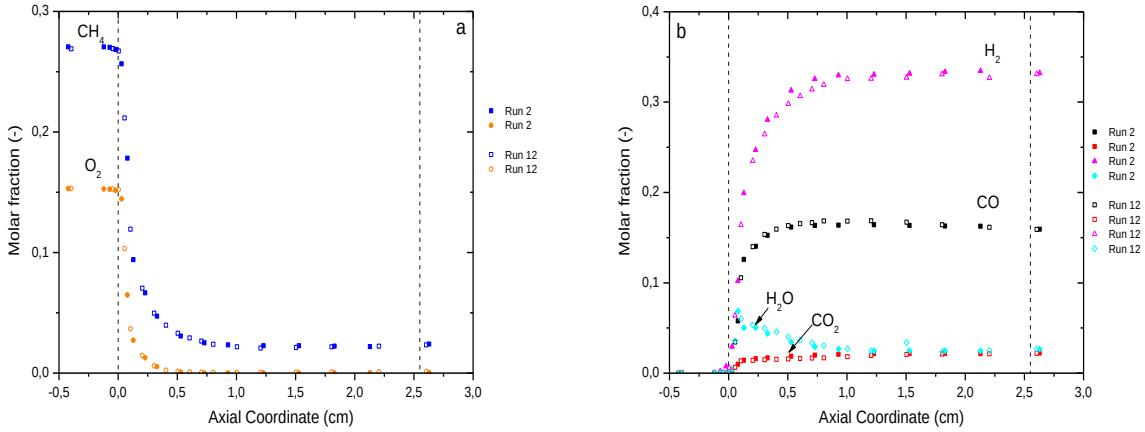

Figure 5.6: Axial concentration profiles of the reactants (panel a) and products (panel b). Honeycomb monolith, Sample FHS 6. Operating conditions: autothermal, C/O=0.9, 10 Nlmin^{-1} flow rate, at atmospheric pressure; filled scatter: first composition analysis (Run 2), empty scatter: last composition analysis(Run 12).

Figure 5.6 shows that the two different profiles (Run 2 and Run 12) are in good agreement, that it means the deactivation, between the first and the last experiments, is negligible.

5.4 MODELLING ANALYSIS

The experimental results are quantitatively analyzed by a 1D, dynamic, heterogeneous, fixed-bed, single-channel model of the adiabatic reactor, described in chapter 4.

The numerical analysis herein reported is fully predictive, with no parameter adjustment. The only input data of the calculations are the catalyst amount, the Rh load and dispersion (20%, as estimated experimentally by H_2 chemisorption measurements), the geometrical parameters and the physical properties of the honeycomb support (Table 3.5).

5.4.1 MODEL PREDICTIONS AT INCREASING PRESSURE IN THE RANGE 1÷4 bar

In this paragraph the thermal behaviour simulation at different pressure conditions will be shown first, the species profiles will be analysed afterwards.

All the simulations are performed at the same inlet temperature and at the same concentration of reactants. Also the flow rate is the same in all simulation as reported in the Table 5.3.

Flow rate Q [Nl min^{-1}]	10
Inlet gas Temperature [°C]	25
Inlet reactants concentrations [%]:	
CH_4	26,7
O_2	15,2
N_2	58.1

Table 5.3: Relevant physical and compositions data input.

In the Figure 5.7 are reported the model prediction at different pressures (from 1 to 4bar) of the temperature behaviour.

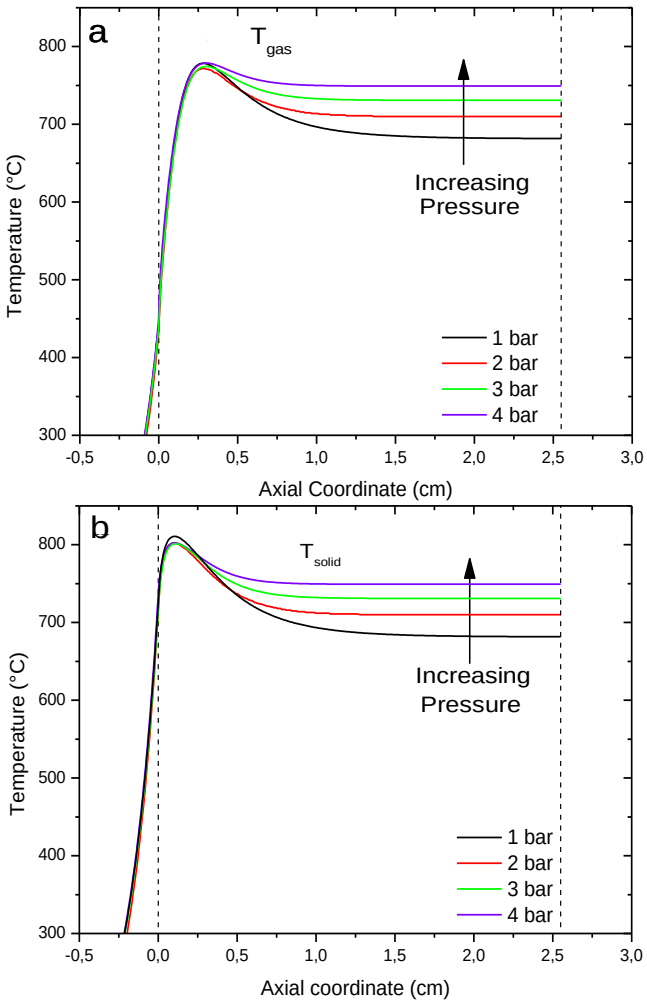

Figure 5.7: Model predictions: Temperature profiles for gas phase (panel a) and for the solid phase (panel b); CH_4 = 26.7%, C/O° = 0.9, flow = 10 Nl/min, Tin = 25°C.

The temperature profiles shows that in the inlet section a hot spot for both phase is observed, the temperature surface also is much higher than the gas temperature as the heat generation at the catalyst surface is much faster than the heat transport to the incoming gas. Then, both the temperature profiles became relatively flat downstream of the hot-spot, thus suggesting that the thermodynamic equilibrium is reached.

The model calculations, about the temperature profiles of gas and solid phases when pressure increases, show that the hot spot at the inlet section does not increase at pressure increase but after the first 5 mm the temperature profiles of the gas and solid phases raise up at pressure increase.

The hot spot temperature of the gas and solid phases are reported in the Table 5.4.

Pressure [bar]	T_{gas} [°C]	T_{solid} [°C]	C/O
1	779	810	0.88
2	772	802	0.88
3	774	802	0.88
4	779	802	0.88

Table 5.4: Model predictions: Values of maximum temperature in the gas phase and in the solid phase.

The temperature behavior of the solid phase shows that only the hotspot of the simulation at 1 bar results a bit warmer than the other hotspots as the Table 5.3 reports.
The increment of the temperature after the first 5 mm of catalyst at pressure increase is due to the achievement of thermodynamic equilibrium. In all simulations the temperature profiles downstream of the hotspot are flat and similar to the thermodynamic equilibrium temperature calculated with STANJAN data bank, Table 5.5.

Pressure [bar]		χ_{CH_4}	σ_{H_2}	σ_{CO}	T_{gas} [°C]	T_{solid} [°C]	α
1	exp	90%	89%	87%	684	671	1.01
	eq.	87%	91%	85%	679	-	
	model	87%	91%	86%	681	681	
2	exp	86%	95%	90%	712	697	1.00
	eq.	85%	90%	86%	711	-	
	model	85%	90%	86%	712	712	
3	exp	85%	93%	90%	736	723	1.01
	eq.	84%	90%	86%	732	-	
	model	85%	90%	87%	732	732	
4	exp	84%	92%	87%	755	736	1.02
	eq.	83%	90%	86%	748	-	
	model	84%	89%	87%	747	747	

Table 5.5: Model predictions: Comparison between the thermodynamic temperature equilibrium calculated by STANJAN data bank ®(1) and by Heterogeneous Model.

The Table 5.5 shows that the model predictions are in good agreement with the experimental data, also it shows that the methane conversion decreases with the pressure increase, in agreement with thermodynamics.

In the model predictions about the reactants species are shown in Figure 5.8.

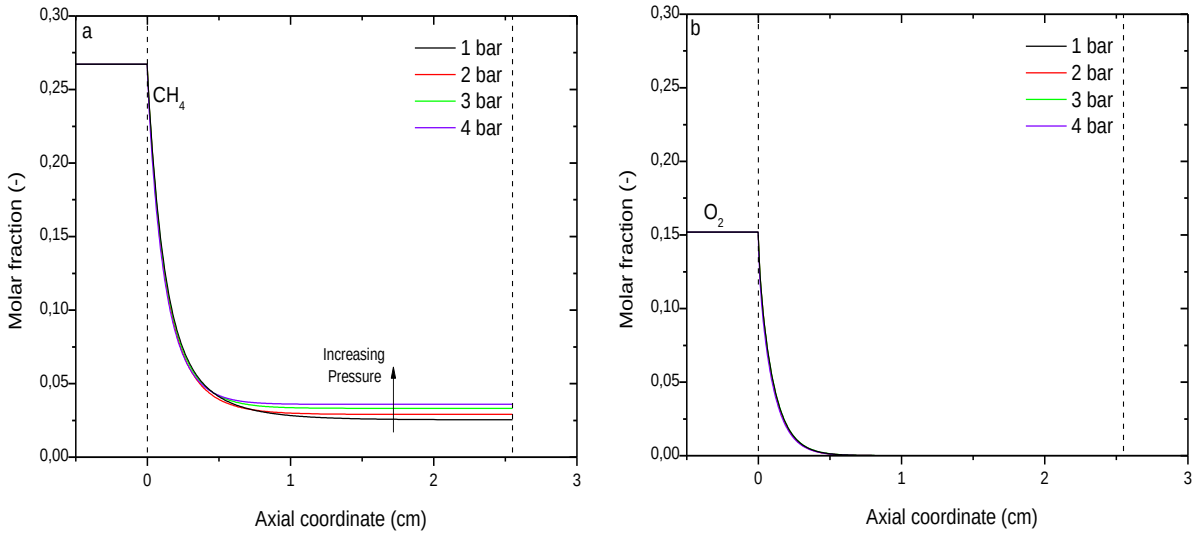

Figure 5.8: Model predictions: Axial concentration profiles of the reactants (a-b) at different pressure 1÷4 bar. CH_4 = 27.3%, C/O = 0.9, flow = 10 Nl/min, Tin = 25°C.

The Figure 5.8 shows that in the first 5 mm of the catalyst, where there is methane and oxygen consumption, the profiles are overlapped. Only the last parts the methane profile shows a specific trend with the pressure increase, the methane residue increases with the pressure in agreement with the thermodynamic equilibrium.

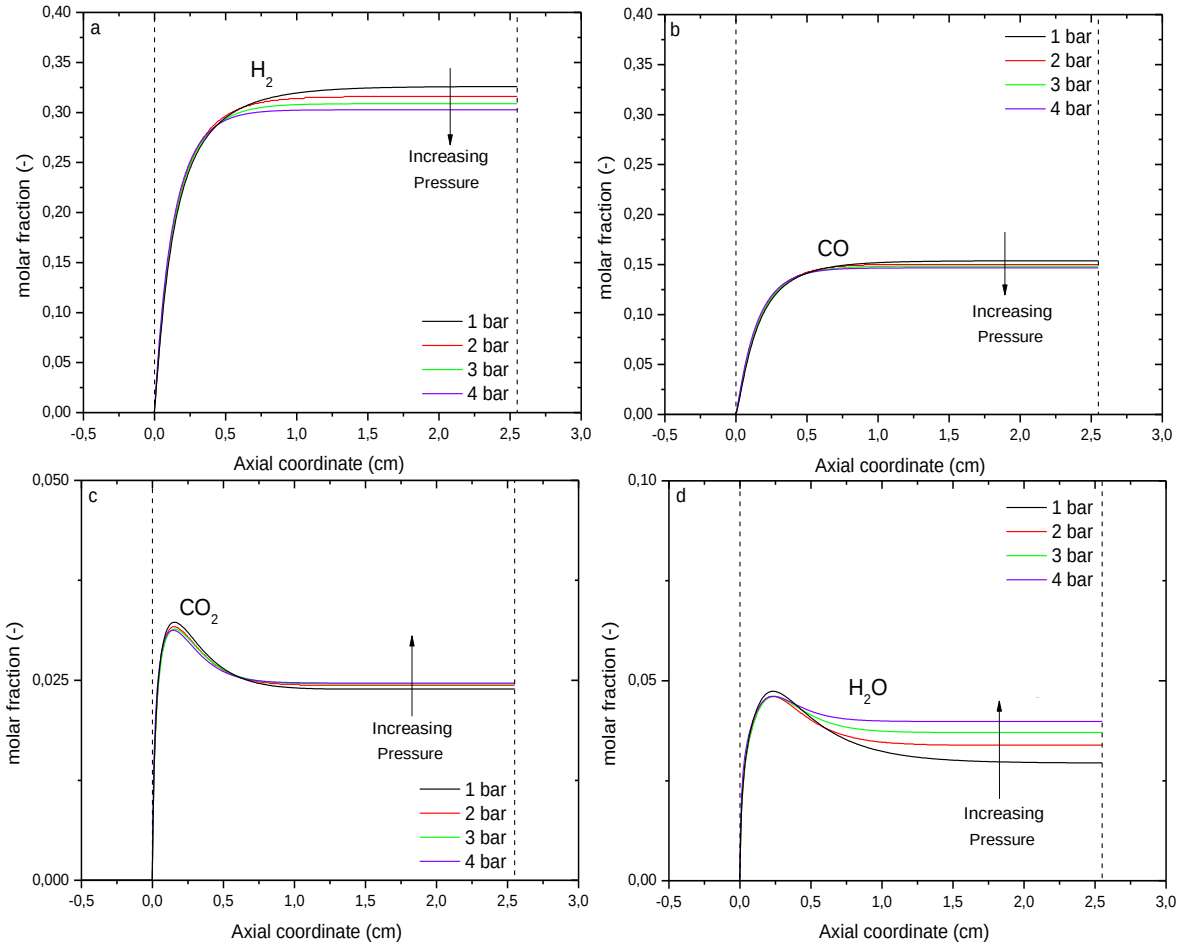

Figure 5.9: Model predictions: Axial concentration profiles of the products (a-d) at different pressure 1÷4 bar. CH_4 = 27.3%, C/O = 0.9, flow = 10 Nl/min, Tin = 25°C.

Like the reactants profiles, the model predicts for syngas products concentration the same value at pressure increase in the first 5 mm of catalyst while the total oxidation products decrease with pressure increase, this is due to the increasing of SR and RWGS rates of reactions. After the first 5 mm of catalyst, the pressure increase generates a decrease of the syngas products and an increase of total oxidation products, as shown in Figure 5.9.

5.4.2 EXPERIMENTS AND MODELING PREDICTIONS AT DIFFERENT PRESSURE

In this paragraph the comparison between the experimental data and the model prediction will be shown.

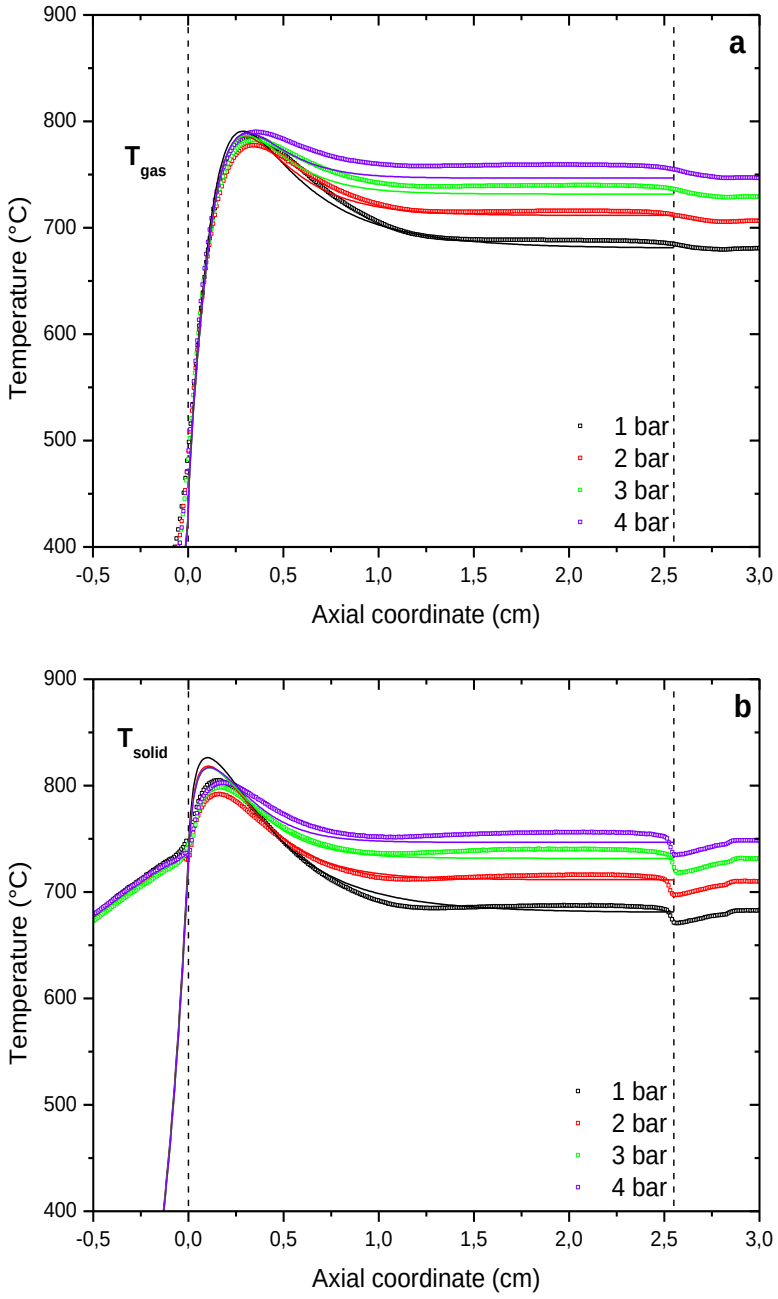

Figure 5.10: Experimental and modeling comparison, axial temperature profiles measured by thermocouple, T_{gas} (a), and by pyrometer, T_{solid}, (b) Honeycomb monolith, Sample FHS 6. Operating conditions: autothermal, C/O=0.9, 10 Nlmin^{-1} flow rate, pressure 1÷4 bar. Symbols: experimental measurements. Solid lines: model predictions.

The Figure 5.10 shows that the axial trends of temperature are described with reasonable accuracy by the model. The model predictions are in agreement with the experimental data along the whole axial profile.

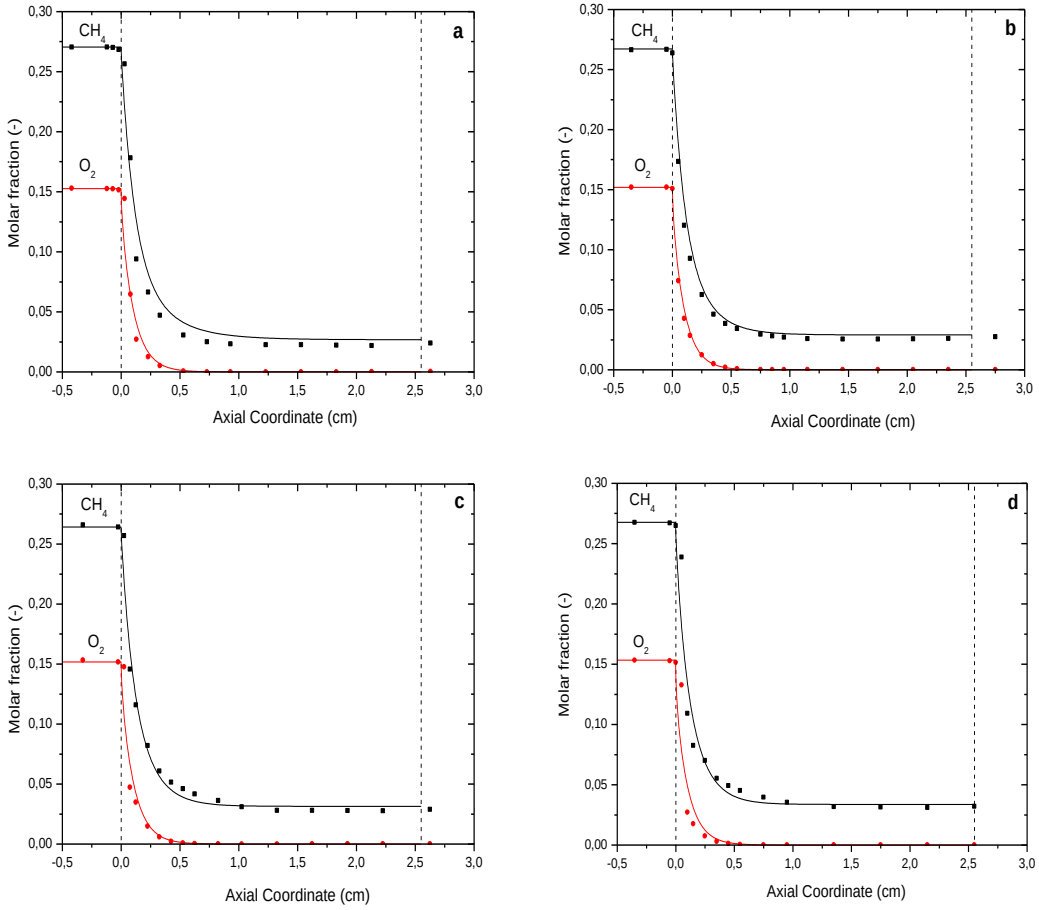

Figure 5.11: Axial concentration profiles of the reactants: comparison between experimental and simulated values in the gas phase at different pressure: 1 bar (a), 2 bar (b), 3 bar (c), 4 bar (d). Honeycomb monolith Sample FSH 6.Operating conditions: autothermal, C/O = 0.9, 10 Nlmin^{-1} flow rate. Symbols: experimental measurements. Solid lines: model predictions.

As shown the Figure 5.11, also the reactants profiles are described with reasonable accuracy by the model in fact, O_2 conversion is complete within 5-6 mm and CH_4 conversion is predicted to reach the equilibrium within 1 mm. At increasing pressure, the model predictions are very accurate although the kinetic scheme was developed at atmospheric pressure.

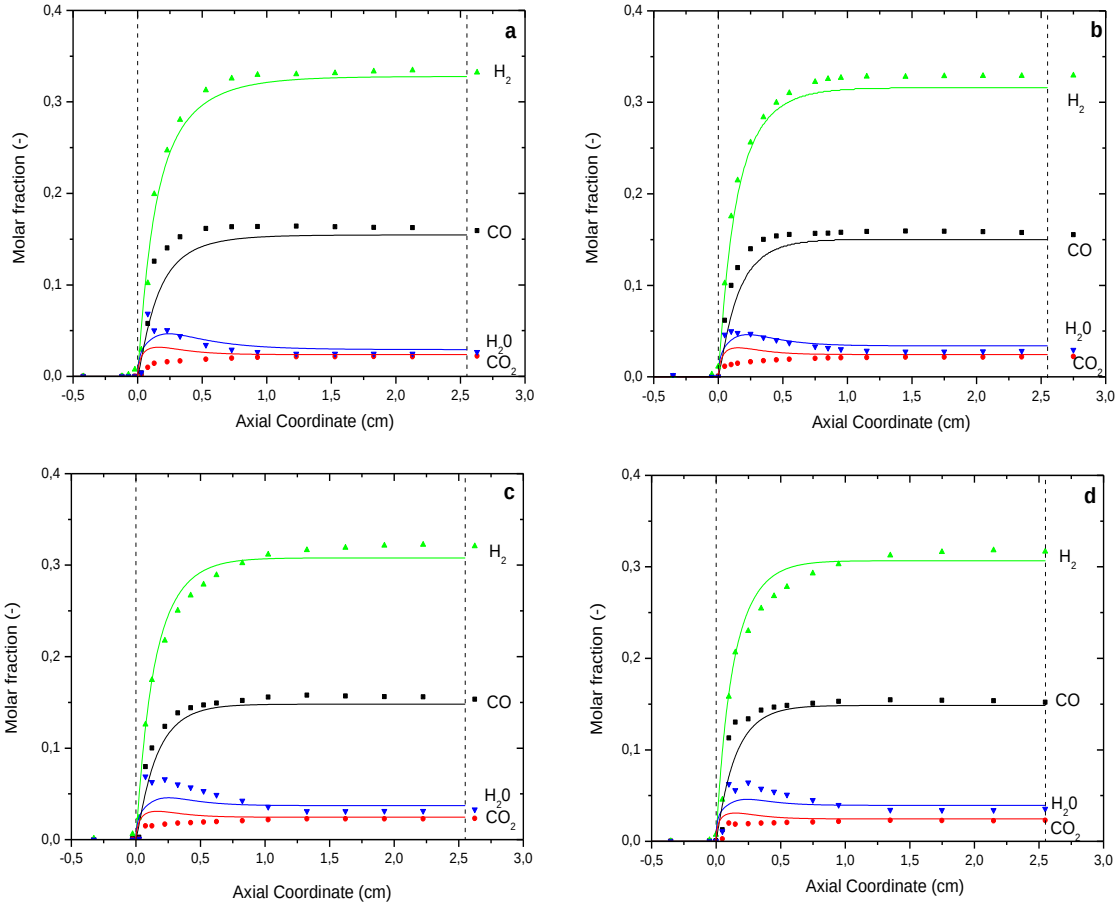

Figure 5.12: Axial concentration profiles of the products: comparison between experimental and simulated values in the gas phase at different pressure: 1 bar (a), 2 bar (b), 3 bar (c), 4 bar (d). Honeycomb monolith Sample FSH 6.Operating conditions: autothermal, C/O=0.9, 10 Nlmin^{-1} flow rate,. Symbols: experimental measurements. Solid lines: model predictions.

As the reactants profiles, the Figure 5.12 shows that the model carefully predicts the products profile along the entire channel.

The good performances of the model demonstrate the possibility to use this heterogeneous model, in which there is implemented an atmospheric kinetic scheme, to analyze the pressure effects with a reasonable accuracy of predictions.

5.5 REACTION RATE PROFILES IN CH_4 CPO AND ROLE OF DIFFUSION RESISTANCE.

After the demonstration of the accuracy of the heterogeneous model to describe the CH_4-CPO tests under pressurized conditions, the model is utilized to gain a deeper insight in the behavior observed in the first part of the catalyst volume (0-5 mm). That is due to understand the reasons behind the apparent independence of the concentration profiles and temperature behavior at different pressures.

The results of the model allowed to predict the axial profiles of the species at the catalyst wall. In particular, a deeper insight into the evolution of the reactants is obtained by analyzing the concentration profiles at the catalyst wall predicted by the model. The comparison between bulk concentration and wall concentration about Methane and Oxygen is reported in Figure 5.13.

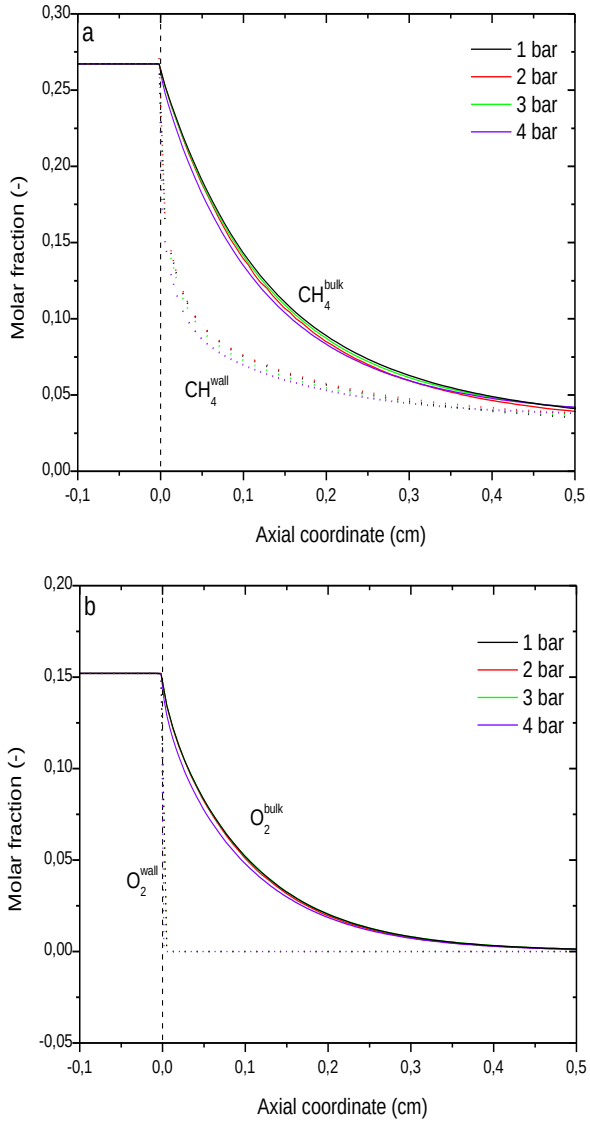

Figure 5.13: Consumption profiles of the reactants: methane (panel a) and oxygen (panel b). Solid lines are model predictions of the molar fraction in the gas bulk. Dashed lines are model predictions of the molar fraction at the catalyst wall. Sample FHS 6. Operating conditions: autothermal, C/O=0.9, 10 Nlmin^{-1} flow rate, at different pressure.

In all the experiments, the consumption of O_2 is governed by external mass transfer, as indicated by the zero concentration of O_2 at the catalyst wall. Coherently, the length for complete O_2 consumption keep almost unchanged, being independent of the O_2 concentration and very weakly dependent on the gas temperature. A different situation emerges when focusing on the profiles of the fuel consumption. The wall concentration of CH_4 is initially lower than the concentration in the gas bulk and slowly decreases until reaching the equilibrium value at the outlet of the monolith. Moreover, it is possible to see a little increment of the methane rate of consumption due to increment of pressure, but this increment is too little to see any effect in the experimental species profiles.

To better rationalize this difference, which suggests the presence of different controlling regimes, the Carberry number for each reactant can be introduced.

$$Ca_i = \frac{C_i^B - C_i^w}{C_i^B - C_i^{eq}}$$

In the equation, C_i^B is the concentration of the i[th] species in the bulk of the gas phase, C_i^w is the concentration at the catalyst wall and C_i^{eq} is the concentration calculated assuming local equilibrium at the composition and temperature of the gas phase.

According to this definition, the external mass transfer regime corresponds to Ca $\rightarrow$ 1 and the chemical regime is represented by Ca $\rightarrow$ 0.

The axial evolution of the Ca numbers, for Methane and Oxygen, is plotted in Figure 5.14.

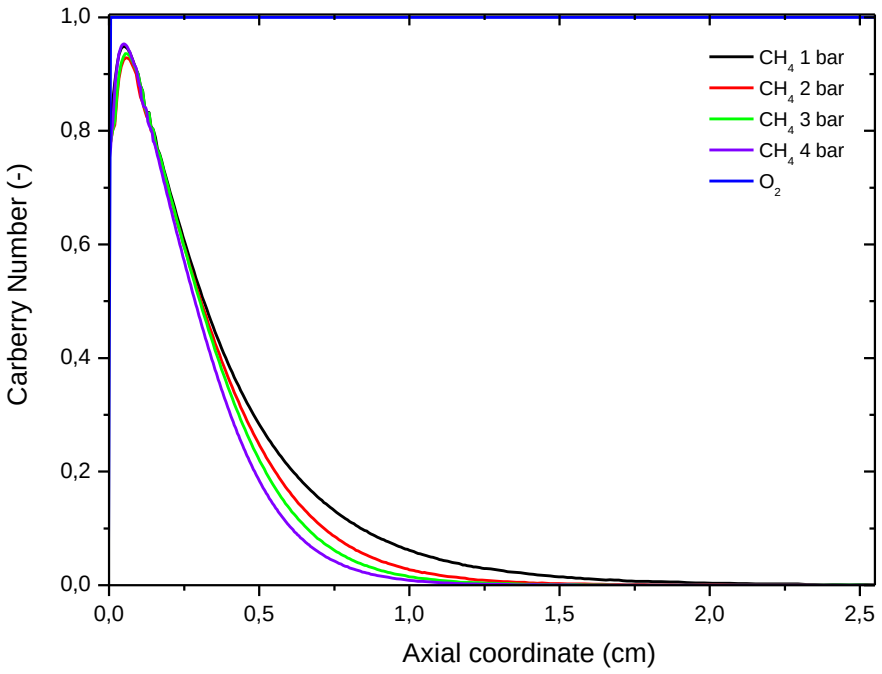

Figure 5.14 : Axial evolution of Carberry numbers for O_2, CH_4 at pressure 1 ÷ 4 bar.

As expected, this analysis confirmed that O_2 consumption is totally limited by external mass transfer at all pressure, conversely the curves showed that CH_4 consumption is mainly controlled by a external mass transfer in the first section of the catalyst (from 0 to 5mm).

After the first 5mm, as Figure 5.13 shows, the value of bulk and wall concentration is the same, for this reason for this reason the Carberry number loses his functionality.

To confirm this hypothesis, we comparison the global consumption rate and the gas-solid mass transfer rate in the limiting case of full external diffusing regime, for both the reactants.

- the global consumption rate is:

$$r_i = \frac{1}{A}\frac{d\dot{F}_i}{dz}$$

where $\dot{F}_i$ is the molar flow rate of the i[th] species, A is reactor section, z is the axial coordinate.

- the gas-solid limit diffusion rate is:

$$r_{i,DIFF} = k_{i,C} \cdot \left(x_{i,g} - x_{i,eq}\right) \cdot a_v \cdot C_{TOT}$$

where $k_{i,C}$ is the mass transfer coefficient, $x_{i,g}$ is the molar fraction of the i[th] species in the gas phase, $x_{i,eq}$ is the molar fraction calculated assuming equilibrium at the composition and temperature of the gas phase, a_v is the specific area. For the oxygen $x_{i,eq} = 0$.

Figure 5.15 shows the comparison valuated at 4 bar.

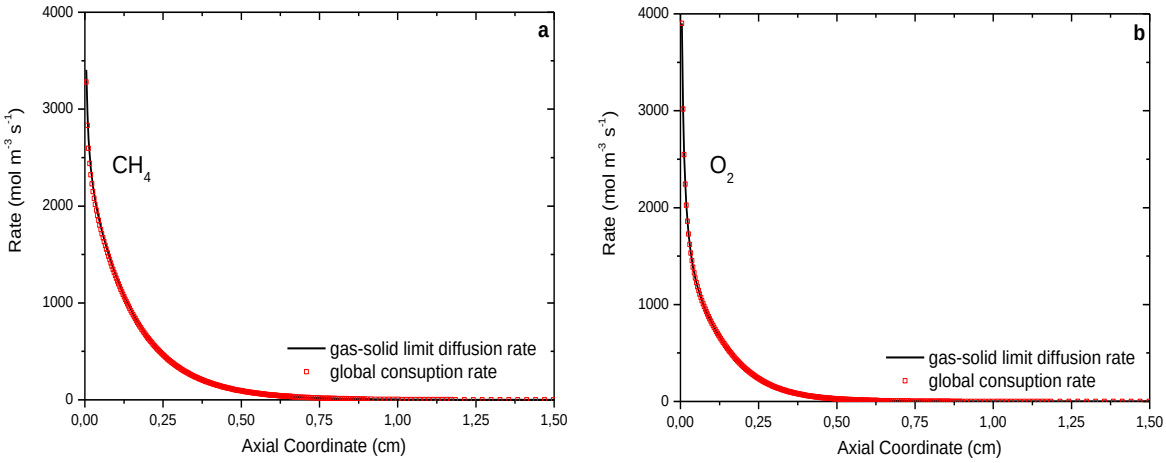

Figure 5.15: Comparison between the gas-solid limit diffusion rate (black line) with the global consumption rate (red scatter) for methane (panel a) and oxygen (panel b). Sample FHS 6. Operating conditions: autothermal, C/O=0.9, 10 Nlmin^{-1} flow rate, at 4 bar.

The Figure 5.15 confirms that the CH_4 and O_2 are controlled by external mass transfer: the value, at every axial position, of the global consumption rate is equal to the value of the gas-solid limit diffusion rate. For the fuel, we also calculated the value of the intrinsic kinetic constant and that of the mass transfer coefficient along the axis of the reactor and we verified that the kinetic constant is ten times higher than the mass transfer coefficient.

After the demonstration of the controlling regime, the independence from the pressure will be demonstrated with the analytic treatment of isothermal plug flow reactor:

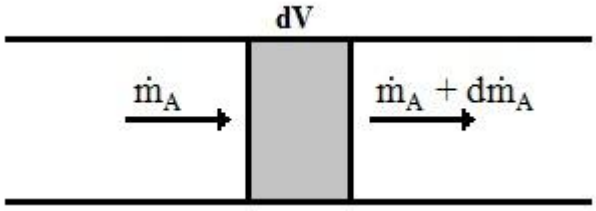

Figure 5.16: PF reactor model.

In this demonstration a irreversible, monomolecular reaction are used: $A \rightarrow P$

Mass balance for the 'A' specie in steady state condition:

$$\frac{d\dot{m}_A}{dV} = -r$$

Where: $\dot{m}_A$ is the mass flow rate for the reactant A [kg s^{-1}], r is the rate of consumption of the A specie [kg m^{-3} s^{-1}].
Since the reactor section (A) and the total mass flow ($\dot{m}_{TOT}$) have a constant values, we can evaluate the balance as:

$$\frac{\dot{m}_{TOT}}{A} \cdot \frac{d\omega_A}{dz} = -r$$

The rate of consumption, in the case of external mass transfer control, is equal (steady state conditions) to the diffusion rate, as the following equation describes:

$$\begin{cases} r = r_{DIFF} = k_m \cdot (\omega_{A,g} - \omega_{A,w}) \cdot a_v \cdot \rho_g \\ \omega_{A,w} = 0 \end{cases}$$

For the external mass transfer control hypothesis, the mass fraction on the catalyst wall ($\omega_{A,w}$) is equal to zero.

$$\frac{\dot{m}_{TOT}}{A} \cdot \frac{d\omega_A}{dz} = k_m \cdot \omega_{A,g} \cdot a_v \cdot \rho_g$$

$$\frac{d\omega_A}{dz} = k_m \cdot \omega_{A,g} \cdot a_v \cdot \rho_g \cdot \frac{A}{\dot{m}_{TOT}}$$

$$\frac{a_v \cdot A}{\dot{m}_{TOT}} = cost = C$$

$$\frac{d\omega_A}{dz} = k_m \cdot \omega_{A,g} \cdot \rho_g \cdot C$$

To simplify the analytic treatment, the Sh number is considered constant, and equal to its asymptotic value:

$$\begin{cases} \rho_g = \frac{P}{RT} PM_{mix} \propto P \\ k_m = \frac{Sh \cdot D}{L} \propto \frac{1}{P} \end{cases}$$

$$\begin{cases} Sh = cost & asymptotic\ \ value \\ D \propto \frac{1}{P} & by\ Fuller\ correlation \end{cases}$$

The final equation shows the dependence of the pressure in a isothermal plug flow reactor:

$$\frac{d\omega_A}{dz} \propto \frac{1}{P} \cdot P = 1$$

This demonstration shows the independence from the pressure in the section of the catalyst controlled by kinetic (first 5mm). Finally the hypothesis, that the diffusion rate calculated by the model, is not influenced by the pressure, is displayed in the Figure 5.17.

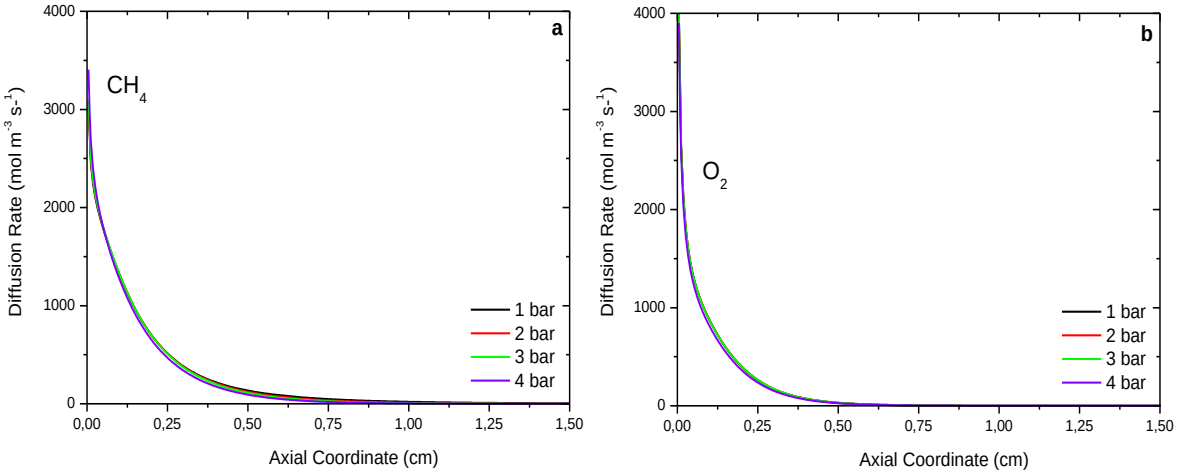

Figure 5.17: Gas-solid limit diffusion rate for methane (panel a) and oxygen (panel b). Sample FHS 6. Operating conditions: autothermal, C/O=0.9, 10 Nlmin^{-1} flow rate, at pressure 1 - 4 bar.

As shown in the analytic treatment, the pressure does not influenced the diffusion rate. This explain the absence of effects in the experimental data and in the modeling predictions.

5.6 THERMODYNAMIC ANALYSIS

To better understand the evolution of the products distribution, we have analyzed the approach to thermodynamic equilibrium of the single reactions, i.e. direct and reverse WGS, Steam Reforming CH_4 (reverse methanation), involve in the global process.

First of all, all the K_{eq} of the different reactions are calculated using the expressions of the relative ΔG^0_R obtained by thermodynamic data for the temperature range 300-850°C and herein reported as function only of the temperature expressed in Kelvin degrees [K]:

$CH_4 + H_2O \leftrightarrow 3H_2 + CO$ $\quad\quad$ ΔG^0_R (T)= 53717 – 60.25*T [cal/mol] $\quad\quad$ (4.1)

$CO + H_2O \leftrightarrow CO_2 + H_2$ $\quad\quad$ ΔG^0_R (T) = – 8514 + 7.71*T [cal/mol] $\quad\quad$ (4.2)

while the K_p are estimated through the following expression:

$$K_p = \prod_{i=1}^{NC} a_i^{\nu_i} \quad (4.3)$$

where a_i is the activity of the i-chemical species, defined as the ratio of the fugacity divided by a reference fugacity to give a dimensionless quantity. The reference fugacity is chosen as 1 atmosphere or 1 bar. Activity depends on temperature, pressure and composition of the mixture, among other things. For ideal gases, the effective partial pressure is usually referred to as fugacity. So that at atmospheric pressure, K_p is simply calculated from the measured species profiles as the product of the molar fractions elevated to the relative stoichiometric coefficient while K_{eq} is evaluated from the measured gas temperature profile as:

$$K_{eq}(T) = \exp\left(-\frac{\Delta G_r^o}{RT}\right) \tag{4.4}$$

Three different situation can be detected:

- $K_p/K_{eq} < 1$ which indicates a thermodynamic driving force for the direct reaction;
- $K_p/K_{eq} = 1$ which indicates the reaching of the equilibrium state;
- $K_p/K_{eq} > 1$ which indicates a thermodynamic driving force for the reverse reaction.

Water Gas Shift: CO + H2O ⇔ CO2 + H2

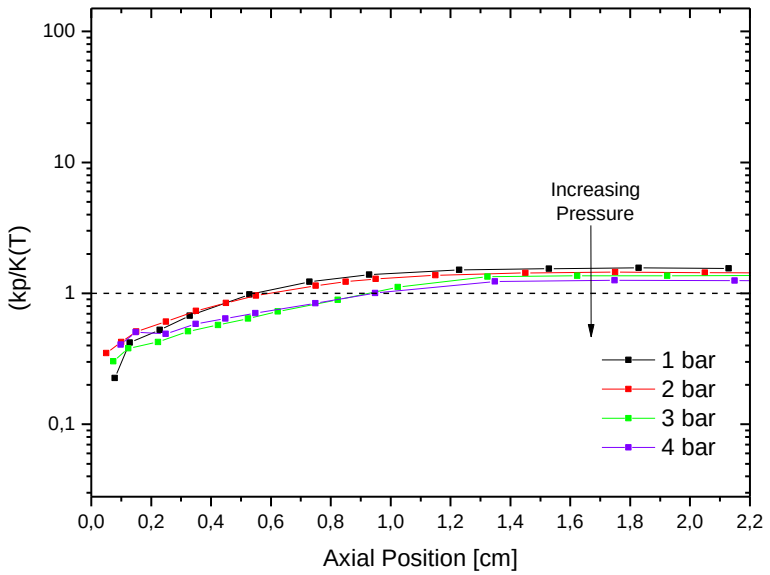

Figure 5.18: Evaluation of the ratio Kp/Keq for WGS reaction at different pressure 1÷ 4 bar.

The Kp/K(T) ratio shows a double trends: in the first part of the catalyst (0- 0.6 cm) the WGS reaction is thermodynamically promoted, after (from 0,6 cm) the WGS reaction reaches the thermodynamic equilibrium.

In the kinetic section (0-0,6 cm) a double trend can be noted: former for the 1-2 bar tests, latter for the 3-4 bar tests. In the second part of the catalyst, pressure has a small effect on the WGS reaction: a decreasing trend of the Kp/K(T) ration can be noted at pressure increase, but the reactions can be considered at the same value, equal to the thermodynamic equilibrium.

Steam Reforming: CH4 + H2O ⇔ CO + 3H2

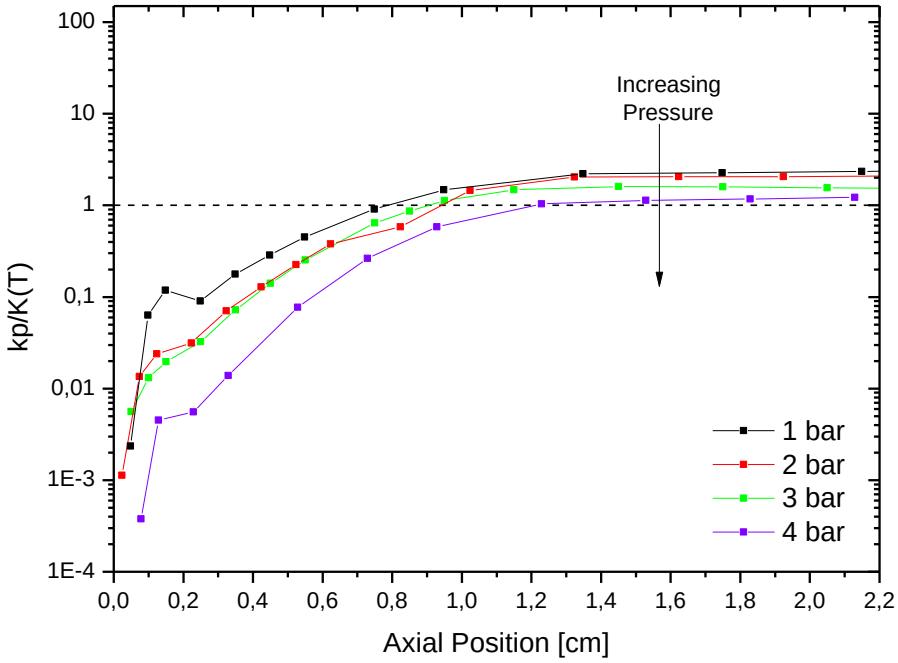

Figure 5.19: Evaluation of the ratio Kp/Keq for CH_4 SR reaction at different pressure 1÷ 4 bar.

The SR Kp/K(T) ratio shows: in the first part of the catalyst the steam reforming of CH_4 is promoted, the driving force of the SR reaction increases at pressure increase. In the last part of the catalyst the thermodynamic equilibrium value is reached.

5.7 CONCLUDING REMARKS

In conclusion, the experimental apparatus is very satisfactory to perform the tests of the temperature and composition profiles. Thanks to these systems was possible to maintain a constant positive pressure inside the reactor.

The tests shows that the pressure influences only the thermodynamic equilibrium, conversely the kinetic does not seem to be influenced by the increment of pressure from1 to 4 bar. The results of the model permitted us to give a possible explanation of the chemical/physical phenomena involve in the first section of the catalyst. According to literature [71], the rate of reactants consumption is governed by gas-solid mass transfer flow, the analytic treatment confirms that, under the hypothesis of external diffusing regime, the pressure has not effect on the global rate of consumption of the reactants.

CHAPTER 6

ANALYSIS OF THE EFFECTS OF THE PRESSURE IN C_3H_8 CPO

6.1 INTRODUCTION

This chapter reports the results of a set of tests that have been performed to better understand the effects of the pressure in a C_3H_8-CPO reformer operating with Rh-coated honeycomb monoliths. All the experiment are carried out in auto-thermal conditions, with Sample FHS 6 (Table 2.3, chapter 2), with 10 NL min^{-1} total flow rate and C/O ratio of 0.85 and progressively increasing of total pressure from 1 to 4 bar. The composition of synthesis gas and temperature of the gas phase are compared with the values obtained by the adiabatic equilibrium.

6.2 EFFECT OF PRESSURE ON THERMAL BEHAVIOR

The honeycomb monolith FHS 6 is tested by raising progressively the pressure of the system from 1 to 4 bar, the effect of the pressure on the thermal behavior in C_3H_8 CPO is thus evaluated. The measured axial temperature profiles obtained are reported in Figure 6.1.

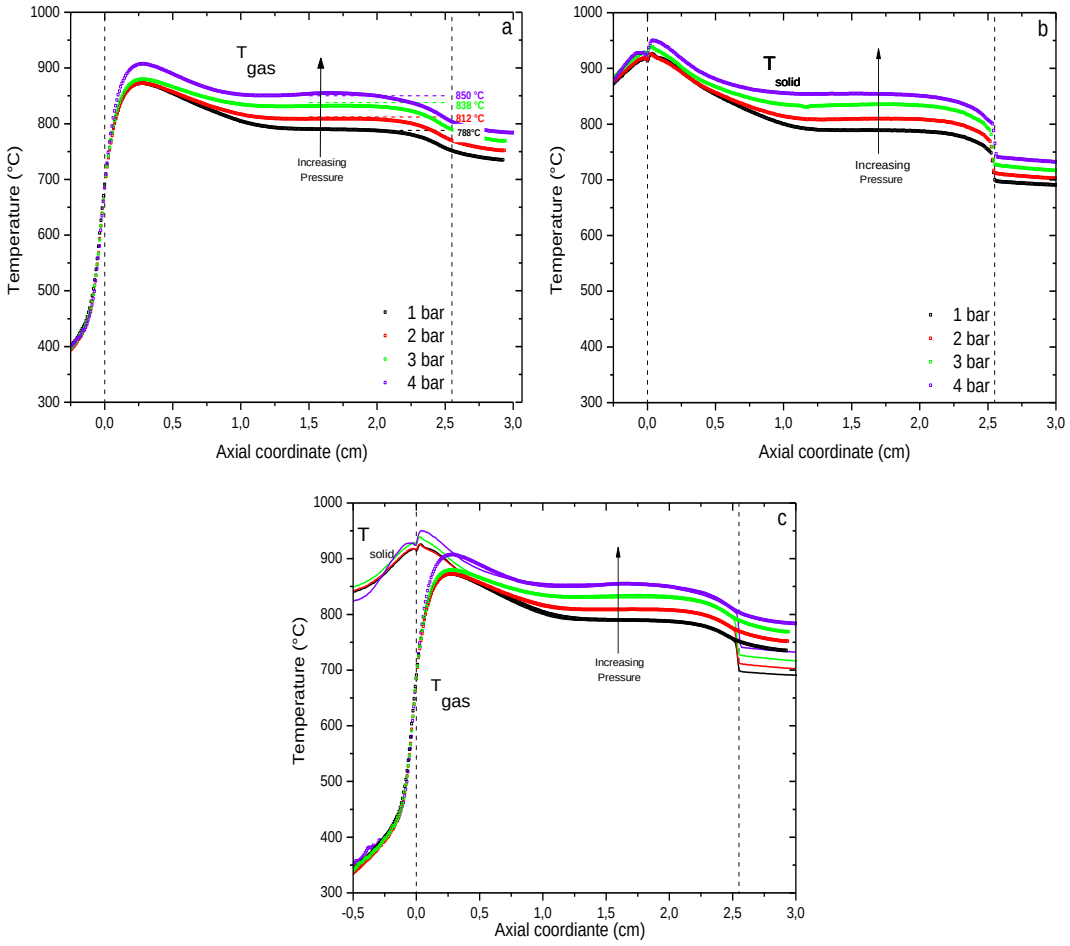

Figure 6.1: Temperature profiles. Panel a: gas phase (scatter) and thermodynamic equilibrium temperature(dashed line); Panel b: solid phase; Panel c: solid (solid lines) and gas(scatter) phases at different pressures. Honeycomb monolith, Sample FHS 6. Operating conditions: autothermal, C/O=0.85, 10 Nlmin^{-1} flow rate; P=1÷4 bar.

The Figure 6.1 shows the thermal behavior at different pressures. The temperature hotspot measured at 1 and 2 bar have the same value, the tests show an increment of the hotspot temperature at higher pressure (3-4 bar). The values of the maximum temperature, measured by thermocouple and pyrometer at different pressure, are reported in the Table 6.1.

Pressure [bar]	T_{gas} [°C]	T_{solid} [°C]	C/O
1	873	926	0.84
2	873	926	0.83
3	880	939	0.81
4	906	950	0.82

Table 6.1: Values of maximum temperature values measured by the thermocouple and by the pyrometer for the gas and the solid phase, respectively, at different pressure for the C_3H_8-CPO tests.

In all the experiments, downstream of the hot-spot, the temperature profile shows a flat trend suggesting that the thermodynamic equilibrium is reached. In this section of the catalyst, the profiles display an increment of the temperature linked to the pressure.

As shown in Figure 6.1.a there is a good correspondence between the equilibrium temperature, measured in the final section of the catalyst, and the temperature of thermodynamic equilibrium calculated by STANJAN® data bank (dotted lines), but at the end of the channel the gas temperature displays a rapid decrease. The values of α (Table 6.2) shows different values according to where (inside/outside the channel) the temperature of the gas phase has been measured. The $\alpha^{(1)}$, calculated through the temperature, measured at the end of the catalyst (Axial Coordinate: 2.5 cm), is smaller than the unit value. In fact the output section of the catalyst undergoes an heavy dissipation of heat due to high temperatures. The heat dissipation in the C_3H_8-CPO test is higher than that measured in CH_4-CPO, this is due to the achievement of higher temperatures in the system C_3H_8-CPO. However, Table 6.2 shows the system can be considered adiabatic inside the channel of the catalyst, where the heat dissipation is smaller. In fact, the $\alpha^{(2)}$ values calculated in the middle part of the channel (Axial Coordinate:1.5 cm) are very similar to the unit value.

Pressure [bar]		$\chi_{C_3H_8}$	σ_{H_2}	σ_{CO}	$T_{gas}^{(1)}$ [°C]	T_{solid} [°C]	$\alpha^{(1)}$	$T_{gas}^{(2)}$ [°C]	$\alpha^{(2)}$
1	exp	100%	88%	88%	759	700	0.94	789	1.00
	eq.	100%	87%	86%	788	-		788	
2	exp	100%	87%	89%	782	712	0.94	809	0.99
	eq.	100%	85%	85%	812	-		812	
3	exp	100%	88%	89%	795	728	0.92	832	0.99
	eq.	100%	85%	86%	838	-		838	
4	exp	100%	85%	86%	810	788	0.93	851	1.00
	eq.	100%	83%	85%	850	-		850	

Table 6.2:Thermodynamic analysis of the C_3H_8-CPO tests at different pressures. Comparison between the thermodynamic equilibrium temperature values, measured by the thermocouple (gas phase), with the STANJAN predictions. α values: calculated at 2.5 cm ($\alpha^{(1)}$) and at 1.5 cm ($\alpha^{(2)}$)of Axial Coordinate.

The selectivity values to syngas are also shown in Table 6.2. these values are in agreement with the thermodynamic equilibrium values calculated by the model.

6.3 EFFECT OF PRESSURE ON THE SPECIES PROFILE

6.3.1 REACTANS SPECIES

After the analysis of the thermal behavior at increasing pressure, the effect of pressure on the reactants profiles has been studied.

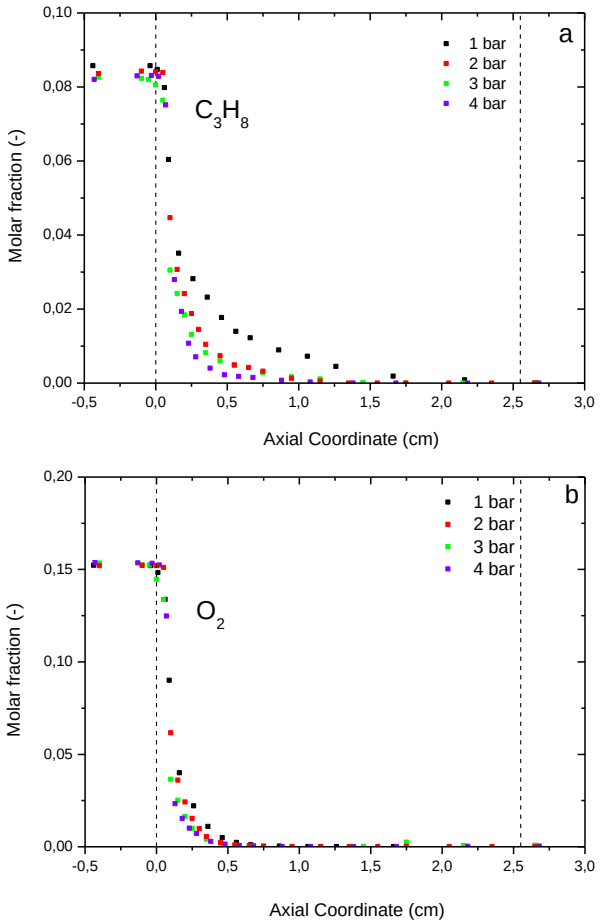

Figure 6.2: Axial concentration profiles of the reactants measured (a-b) at different pressure 1÷4 bar. Honeycomb monolith, Sample FHS 6. Operating conditions: autothermal, C/O=0.85, 10 Nlmin^{-1} flow rate.

The tests show, in the first 0,5 cm of catalyst, a progressive increase of propane consumption when the pressure increases. In the tests at 2-3-4 bar, propane is totally converted after 1.1 cm. The profile at atmospheric pressure shows a much lower rate of consumption but probably this is due to experimental errors occurring during that test. At the end of the

catalyst, the conversion of the propane approached very well the equilibrium values calculated by the model.

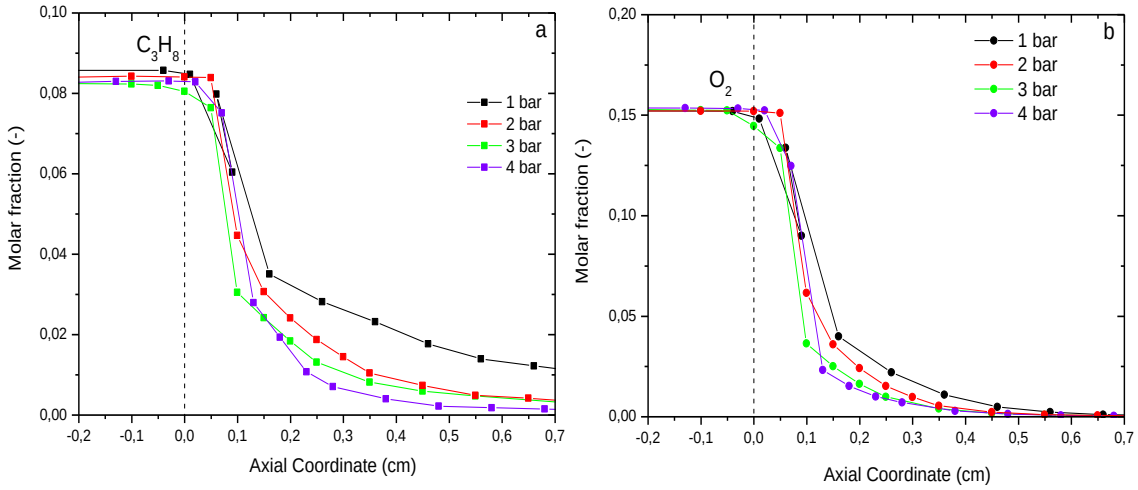

Figure 6.3: Magnification of the first 5mm of the catalyst: axial concentration profiles of the reactants measured (a-b) at different pressure 1÷4 bar. Honeycomb monolith, Sample FHS 6. Operating conditions: autothermal, C/O=0.85, 10 Nlmin^{-1} flow rate.

In Figure 6.3 the oxygen profiles, measured at different pressure, are displayed: the oxygen consumption does not change. Each test shows the total consumption of oxygen was reached in about 5-7 mm. The consumption trend of the oxygen appears to be independent from pressure variation. Previously works showed the presence of a complete control of mass transfer on O_2 consumption [74]. As suggested in Livio et al. [75], in high concentration of propane the behavior is similar to the O_2, with a presence of a control of mass transfer.

Data suggest that at sufficiently high temperatures also the consumption of the fuel is significantly controlled by diffusive limitations. These factors will be better analyzed in the following paragraphs, based on a predictive modeling analysis.

6.3.2 PRODUCTS SPECIES

The analysis of the products species are divided into three groups: first of all the syngas products are analyzed, then the total oxidation products and hydrocarbon products will be shown.

➢ PARTIAL OXIDATION PRODUCT: H_2 and CO

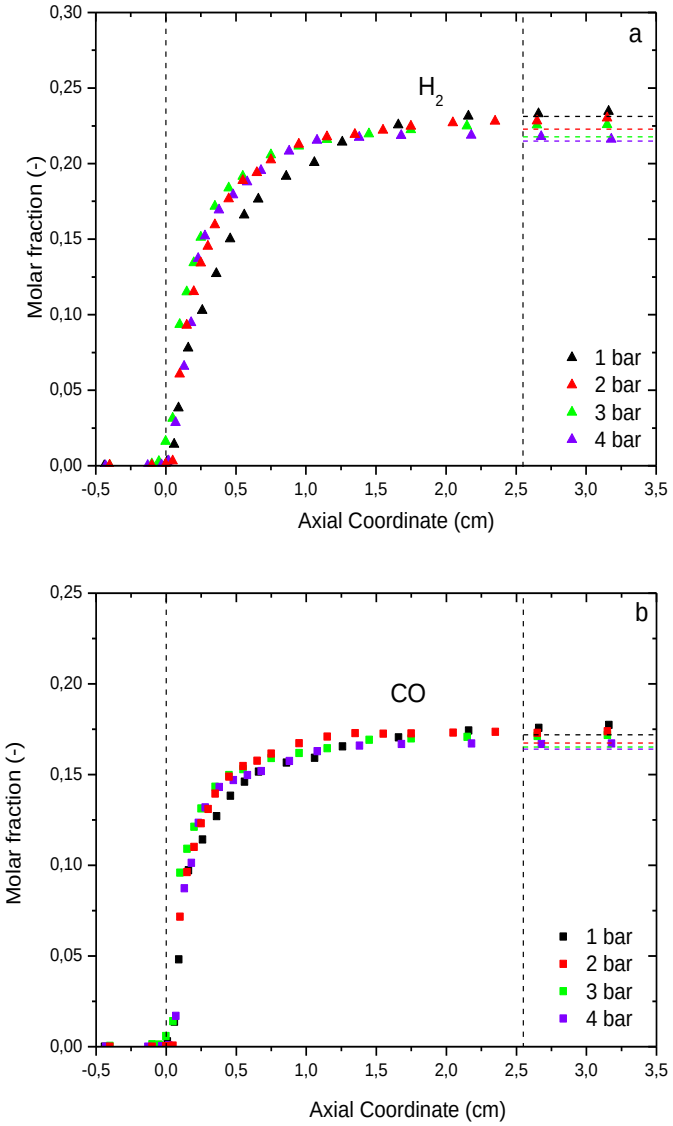

Figure 6.4: Axial concentration profiles of the syngas products: H_2 measured (Panel a)and CO measured at different pressure 1÷4 bar. Honeycomb monolith, Sample FHS 6. Operating conditions: autothermal, C/O=0.85, 10 Nlmin^{-1} flow rate.

The catalyst is very active: H_2 and CO are detected in the very inlet part of the reactor and are not further oxidized to CO_2 and H_2O because O_2 concentration drops to zero at the catalyst wall. At the end of the catalyst, the products concentration approaches the equilibrium values (dotted lines). The H_2 and CO profiles show a very similar trend: there is a steep increase of concentration in the first centimeter followed by a flat trend, approaching the equilibrium value.

The trends of syngas formation do not change in the first part of the catalyst when the pressure raises. After the first 1.3-1.5 cm, where the thermodynamic equilibrium is reached, a decrease of syngas products concentrations has been detected as the pressure increases.

➢ **TOTAL OXIDATION PRODUCTS: H_2O and CO_2**

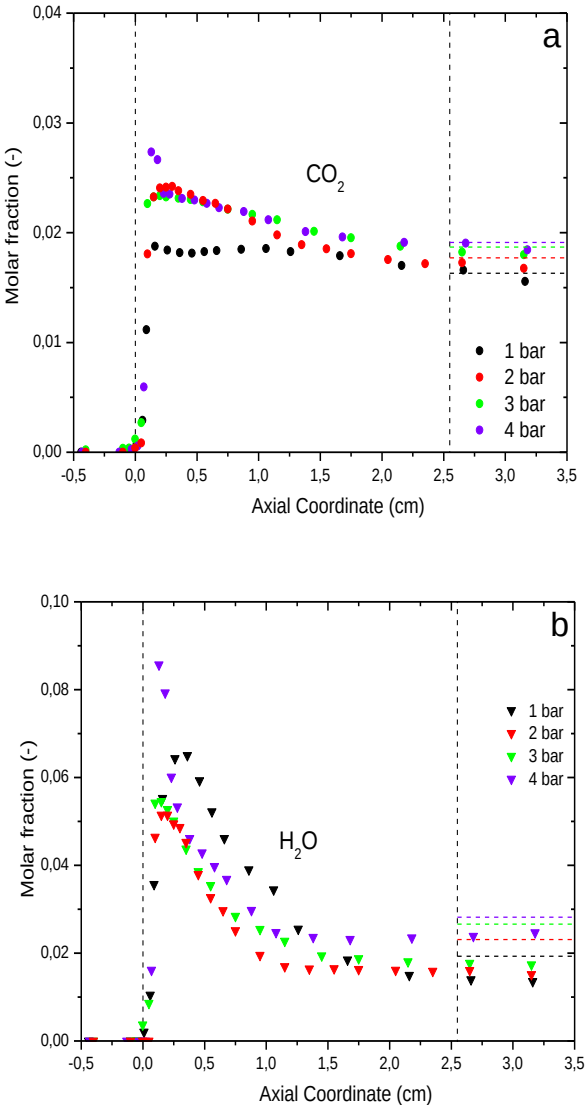

Figure 6.5: Axial concentration profiles of the total oxidation products CO_2 measured (Panel a)and H_2O measured at different pressure 1÷4 bar. Honeycomb monolith, Sample FHS 6. Operating conditions: autothermal, C/O=0.85, 10 Nlmin^{-1} flow rate.

The peak of water concentration profiles increases when the pressure increases as well. The maximum of CO_2 concentration maintains constant when the pressure is raised from 2 to 4 bar. In the outlet of the catalyst, the concentration profiles of the products approached the

equilibrium values. As predicted by thermodynamic equilibrium (dotted lines) at the increasing pressure, the concentration of the total oxidation products increases.

The H_2O and CO_2 peaks formation is a consequence of the coupling between oxidation and steam reforming, the reactor can be divided in two zones: in a first area (0-4 mm) of the catalyst, CO_2 and H_2O are produced by total oxidation reaction; in the second zone the same species are consumed by endothermic reactions of steam reforming.

➢ HYDROCARBON PRODUCTS : CH_4 AND SOOT PRECURSORS.

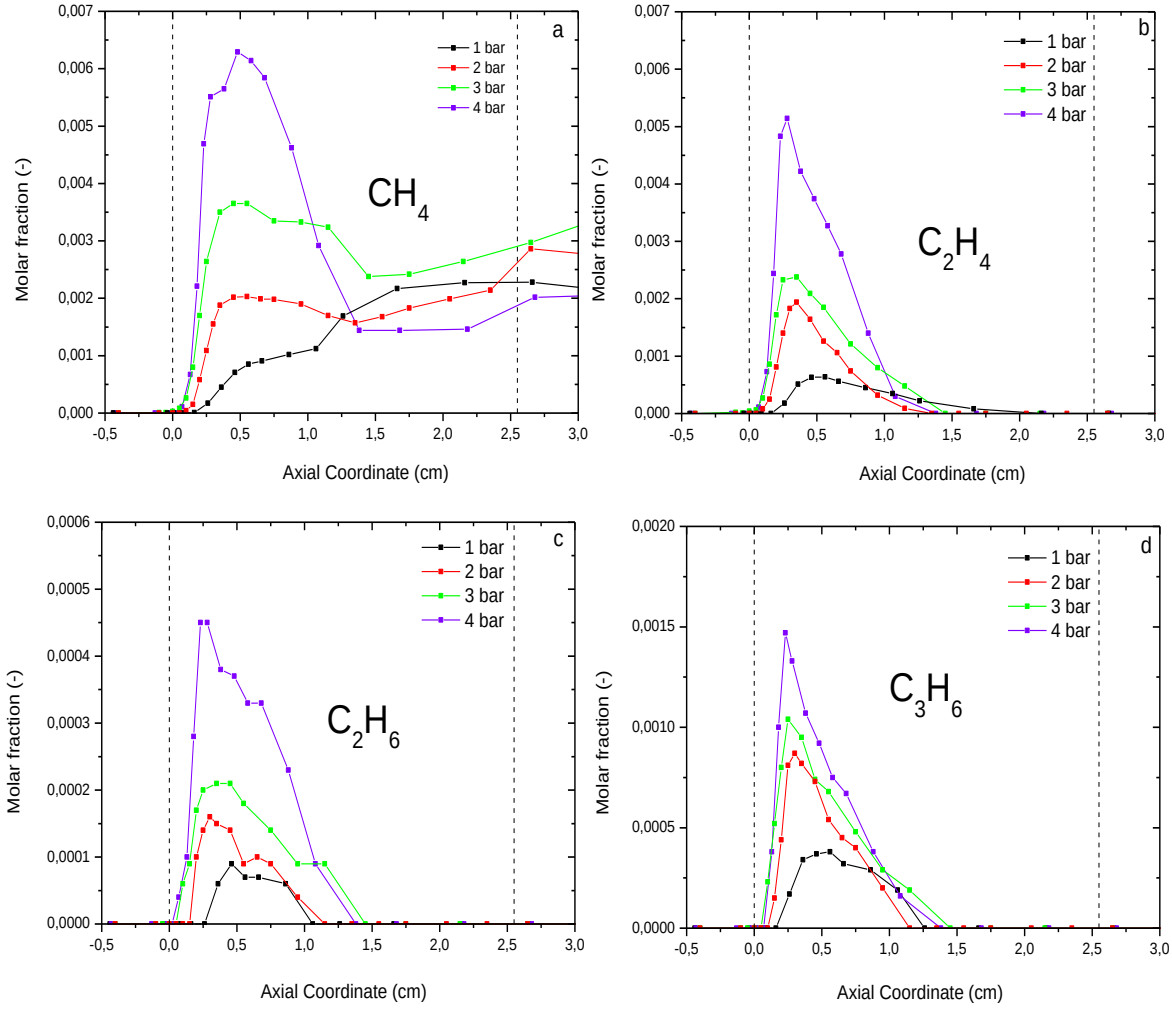

Figure 6.6: Axial concentrations profiles of CH_4 (a), C_2H_4 (b),C_2H_6 (c), C_3H_6(d). Operating conditions: autothermal; C/O=0.85; 10Nlmin^{-1} flow rate; Pressure 1÷4.

Figure 6.6 shows the hydrocarbon products observed in the C_3H_8-CPO tests: CH_4 , C_2H_4, C_2H_6 and C_3H_6. The spatially resolved measurements reveal an increase of concentration of these species with the increase of pressure. These species are initially formed in the first part of the catalyst, likely due to the high temperatures reached. After the peaks of concentration (close to the hot-spot temperature) C_2H_4, C_2H_6 and C_3H_6 are completely consumed before the ending section of the catalyst. CH_4 shows an interesting evolution: the concentration passes through a maximum value that is close to the hot-spot temperature zone, followed by a slightly increasing, approaching the equilibrium value. A possible explanation for this particular trend is the one suggesting that the methane is produced by the cracking of C_3H_8 in the first part of catalyst (0 ÷ 0,5 cm) where high temperatures are reached. Then the methane is consumed by steam reforming (0,5 ÷ 1,5). In the last part of the catalyst, the syngas is converted to CH_4 by methanation reaction (after 1,5 cm).

On the one hand, since the formation of hydrocarbon species such as olefins cannot be explained by the syngas formation pathways on rhodium, this experimental finding provided evidence of gas-phase chemistry. On the other hand, the gas-phase chemistry alone could not explain the outlet-selective formation of syngas. Hence, a possible scenario could be that the intermediates generated in the gas phase adsorbed back onto the catalyst surface and eventually converted to syngas, as shown in a previous study [76].

The idea of the presence of the gas-phase chemistry is reinforced by the rise of the concentration at increasing pressure. The gas phase are bimolecular reactions, for this reason these reactions are directly proportional to the P^2 , at pressure increase also the rate of production of these species increases as well.

During the test at 4 bar, we have verified the possible presence of C_4 species by a specifically tuned GC-analyzer. It is in fact known [65] that the olefin species (C_2H_4, C_3H_6) could condense to larger molecules.

The search for C_{4+} species was done in correspondence with the section of the reactor where the olefin species are consumed.

In the Figure 6.7 the dashed box highlights the region wherein the olefins concentration decreases so, where the formation of C_{4+} species could take place.

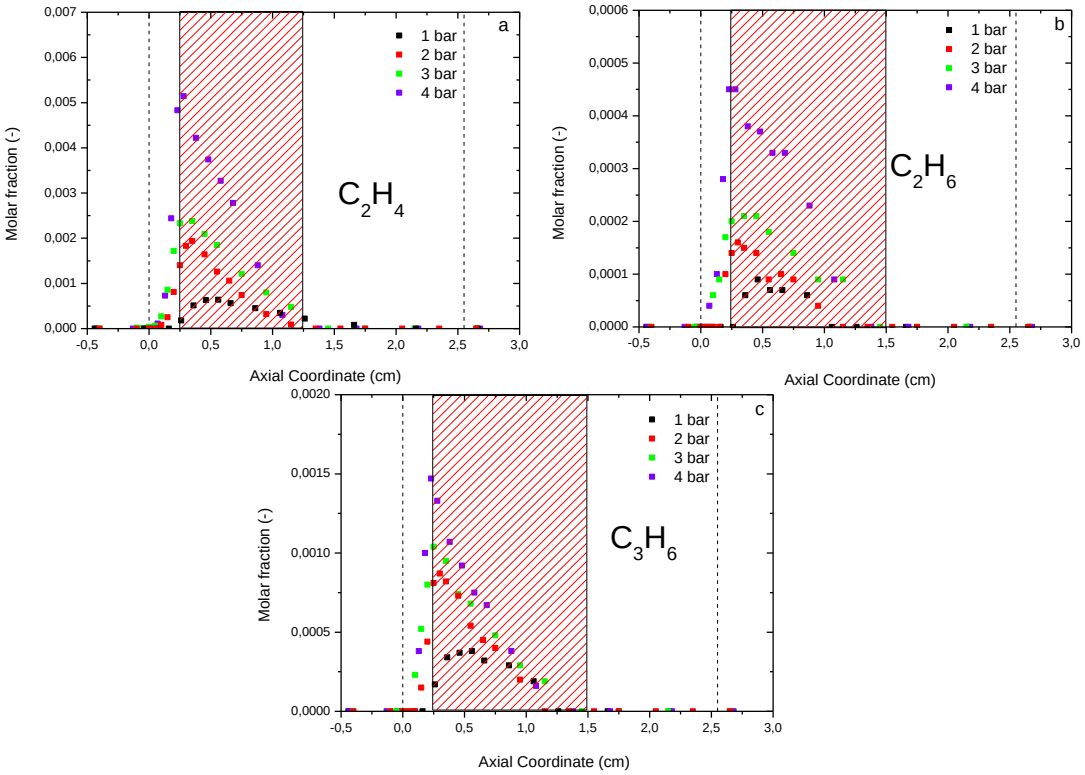

Figure 6.7: Trend of olefins in C_3H_8 CPO at different pressure (1 ÷ 4 bar),C_2H_4 (panel a), C_2H_6 (panel b), C_3H_6 (panel c) . In the dashed box the section of olefins reduction. Honeycomb monolith, Sample FHS 6. Operating conditions: auto-thermal, C/O=0.85, 10 Nlmin^{-1} flow rate.

First of all, we had to calibrate the MicroGC in order to analyze the C4+ species eventually present. We set up the temperature of Plot Q column at 100°C, in order to reduce the retention time of the species. A n-C4 flow was used to individuate the time range of analysis where the C_4 species are detected. This analysis showed that the optimal time, to view these species in the gas-chromatogram, is 9 minutes.

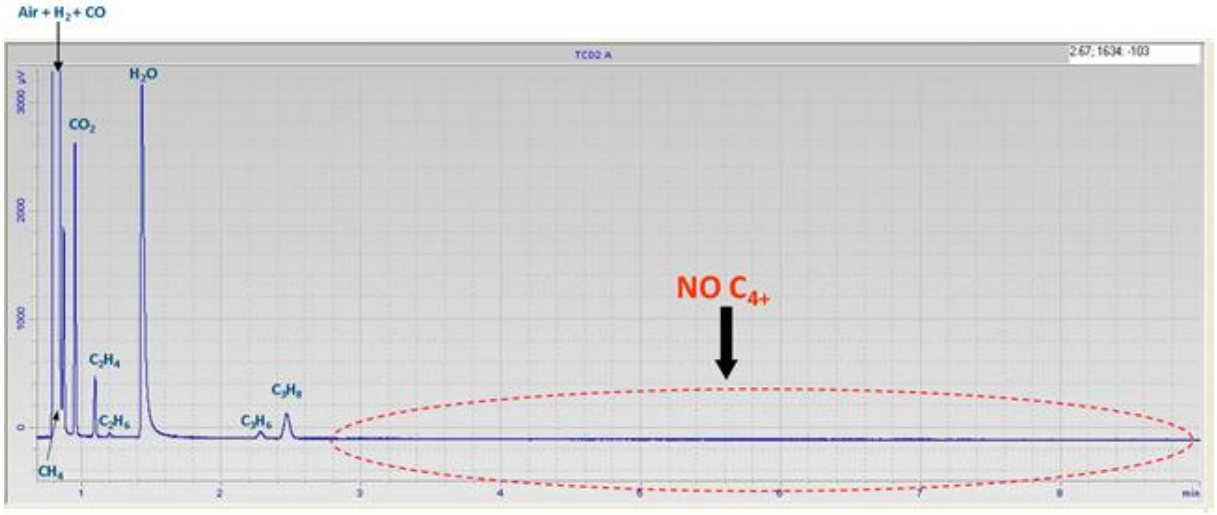

Figure 6.8: Gas-chromatogram at 0.7 cm of C_3H_8 CPO test. Honeycomb monolith; Sample FSH 6. Operating conditions: autothermal; C/O= 0.85; 10 Nl min $^{-1}$ flow rate; P=4 bar.

Figure 6.8 shows a typical analysis of the gas sampled from the dashed zone (Figure 6.7) of the catalyst in a C_3H_8-CPO test at 4 bar. The gas chromatogram shows that, after the propane peak, other peaks are not observed, which means that the condensation is not the predominant way of the olefin consumption.

6.4 MODELYNG ANALYSIS

6.4.1 INTRODUCTION

The experimental results are quantitatively analyzed by a 1D, dynamic, heterogeneous, fixed-bed, single-channel model of the adiabatic reactor (the model is described in chapter 4), The model included both homogeneous and heterogeneous kinetic schemes. Gas phase reactions for $C_1 – C_3$ species were taken into account according to the detailed scheme by Ranzi and co-workers [70]. A molecular kinetic scheme was adopted to describe the heterogeneous chemistry of C_3H_8-CPO. This scheme was independently derived on the basis of a study performed in an isothermal annular reactor, which represents an extension of previous works on CH_4 [51]. Experiments of CPO and steam reforming of C_3H_8 were carried out within the temperature range 300 – 850°C, at varying space velocity (GHSV=$7x10^5 – 9x10^6$ h^{-1}), C/O ratio (0.5 – 0.9), reactants dilution (C_3H_8 = 0.25 – 4%) and co-feed of products (H_2O = 1 – 2 %, H_2, CO = 0.5 – 1%). The kinetic scheme was derived by analyzing the experimental data with a 1D mathematical model of the annular reactor and it consisted of the whole set of CH_4-

CPO reactions (CH_4 total oxidation, CH_4 steam reforming, direct and reverse water gas shift, H_2 and CO oxidation) plus several additional reaction steps, namely C_3H_8 total oxidation, C_3H_8 steam reforming, CO methanation and the steam reforming of some $C_2 - C_3$ intermediates (C_2H_6, C_2H_4, C_3H_6). The complete set of rate expressions and kinetic parameters is reported in chapter 4. In line with the rate expressions for CH_4 conversion, C_3H_8 oxidation and steam reforming were found to be first order dependent on C_3H_8 partial pressure and independent from the concentration of the co-reactant (O_2 or H_2O). It was also assessed that the rate constants of the oxidation and the steam reforming of C_3H_8 are about 2.5 times greater than those of CH_4, with comparable activation energy. The kinetic parameters of $C_2 – C_3$ intermediates were set equal to those of C_3H_8 both in total oxidation and steam reforming. The simplifying character of the kinetics herein adopted for such steps (equaled to the rate of steam reforming of propane) is due on one side to the absence at this stage of the work of specific pieces of evidence, and on the other side to the satisfactory response of the model.

The numerical analysis herein reported is fully predictive, with no parameter adjustment. The only input data of the calculations were the catalyst amount, the Rh load and dispersion (20%, as estimated experimentally by H_2 chemisorptions measurements), the geometrical parameters and the physical properties of the honeycomb support.

6.4.2 MODEL PREDICTIONS AT INCREASING PRESSURE 1÷4 bar

In this paragraph the thermal behaviour simulation at different pressure conditions will be shown.

All the simulations are made at the same inlet temperature and at the same concentration of reactants. Also the flow rate is the same in all simulation as reported in the Table 6.3.

Flow rate Q [Nl min^{-1}]	10
Inlet gas Temperature [°C]	25
Inlet reactants concentrations [%]:	
C_3H_8	8.600
O_2	15.270
N_2	75.630
C/O	0.85

Tabel 6.3: Relevant physical and compositions data input.

In the Figure 6.9 are reported the temperature behaviours at different pressure values (from 1 to 4 bar).

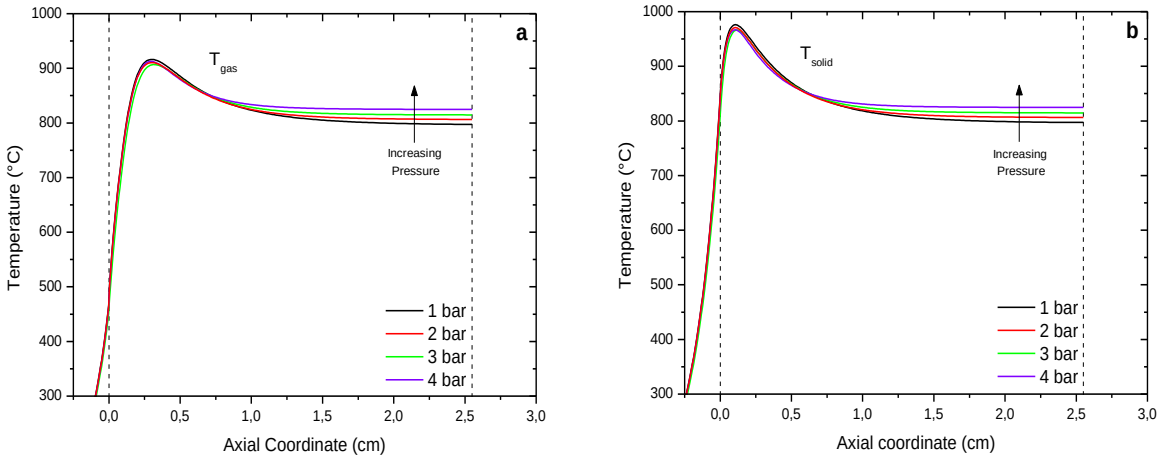

Figure 6.9: Model predictions: Temperature profiles for gas phase (panel a) and for the solid phase (panel b). Honeycomb monolith, Sample FHS6. Operating conditions: autothermal, C/O=0.85, 10 Nl min^{-1} flow rate, pressure 1÷4 bar, Tin = 25°C.

The model simulations of the temperature profiles of gas and solid phase at increasing pressure shows that the hot spot at the inlet section does not significantly change when the pressure raises, but after the first 7 mm, where the approach to the thermodynamic equilibrium prevails, the temperature profiles of gas and solid phases show an increment of temperature.

The hot spot temperature of the gas and solid phases are reported in the Table 6.4.

Pressure [bar]	T_{gas} [°C]	T_{solid} [°C]	C/O
1	920	977	0.85
2	917	972	0.85
3	916	971	0.85
4	916	970	0.85

Table 6.4: Model predictions: Values of maximum temperature in the gas phase and in the solid phase.

The peak temperature of the gas phase varies between 916 to 920 °C, there is a decreasing trend of the hotspot temperature when the pressure increases, conversely with the data measure during the experimental tests.

Pressure [bar]		$\chi_{C_3H_8}$	σ_{H_2}	σ_{CO}	$T_{gas}^{(1)}$ [°C]	T_{solid} [°C]	$\alpha^{(1)}$	$T_{gas}^{(2)}$ [°C]	$\alpha^{(2)}$
1	exp	100%	88%	88%	759	700	0.94	789	1.00
	eq.	100%	87%	86%	788	-		788	
	model	100%	87%	86%	797	797		797	
2	exp	100%	87%	89%	782	712	0.94	809	0.99
	eq.	100%	85%	85%	812	-		812	
	model	100%	86%	86%	813	813		813	
3	exp	100%	88%	89%	795	728	0.92	832	0.99
	eq.	100%	85%	86%	838	-		838	
	model	100%	85%	86%	845	845		845	
4	exp	100%	85%	86%	810	788	0.93	851	1.00
	eq.	100%	83%	85%	850	-		850	
	model	100%	85%	86%	857	857		857	

Table 6.5: Model predictions: Comparison between the experimental data, thermodynamic temperature equilibrium calculated by STANJAN data bank ® and by Heterogeneous Model. $\alpha^{(1)}$ is the thermal efficient outside the catalyst, $\alpha^{(2)}$ is thermal efficient at 1,5 cm.

As Table 6.5 shows the selectivity of H_2 and CO decreases when pressure increases, propane is always totally consumed.

The model predictions about the reactants species are shown in Figure 6.10.

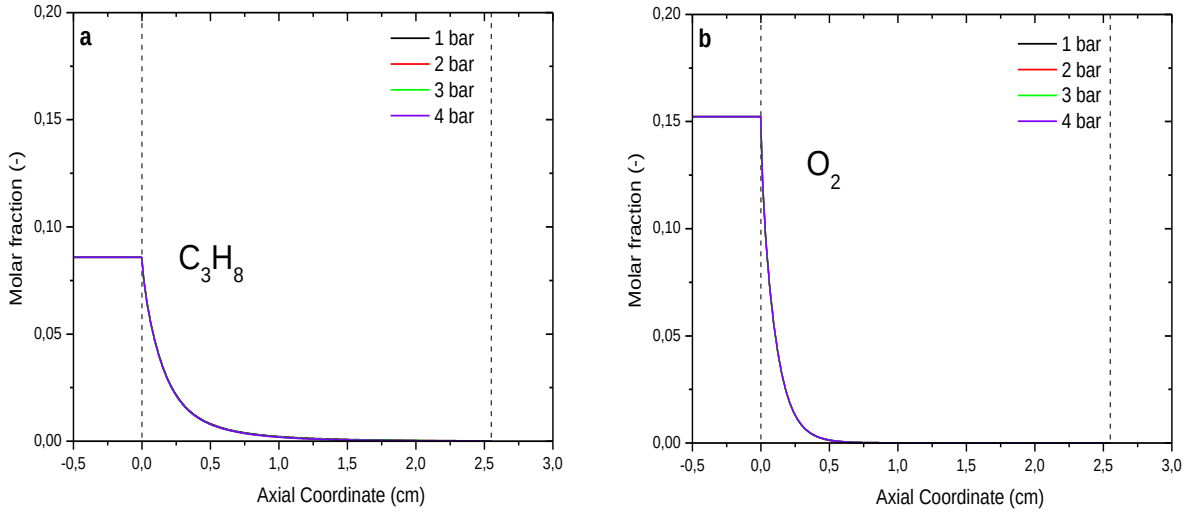

Figure 6.10: Model predictions: Axial concentration profiles of the reactants at different pressure: Propane (panel a), Oxygen (panel b). Honeycomb monolith, Sample FSH6.Operating conditions: autothermal, C/O=0.85, 10 Nlmin^{-1} flow rate, Tin = 25°C.

The simulations show that the profiles are completely overlapped at different pressures: the rate of consumption and the length of totally conversion are the same at changing pressure. Differently from CH_4-CPO, both of the reactants are totally consumed and the outlet concentration of propane and oxygen are equal to zero.

In the first 5 mm of catalyst, the model predicts, for each product, the same value at pressure increasing. Just the peaks of water and carbon dioxide are little influenced by pressure in opposite way: in fact, the peak of water concentrations decreases when pressure increase, while the peak of carbon dioxide raises when pressure increase, Figure 6.9. In the thermodynamic section (after the first 5 mm of catalyst) the rise of pressure generates a decrease of syngas products concentrations. Total oxidation products display an inverse trend, Figure 6.11.

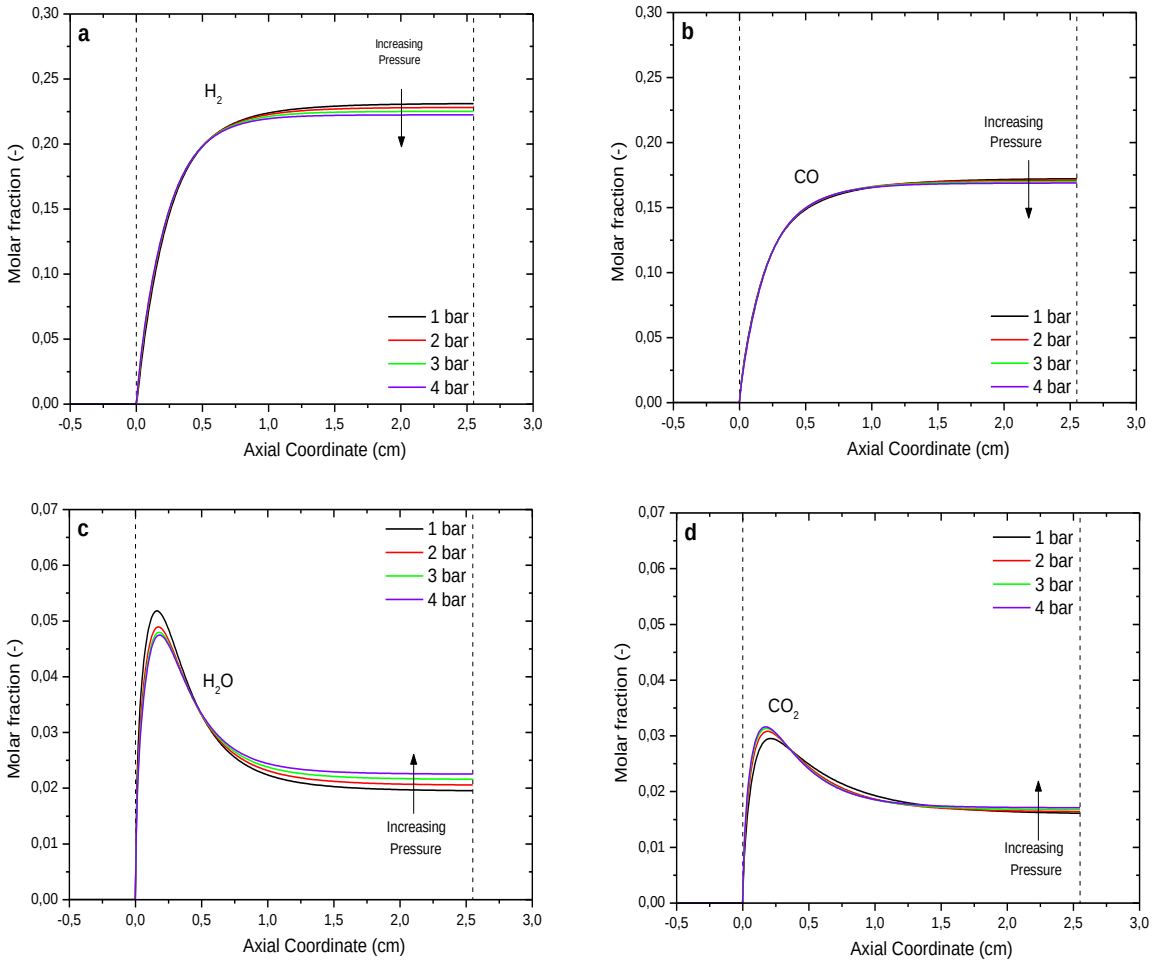

Figure 6.11: Model predictions: Axial concentration profiles of the products at different pressure: H_2(panel a), CO (panel b), H_2O (panel c), CO_2 (panel d). Honeycomb monolith, Sample FSH6.Operating conditions: autothermal, C/O=0.85, 10 Nlmin^{-1} flow rate, Tin = 25°C.

Through C_3H_8-CPO tests, the species hydrocarbon products have been considered: methane, ethane, ethylene and propylene. This is due to relevance of the homogeneous reactions that, in this case are not negligible, as shown in Figure 6.12.

The pressure rise involves an increment of the hydrocarbon products species, this is due to a greater contribution of the homogeneous reactions. The simulation shows a total consumption in the second part of the catalyst of ethane, ethylene and propylene. The peaks raise is predicted by the model. The methane has a different behavior than ethane, ethylene and propylene: in fact, at the beginning the CH_4 concentration grows, later the concentration decreases. Consecutively, the CH_4 concentration grows again.

Concerning the complex evolution of CH_4, the simulations show that this experimental result could be very well explained by a series of contributions consisting of:

1) gas-phase formation of methane by propane cracking,
2) its catalytic consumption by steam reforming,
3) its catalytic formation by methanation, kinetically favored by the increasing partial pressures of H_2 and CO and thermodynamically favored by the decreasing temperatures.

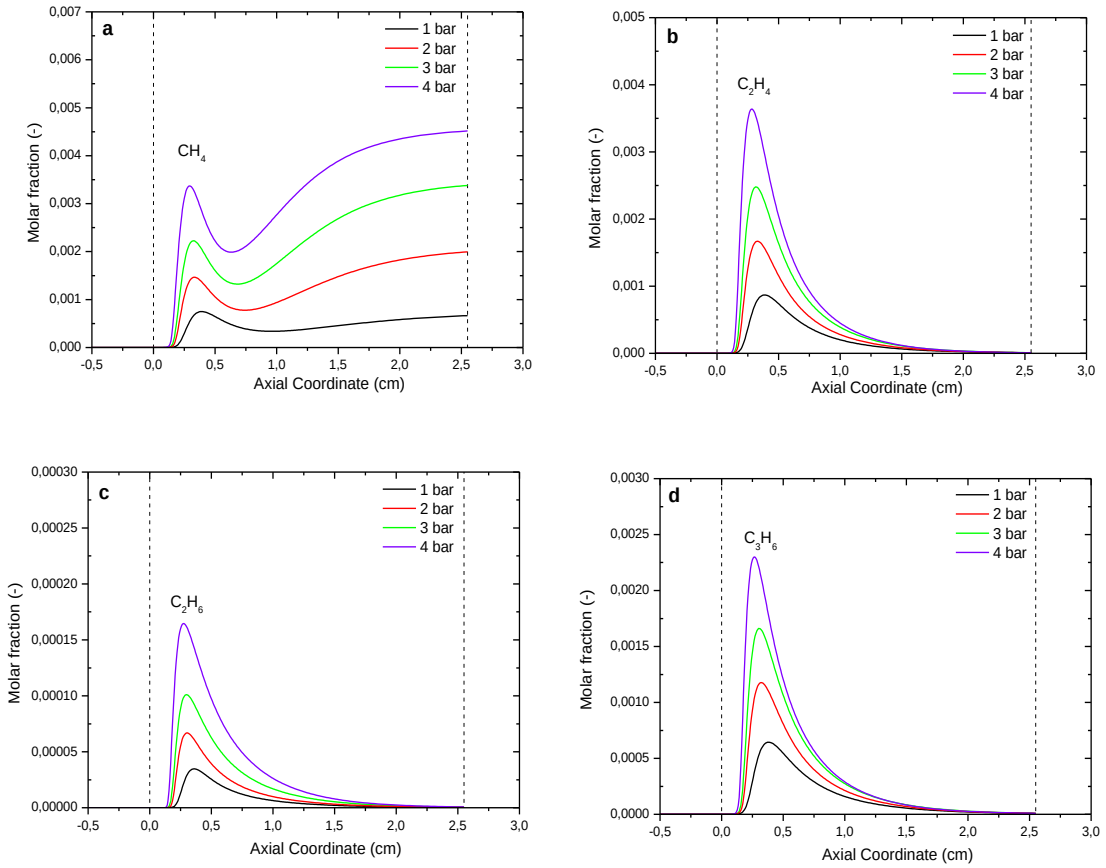

Figure 6.12: Model predictions: Axial concentration profiles of the C_1-C_3 products at different pressure: CH_4 (panel a), C_2H_4 (panel b), C_2H_6 (panel c), C_3H_6 (panel d). Honeycomb monolith, Sample FSH6.Operating conditions: autothermal, C/O=0.85, 10 Nlmin^{-1} flow rate, Tin = 25°C.

The trends of temperature behavior for the gas and solid phases, and of concentrations profiles, shown in this paragraph, are very similar to the experimental values previously described. In the next paragraph the comparison between the model predictions and the experimental data will be shown.

6.4.3 COMPARISON BETWEEN EXPERIMENAL DATA AND MODELING PREDICTIONS AT DIFFERENT PRESSURE

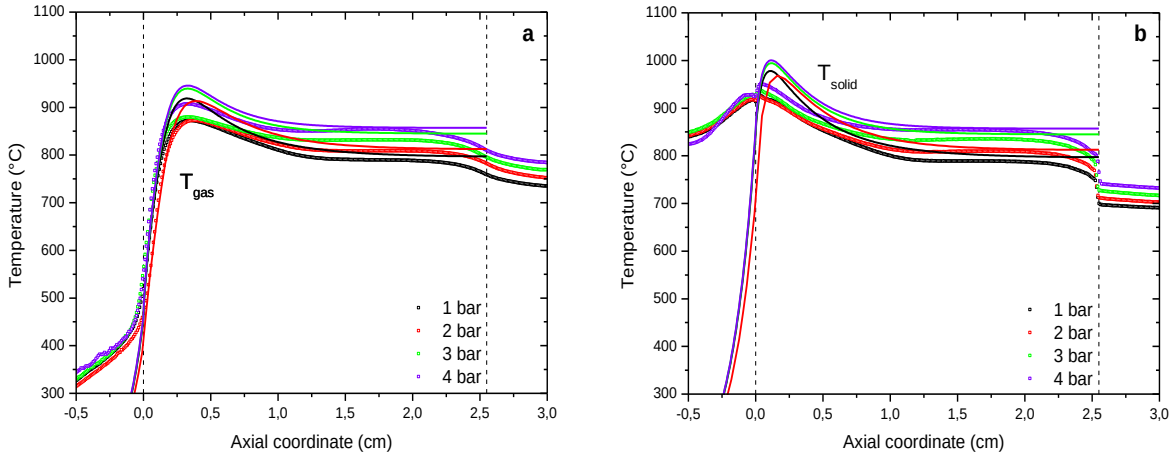

Figure 6.13: Experimental and modeling comparison, axial temperature profiles measured by thermocouple, T_{gas} (panel a), and by pyrometer, T_{solid}, (panel b) Honeycomb monolith, Sample FHS6. Operating conditions: autothermal, C/O=0.85, 10 Nlmin^{-1} flow rate, pressure 1÷4 bar. Symbols: experimental measurements. Solid lines: model predictions.

As previously discussed, the numerical analysis herein reported is fully predictive, with no parameter adjustment.

The only input data of the calculations were the catalyst amount, the Rh load and dispersion (20%, as estimated experimentally by H_2 chemisorptions measurements), the geometrical parameters and the physical properties of the honeycomb support.

The axial temperature profiles obtained by applying the spatial sampling technique are compared to those predicted by the model in Figure 6.13. The temperature simulations appear to overestimate the peaks temperature, due to an absence of front heat shield. As described in previously work [67], with propane feed, the temperature of solid and gas phase is higher than CH_4-CPO, for this reason the dissipation, due to the absence of heat shield, is not negligible.

Now the comparison between experimental composition data and model predictions will be illustrated.

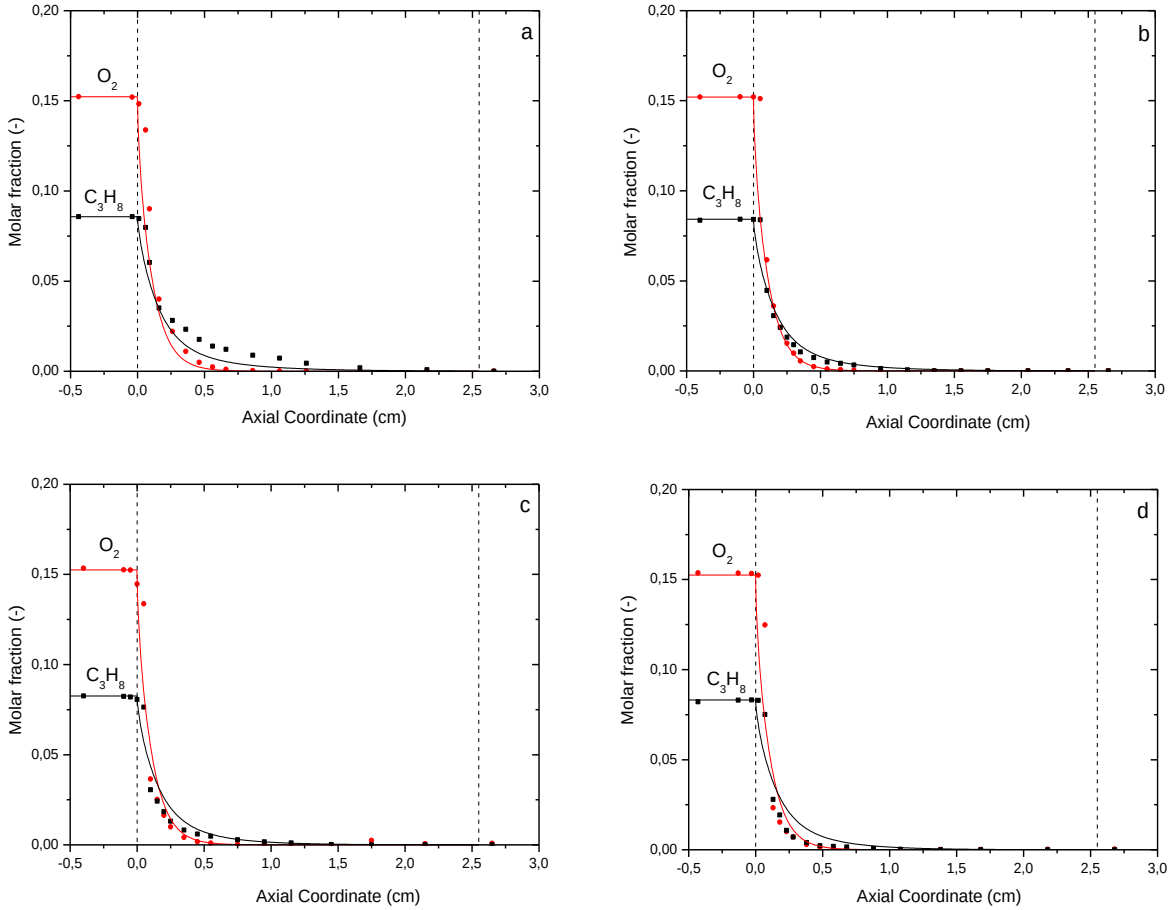

Figure 6.14: Axial concentration profiles of the reactants: comparison between experimental and simulated values in the gas phase at different pressure: 1 bar (panel a), 2 bar (panel b), 3 bar (panel c), 4 bar (panel d). Honeycomb monolith, Sample FSH 6.Operating conditions: autothermal, C/O=0.85, 10 Nlmin^{-1} flow rate, Tin = 25°C. Symbols: experimental measurements. Solid lines: model predictions.

The calculated profiles of the species are in close agreement with the experimental evidence. In fact, O_2 conversion is complete within 5-6 mm and C_3H_8 conversion is complete within 1 cm. Through the increase of pressure, the accuracy of prediction of the reactants profiles does not change.

Figure 6.15 shows the comparison between the simulations and the products profiles.

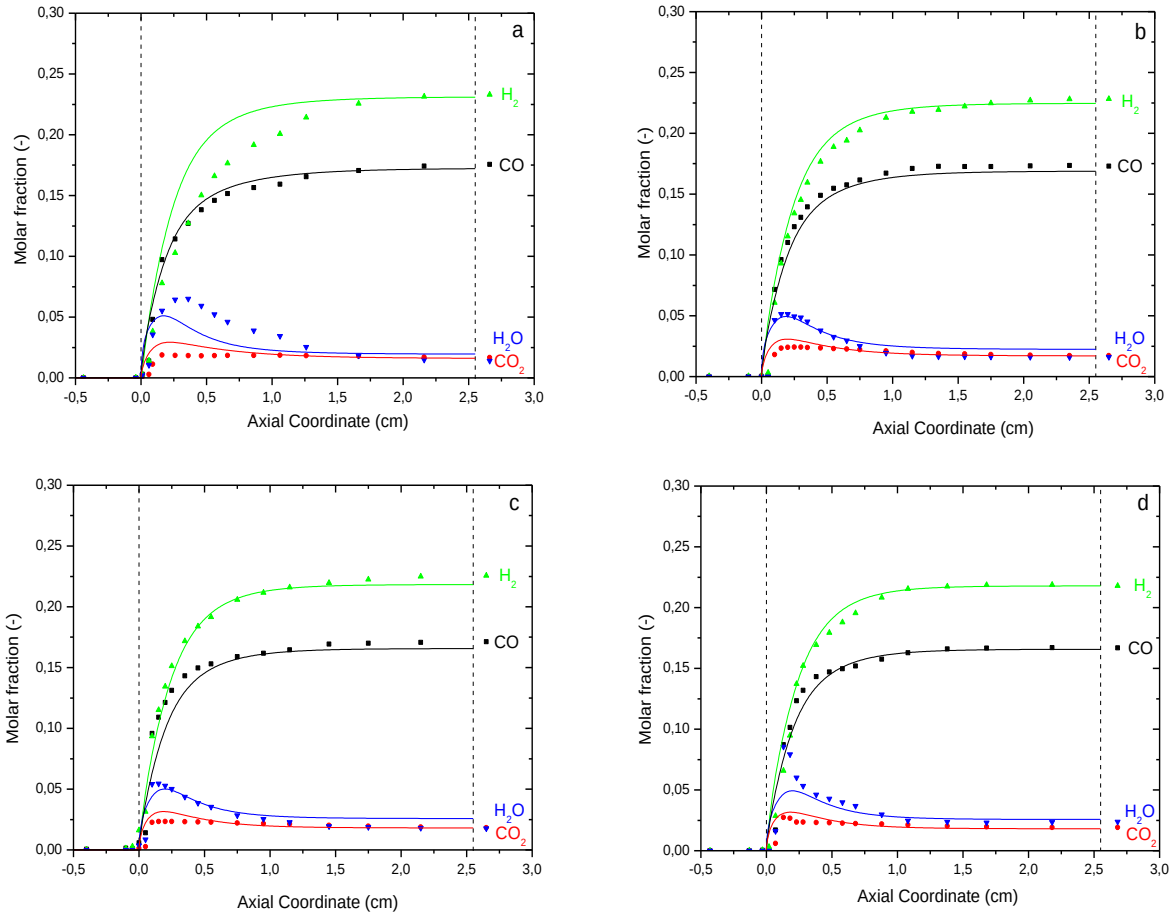

Figure 6.15: Axial concentration profiles of the products: comparison between experimental and simulated values in the gas phase at different pressure: 1 bar (panel a), 2 bar (panel b), 3 bar (panel c), 4 bar (panel d). Honeycomb monolith, Sample FSH6.Operating conditions: autothermal, C/O=0.85, 10 Nlmin^{-1} flow rate, Tin = 25°C. Symbols: experimental measurements. Solid lines: model predictions.

There is a good agreement between experimental data and simulation profiles, although the kinetic scheme used in the heterogeneous model was developed only at atmospheric pressure. The profiles at 1 bar show an unexpected trend: that experimental data and simulation profiles are not in agreement, especially in the first part, but in the end of catalyst the experimental data and the simulation profiles converge to a value of the thermodynamically equilibrium.

Lastly the comparison between experimental data and model predictions about the hydrocarbon products will be shown: methane, ethane, ethylene and propylene.

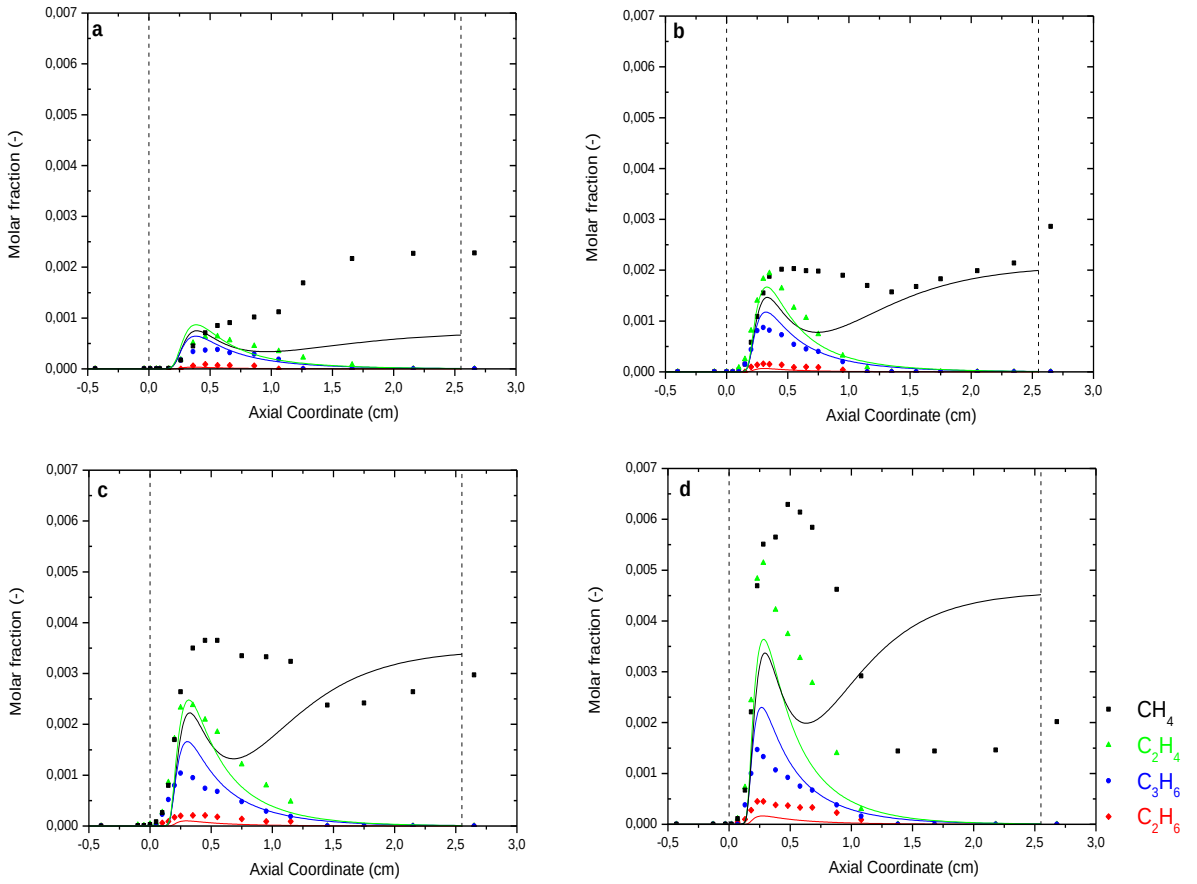

Figure 6.16: Axial concentration profiles of the hydrocarbon products: comparison between experimental and simulated values in the gas phase at different pressure: 1 bar (panel a), 2 bar (panel b), 3 bar (panel c), 4 bar (panel d). Honeycomb monolith, Sample FSH6. Operating conditions: autothermal, C/O=0.85, 10 Nlmin^{-1} flow rate, Tin = 25°C. Symbols: experimental measurements. Solid lines: model predictions

Deviations are noticed between measured and calculated profiles of the hydrocarbons species. However, the deviations has a negligible impact on the consumption of the reactants and on the thermal behavior of the reactor. A source of inaccuracy could be the adoption of a lumped description of cross sectional concentration and temperature profiles in the honeycomb channel.

The hydrocarbon products (CH_4 and C_2H_6, C_2H_4 and C_3H_6) are present in small amount and they show a complex evolution. In order to better understand the interpretation of the experiments, as already mentioned, a detailed gas-phase chemistry is incorporated in the heterogeneous 1D model, taken from Ranzi et al [70]. The propane scheme is extended to account for the catalytic conversion of hydrocarbon intermediates, especially at higher pressure where the concentrations of this species, which are generated in the gas phase, are

considerable. Anyway, all the general trends of product distribution were captured by the model.

As described in previously work [76], the model analysis revealed that gas-phase activation of C_3H_8 is responsible for the production of all the hydrocarbon species observed at the reactor inlet.

6.4.4 REACTION RATE PROFILES IN C_3H_8-CPO AND ROLE OF DIFFUSION RESISTANCE.

The heterogeneous model and the spatial sampling technique are highly informative tools in fact they allow to characterize the behavior of the system and not only with the outlet temperature and composition (integral measurements), but especially with axial profiles (local measurements), which are very important because the system is characterized by sharp temperature and composition gradients. The good performances of the model prediction in the temperature, and species profiles description demonstrate the possibility to use this heterogeneous model, in which there is an atmospheric kinetic scheme, to analyze the pressure effects with a good accuracy of prediction.

The model is utilized in order to understand the phenomena of the kinetic section of the catalyst (first 5 mm).
The prediction of the model allows to comprehend the axial profiles of the species in the catalyst wall. Particularly, a deeper insight into the evolution of the reactants, was obtained by analyzing the concentration profiles in the catalyst wall. The comparison between bulk concentration and wall concentration about propane and oxygen is reported in Figure 6.17.

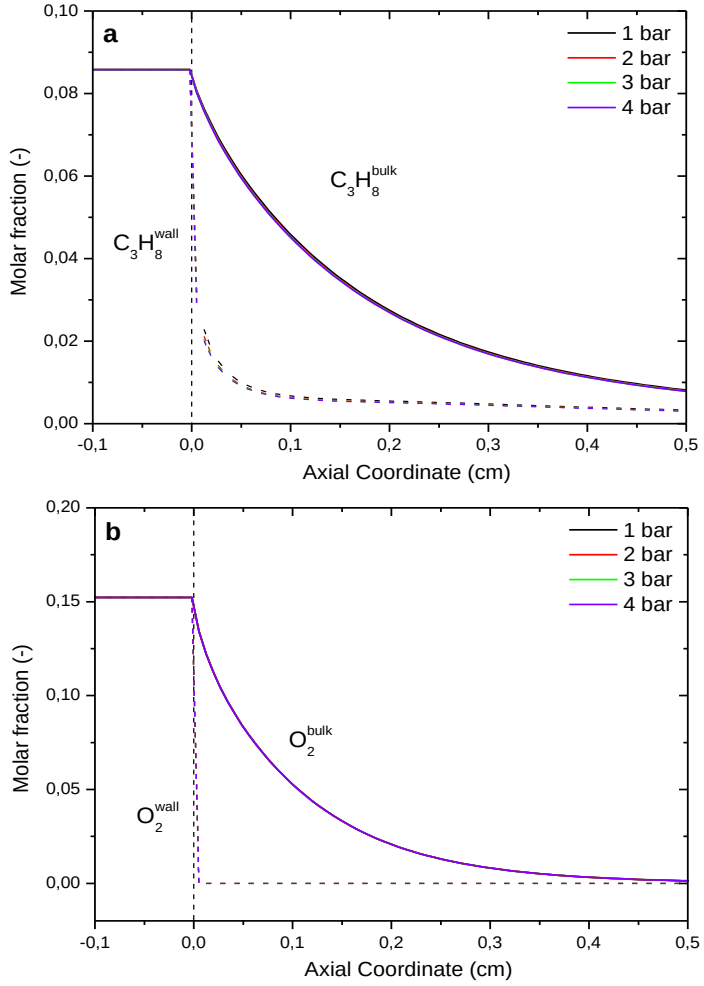

Figure 6.17: Comparison between wall and bulk concentrations: propane (panel a) and oxygen (panel b). Solid lines are model predictions of the molar fraction in the gas bulk. Dashed lines are model predictions of the molar fraction at the catalyst wall. Honeycomb monolith, Sample FSH 6. Operating conditions: autothermal, C/O=0.85, 10 Nlmin^{-1} flow rate, Tin = 25°C, pressure from1 to 4 bar.

In each experiment the consumption of O_2 is governed by external mass transfer, as indicated by the zero concentration of O_2 in the catalyst wall. Coherently, the length for complete O_2 consumption is almost unchanged. Focusing on the profiles of the fuel consumption, differently of methane, the propane consumption shows a trend similar to the one of oxygen: the wall concentration rapidly dropped to zero after the catalyst entrance (< 1mm), while the consumption of C_3H_8 in the gas phase spread over 1 cm.

To better rationalize this difference, as done with CH_4-CPO, the Carberry number for each reactant can be introduce.

The axial evolution of the Ca numbers, for propane and oxygen, are plotted in Figure 6.18.

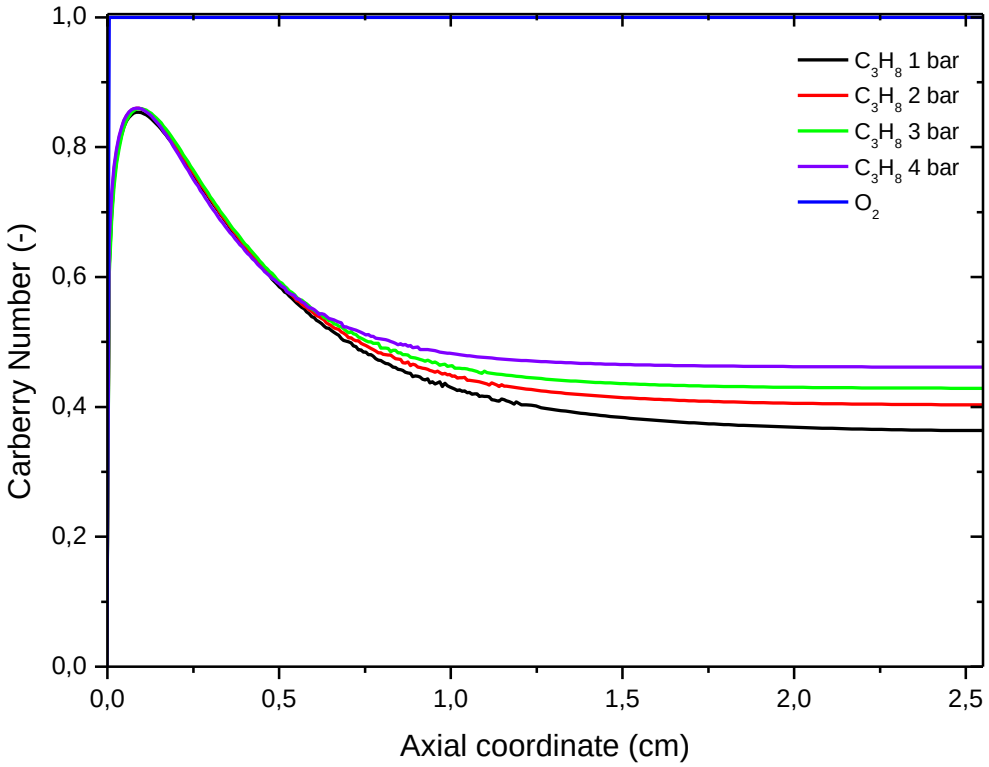

Figure 6.18: Axial evolution of Carberry numbers for O_2, C_3H_8 at 1 ÷ 4 bar of pressure.

As expected, this analysis confirmed that O_2 consumption is totally limited by external mass transfer at each pressure, while the propane consumption, in agreement to methane consumption shown in chapter 5, is mainly controlled by a external mass transfer in the first section of the catalyst (from 0 to 5mm). After the first 5mm, as Figure 6.16 shows, the value of bulk and wall concentration is the same, for this reason for this reason the Carberry number loses his functionality.

To confirm this hypothesis, as it was displayed in the chapter 5, we compared the global consumption rate and the gas-solid mass transfer rate in the limiting case of full external diffusing regime for both the reactants.

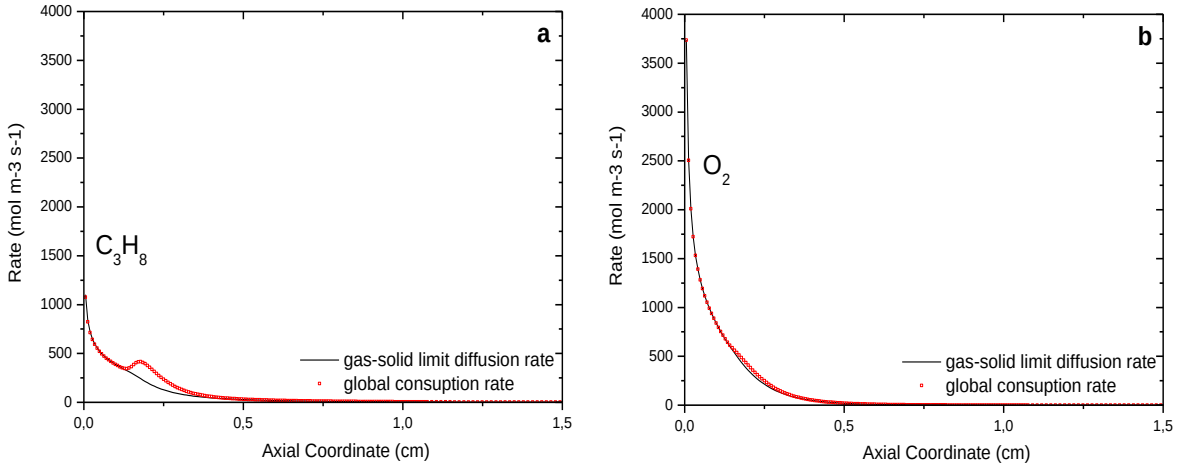

Figure 6.19: Comparison between the gas-solid limit diffusion rate (black line) with the global consumption rate (red scatter) for propane (panel a) and oxygen (panel b). Sample FHS 6. Operating conditions: autothermal, C/O=0.85, 10 Nlmin^{-1} flow rate, at 4 bar.

The Figure 6.19 confirms that the C_3H_8 and O_2 are controlled by external mass transfer: the value, at every axial position, of the global consumption rate is equal to the value of the gas-solid limit diffusion rate. Moreover the trend of the rate consumption of propane shows the presence of a peak at 2mm, which means the consumption of the propane by cracking in the gas phase. The Figures 6.17-19 support the hypothesis, also in C_3H_8-CPO tests, that the consumption of reactants is mainly influenced by external mass transfer.

Similarly to the case described in chapter 5, an analytical treatment of a isothermal plug flow reactor suggests that the rates of consumption of propane and oxygen are independent from the pressure. This results are displayed in the Figure 6.20.

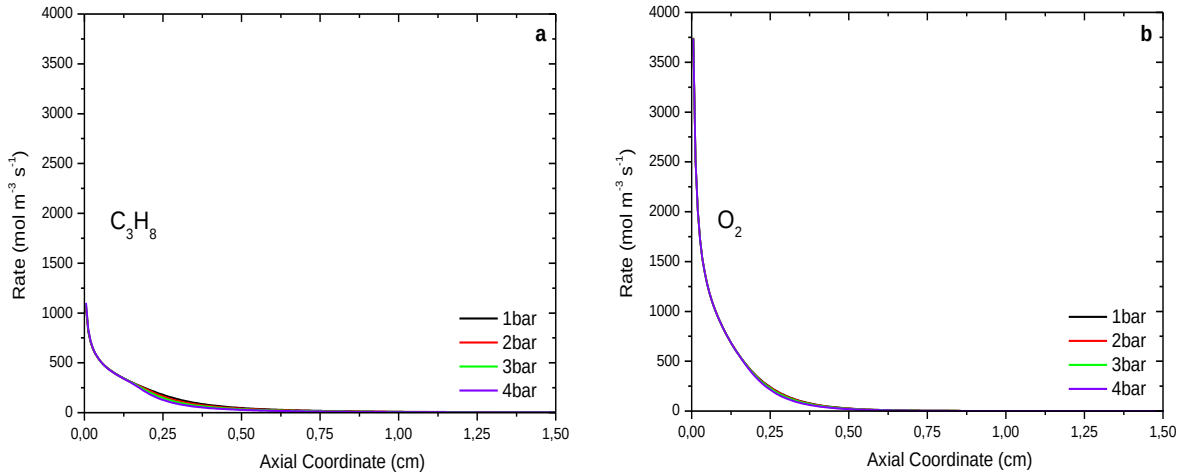

Figure 6.20: gas-solid limit diffusion rate for propane (panel a) and oxygen (panel b). Sample FHS 6. Operating conditions: autothermal, C/O=0.85, 10 Nlmin^{-1} flow rate, at pressure 1 - 4 bar.

The gas-solid limit diffusion rate profiles do not show a substantial variations due to the pressure increase.

6.5 THERMODINAMIC ANALISYS

To better understand the evolution of the distribution of the products we have analyzed the approach to thermodynamic equilibrium of single reactions, i.e. direct and reverse WGS, SR CH_4 (reverse methanation) and SR C_3H_8, involved in the global process.
The Keq of the different reactions are calculated using a linearized expressions for $\Delta G_R^0(T)$:

$CH_4 + H_2O \leftrightharpoons 3H_2 + CO$ $\quad \Delta G_R^0(T) = 53717 - 60.25 * T \quad [cal/mol]$ (6.1)

$CO + H_2O \rightarrow CO_2 + H_2$ $\quad \Delta G_R^0(T) = -8514 - 7.71 * T \quad [cal/mol]$ (6.2)

$C_3H_8 + 3H_2O \leftrightharpoons 3CO + 7H_2$ $\quad \Delta G_R^0(T) = 147521 - 207.76 * T \; [cal/mol]$ (6.3)

while the Kp are estimated through the following expression:

$$K_p = \prod_{i=1}^{NC} a_i^{v_i} \tag{6.4}$$

Kp is simply calculated from the measured species profiles as the product of the molar fractions elevates to the relative stoichiometric coefficient while Keq is evaluated from the measured gas temperature profile as:

$$K_{eq}(T) = exp\left(-\frac{\Delta G_R^0}{RT}\right) \tag{6.5}$$

Figure 6.21 - 6.23 show the evaluation of the ratio Kp/Keq for the single reactions. Three different situation can be detected:

- Kp/Keq < 1 which indicates a thermodynamic driving force for the direct reaction;
- Kp/Keq = 1 which indicates the reaching of the equilibrium state;
- Kp/Keq > 1 which indicates a thermodynamic driving force for the reverse reaction.

➢ **WGS: $CO + H_2O \leftrightharpoons CO_2 + H_2$**

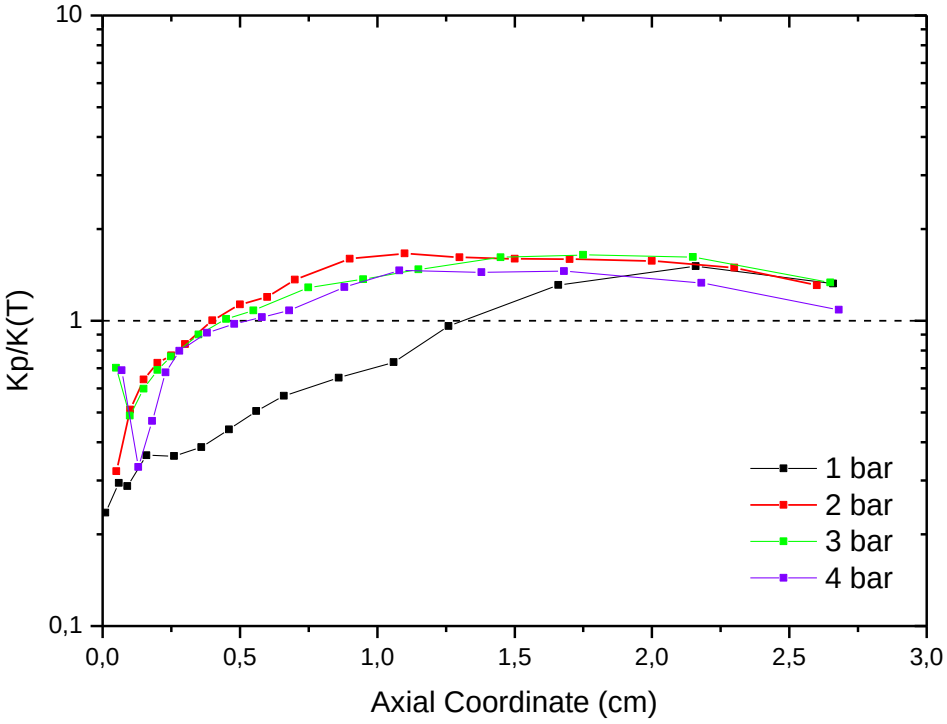

Figure 6.21: Evaluation of the K_p/K_{eq} ratio for WGS reaction.

In all the cases, the reaction advances and goes apparently beyond the equilibrium value, due to the simultaneous occurrence of oxidation process which forms H_2O and CO_2,while the steam reforming produces H_2 and CO. In the reactor outlet, the relative amounts of these species seem largely in line with the WGS equilibrium value. Inside the channel the presence of additional reactions prevails on the WGS equilibrium point. As shown the Figure 6.21 the pressure do not produce any particular effects on this profile.

➢ **CH_4 SR: $CH_4 + H_2O \leftrightharpoons 3\,H_2 + CO$**

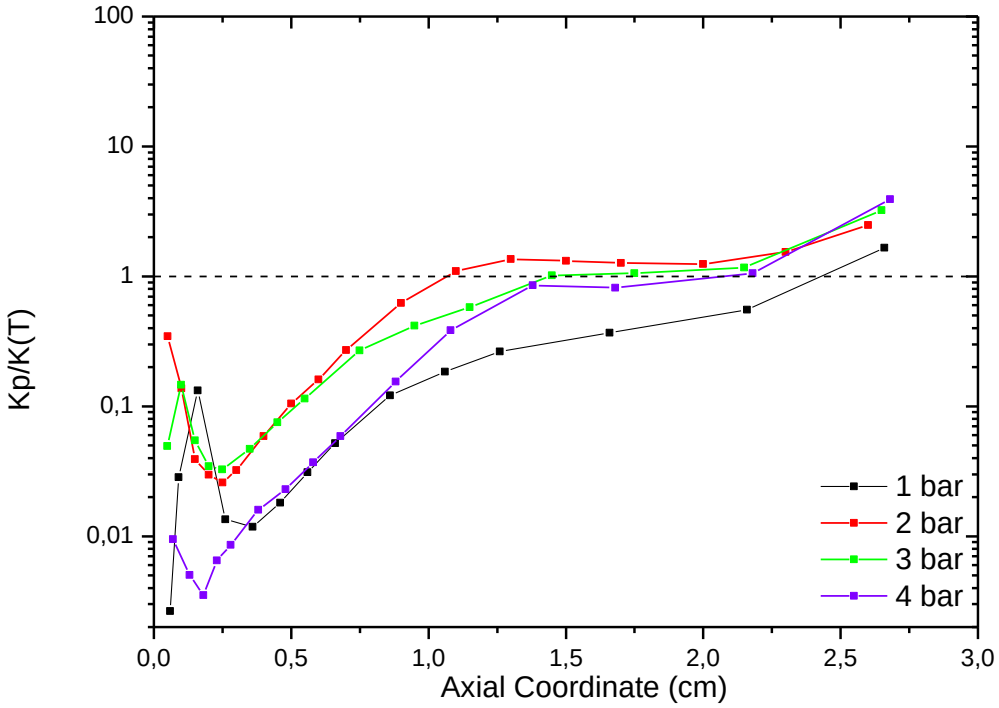

Figure 6.22: Evaluation of the K_p/K_{eq} ratio for CH_4 SR reaction.

The trends are less flat and generally reach higher values of the ratio Kp/Keq compares to those of WGS reaction. It is possible to identify three different driving force zones:

- an inlet zone (0-0.5 cm) where methane formation occurs in the gas phase and there is no thermodynamic control, so increase the driving force of SR;
- a second zone (0.5-2 cm) where steam reforming and oxidations decrease the potential of CH_4 conversion by steam reforming reactions and the thermodynamic equilibrium is reached
- a third zone (2 cm- end of catalyst) where the driving force of methanation (reverse steam reforming) prevails and could explain the observed increased trends of CH_4 concentrations accompanying the decreasing concentrations of CO and H_2.

➢ **C_3H_8 SR: $C_3H_8 + 3\ H_2O \leftrightharpoons 7\ H_2 + 3\ CO$**

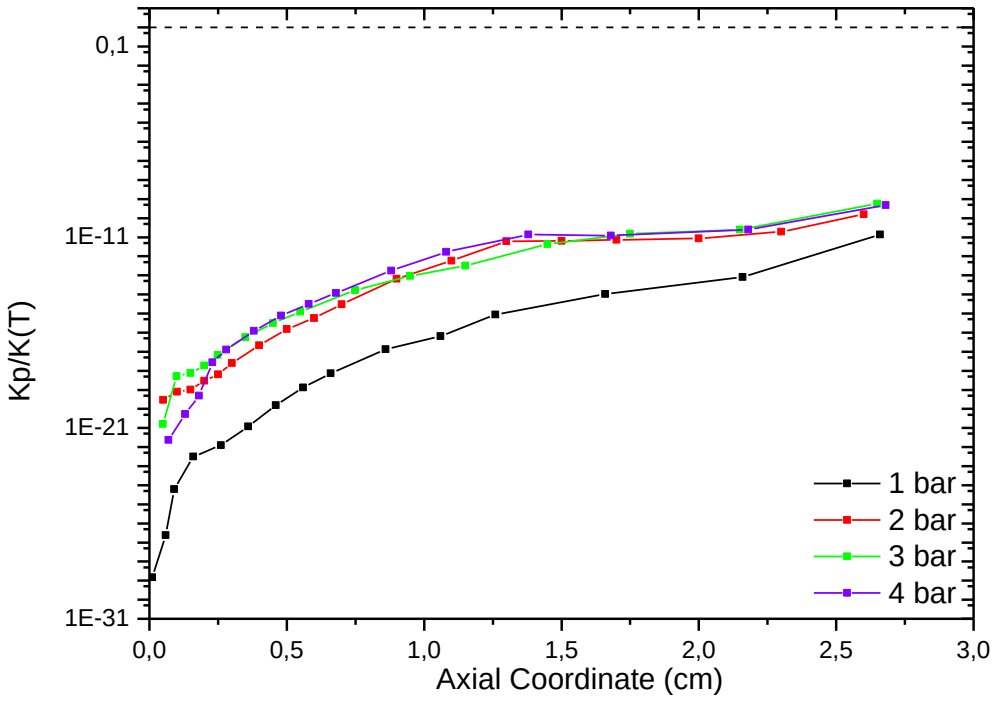

Figure 6.23: Evaluation of the K_p/K_{eq} ratio for C_3H_8 SR reaction.

It seems that SR C_3H_8 is far to reach the equilibrium state, the pressure does not have any effects on C_3H_8 SR.

As Figures 6.21 - 6.23 show, a different influence of pressure can be observed in these reactions. In WGS and in C_3H_8 SR the pressure does not modify the trend in the inlet part of the catalyst but only in the last part, where reflects the different composition at different pressure. Only the CH_4 SR is influenced by pressure in the inlet part of catalyst when pressure is higher than 3 bar.

6.6 FURTHER INVESTIGATIONS OF THE FORMATION AND CONSUMPTION OF HYDROCARBON INTERMEDIATES

Aim of this paragraph is to verify, with an experimental test, the hypothesis of catalytic consumption of C_2H_4, C_2H_6 and C_3H_6 by steam reforming which was formulated by Donazzi et al. [76].

They explained the evolution of these species based on model predictions with and without incorporation of the "post-reforming" reactions of the gas-phase intermediates.

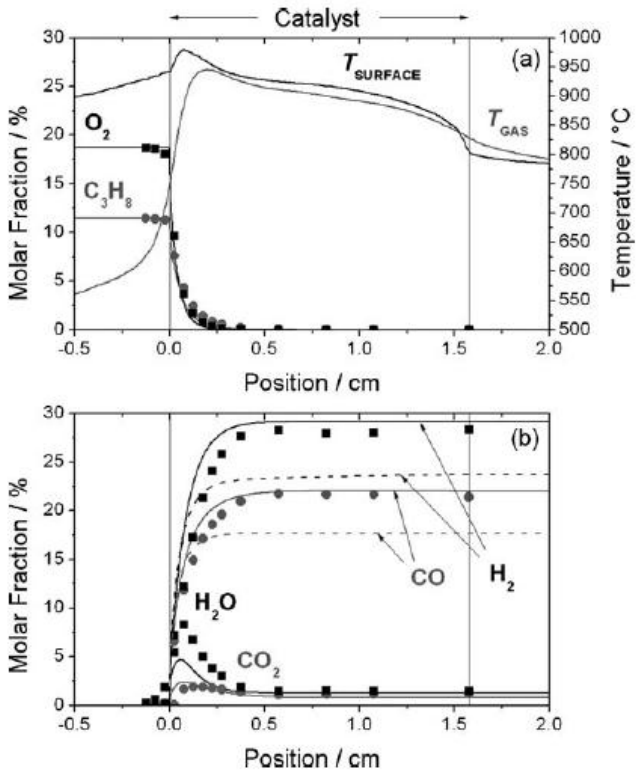

Figure 6.24:. Spatially resolved profiles of temperature and composition for a C_3H_8 CPO experiment. a) Reactants and temperature. b) Products. 2 wt% Rh/a-Al_2O_3 catalyst supported over a 400 cpsi cordierite honeycomb. Flow rate=5 Lmin_1 (STP), P=1 atm. Feed: C_3H_8/air, C_3H_8=11 vol%, O/C=1.12. Experimental results (symbols) and calculations according to the kinetic model (lines; see text for details) are reported. The temperature profiles are experimental measurements. Dashed lines are calculations obtained by neglecting the steam reforming reactions of C_2H_6, C_2H_4, and C_3H_6 in the heterogeneous kinetic scheme. cpsi=cells per square inch.

In the simulations where the heterogeneous conversion of hydrocarbon intermediates generated in the gas phase was neglected, they verified that the evolution of the products was not correctly described (see dashed lines in Figure 6.24 and Figure 6.25). The overall production of H_2 and CO was greatly underestimated (Figure 6.24b), while the outlet

composition would be rich in olefins and other hydrocarbons (Figure 6.25a). On the opposite, if the steam reforming reactions of C_{2+} hydrocarbons were taken into account (solid lines), the model predictions were consistent with the experimental data: in particular the model described correctly the production of syngas and bell-shape concentration of the C_2H_4, C_2H_6, and C_3H_6 (Figure 6.25).

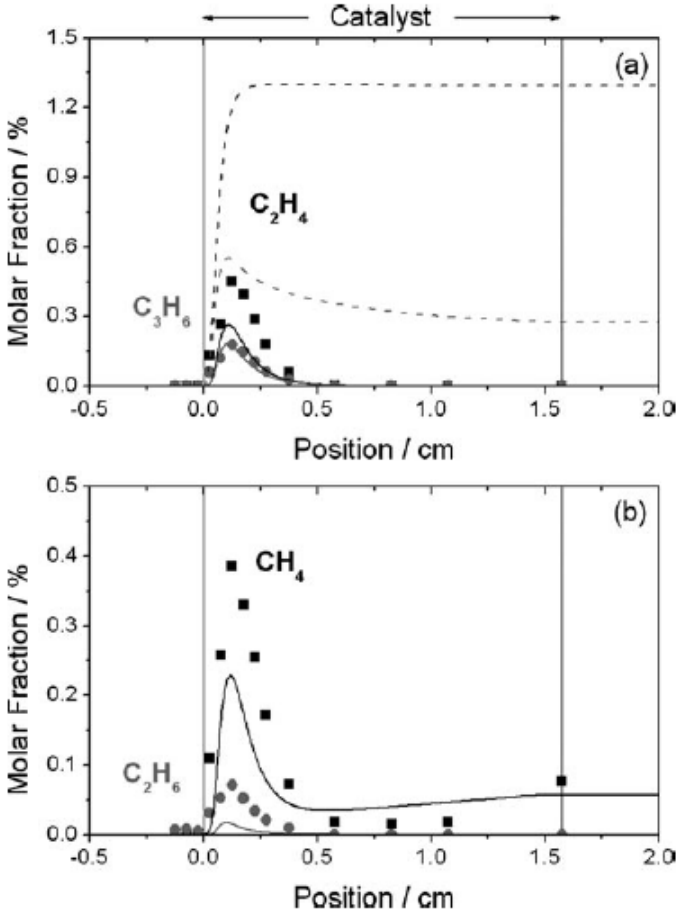

Figure 6.25. Spatially resolved composition profiles in a C_3H_8 CPO experiment. a) Unsaturated by-products. b) Saturated by-products. Conditions, lines, and symbols as in Figure 6.24.

In this work we have further verified experimentally these assumptions [67] by running a test where a very short monolith was used (long enough to guarantee the complete O_2 conversion and produce the required local high temperature, but short enough to avoid the "post-reforming" reaction of C_{2+} hydrocarbons), followed by an empty volume where gas-phase reaction could proceed.

The Figure 6.26 shows the reactor configuration.

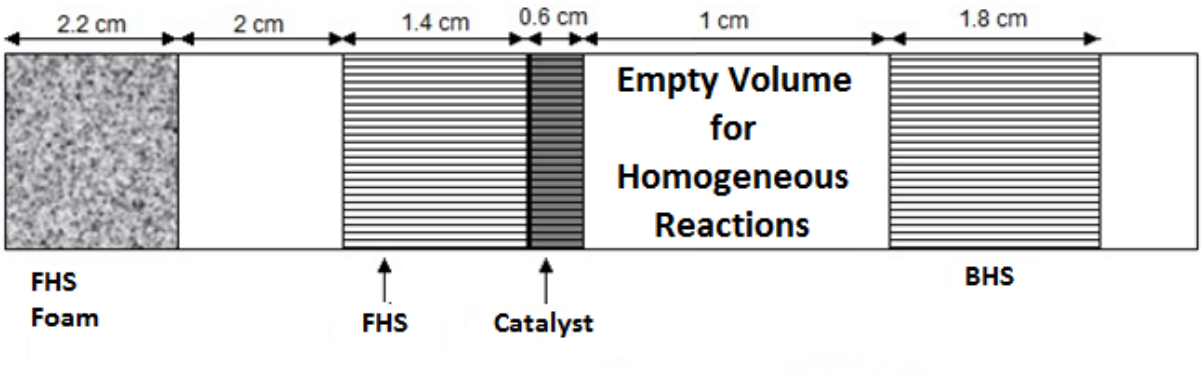

Figure 6.26: Reactor configuration.

The experiment was performed at 4 bar: as described in the paragraph 6.3.2, the high pressure accelerated the gas phase chemistry ($\propto P^2$), in order to have the higher concentration of C_{2+} species so, to facilitate the analysis.

Following the obtained experimental data will be displayed. The thermal behavior is showed in the Figure 6.27.

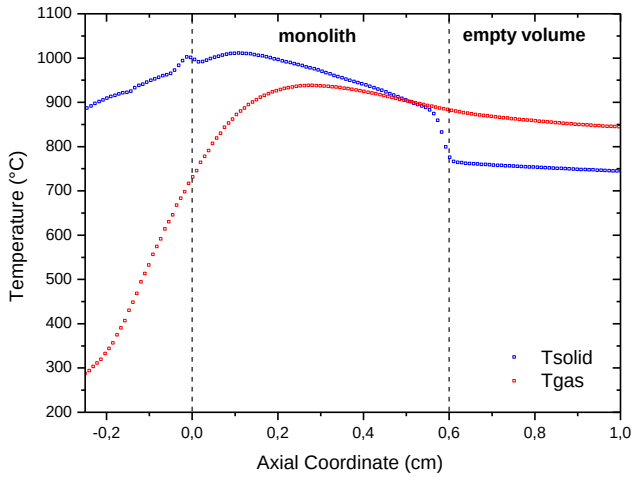

Figure 6.27:Temperature behaviors of gas (red signal) and solid phase (blue signal). Honeycomb monolith; Sample FHS 2;Operating Conditions: autothermal; C/O=0.85; 15 Nl min $^{-1}$ flow rate; P=4 bar.

The temperature profiles show a fairly flat trend, due to the higher flow rate. In fact the increase of the flow rate caused an enlargement of the oxidation zone (exothermic reaction), accordingly the temperature peak is less pronounced [67].

The concentration profiles of propane during a C_3H_8-CPO test is reported in Figure 6.28.

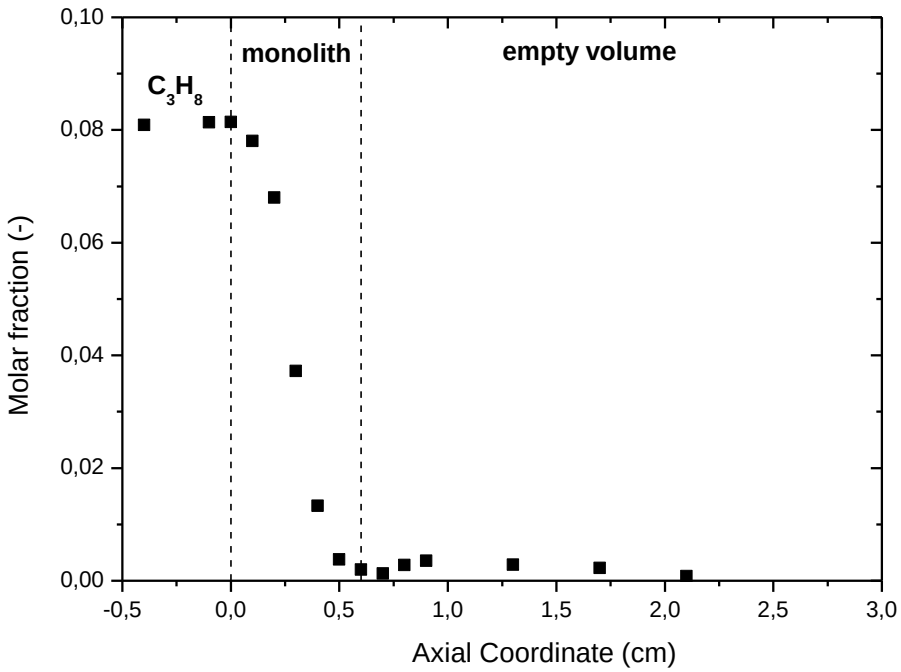

Figure 6.28: Axial concentration profile of the propane. Honeycomb monolith, Sample FHS 2. Operating conditions: autothermal, C/O=0.85, 15 Nlmin^{-1} flow rate; P = 4 bar.

The C_3H_8 profile shows a complete consumption at the outlet of the catalyst. From 0,7 to 1,0 cm the C_3H_8 concentration increase could be due to a cup-mixing: differently from the central channel (illustrated in Figure 6.28), which guaranteed the total conversion of propane at the outlet of the catalyst, the peripheral channels (with lesser activity due to the break of the washcoat layer during the assembly of the quartz tube reactor) could not guarantee the total conversion of propane.
Subsequently the propane concentration decreases again (from 1 cm): this particular trend suggests the presence of gas-phase chemistry in the section downstream the catalyst (from 1 cm).

At the same time, Figure 6.29 shows the trend about the product species: in the catalyst the reactants are converted into the syngas products (H_2, CO) and partially into the total oxidation products. Downstream the catalyst the concentration of H_2 and CO decreases.

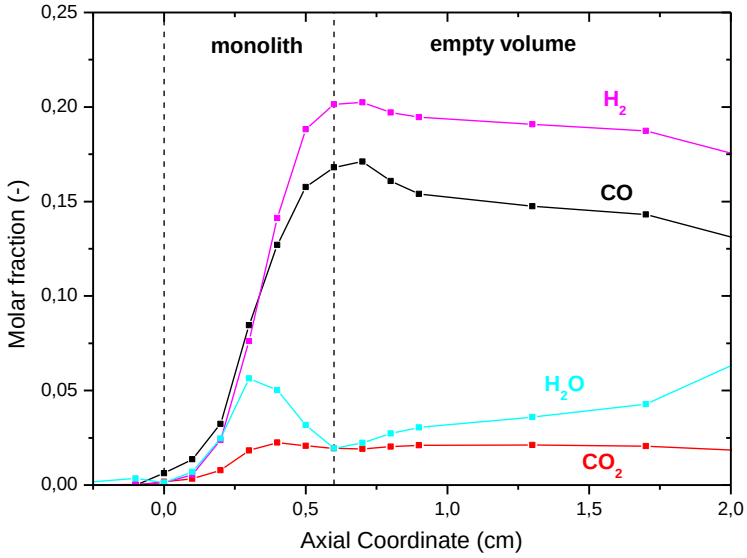

Figure 6.29 Axial concentration profiles of the products. Honeycomb monolith, Sample FHS 2. Operating conditions: autothermal, C/O=0.85, 15 Nlmin^{-1} flow rate; P = 4 bar.

Figure 6.30 shows the hydrocarbon products profiles. The study, of the propane profile and the trend about these species, permits to understand the role about the gas phase chemistry and the role of the catalyst surface in this system.

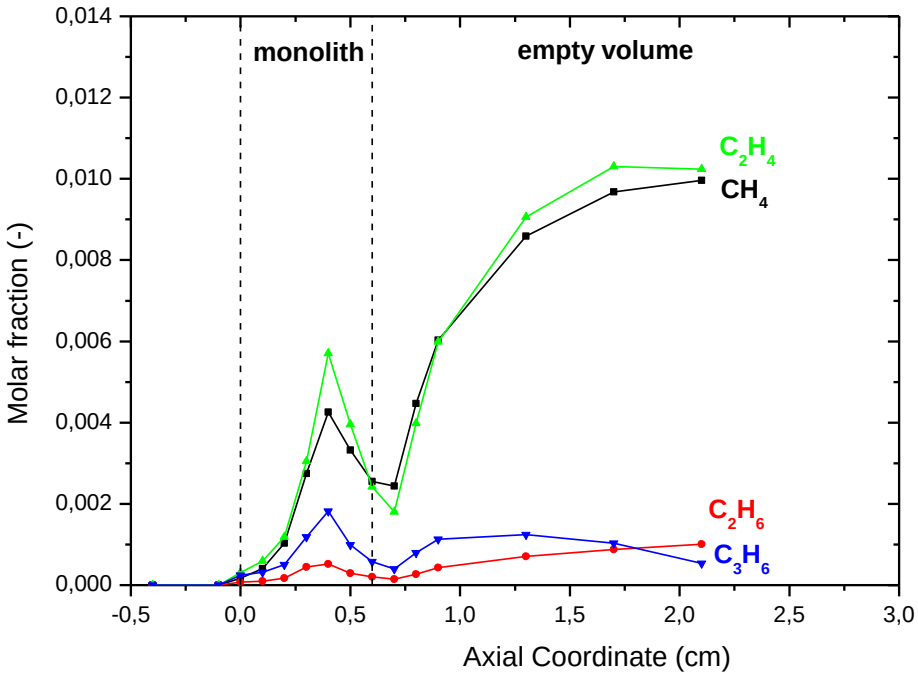

Figure 6.30 Axial concentration profiles of the hydrocarbon products: CH_4, C_2H_4,C_2H_6,C_3H_6. Honeycomb monolith, Sample FHS 2. Operating conditions: autothermal, C/O=0.85, 15 Nlmin^{-1} flow rate; P = 4 bar.

The experimental data show that, in the inlet of the catalyst (0 – 0,4 cm), the concentration of C_2H_4, C_2H_6, C_3H_6 increases (cracking reaction of propane). Between the 0,4- 0,6 cm these species show a decrement due to the starting of the heterogeneous steam reforming reactions promoted by the last part of the catalyst. Downstream the catalyst, the concentrations increase with the same velocity displayed in the inlet part of the catalyst, where these species are produced by the gas phase reaction.

The model simulations were performed to compare the experimental concentration with the model prediction. Since we can not describe this reactor configuration with the model because is not possible to introduce an empty volume after the catalyst; the simulation was carried out with a catalyst of 3 cm in length and neglecting the steam reforming reactions of C2H6, C2H4, and C3H6. The Figure 6.31 shows the obtained hydrocarbon profiles.

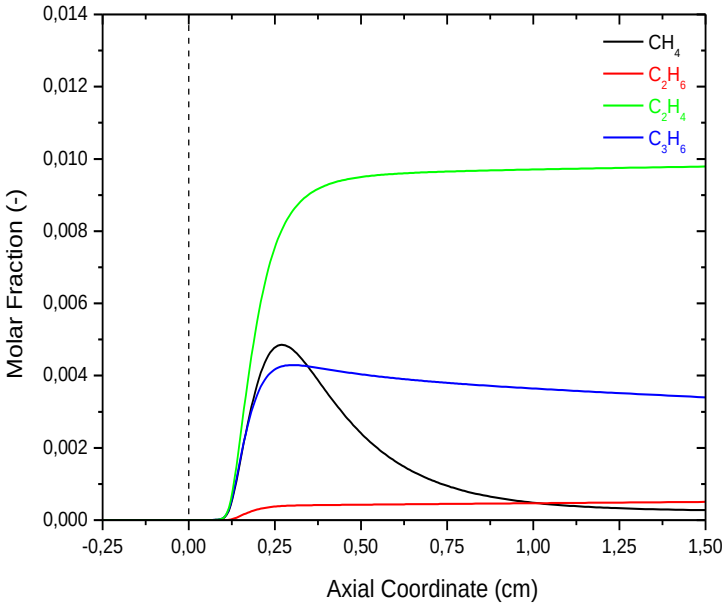

Figure 6.31: Model predictions, hydrocarbon profiles obtained by neglecting the steam reforming reactions of C_2H_6, C_2H_4, and C_3H_6. Operating Conditions: autothermal; C/O=0.85; 15 Nl min $^{-1}$ flow rate; P=4 bar.

The Figures 6.30-31 show that the concentration, downstream the catalyst, of C_{2+} species is reasonably the same, for this reason we can assume that the only way of consumption of these species is the "post-reforming" reaction.

This is the experimental evidence of the hypothesis, which was formulated by Donazzi et al., is justified. For this reason the catalyst can be considered a “chemical quench” because it cleans the gas flow from the olefins, which are the intermediates species of the PAH production.

6.7 CONCLUDING REMARKS

The experimental investigation herein presents, bases on the detailed measurement of in-situ surface and gas-phase temperature profiles by state of the art tools, shows that, at increasing pressure, temperatures raise up only in the last part of catalyst, but the temperature in the hot spot has a little shift. These experiments demonstrate that a CPO reformer fuelled with stoichiometric propane/air mixtures can operate steadily with time on stream, at least under the same conditions as those herein tested.

These tests also show that the pressure influences only the thermodynamic equilibrium, conversely the kinetic does not seem to be influenced by the increment of pressure from1 to 4 bar. The results of the model permitted us to give a possible explanation of the chemical/physical phenomena involve in the first section of the catalyst. According to literature [71], the rate of reactants consumption is governed by gas-solid mass transfer flow, the analytic treatment confirms that, under the hypothesis of external diffusing regime, the pressure has not effect on the global rate of consumption of the reactants.

Furthermore, our analysis confirmed that the hypothesis of the consumption of the hydrocarbon products by heterogeneous steam reforming on the catalytic surface. Therefore the catalyst surface acts as a chemical quench: the gas flow is cleaned flow soot precursor by the catalyst.

CHAPTER 7

CARBON FORMATION

7.1 INTRODUCTION

As discussed in the previous chapter, during the tests of C_3H_8-CPO under pressurized conditions, an increase of carbon deposition was observed in the quartz reactor downstream from the catalyst and inside the lines that connected the metal reactor to the vent. The carbon deposition inside the lines was associated with the pressure regulation. As a matter of fact, the pressure regulation valve was completely blocked by carbon deposition with a consequent increase of the pressure inside the metal case. No carbon deposit were ever detected on the catalyst surface.

Figure 7.1 shows the catalytic honeycomb and the back heat shield at the end of a C_3H_8-CPO test.

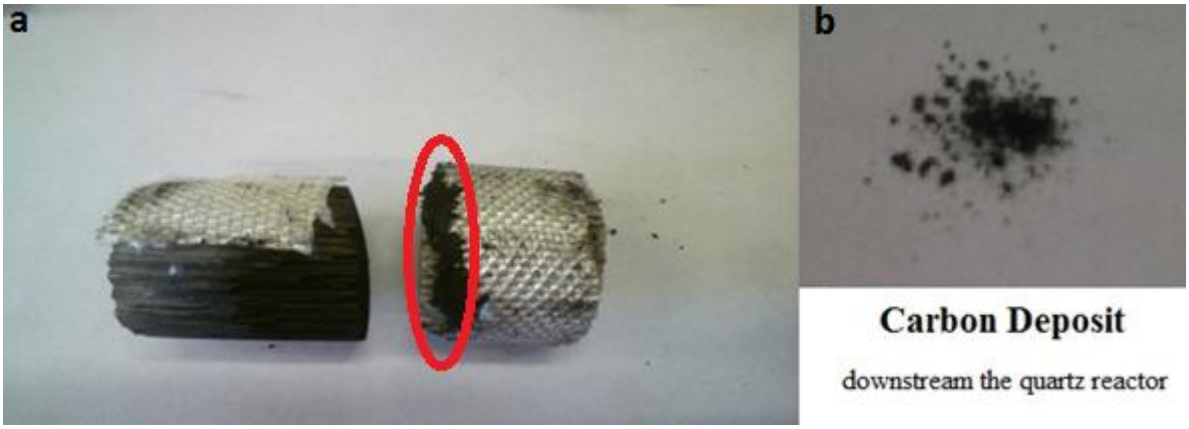

Figure 7.1: Typical carbon deposition after a C_3H_8 test at 4 bar for 7 hours. Panel a: catalyst on the left, Back Heat Shield on the right; panel b carbon deposit collected on the flange surface.

Figure 7.1 shows the results of carbon deposition after a C_3H_8 CPO test, equipped with FeCrAlloy filters calcined at 950°C, at 4 bar for 12 hours. The catalyst did not show "crust" of carbon deposited, but deposited carbon could be observed on the BHS surface (highlighted by the red circle, Figure 1), deposited as a powder. On the flange surface (downstream the quartz tube), on the thermocouple and in the lines between the metal reactor and the vent were also observed carbon deposit. Figure 7.2 displayed the carbon deposits on the backside thermocouple:

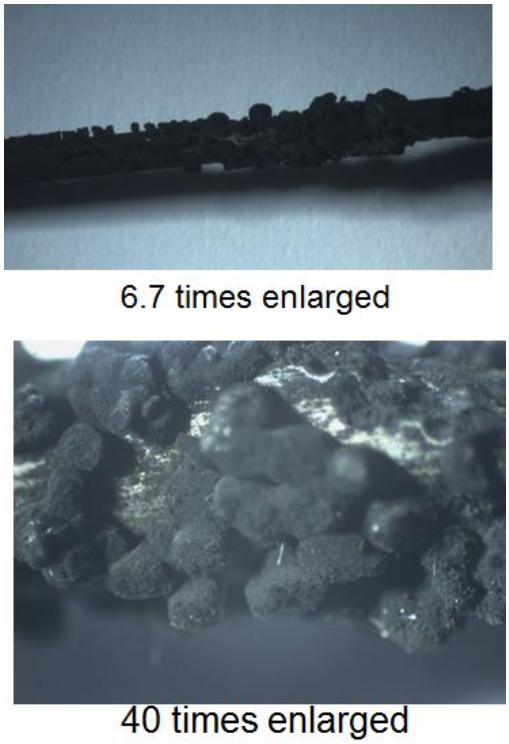

Figure 7.2: Details of carbon deposited on the thermocouple placed at the outlet of the reactor after C_3H_8 CPO test, equipped with FeCrAlloy filters calcinated at 950°C, at 4 bar for 12 hours. First row is 6.7 magnification, second row is 40 times magnification.

After 12 hours of C_3H_8 test the amount of carbon, collected on the flange surface , was 220 mg. Also on the glass fabric tape wrapped around the back heat shield, a "crust" of carbon deposited (20 mg) was observed.

7.2 POSSIBLE WAYS OF C-FORMATION

In light of the observed carbon deposition, it is interesting to further investigate the formation of C during C_3H_8-CPO tests. Initially we looked for possible ways of carbon formation. These following possible ways of carbon formation are proposed:

- **Carbon formation from olefins**: In literature [61,64] is reported a way of soot formation by condensation of olefinic species. In the chapter 6 the presence of olefins, in C_3H_8-CPO, was observed in the first section of the catalyst.

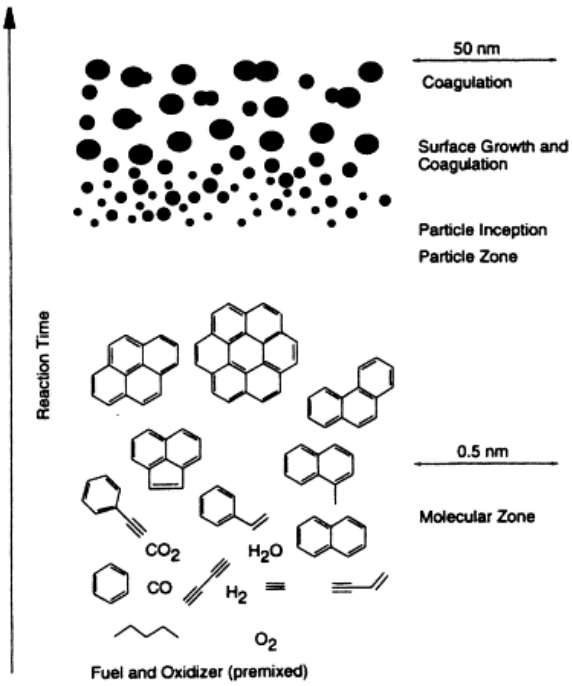

Figure 7.3: Soot formation from olefins to PAH [64].

However in the chapter 6 the consumption of the olefinic species, by gas phase reaction of condensation to soot precursors, was excluded. In fact the heterogeneous steam reforming was the predominant way of consumption of these species (chemical quench of the catalyst).

- **C_1 to Carbon**: analyzing the gas composition downstream from the catalyst, the only sources of carbon is the CH_4 and CO. A typical composition of C_3H_8 CPO at 4 bar is shown in Table 7.1.

	C_3H_8	O_2	H_2	CO	H_2O	CO_2	CH_4
xi [%]	0	0	21,68	16,72	2,47	1,84	0,21
Pi [bar]	0	0	0,864	0,669	0,099	0,074	0,008

Table 7.1: Typical values of composition outside the catalyst.

In literature [66], the following reactions, which involved the CH_4 or CO, are reported:

- Methane pyrolysis $CH_4 \rightarrow 2\ H_2 + C$;
- CO disproportionation $2\ CO \rightarrow CO_2 + C$.

A thermodynamic analysis is conducted to evaluate if the CH_4 pyrolysis and CO disproportionation reactions, which lead to carbon formation, are thermodynamically favored under the operating conditions adopted. Finally, the results of the characterization analysis performed on the carbon will be presented.

7.2.1 CARBON FORMATION FROM C_1: THERMODYNAMIC ANALYSIS

This paragraph reports the thermodynamic analysis of CH_4 pyrolysis and CO disproportionation in the C_3H_8-CPO test at 2 bar and in the C_3H_8-CPO test at 4 bar.
Kp was estimated through the following expression:

$$K_p = \prod_{i=1}^{NC} P_i^{vi} \tag{7.1}$$

Kp is simply calculated from the measured species profiles, as the product of the partial pressure which are elevated to their relatives stoichiometric coefficients.
Keq is evaluated from the measured gas temperature profile as:

$$K_{eq}(T) = \exp\left(-\frac{\Delta G_R^{\circ}}{RT}\right) \tag{7.2}$$

The ratio, between Kp and Keq, shows that:

- Kp/Keq < 1 which indicates a thermodynamic driving force for the direct reaction;
- Kp/Keq = 1 which indicates the reaching of the equilibrium state;
- Kp/Keq > 1 which indicates a thermodynamic driving force for the reverse reaction.

METHANE PYROLYSIS

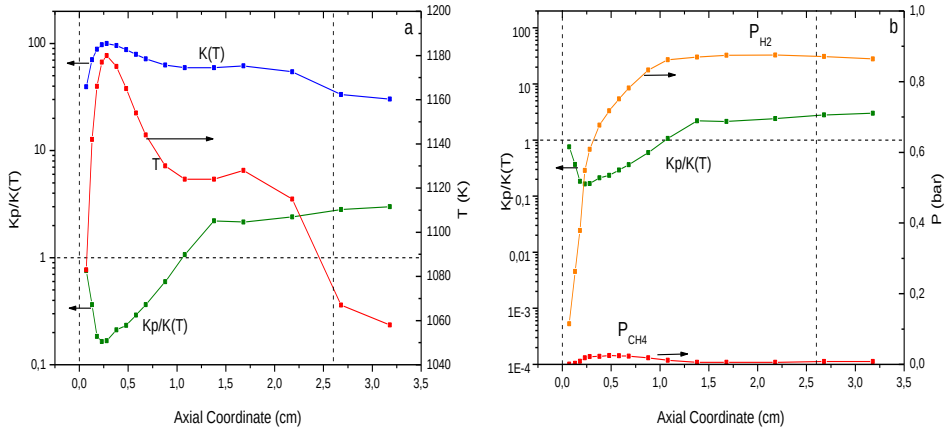

Figure 7.4: Thermodynamic Analysis of methane pyrolysis in C_3H_8-CPOat 4 bar, panel a shows the trend of: Keq (blue line), T_{gas} (red line) and Kp/Keq ratio (green line); panel b shows the trend of: partial pressure of hydrogen (orange line) and methane (red line). Honeycomb monolith, Sample FHS 6. Operating conditions: autothermal, C/O=0.85, 10 Nl min^{-1} flow rate, Tin = 25°C.

Figure 7.4 shows the thermodynamic analysis of the methane pyrolysis reaction during the C_3H_8-CPO test at 4 bar. In the first part of the catalyst (from 0 to 1cm), the Kp/Keq ratio (green line) is lower than the unit value, this means that the methane pyrolysis is thermodynamically favored. In the second part of the catalyst (from 1 cm), the Kp/Keq ratio is greater than one, this means the methane pyrolysis is not thermodynamically favored, whereas the reverse reaction is favored.

Figure 7.5 shows the thermodynamic analysis of the methane pyrolysis in C_3H_8 CPO at 2 bar.

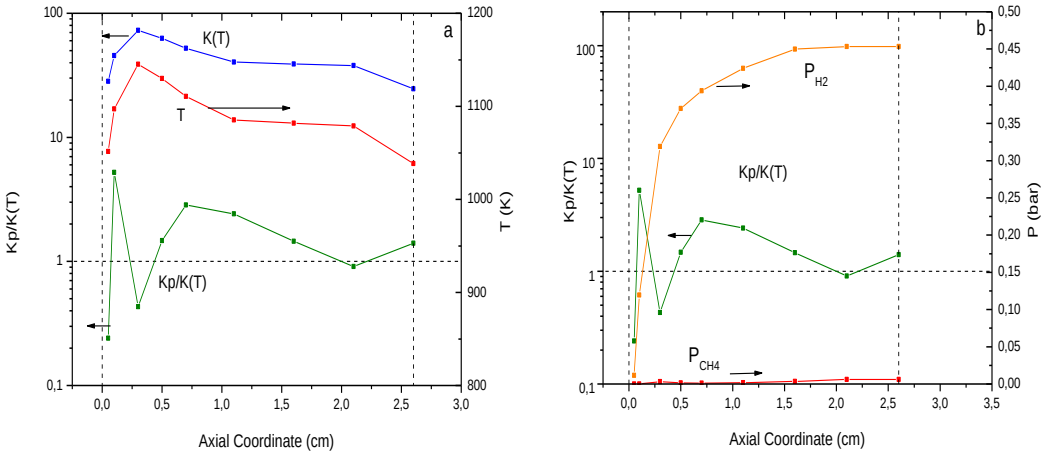

Figure 7.5: Thermodynamic Analysis of methane pyrolysis in C_3H_8-CPO at 2 bar, panel a shows the trend of: Keq (blue line), T_{gas} (red line) and Kp/Keq ratio (green line); panel b shows the trend of: partial pressure of hydrogen (orange line) and methane (red line). Honeycomb monolith, Sample FHS 6. Operating conditions: autothermal, C/O=0.85, 10 Nl min^{-1} flow rate, Tin = 25°C.

Figure 7.5 shows the thermodynamic analysis of the methane pyrolysis reaction during the C_3H_8-CPO test at 2 bar. In this case the Kp/Keq ratio (green line) is greater than one along only the catalyst length, this means the methane pyrolysis is never thermodynamically favored, whereas the reverse reaction is favored.

CO DISPROPORTIONATION

Afterwards, the thermodynamic analysis on CO disproportionation is carried out. Figure 7.6 reports the behavior of Kp/Keq ratio in C_3H_8 CPO at 4 bar.

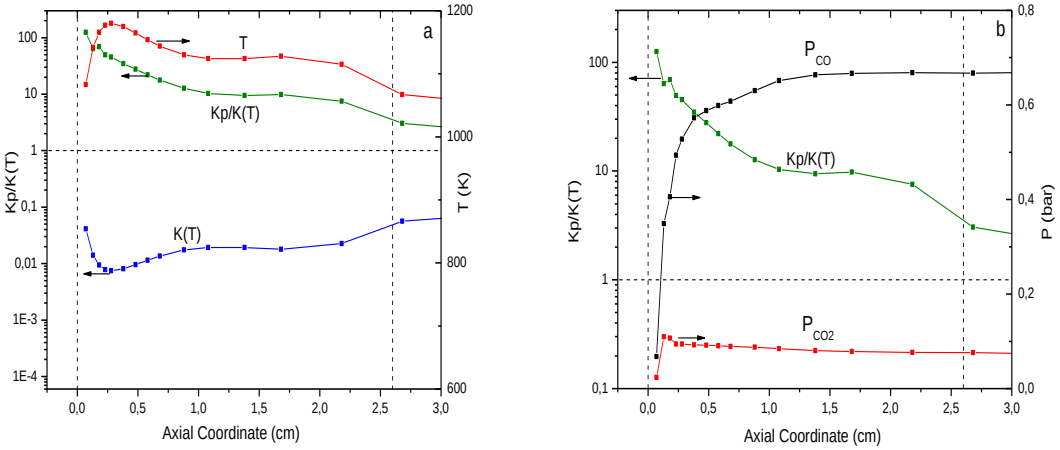

Figure 7.6: Thermodynamic Analysis of CO disproportionation in C_3H_8-CPO at 4 bar, panel a shows the trend of: Keq (blue line), T_{gas} (red line) and Kp/Keq ratio (green line); panel b shows the trend of: partial pressure of hydrogen (orange line) and methane (red line). Honeycomb monolith, Sample FHS 6. Operating conditions: autothermal, C/O=0.85, 10 Nl min^{-1} flow rate, Tin = 25°C.

The thermodynamic analysis shows than the Kp/Keq ratio (green line) is always higher than one along the catalyst axis, with a decreasing trend associated to the temperature (Figure 7.6 panel a). Because the composition downstream the catalyst is constant, and the temperature displays a decreasing trend, the Kp/Keq ratio probably drops below the value of one and this reaction may become thermodynamically favored.

The trend of CO disproportionation has also been studied at 2 bar, Figure 7.8.

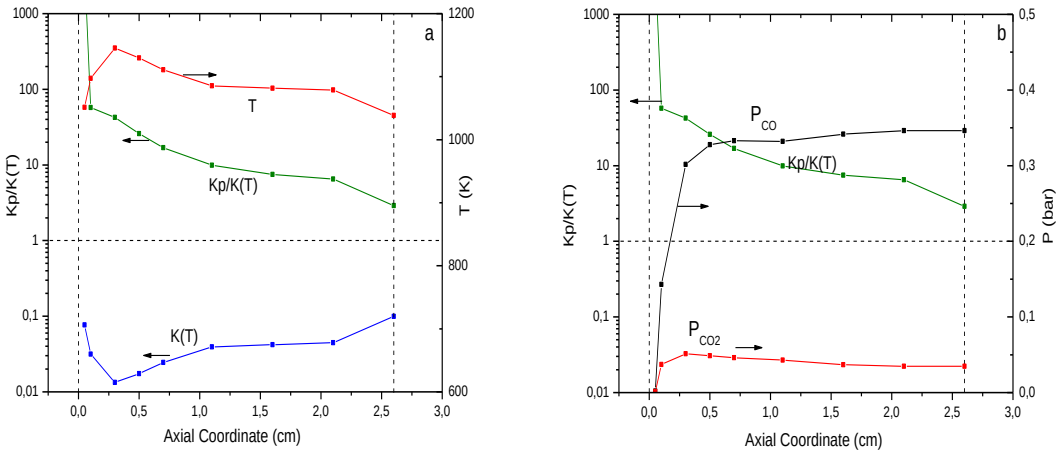

Figure 7.7: Thermodynamic Analysis of CO disproportionation in C_3H_8-CPO at 2 bar, panel a shows the trend of: Keq (blue line), T_{gas} (red line) and Kp/Keq ratio (green line); panel b shows the trend of: partial pressure of hydrogen (orange line) and methane (red line). Honeycomb monolith, Sample FHS 6. Operating conditions: autothermal, C/O=0.85, 10 Nl min^{-1} flow rate, Tin = 25°C.

The trend of Kp/Keq ratio at 2 bar is the same of the one at 4 bar. Also at 2 bar it appears that the behavior is related to the trend of the temperature, and downstream the catalyst, where the temperature decreases, there is a driving force to the direct reaction of CO disproportionation. That is the reason why in conclusion, the disproportionation of CO is a possible way of carbon deposition.

Indeed, during a C_3H_8-CPO test at 4 bar, the temperature, downstream the quartz tube (near the flange) was measured with the backside thermocouple to demonstrate if one of the reaction described before is effectively favorite. The temperature resulted be equal to 670 °C. At this temperature, the Kp/Keq ratio results equal to:

- 1.6 for the CH_4 pyrolysis reaction;
- 0.3 for the CO disproportionation.

For this reason the carbon formation is probably due only to CO disproportionation reaction.

7.3 CARBON COLLECTION

In this paragraph different kinds of filters are used in order to collect carbon. The aim of these tests was the analysis of the carbon deposits in order to understand its chemical composition and its crystallographic structure. Two different kind of filters were used:

- Industrial FeCrAlloy® (Fe, Cr=20-24%,Al=4.8-5.5%, Y trace) filters;
- Homemade ceramic filters;

We used the FeCrAlloy filters due to their high filtering capacity [68], these filters consist of FeCrAlloy fibers closely packed in the form of a mat of 1 mm in thick, this was cut to have disks suitable to be placed in the quartz tube, downstream of the BHS. The physical proprieties of the FeCrAlloy filters are reported in the Table 7.2:

ε[-]	0.86
Φ_{av}[μm]	25.2
A_{spec}[cm^2/cm^3]	223.86

Table 7.2: Physical proprieties of FeCrAlloy filters.

This filters were calcined in order to avoid the catalytic effect, in carbon formation reactions, by the metallic surface: the calcination produced a thin layer of α-Al_2O_3. We made the homemade ceramic filters in order to avoid the catalytic phenomena described before.

The reactor configuration, which used in this test, is reported in Figure 7.8.

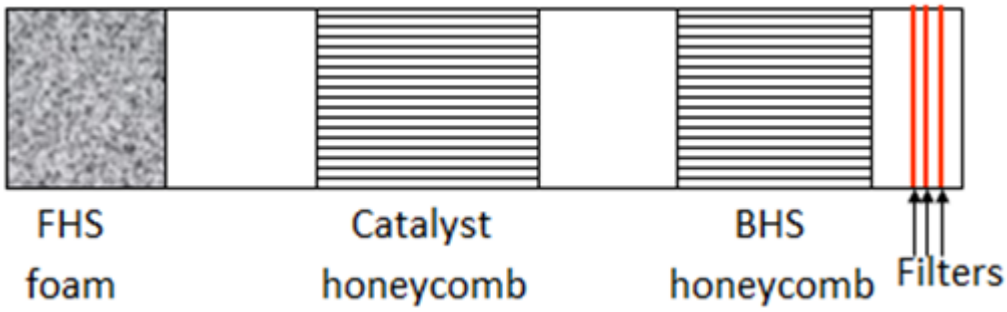

Figure 7.8 :Reactor configuration.

Following the results, with the different type of filters, will be displayed.

FeCrAlloy filters calcined at 950°C:

The filters were first cleaned in ethanol in an ultrasound bath in order to eliminate the impurities, then they are dried at 110°C for 20 minutes in air. Finally the filters were calcined at 950°C for 10 hours (temperature ramps 5 °C/min) under air circulation.

After the preparation of filters, a C_3H_8 CPO test was performed at 4 bar for 7 hours. The configuration is shown in Figures 7.9.

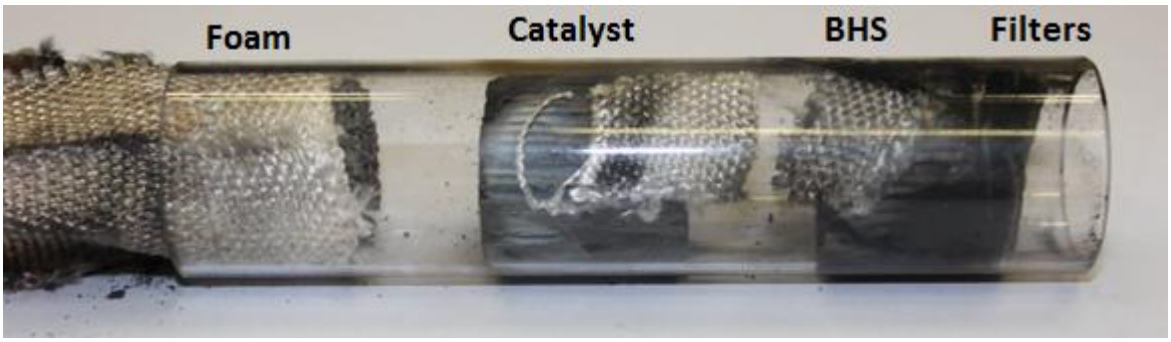

Figure 7.9: Quartz reactor after C_3H_8 CPO test at 4 bar for 7 hours with FeCrAlloy filters calcined at 950°C.

The Figure 7.9 shows a carbon deposit between the catalyst and the BHS, and also in the outside of the quartz reactor (right side).

Filters were extracted and analyzed at the optical microscope to verify the morphology of carbon deposits.

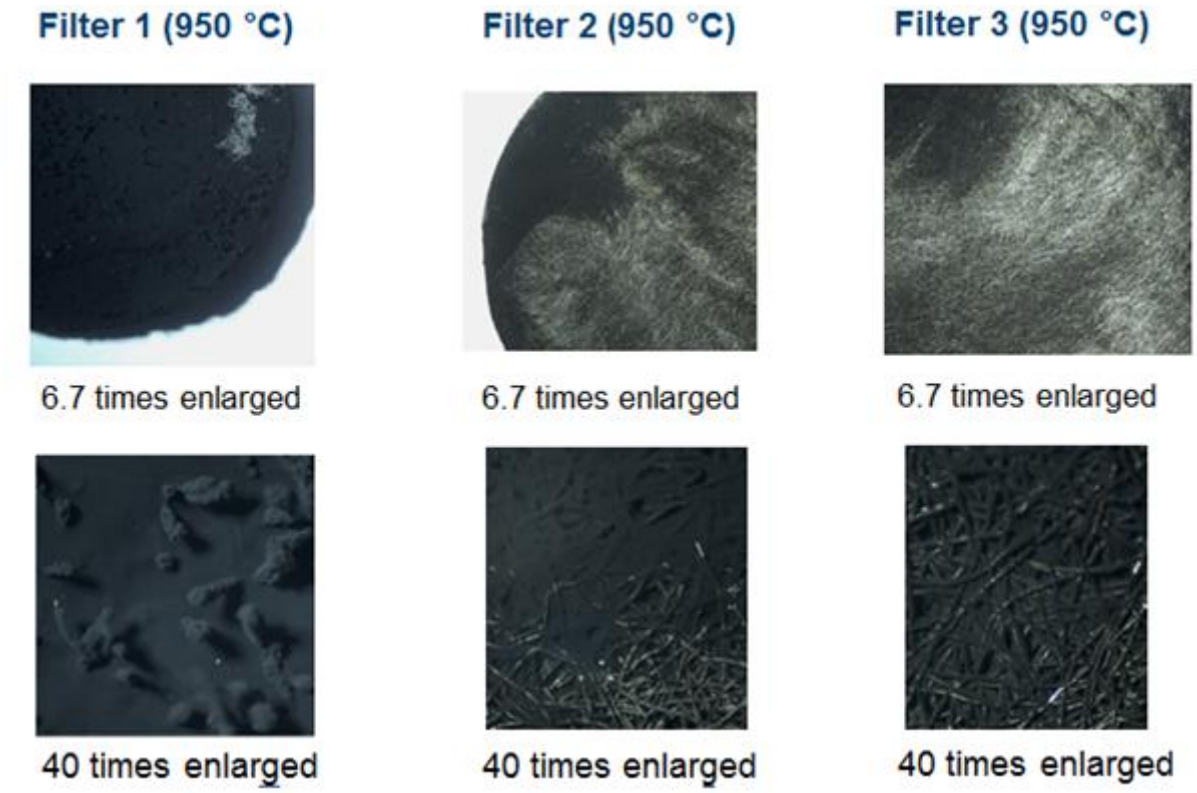

Figure 7.10: Details of the filters calcined at 950°C after a C_3H_8-CPO at 4 bar for 7 hours. First row is 6.7 magnification, second row is 40 times magnification.

As shown in Figure 7.10, a coke cake was formed on the first filter; second and third filters were also coked on the edges, this was due to the preferential pathways at the edge of the quartz tube, where the pressure drops were lower. The large amount of coke deposits on these filters was due to a low temperature used to calcine them in fact, the literature [68] reports that, at this temperature, the quantity of α-Al_2O_3 is not sufficient to cover the filter surface.

FeCrAlloy filters calcined at 1100°C:

The FeCrAlloy filters were calcined at 1100°C under air circulation for 10 hours (temperature ramp 5 °C/min), in order to form an adequate layer of α-Al_2O_3 to cover the entire surface of the filters [68].

After the calcination, a C_3H_8 CPO test was carried out at 4 bar for 7 hours. The configuration is shown in Figures 7.11.

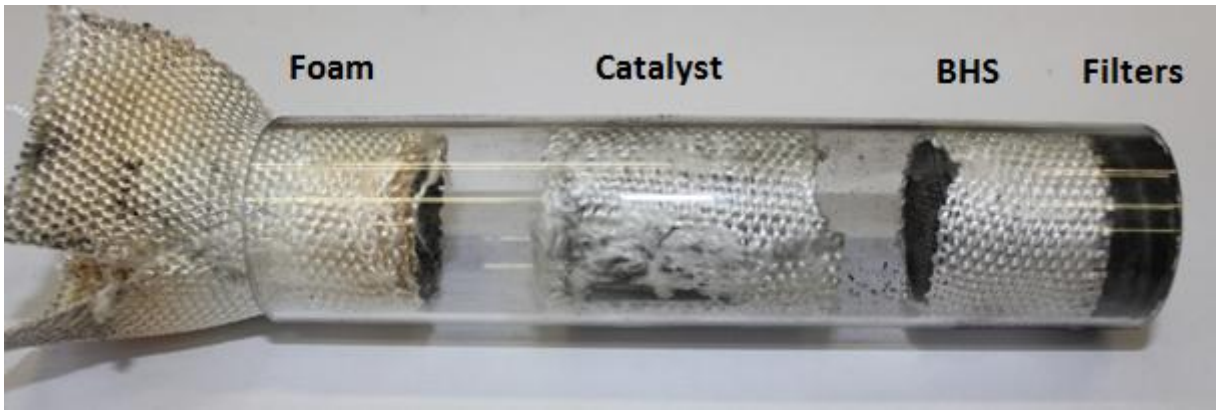

Figure 7.11: Quartz reactor after C_3H_8 CPO test at 4 bar for 7 hours, with FeCrAlloy filters calcined at 1100°C.

After the C_3H_8 CPO test, the quartz tube is cleaner than the one described before. Also in this configuration there is a presence of soot between the catalyst and the BHS.

Filters were extracted and analyzed at the optical microscope to verify the morphology of carbon deposits.

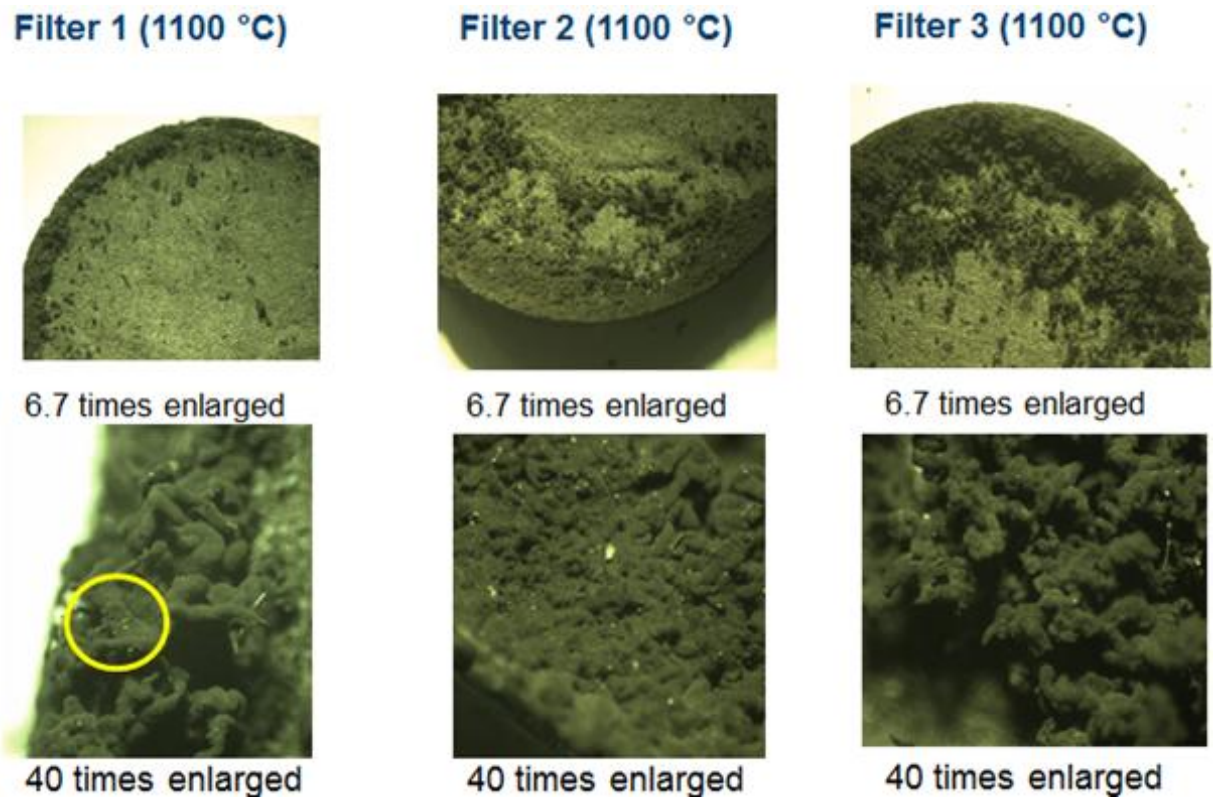

Figure 7.12: Details of the filters calcined at 1100°C after a C_3H_8-CPO at 4 bar for 7 hours. First row is 6.7 magnification, second row is 40 times magnification.

In this case the layer of α-Al_2O_3 resulted more efficient than the filters previously showed in fact the amount of carbon deposits was lower. A small amount of carbon was observed only on the edges of filters, this was probably due to the destruction of α-Al_2O_3 layer during the preparation of the system before the test.

γ-Al_2O_3 coated FeCrAlloy filters

After the calcination at 1100°C, the FeCrAlloy filters were coated with 10% wt/wt disperal (bohemite gel), the residue was drained from pores by putting filters in a bűchner funnel and this is connected to a vacuum pump. After the filters were dried at 110°C for 1 hour and calcinated at 700°C for 10 hours (temperature ramp 10 °C/min) under air circulation. This procedure lead to the formation of a thin film of γ-Al_2O_3 on the filter surface in order to better inertize the filters.

After the calcination, a C_3H_8 CPO test was carried out at 4 bar for 7 hours. The configuration is shown in Figures 7.13.

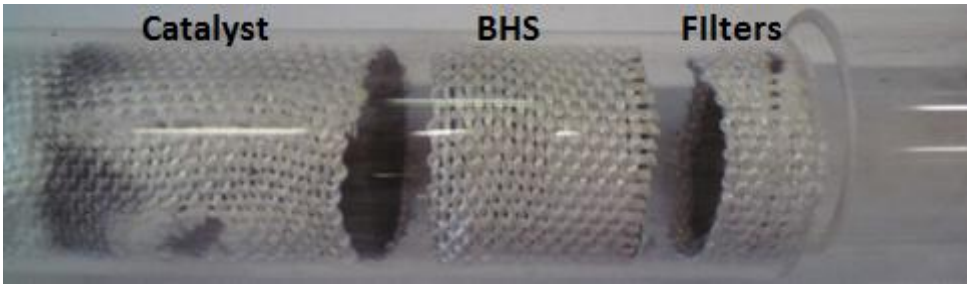

Figure 7.13: Quartz reactor after C_3H_8 CPO test at 4 bar with FeCrAlloy filters calcined at 1100°C and coated with γ-Al_2O_3.

Filters were extracted and analyzed at the optical microscope to verify the morphology of carbon deposits.

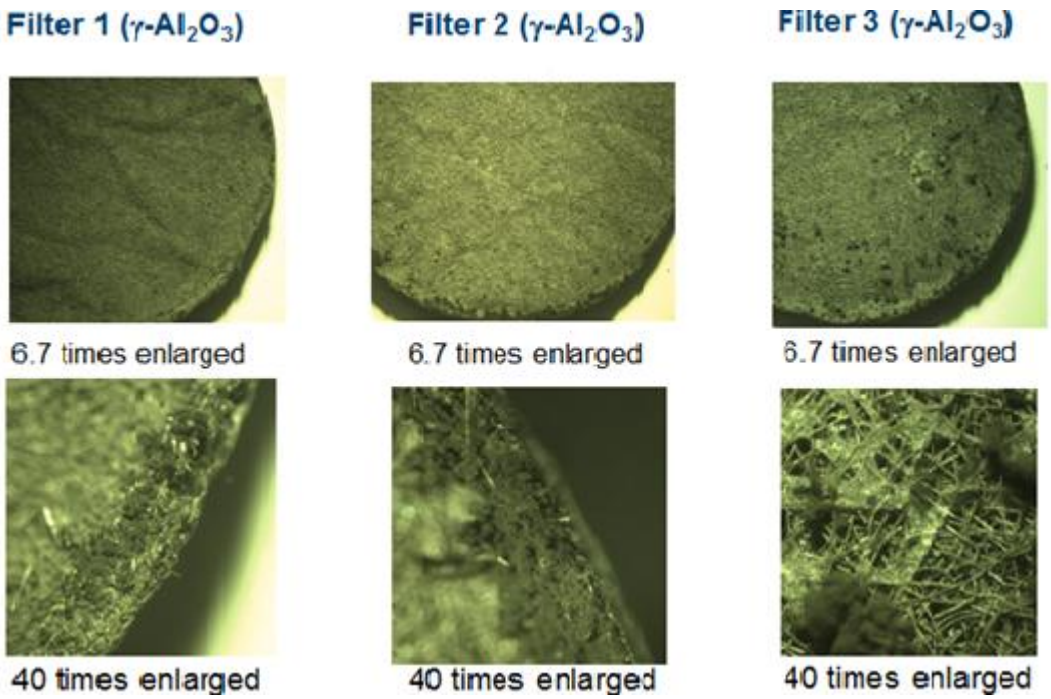

Figure 7.14: Details of the filters calcined at 1100°C after a C_3H_8-CPO at 4 bar for 7 hours. First row is 6.7 magnification, second row is 40 times magnification. The filters are coated with γ-Al_2O_3 prior to the use.

In this case the layer of γ-Al_2O_3 resulted more efficient than the filters previously showed in fact the amount of carbon deposits was lower. A very little amount of carbon was observed only on the edges of filters, for the same reason described in FeCrAlloy filter calcined at 1100 °C.

Homemade ceramic filters

Ceramic filters were homemade by using the glass fabric tape. The idea was to realize a filter with completely metal-free surface. The glass fabric tape is inert and fireproof up to high temperatures. A piece of glass fabric tape was wrapped up on an inert support of cordierite. Figure 7.15 reports the configuration of the system with the glass filters.

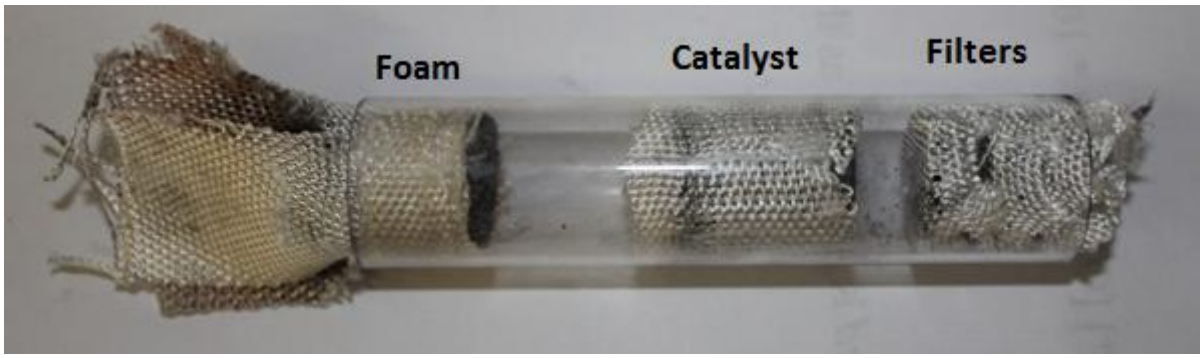

Figure 7.15: Quartz reactor after C_3H_8 CPO test at 4 bar with homemade ceramic filters.

Filters were extracted and analyzed at the optical microscope to verify the morphology of carbon deposits.

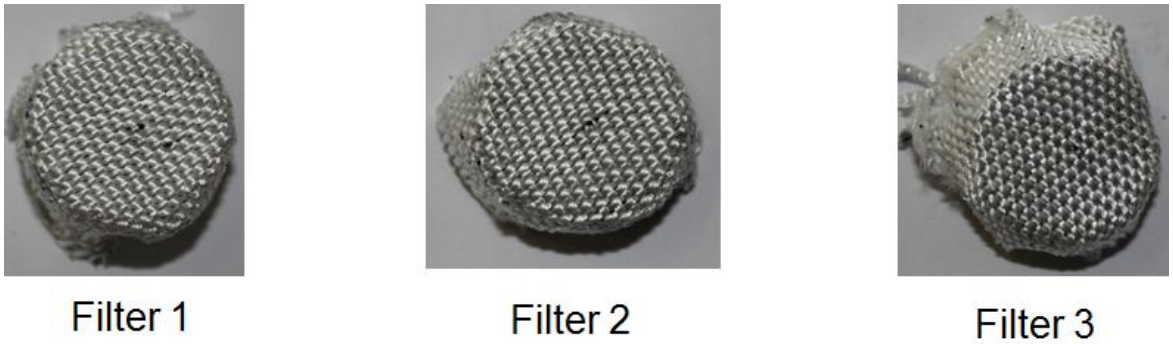

Figure 7.16: Details of the homemade ceramic filters after a C_3H_8 CPO test at 4 bar .

In this case, no carbon deposits were found.

The Figure 7.17 summarize the carbon deposition on the filters with different inert surface.

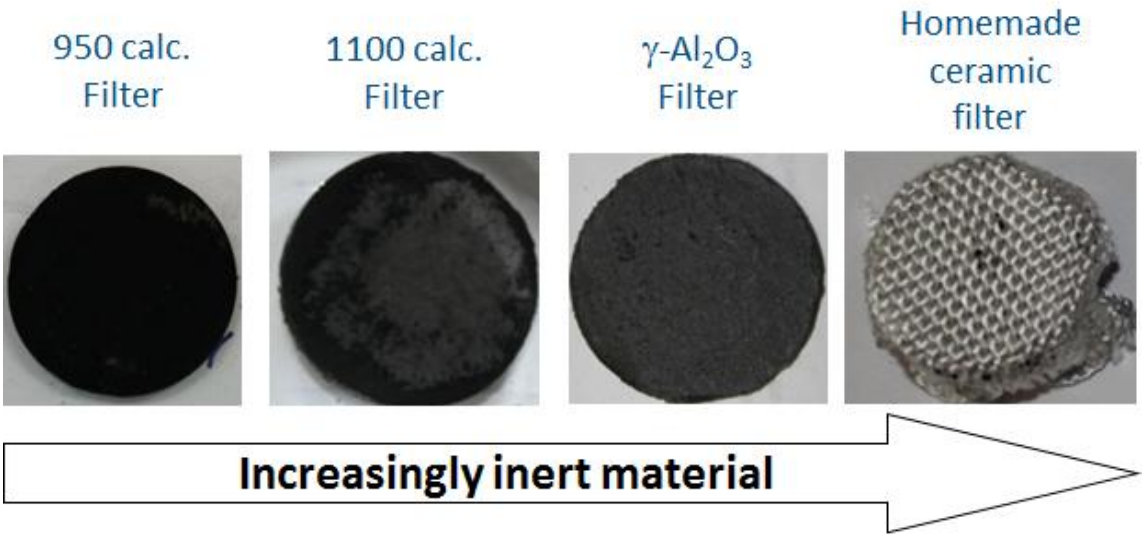

Figure 7.17: Carbon deposition on the filters with different inert surface.

These tests shows that the metallic surfaces (like Ni and Fe) are required to generate the c-deposits. Despite that the reactor and the lines are made of stainless steel, aging and mechanical treatments (grinding, scratching) had created catalytically active sites.

7.4 CHARACTERIZATION OF C-DEPOSITS

After the C_3H_8 CPO at 4 bar with filters, the samples of carbon deposit were analyzed through TPO analysis, Raman analysis and XRD analysis. The purpose of these tests is to know the type of deposit to better understand the mechanism of formation. Initially a TPO analysis was performed:

Temperature-programmed Oxidation (TPO):

Temperature-programmed Oxidation (TPO) is a technique for the characterization of solid materials and is often used in the field of heterogeneous catalysis to find the most efficient oxidative conditions and the oxidation behavior of a sample, the sample is submitted to a programmed temperature rise while a oxidative gas mixture is flowed over it. The analysis was performed with the following operating conditions:

- C_{O2}=2% v/v with He complementary gas;
- Q= 98 cc min^{-1} total flow;
- Tstart= 40°C;
- Tfinal=1050°C;
- ΔT = 10°C min^{-1}

The graph shows a signal in mV (correlated to the concentration of the oxygen) linked to temperature.

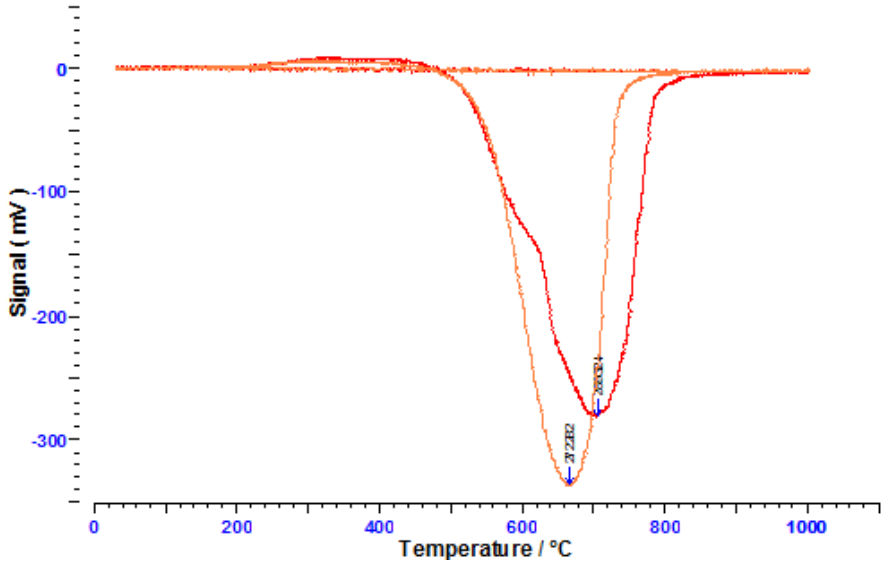

Figure 7.18: TPO Analysis: comparison between an artificial soot as reference (orange signal) and the sample collected at the external part of the reactor after the test with FeCrAlloy Filters calcined.(red signal) Operating Conditions: C_{O2}=2% v/v with He complementary gas; Q= 98 cc min^{-1} total flow; Tstart= 40°C; Tfinal=1050°C; ΔT = 10°C min^{-1}.

The test (Figure 7.18) shows the sample analysis and the comparison with a sample of artificial soot as reference. The test shows that the curve of the sample is similar to the curve of reference, however the sample collected, differently from the reference sample, shows a presence of two peaks, this means the carbon deposit has an heterogeneous structure.

XRD analysis:

The next Figure shows a XRD analysis (described in chapter 2): with this test is possible to analyze the type of crystalline structure of the sample,

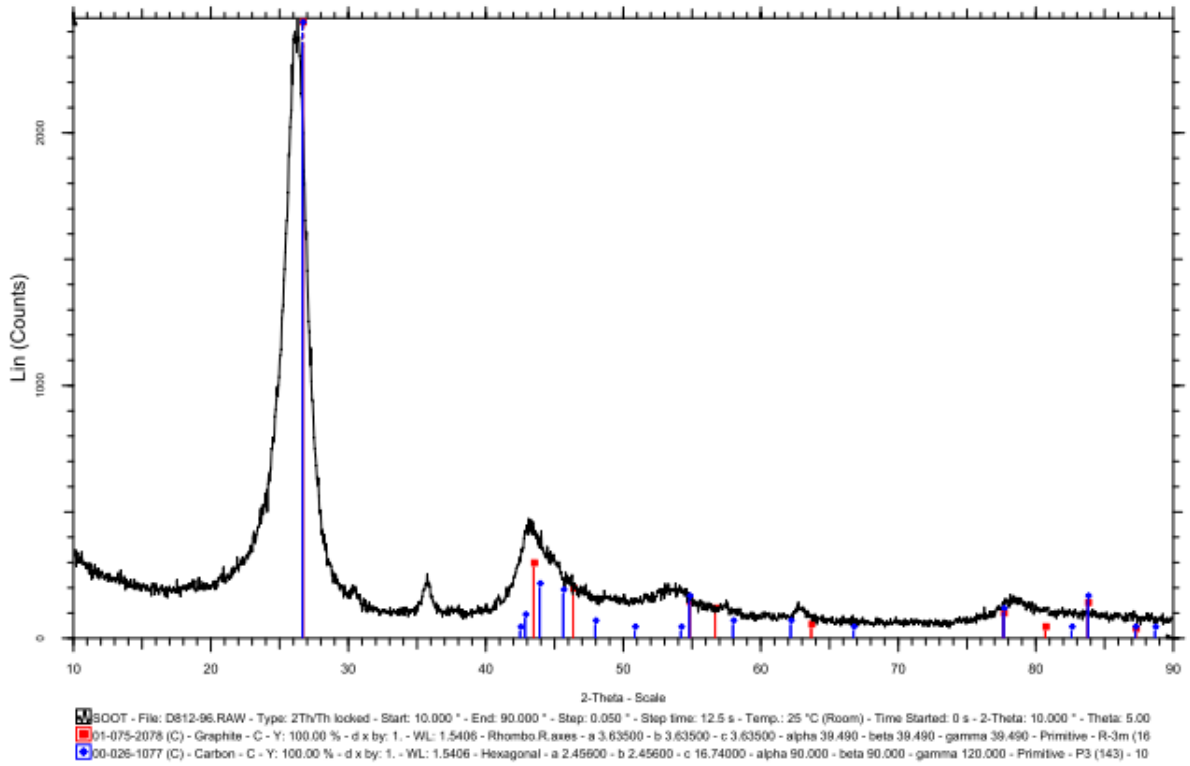

Figure 7.19: XRD analysis : Sample collected after C_3H_8-CPO test (with FeCrAlloy filters calcined at 950°C) at 4 bar for 7 hours. The Sample is collected in external part of the reactor.

A diffraction pattern is obtained by measuring the intensity of scattered waves as a function of scattering angle (2 θ). The analysis was performed on the sample, which was collected on the flange surface, after a C_3H_8-CPO test (with FeCrAlloy filters calcinad at 950°C) at 4 bar for 7 hours. The analysis shows that the peaks occur in close correspondence of the reflex of amorphous carbon and graphitic carbon. The broad peaks suggest also that the carbon deposit is mostly in an amorphous form.

Raman spectroscopy:

After the XRD analysis a Raman spectroscopy analysis was performed.
Raman analysis is a spectroscopic technique used to study vibrational, rotational, and other low-frequency modes. It relies on inelastic scattering, or Raman scattering, of monochromatic light, usually from a laser in the visible, near infrared, or near ultraviolet range. The laser light interacts with molecular vibrations, phonons or other excitations in the system, resulting in the energy of the laser photons being shifted up or down. The shift in energy gives information about the vibrational modes in the system.
The operating conditions of the analysis are the following:

- Red laser excitation wavelength = 785 nm;
- Resolution = 5 cm^{-1};
- Spectral range = 175 – 3200 cm^{-1}.

The Raman analysis displayed different types of peaks that describe the different morphology of carbon [69]:

- D peak (Disorder, 1350 cm^{-1} of wave length) identifies the presence of amorphous carbon;
- G peak (Graphite, 1575 cm^{-1} of wave length) identifies the presence of graphitic structures;
- RBM (Radial Breathing Mode, 200-400 cm^{-1} of wave length) peaks show the presence of nanotubes.

Figure 7.20 shows the results obtained with the sample, collected downstream the quartz tube (near the flange):

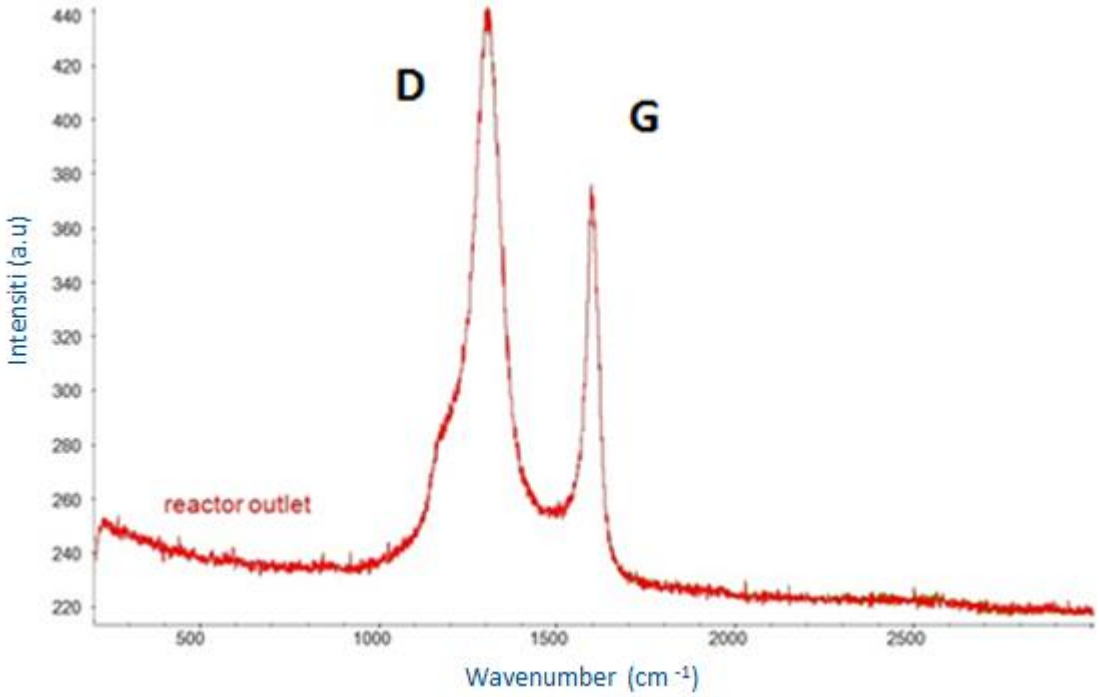

Figure 7.20: Raman spectroscopy analysis of a sample collected at the outlet of the reactor after a C_3H_8-CPO test at 4 bar with FeCrAlloy Filters calcined at 950°C. D-peak at 1350 cm^{-1} of wave length , G-peak at 1575 cm^{-1} of wave length . Operating Conditions: 785 nm of laser wavelength; resolution 5 cm^{-1} ;Spectral range 175-3200 cm^{-1}.

This analysis shows that the sample is composed by an amorphous carbon and graphite, the absence of the peaks in the region between 200-400 cm^{-1} of wave length, suggest that the nanotubes were not formed.

CONCLUSION

In this work, we address an experimental and theoretical investigation of the CH_4-CPO and C_3H_8-CPO reformer over Rh-supported honeycomb catalysts under pressurized conditions. The purpose of the study is the characterization of the effect of the pressure on the performances of the CPO reformer. The tests were performed at 10 Nl min^{-1} flow rate by maintaining the C/O ratio at 0.9 for CH_4-CPO and at 0.85 for C_3H_8-CPO and at progressively increasing pressure from 1 to 4 bar.

The study was performed with the application of the spatially sampling technique and by analyzing the results with a mono-dimensional, dynamic, adiabatic, heterogeneous model of the reactor, incorporating the role of homogeneous reactions.

The experimental data, displayed in chapter 5-6, showed that the pressure influenced only the second part of the catalyst (from 0,6 mm) in which the temperatures and the concentration profiles reached the thermodynamic equilibrium value. However, in the first part of the catalyst, where the evolution of the profiles was controlled by kinetics, the pressure did not have any remarkable effects on the temperatures and on the concentration profiles. The modeling analysis, based on independently validated kinetic scheme, allowed to comprehend the nature of the observed phenomena. During our work, we reached the following conclusions:

- O_2 consumption is totally limited by external mass transfer;
- CH_4 and C_3H_8 consumptions are mainly limited by external mass transfer in the first part of the catalyst;

Under constant mass flow rate, the gas-solid diffusion rate is totally independent from the pressure.

The C_3H_8-CPO experiments at increasing pressure verified the hypothesis of the presence of the homogeneous chemistry in the first part of the catalyst. In fact, increasing concentrations of intermediates species (hydrocarbon C_{2+}) linked to the rise of pressure is an indicator of the presence of the homogeneous chemistry ($\propto P^2$). Afterward, a specific test highlighted the role of the catalyst in the consumption of the hydrocarbon species. This test was carried out to understand the mechanism of consumption of the hydrocarbon species. The experiment was

performed with a short catalyst and high flow rate to avoid the expected consumption of the hydrocarbon species by heterogeneous steam reforming on the catalyst surface. During this test, the trend of the hydrocarbon species had experimentally confirmed the consumption of hydrocarbon species is due to the steam reforming reactions on the catalyst surface. Therefore the catalyst acts as a chemical quench: the gas stream is cleaned from precursors of soot by the catalyst surface. This is an important conclusion for a scale-up of this technology on a large scale, because the deactivation of the catalyst by carbon deposits (fouling) could compromise the lifetime of the catalyst.

During the C_3H_8-CPO tests under pressurized conditions, we observed an increase of the carbon deposits. For this reason, the carbon deposits was collected and analysed. Also thermodynamic analysis was carried out to better understand this phenomenon.

Nevertheless the reactor and the lines downstream of the metal case are made by stainless steel, aging of the system (thermal and mechanical stress) had entailed the formation of catalytically active sites (Ni, Fe), which catalyse to the formation of carbon deposits.

After the morphological analysis and thermodynamics analysis, we reached the following conclusions on the carbon formation:

- CH_4 pyrolysis reaction is not thermodynamically favoured downstream the catalyst;
- CO disproportionation reaction is thermodynamically favoured downstream the catalyst;
- The metallic surfaces catalyse the reaction of carbon formation;
- The coke deposits are mainly constituted by amorphous carbon and graphite.

BIBLIOGRAPHY

[1] Sergio Carrà -*Energia* - Storia della scienza, Enciclopedia Treccani.

[2] http://www.iea.org.

[3] A.P.E York, T. Xiao, and M.L.H. Green - *Brief overview of partial oxidation of methane to synthesis gas.* - Topics in Catalysis, 22 (2003).

[4] S.S. Bharadwaj L.D. Schmidt - *Catalytic partial oxidation of natural gas to syngas.* -Fuel Proc. Techn. 42, 109-127 (1995).

[5] *Enciclopedia degli idrocarburi.*

[6] K. Aasberg-Petersen, I. Dybkiaer, C.V. Ovensen, NC. Schodt, J. Sehested, S.G.Thomsen - *Natural gas to synthesis gas-catalyst and catalytic process.* - Journal of Natural Gas Science and Engineering, 3 (2011), 423-459.

[7] Jacob A. Mounlijn, Michiel Makkee, Annelies Van Diepen - *Chemical Process Technology.* - Wiley.

[8] A. Beretta, I. Tavazzi, T. Bruno, G. Groppi, V. Dal Santo, L. Sordelli, C. Mondelli - *La produzione di idrogeno di piccola scala.* - La Chimica e l'Industria (2006).

[9] L. Maiocchi - *Ossidazione parziale di metano per la produzione del gas di sintesi su catalizzatori supportati a base di Rh*. - PhD thesis, Politecnico di Milano, 1999.

[10] H. Liander - Trans. Faraday Soc. 25, 462, 1929.

[11] C. Padovani, P. Facchinetti - Giorn. Chem. Ind. Appl. Catal. 15, 429, (1933).

[12] M. Prettre, Ch. Eichner and M. Perrin - Trans Faraday Soc. 42, 335, 1946.

[13] K. Huszar, G. Racz, G. Szekely. *Investigation of the partial catalytic oxidation of methane, conversion rates in a single-grain reactor*. - Acta Chim. Acad. Sci. Hungar, 70:287-299, 1971.

[14] D.A Hickman, L.D. Schimdt – *Synthesis gas formation by direct oxidation of methane over Pt monoliths* - J. Catal., 138, 267, 1992.

[15] D. A. Hickman, E. A. Haupfear, and L. D. Schmidt - *Synthesis gas formation by direct oxidation of methane over Rh monoliths*. - Catalysis letters 17, 223-237, 1993.

[16] Biorn Christian Enger, Rune Lodeng, Anders Dolmen - *A review of catalytic partial oxidation of methane to synthesis gas with emphasis on reaction mechanism over transition metal catalysts.* - Applied Catalyst A: General, 346, 2008.

[17] D.A. Hickman, L.D. Schmidt - AlChE J. 39 (1993), 1164.

[18] M. Hartmann, T. Kaltschmitt, O. Deutshmann - *Catalytic partial oxidation of higher hydrocarbon fuel components on Rh/Al_2O_3 coated honeycomb monolith* - Catalyst Today, 147S, 2009.

[19] I. Tavazzi, A. Beretta, G. Groppi, A. Donazzi, M. Maestri, E. Tronconi, and P. Forzatti- *Catalytic partial oxidation of CH_4 and C_3H_8: experimental and modeling study of the dynamic and steady-state behavior of a pilot-scale reformer* - Studies in Surface Scienceand Catalysis (167), 2007.

[20] D.A. Hickmann, L.D. Schmidt - Science 259, 1993, 343.

[21] P.D:F: Vernon, M.L.H. Green, A.K. Cheetham, A.T. Ashcroft - Catal. Lett. 6 (1990)181.

[22] Raimund Horn, Nick J. Degenstein, Kenneth A. Williams and Lanny Schmidt – *Spatial and temporal profiles in millisecond partial oxidation process*. - Catalysis letters, 110, 2006.

[23] R. Horn, K.A. William, N.J. Degenstein, L.D. Schmidt.- *Syngas by catalytic partial oxidation of methane: mechanism conclusion from spatially resolved measurement and numerical simulations* - Journal of Catalysis 242(2006), 92-102.

[24] R. Horn, K.A. William, N.J. Degenstein, L.D. Schmidt - *Mechanism of H_2 and CO formation in the catalytic partial oxidation on Rh probed by steady-state spatial profiles and spatially resolved transients* - Chemical Engineering Science 62, 2007, 1298-1307.

[25] R. Horn, K.A. William, N.J. Degenstein, A. Bitsch-Larsen, D. Dalla Nogare, S.A. Tupy, L.D. Schmidt - *Methane catalytic partial oxidation on autothermal Rh and Pt foam catalyst:*

oxidation and reforming zones, transport effects, and approach to thermodynamic equilibrium.- Journal of Catalysis 249 (2007), 380-393.

[26] Ivan Tavazzi, Alessandra Beretta, Gianpiero Groppi, Pio Forzatti - *Development of a molecular kinetic scheme for methane partial oxidation over a Rh/ α-Al_2O_3 catalyst* - Journal of Catalysis, 241, 2006, 1-13.

[27] J. Rostrup-Nielsen, K. Aaserberg- Handbook of fuel cells. Foundamentals, technologies and applications. – Volume 3: Fuel cell technology and applications: Part 1. Chapter 14 (John Willey & Sons, Ltd).

[28] Konrad Herbst , Gurli Mogensen, Florian Huber, Martin Østberg, Martin Skov Skjøth-Rasmussen – *Challenges in applied oxidation catalysis* – Catalysis Today 157 (2010), 297-302.

[29] K. Heitnes Hofstad, J. H. B. J. Hoebink, A. Holmen, and G. B. Marin – *Partial oxidation of methane to synthesis gas over rhodium catalysts* - Catalysis Today, 40:157– 170, 1998.

[30] E. P. J. Mallens, J. H. B. Hoebink, and G. B. Marin - *An investigation on the reaction mechanism for the partial oxidation of methane to synthesis gas over platinum* – Catalysis Letters, 3:291–304, 1995.

[31] K. Heitnes Hofstad, O. A. Rokstad, and A. Holmen - *Partial oxidation of methane over platinum metal gauze*- Catalysis letters, 36:25–30, 1996.

[32] K. Heitnes Hofstad, T. Sperle, O. A. Rokstad, and A. Holmen - *Partial oxidation of methane to synthesis gas over a Pt/10% Rh gauze* - Catalysis letters, 45:97–105, 1997.

[33] L. D. Schmidt and M. Huff. - *Partial oxidation of CH_4 and C_2H_6 over metal coated monoliths* - Catalysis Today, 21:443–454, 1994.

[34] J. C. Slaa, R. J. Berger, and G. B. Marin. - *Partial oxidation of methane to synthesis gas over Rh/ α- Al_2O_3 at high temperatures* - Catalysis Letters, 43:63–70, 1997.

[35] K. Heitnes Hofstad, S. Lindberg, O. A. Rokstad, and A. Holmen - *Catalytic partial oxidation of methane to synthesis gas using monolithic reactors* - Catalysis Today, 21:471–480, 1994.

[36] Ingrid Aartun, Bozena Silberova, Hilde Venvik, Peter Ptfeir, Oliver Gorke, Klaus Schurbert, Anders Holmen – *Hydrogen production from propane in Rh-impregnated metallic microchannel reactors and alumina foams* – Catalysis Today 105 (2005) 469-478.

[37] R. Mark Ormerod – *Solid fuel cells* – Chem. Soc. Rev., 2003, 32, 17-28.

[38] J. Ogrzewalla C. Severin, S. Pischinger - *Compact gasoline fuel processor for passenger vehicle APU.* - Journal of Power Sources, 145:675–682, 2005.

[39] Walter Ray Laster – *Catalytic combustion in large frame industrial gas turbines.*

[40] M. Lualdi - *High temperature catalytic processes for energy applications*- Master's thesis, Politecnico di Milano, 2007.

[41] M. Valentini - *Deposizione di strati catalitici a base di γ-Al_2O_3 e ZrO_2 su sopporti ceramici e metallici per applicazioni industriali* - Tesi di Dottorato presso il Politecnico di Milano, 2001.

[42] I.M. Axelsson, L. Lonwedndahl, J. E. Otterstedt – Appl. Cat. 44 (1988), 251.

[43] M. Maestri.- *Modellazione matematica di reattori autotermici a letto fisso per l'ossidazione parziale di metano* - PhD thesis, Politecnico di Milano, 2004.

[44] K. B. Bischoff and G. F. Froment - *Chemical Reactors Analysis and Design* - Wiley and Sons, 1979.

[45] M. Bizzi, L. Basini, G. Saracco, and V. Specchia - *Modeling a transport phenomena limited reactivity in short contact time catalytic partial oxidation reactors* - Industrial & Engineering Chemistry Research, 42:62 –71, 2002.

[46] A. Frassoldati, T. Faravelli, E. Ranzi - International Journal of Hydrogen Energy 31(2006) 2310-2328.

[47] O. Deutscmann, LD Schmidt - AlCHE Journal 44 (1998) 2465-2477

[48] R. J. Kee, F. M. Rupley, and J. A. Miller. *The CHEMKIN thermodynamic data base.* Technical report, Sandia National Laboratories, 1987.

[49] D. Manca, G. Buzzi-Ferraris, T. Faravelli, and E. Ranzi - *Numerical problems in the solution of oxidation and combustion problems* - Combustion Theory and Modelling, 5:185–199, 2001.

[50] http://www.chem.polimi.it/homes/gbuzzi.

[51] A. Donazzi, A. Beretta, G. Groppi, and P. Forzatti - *Catalytic partial oxidation of methane over a 4% Rh/ α - Al_2O_3 catalyst: Part I: Kinetic study in annular reactor* – Journal of Catalysis, 255:241–258, 2008.

[52] A. Donazzi, A. Beretta, G. Groppi, and P. Forzatti - *Catalytic partial oxidation of methane over a 4% Rh/ α - Al_2O_3 catalyst: Part II role of CO_2 reforming* – Journal of Catalysis 255 (2008), 259-268.

[53] M.Maestri, D.G. Vlachos, A. Beretta, G. Groppi, E. Tronconi – AlChE Journal 55 (2009) 993-1008.

[54] A.B. D.G. Vlachos – Journal of Physical Chemistry B 109 (2005), 16819-16835.

[55] Salvatore Belcastro, Davide Pagani – *Ossidazione parziale e steam reforming di propano su catalizzatori Rh/ α -Al_2O_3* –Tesi di Laurea specialistica, Politecnico di Milano 2010.

[56] S. T. Lee and R. Aris - *On the effects of radiative heat transfer in monoliths* -Chemical Engineering Science, 32:827–837, 1977.

[57] A. Urakawa. A. Baiker – Top Catal. 52 (2009) 1312-1322.

[58] Alessandro Donazzi, Dario Livio, Alessandra Beretta, Gianpiero Groppi, Pio Forzatti - *Surface temperature profiles in CH4 CPO over honeycomb supported Rh catalyst probed with in situ optical pyrometer.* - Applied Catalysis A: General.

[59] Instalments of the course “Misure e strumentazione Industriale”.

[60] Susanne Dalley – *Pyrometer handbook*- Mikron Infrared.

[61] H. Richter, J.B. Howard - *Formation of polycyclic aromatic hydrocarbons and their growth to soot—a review of chemical reaction pathways* - Progress in Energy and Combustion Science 26 (2000) 565–608.

[62] http://navier.engr.colostate.edu/tools/equil.htm.

[63] S. Ding, Y. Yang, Y, Jin and Y. Cheng - Ind Eng. Chem. Res. 48 (2009) 2878.

[64] G. Bozzano, M. Dente, T. Faravelli, E. Ranzi - *Fouling phenomena in pyrolysis and combustion processes* - Applied Thermal Engineering 22 (2002) 919–927.

[65] T. Faravelli, A. Goldaniga, E. Ranzi - *Kinetic modeling of soot precursors in ethylene flames*, Proc. Comb. Instit - 27 (1998) 1489–1495.

[66] John B. Claridge, Malcolm L.H. Green, Shik Chi Tsang, Andrew P.E. York, Alexander T. Ashcroft and Peter D. Battle - *A study of carbon deposition on catalysts during the partial oxidation of methane to synthesis gas* - Catalysis Letters 22 (1993) 299-305.

[67] Michela Martinelli – *Application of the spatially resolved sampling technique to the analysis and optimal design of a CH4–CPO reformer with honeycomb catalyst* –Tesi di Laurea specialistica, Politecnico di Milano 2011.

[68] D. Novati, A. Perico – *Caratterizzazione dello scambio di materia in filtri metallici utilizzati come supporti per catalizzatori strutturati* - Tesi di Laurea specialistica, Politecnico di Milano 2005-06.

[69] A.Donazzi, D.Pagani, A.Lucotti, M. Tommasini, A. Beretta, G.Groppi, C.Castiglioni, P.Forzatti – *Kinetic analisys and Raman surface characterization in the CPO of methane and propylene*- 2012.

[70] E. Ranzi, A. Sogaro, P. Gaffuri, G. Pennati, T. Faravelli, Combust. Sci. Technol. 1994, 96, 279 – 325.

[71] A. Bitsch-Larsen, R. Horn L.D. Schmidt - *Catalytic partial oxidation of methane on rhodium and platinum:Spatial profiles at elevated pressure* - Applied Catalysis A: General 348 (2008) 165–172.

[72] C.T Goralski Jr., L.D Schmidt -*Modeling heterogeneous and homogeneous reactions in the high-temperature catalytic combustion of methane*-Chem. Eng. Sci. 54 (1999) 5791.

[73] M. Hartmann *, T. Kaltschmitt, O. Deutschmann - *Catalytic partial oxidation of higher hydrocarbon fuel components on Rh/Al2O3 coated honeycomb monoliths* - Catalysis Today 147S (2009) S204–S209.

[74] Aniello Fierro - *Short contact time CPO of light hydrocarbons explored through advanced experimental and modeling techniques*- Tesi di Laurea specialistica, Politecnico di Milano 2012.

[75] Livio et al. - *Experimental and Modeling Analysis of the Thermal Behavior of an Autothermal C3H8 Catalytic Partial Oxidation Reformer* - Ind. Eng. Chem. Res. 2012, 51, 7573–7583.

[76] A. Donazzi, D. Livio, M. Maestri, A. Beretta,* G. Groppi, E. Tronconi, P. Forzatti - *Synergy of Homogeneous and Heterogeneous Chemistry Probed by In Situ Spatially Resolved Measurements of Temperature and Composition* - Angew. Chem. Int. Ed. 2011, 50, 3943 – 3946.